University of Oviedo

Ph.D. Program in Energy and Process Control

Hydrodynamic self-excited vibrations in leaking spherical valves with annular seal

Hesham EL-Sayed Saber EL-Sayed

Ahmed Awad

Hydrodynamic self-excited vibrations in leaking spherical valves with annular seal

A dissertation submitted in accordance with the requirements of the
degree of Doctoral of Philosophy (Energy and Process control)

Submitted By:

Hesham EL-Sayed Saber EL-Sayed Ahmed Awad

Fluid Mechanics Area

Department of Energy

University of Oviedo

Gijon, Asturias, Spain

November – 2021

DECLARATION

I hereby certify that this work, submitted by me for assessment on the programme of study leading to the award of Doctor of Philosophy, is all my own work and contains no Plagiarism. By submitting this work, I agree to the following terms:

> *Any text, diagrams or other material copied from other sources (including, but not limited to, books, journals, and the internet) have been clearly acknowledged and cited followed by the reference number used; either in the text or in a footnote/endnote.*

PhD candidate: Hesham EL-Sayed Saber EL-Sayed Ahmed Awad

Registration number:

Email:

Signed:

Date:

ACKNOWLEDGMENT

The Ph.D. candidate acknowledges firstly his family for the continuous support through the whole period of study. The candidate also appreciates prof. Jorge Parrondo for his patience, support, good manners, and his abundant explanation through the problems countered during the study. In addition, I want to thank him for showing me many places in Spain like Oviedo, fishermen village and many other places.

The candidate acknowledges the financial support received from the Arab Academy for Science, Technology & Maritime Transport (AASTMT) for Ph.D. financial support, as well as the Erasmus scholarship grant KA107 awarded to the candidate.

Special thanks are given to Mr. Alberto Rúa-Figueroa, manager of the Salime hydropower plant, for his collaboration and assessment. Besides, I want to thank all the other Ph.D. students in the department for their help through the whole period and for pushing each other to achieve the degree.

ABSTRACT

In hydraulic systems with large diameter pipes, such as the penstocks of hydro power plants, ball or spherical valves are frequently used because they are robust and, in closed state, they allow to obtain watertight closures even under large pressure differences. To preclude possible water leakage between the internal rotary sphere and the casing, those valves have a metallic annular seal that can be tightened axially onto the ball, thus blocking the clearance. However during the last decades there have been several cases of violent vibrations developed in hydraulic systems that use that type of spherical valves, such as the Salime hydro power plant in Asturias (Spain). These vibrations happen to take place when the valves are closed, and are associated to the successive tapping of the annular seal against its seat on the ball. At the same time, large pressure fluctuations are induced in the piping as well as periodic leakage flow through the gap between seal and sphere. Since plant security requirements make these vibrations unacceptable, at the Salime hydro plant the problem was finally solved by installing an external pneumatic drive to strengthen the tightness of the seals. However, the nature of the vibration excitation and the conditions that originated it were still not understood, and so that encouraged the research of the present doctoral thesis.

The general purpose of this research has been to establish a simplified theoretical model for the hydraulic-mechanical system of interest, so that the model can reproduce the vibration excitation mechanism, simulate the transient behavior of the system as a function of the most relevant physical and geometrical parameters and advise on the conditions needed for safe operation without vibrations.

As a starting hypothesis, it was assumed that the vibration excitation only takes place if, due to manufacturing or mounting defects, the seal closure is not perfect and so there exists some initial leak flow. On that hypothesis a simplified physical-geometrical model was proposed to represent the flow-structure system of interest, which includes the penstock of the hydro station, the annular seal of the valve as a mobile structural element and an auxiliary pilot conduit to govern the tightness of the seal. The seal was modeled as a second order mechanical system subject to fluid-dynamic pressure forces, whereas each duct in the system was represented by the

basic equations of continuity and energy conservation for 1D viscous unsteady flow, with incompressible and compressible flow versions. All this results in a closed system of non-linear differential equations with time-dependent variables such as the flow rate at each pipe section, the head energy at the nodes of the system and the displacement of the annular seal.

To begin with, the flow in the ducts was considered to be incompressible. After linearizing the equation system under the assumption of small amplitude harmonic disturbances around an equilibrium state, an algorithm for iterative resolution was elaborated that ultimately allows determining the frequency and the net damping of the coupled flow-structure system. According to this model, the development of high amplitude vibrations takes place when the net damping is negative, i.e., vibrations are self-excited and the underlying mechanism is a damping-controlled dynamic instability. For the second model, the flow in the pipes was considered to be subject to compressibility and pipe wall elasticity and so it was modelled with the usual equations in water hammer studies. In this case, a frequency domain formulation was chosen based on transfer matrices between nodes along the system piping. Again, the model allows to estimate the fluid-dynamic forces on the annular seal and to analyze the stability conditions for the coupled flow-structure system.

A dimensional analysis based on these models led to establish the non-dimensional parameters relevant in the phenomenon under study, which include ratios between mechanical energy, head loss and inertia head terms, ratios between geometrical variables, parameters involving the seal structural variables and, in the case of the compressible flow model, ratios between acoustic and mechanical variables. For both incompressible and compressible flow models, iterative resolution algorithms were designed and special computation programs were developed by means of the Matlab software. Computations were performed to characterize the dynamic behavior of the system and determine the critical conditions for stability under different configurations of the physical and geometrical parameters. As a whole, the results so obtained are consistent with the previous observations at the Salime hydro power plant on the vibration phenomenon, including the suppression of the vibrations when strengthening the seal tightness by external means. Therefore, it follows that the self-excitation mechanism implicitly assumed in the theoretical models can be considered

correct. Besides, the results show that the compressibility of the medium and acoustic transmission can have a decisive effect on the fluid-dynamic forces on the seal and on the system stability; in the case of the Salime hydro plant, consideration of flow compressibility is necessary. In all cases, the operating range of the system under stability conditions was enlarged when increasing the hydraulic resistance of the pilot line, e.g. by means of a partially closed valve.

RESUMEN:

En sistemas hidráulicos con tuberías de gran diámetro, como las tuberías forzadas de centrales hidroeléctricas (C.H.), se suelen usar válvulas de bola o esféricas, pues son robustas y, con la válvula cerrada, consiguen cierres estancos incluso ante grandes saltos de presión. En concreto, para impedir fugas de agua entre la esfera interior rotatoria y la carcasa, esas válvulas disponen de un sello o junta anular metálica que se puede apretar axialmente contra la esfera en el intersticio, bloqueándolo. Sin embargo, en las últimas décadas se han registrado varios casos de vibraciones violentas en sistemas hidráulicos que emplean ese tipo de válvulas, como por ejemplo en la C.H. de Salime (Asturias). Estas vibraciones suceden con las válvulas en estado de cierre, se asocian al sucesivo golpeteo del sello anular contra su asiento y van acompañadas de grandes fluctuaciones de presión en los conductos y de caudal de fuga periódico. Estas vibraciones son inaceptables para la seguridad de la instalación, y en la C.H. de Salime se lograron suprimir mediante un accionamiento neumático externo para reforzar el apriete de los sellos. Aun así, seguía sin comprenderse la naturaleza de la inducción de las vibraciones ni en qué condiciones se originaban, lo que dio pie a la presente investigación.

El propósito general del estudio ha sido establecer un modelo teórico simplificado para el sistema mecánico-hidráulico de interés que fuera capaz de reproducir el mecanismo de excitación de vibraciones, simular el comportamiento transitorio del sistema en función de sus parámetros físicos y geométricos y asesorar sobre las condiciones necesarias para asegurar la operación de estos sistemas sin vibraciones.

Para ello, se asumió como hipótesis inicial que la excitación de vibraciones solo ocurre si, por defectos de fabricación o montaje del sello, el cierre no es perfecto y existe pues un cierto caudal de fuga. Sobre esa idea se ha propuesto un modelo físico-geométrico simplificado que incluye la tubería forzada de la central, el sello anular de la válvula como elemento estructural móvil y una conducción auxiliar de pilotaje que gobierna el apriete del sello. El sello se modeló como un sistema mecánico de segundo orden sujeto a fuerzas fluidodinámicas de presión, mientras que en cada conducto del sistema se consideraron las ecuaciones básicas de continuidad y energía mecánica para flujo 1D viscoso y no estacionario, con versiones de flujo incompresible y compresible. Todo ello resulta en un sistema cerrado de ecuaciones diferenciales no lineales con diversas variables dependientes del tiempo, que incluyen el caudal en cada tramo, la altura de energía en distintos nodos del sistema y el desplazamiento del sello anular.

Primero se contempló el caso simplificado de flujo incompresible. Tras linealizar el sistema de ecuaciones asumiendo perturbaciones armónicas de pequeña amplitud en torno al punto de equilibrio, se elaboró un algoritmo de resolución iterativa que, en último término, permite determinar la frecuencia y el amortiguamiento neto del sistema acoplado flujo-estructura. Según este modelo, las vibraciones se desarrollan cuando el amortiguamiento neto es negativo, concluyendo pues que se trata de un fenómeno de inestabilidad dinámica o autoexcitación controlada por amortiguamiento. Para el segundo modelo se consideró flujo con compresibilidad y tuberías de pared elástica, según las ecuaciones habituales en estudios de golpe de ariete. En este caso, se adoptó una formulación en el dominio frecuencial basada en matrices de transferencia entre nodos del sistema hidráulico. De nuevo, el modelo permite determinar las fuerzas fluidodinámicas sobre el sello y analizar las condiciones de estabilidad del sistema acoplado flujo-estructura.

Sobre estos modelos se realizaron análisis para establecer los parámetros adimensionales relevantes, incluyendo relaciones entre términos de energía mecánica, pérdidas de carga y alturas de inercia de conductos, variables geométricas, variables estructurales del sello y, en el caso de flujo compresible, variables acústicas. Para ambos modelos se diseñaron y desarrollaron sendos programas de cálculo iterativo mediante Matlab, y se realizaron cálculos sobre el comportamiento dinámico del sistema y las condiciones límite de estabilidad bajo distintas configuraciones de los parámetros físico-geométricos. En conjunto, los resultados obtenidos son consistentes con las observaciones previas disponibles sobre el fenómeno en la C.H. de Salime, por lo que se considera que el mecanismo de autoexcitación implícito en los modelos es acertado. Además, los resultados muestran que la compresibilidad del medio tiene un efecto decisivo en las fuerzas sobre el sello y en la estabilidad del sistema, por lo que, en el caso de la C.H. de Salime, su inclusión es necesaria. En todos los casos, la estabilidad del sistema mejora al aumentar la resistencia hidráulica en la línea de pilotaje.

TABLE OF CONTENTS

LIST OF FIGURES

LIST OF TABLES

NOMENCLATURE

ν	Kinematic viscosity	$m^2\ s^{-1}$
ζ	Damping ratio (damping coefficient relative to critical damping)	
ρ	Fluid density	$kg\ m^{-3}$
ϕ	Seal diameter	m
ω	Angular frequency	$rad\ s^{-1}$
ω_{ref}	Reference angular frequency	$rad\ s^{-1}$
a_j	Sound speed at pipeline *j*	$m\ s^{-1}$
A_g	Seal clearance cross-section area	m^2
A_j	Cross-section area of pipeline *j*	m^2
A_{os}	Annular seal external surface area facing pilot pipeline	m^2
A_{ss}	Annular seal surface area facing gap flow	m^2
c_s	Seal structural damping coefficient	$N\ s\ m^{-1}$
c_{sg}	Seal structural damping coefficient corresponding to the circumferential length of the seal gap	$N\ s\ m^{-1}$
c^*_{eq}	Dimensionless equivalent damping coefficient	
c^*_w	Dimensionless added water damping coefficient	

d_j	Diameter of pipeline j	m
E	Modulus of elasticity	Pa
f^*	Dimensionless frequency	
f_j	Friction factor at pipeline j	
F	Equivalent hydro-dynamic force acting on the seal	N
g	Gravitational acceleration	m s^{-2}
H_{ej}	Total energy head at section j	m
h_{ej}	Time-dependent component of the energy head at section j	m
H_{oej}	Steady-state component of the energy head at section j	m
H_j	Total pressure head at section j	m
h_j	Time-dependent component of the pressure head at section j	m
H_{oj}	Steady-state component of the pressure head at section j	m
I	Seal area moment of inertia	m^4
I_j	$= L_j / (a_j Aj)$ = inertial head coefficient for pipeline j	s^2 m^{-2}
I_m	Imaginary component of a complex number	
k_s	Structural stiffness of the annular seal	N m^{-1}

$k_{s\,g}$	Equivalent structural stiffness of the annular seal corresponding to the circumferential length of the gap	N m^{-1}
k_{eq}^{*}	Dimensionless equivalent stiffness coefficient	
k_{w}^{*}	Dimensionless added water stiffness coefficient	
K_{j}	Hydraulic resistance through section *j*	m^{-5} s^{2}
K_{Lj}	Head loss coefficient for laminar flow through section *j*	m^{-2} s
L_{j}	Length of pipeline *j*	m
L_{o}	Circumferential length of the seal gap	m
L_{s}	Total circumferential length of the annular seal	m
m_{s}	Mass of the annular seal	kg
m_{sg}	Equivalent mass of the annular seal corresponding to the circumferential length of the gap	kg
m_{eq}^{*}	Dimensionless equivalent mass coefficient	
m_{w}^{*}	Dimensionless added water mass coefficient	
P_{j}	Static pressure at section *j*	Pa
Q_{j}	Total flow rate at section *j*	m^{3} s^{-1}
$Q_{o\,j}$	Steady-state component of the flow rate at section *j*	m^{3} s^{-1}

q_j	Time-dependent component of the flow rate at section j	$m^3\ s^{-1}$
Re	Real component of a complex number	
t	Time	s
v_{og}	Steady-state gap flow velocity	$m\ s^{-1}$
x	Distance along pipeline	m
y	Seal vibration displacement	m
y^*	$= y / y_{og}$ = dimensionless seal vibration displacement	
$\dot{y}$	Seal vibration velocity	$m\ s^{-1}$
$\ddot{y}$	Seal vibration acceleration	$m\ s^{-2}$
y_{og}	Average seal gap for the statically strained annular seal	m
y_{gu}	Average seal gap for the unstrained annular seal	m

1. CHAPTER ONE: INTRODUCTION

1.1 Spherical valves in hydro-electric power plants

Hydroelectric power plants have been in continuous development and use since the late nineteenth century. For many years until recent decades, they have been virtually the only power generation plants using purely renewable sources, namely the rainfall and snow precipitation at a certain altitude, in order to harness the associated gravitational potential energy. In 2020, the global cumulative installed capacity of hydropower stood at 1330 GW and the global hydroelectric generation reached about 4500 TW·h *(IEA 2021)*. The latter represents approximately one sixth of the world's total electricity consumption as in figure (1.1).

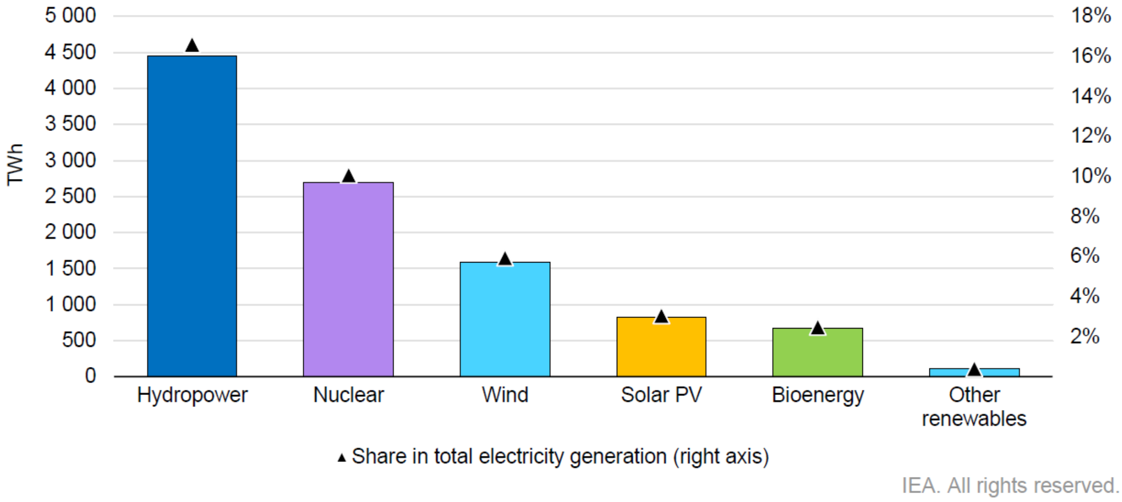

Figure 1.1: Low-carbon electricity generation by technology and shares in global electricity supply, 2020. Source: IEA (2021).

Especially in OECD countries, the potential for further deployment of hydroelectric plants is limited due to topographical restrictions, and so the projects developed in the last two decades have taken place mostly in emerging economies, in particular in China and the Asia-Pacific area as in figure (1.2) *(IEA 2021)*.

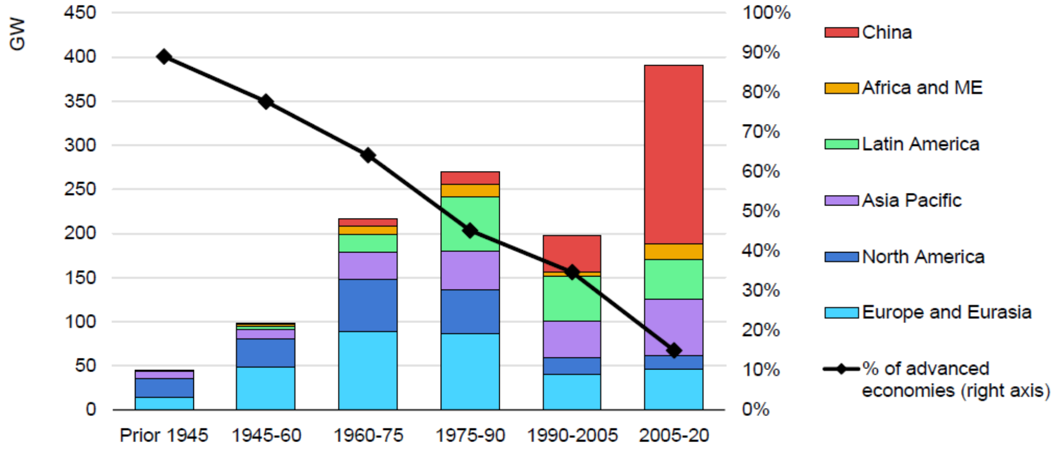

IEA. All rights reserved.

Notes: ME = Middle East. “Advanced economies” refers to OECD member countries and non-OECD EU member states.

Figure 1.2: Hydropower capacity additions by region. Source*: IEA (2021)*.

Despite the difficulties for the construction of new hydro plants, in the current scenery of worldwide transition to energy sources that are renewable, non-polluting and free of greenhouse gas emissions, the importance of the hydroelectric generation is growing quickly. This is so because the hydro power generation offers several advantages in comparison to other renewable energy sources:

- Accumulation: hydro energy associated to rain or snow can be accumulated as water at reservoirs with dams so that generation is not subject to sun exposure in daytime (like photovoltaic panels) or to weather conditions (like wind turbines).

- Flexibility: hydroelectric energy production can be easily regulated by controlling the water flow through the plant turbines in order to adapt it in real time to the fluctuations in electricity demand as well as in production from other sources (such as wind or photovoltaic).

- Surplus energy storage: in case of excessive electricity production from other sources (nuclear, wind, photovoltaic…) with respect to the demand, the surplus energy can be stored by means of hydro plants with pumped storage.

Conventional hydro power plants with dam and reservoir include the following hydraulic components: water intakes, penstocks, turbines, draft tubes and valves. Figure (1.3) shows a typical lay-out with the main elements.

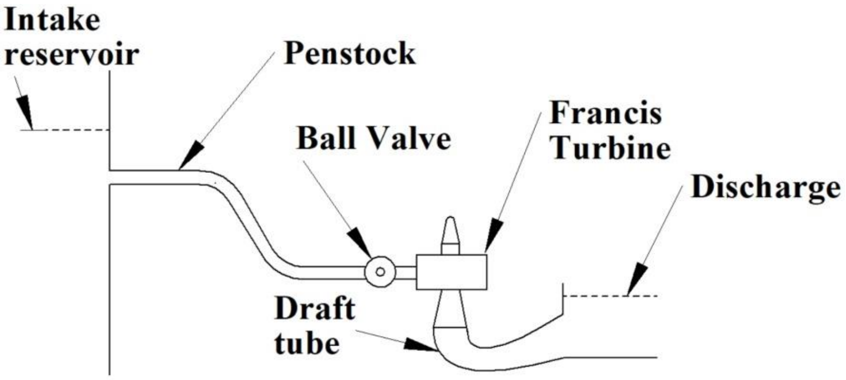

Figure 1.3: Schematic diagram with the main hydraulic elements in hydro plants.

As seen in figure (1.3), a butterfly valve is usually located close to the water intake and a spherical valve is placed at the downstream end of the penstock, right upstream of the turbine *(Gummer 2016, USSD 2017)*. These valves are not intended for regulation but to close the penstock and shut off the water flowing through the turbine when production stops. If a stop occurs during the usual operation periods due to temporary low demand, then only the spherical valve is closed, whereas in case of longer maintenance stops the upstream butterfly valve is to be closed as well.

Spherical valves consist in a large ball with a through bore that has the same diameter of the pipe *(Smith-Zappe 2004)*. The ball can be rotated 90 degrees inside a casing as in figure (1.4), so that the bore can quickly change from full alignment with the inlet and outlet ports (open state) to the perpendicular direction (closed state), with the only limitation in time maneuver due to water hammer (*Karadžić et al. 2010, Kolesnikov and Nikiforov 2014*). This design leads to valves that are robust and less prone to vibrations during maneuvers than other types while virtually no head losses are induced in the flow in open state even for large flow-rates. Additionally, spherical valves in closed state can achieve water tightness despite having to withstand high pressure jumps from one port to another of the valve. Because of this, spherical valves are especially suitable for applications involving the isolation of piping sections in hydraulic systems with large pipe diameter and high pressure differences, like in the case of reservoirs with dams. In particular, that is usually the case at the lower end of the penstocks in medium and high head hydropower plants, i.e. just upstream the turbine or the turbine governor.

Figure 1.4: A partially opened spherical valve (*Vortex Hydra Dams, 2021*).

In order to achieve water tightness when the spherical valves are closed (*Smith-Zappe 2004*), they usually incorporate two metallic seal rings that can be tightened onto an annular seat on the valve ball (shown partially in Figure (1.4)), so that the clearance between the rotating ball and the external casing of the valve becomes blocked. One of the ring seals, denoted as maintenance seal, is located at the upstream side of the valve, and the other one, denoted as service seal, is located at the downstream side. In general, the maintenance seal is applied only during long shutdowns for valve maintenance purposes. Instead, the service seal is always applied after the valve closure whenever the turbine stops for short periods of no energy demand during the daily operation of the hydro plant. When the turbine is to resume operation, first the service seal has to be released from the ball seat by shifting it a few millimeters, and then the ball can be rotated 90° to open state.

A high force needs to be applied on the seal ring for the back and forth sliding motion and, overall, to keep it tighten on the ball while in closed state. In the case of hydro power plants, it is customary to obtain such high force by using the upstream water pressure as in figure (1.5). The latter is conveniently transmitted onto an internal (release) or external (tightening) surface of the seal by means of an auxiliary or pilot line equipped with a directional valve as in figure (1.5).

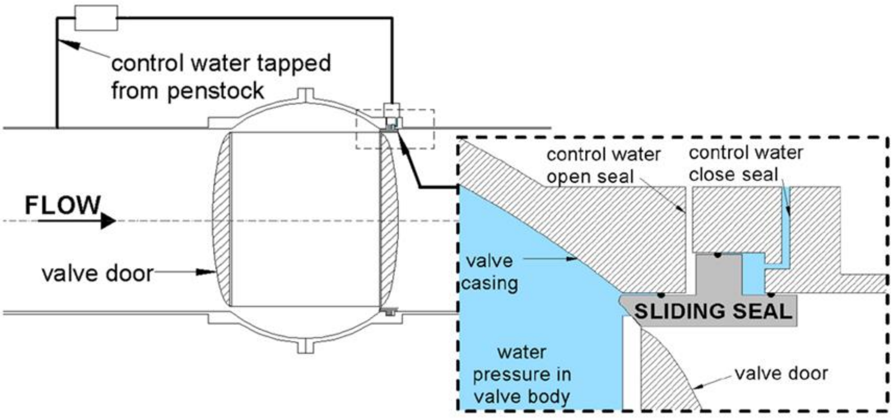

Figure 1.5: Sectional view of a spherical valve and detail of the annular sliding seal with opening and closing pressure lines (from *Kube et al. 2010*, adapted from *Nishihara et al. 2003*).

1.2 Vibration events with closed spherical valves at the Salime hydro power plant

The Salime hydroelectric power plant (*Saltos del Navia 2021*) is located in the south-western area of Asturias, Spain, in the middle course of the Navia River. It is an impoundment plant with a 128 m high gravity dam as in figure (1.6) and a nominal power of 160 MW, divided in four power units of 40 MW.

Figure 1.6: Dam, spillways, electrical substation and water discharge area of the Salime power plant

Each unit consists in a Francis turbine (nominal net head of 105 m and water flow of 42.5 m^3/s) coupled to an electric generator on a vertical shaft. The effective net head, however, can be up to 40% lower than the nominal value due to the variation in free surface level of the Salime reservoir depending on the time of year.

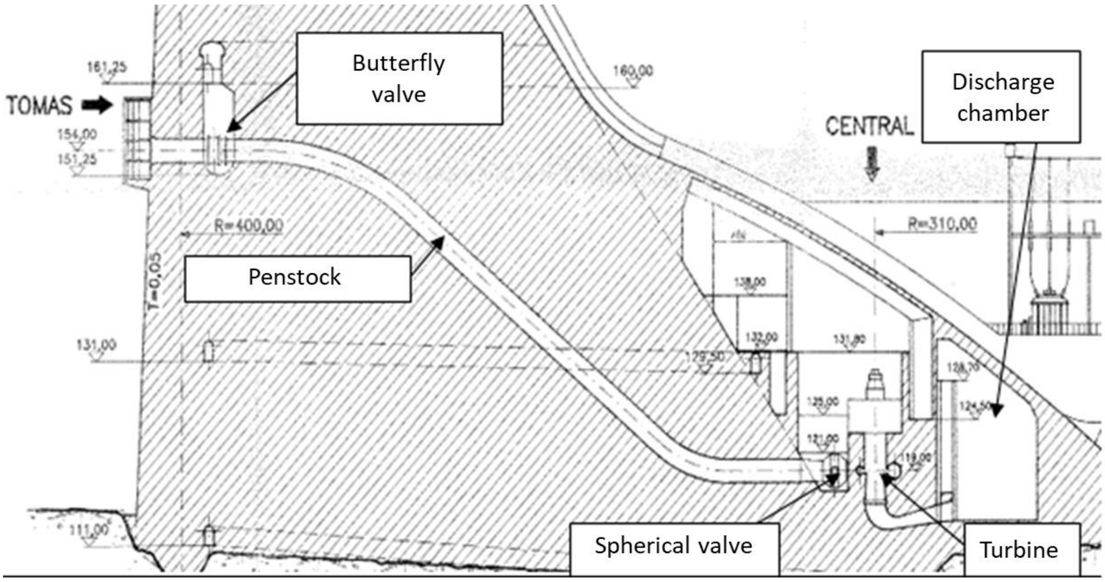

Figure 1.7: Lay-out of the main hydraulic elements for each unit of the Salime power Plant.

As a peculiarity of the Salime plant, the power house with the four turbine-generator units is located underneath the spillways of the dam as in figure (1.7). Besides, each unit possesses an individual penstock of 80 m long and 2.5 m in diameter as well as individual valves and control elements, so that every unit can operate independently of the others

In operation since the 1950s, the plant was progressively refurbished during the 2000s and early 2010s. In particular, the old spherical valves used inflatable seals to prevent leakage in closed state, but they presented some operation issues. Therefore, they were replaced by modern spherical valves with maintenance and service metallic ring seals (upstream and downstream side respectively). Figure (1.8) shows two pictures of the new spherical valves in the Salime plant, one before installation and the other one already installed in the penstock close to a turbine (seen from above).

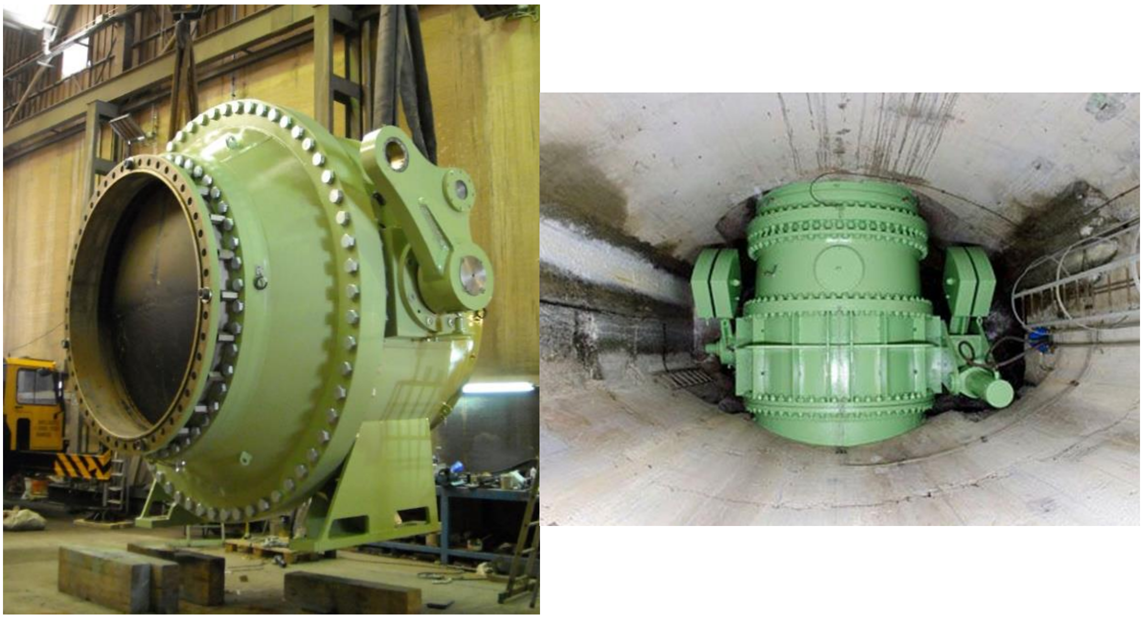

Figure 1.8: Spherical valves at the Salime power house, before (left) and after (right) installation.

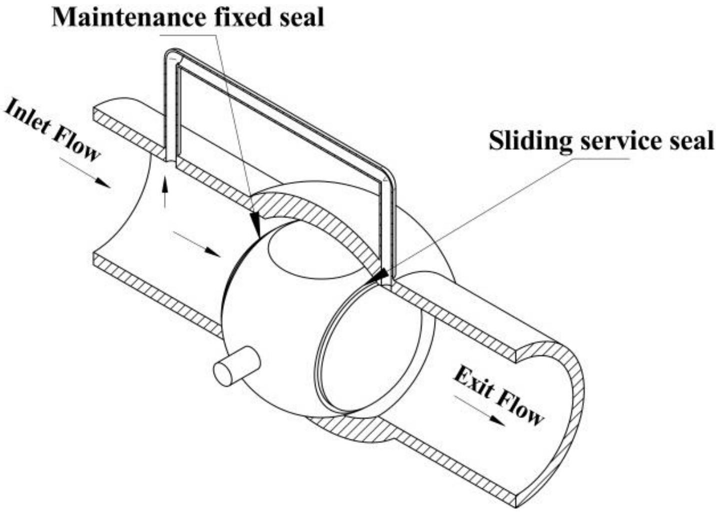

Figure 1.9: Spherical valve in closed position with auxiliary duct to transmit the penstock pressure

In practice the maintenance seal always remains fixed and only the service seal can slide to either opened or closed state, in a way similar to that of figure (1.5). An outline of the valve in closed state is presented in figure (1.9), including the auxiliary duct that transmits the upstream pressure to drive the service seal. Figure (1.10) shows a sectional view of the annular seal tightened on the ball seat, thus avoiding water leakage as corresponds to closed position. The seal has an internal diameter of 2.2 m

(6.9 m in perimeter) and the cross-section has a boot shape with 50 mm in the sliding direction as the largest dimension. Figure 1.11 shows a spare ring seal as well as the corresponding annular seats to be mounted on the ball surface and on the internal surface of the casing.

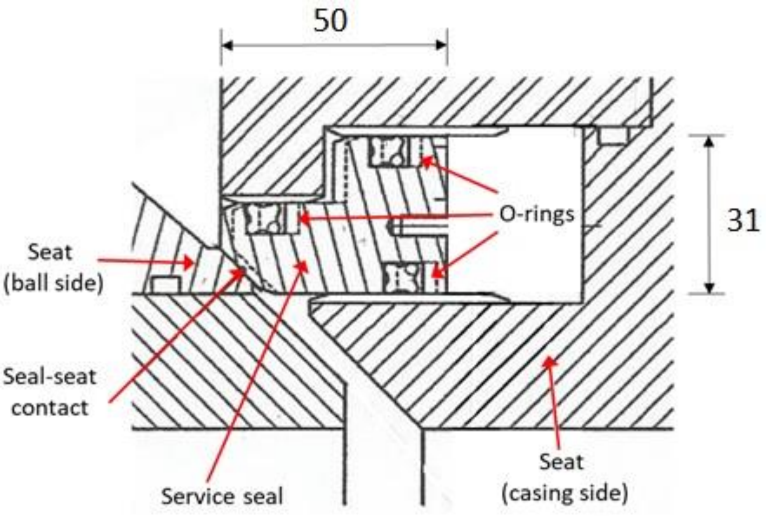

Figure 1.10: Sectional view of the service seal tightened on the ball seat (closed position). Dimensions in mm.

Figure 1.11: Replacement annular seal and annular seats at the Salime power house.

However, sometime after the refurbishment of the power units and the spherical valves, the technicians of the plant began to observe events of violent vibrations in the hydraulic system of some power units when they were off. At first, the vibratory episodes were sporadic and seemed to affect only unit #2, but progressively similar vibratory events were reproduced at the other power units as well. These vibrations, which happened to take place once the spherical valves were closed and the annular seals tightened, were associated to the successive hitting of the seal against its seat on the ball, and so they would be accompanied by periodic leakage flow through the intermittent gap between ball and seal. According to the subjective perception of the plant technicians, the tapping frequency would be of the order of 1-2 Hz. Additionally, the likeliness of the vibratory events might increase when the water level in the reservoir was below the highest value, but no clear trend was established by the technicians.

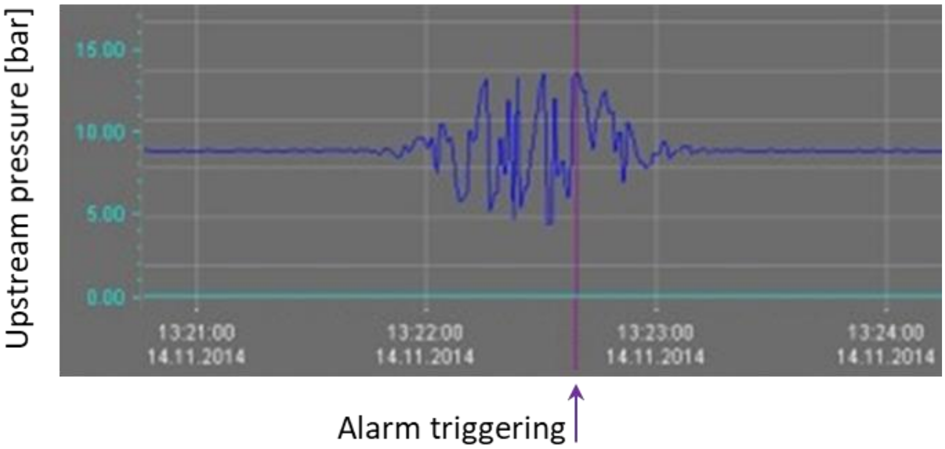

Figure 1.12: Upstream pressure signal recorded during a vibratory episode of the valve of unit #3 (*Saltos del Navia 2014*).

Simultaneously with the vibrations in a spherical valve, large pressure fluctuations were induced in the penstock and auxiliary piping. The latter was verified by means of pressure transmitters located at an auxiliary duct that connected the penstocks upstream the spherical valves. Figure (1.12) shows the pressure signal recorded during a vibratory episode at power unit #3 on the 14th of November of 2014, several minutes after a shutdown of that unit (*Saltos del Navia 2014*). The level at the reservoir was 24.9 m below the highest value, which represents a gross head 23% lower than in nominal conditions. During the vibratory episode, the power unit #1 continue with normal operation at 10 MW, whereas the other two groups had already been stopped for some time and did not develop any vibration.

The acquisition system available at the Salime plant allows to register only one data per second and so the signal quality is too poor to attempt a proper dynamic analysis. However, it is readily seen in figure (1.12) that pressure at the sensor position fluctuated with increasing amplitude until reaching a value of 13.5 bar. At that point a security alarm was automatically triggered, which led to the disconnection of the hydraulic unit and to the closure of the double butterfly valve located close to the penstock intake. As seen in figure (1.12), this operation was effective in stopping the vibration episode, but in general it is considered an undesirable measure because:

- there may be a high water leak,
- the subsequent start-up operation of the power unit is more complex and longer than under usual conditions and
- there are no more security measures to be taken in case of another unexpected event.

In any case, these vibration phenomena are unacceptable due to both security and operating reasons, and other correction measures had to be explored to prevent the vibration events in the Salime hydro plant. Considering that the vibrations might develop due to an insufficient tightening force on the seals from the upstream water pressure, it was decided to strengthen the seal tightness of a valve by applying an independent force, in particular by means of an external pneumatic drive. This proved to be effective in preventing the vibrations and so the problem could be solved at the Salime plant by installing the same system for the four power units. Even so, new vibratory events could still be observed in the plant when the pneumatic drives were not in operation.

Indeed, these vibration phenomena are likely to have occurred at other plants or sites with similar spherical valves. However, to our knowledge no case has been analyzed in the scientific literature in recent years, and only a few cases appear to have been reported in professional congresses of the hydro power sector more than ten years ago. Probably the most documented case corresponds to the Gordon power station in Tasmania (Australia), a hydro plant with 3 units of 150 MW each. *Caney and Zulovic (2004)* reported a severe incident with self-excited pressure pulsation in the penstocks when the plant was totally shut down. To study the phenomenon, special tests were conducted which included inducing controlled pressure pulsations in the penstocks.

After a process of elimination, the research focused on the service seals of the spherical valves, and three possibilities were considered for the cause of the excitation: leakage past the main sealing face, leakage past the O-rings of the seal and malfunction of the directional valve that connects the high pressure water to open or close the seal. Finally, the root of the problem was attributed to a damaged sealing face for the valve of Unit #2, which possibly produced some leakage flow. According to their report, no special correcting measure needed to be adopted. Later *Kube et al. (2010)* attempted to simulate the dynamic behavior of the Gordon hydro plant as observed in *Caney and Zulovic (2004)* dynamic tests, as a first step towards explaining the occurrence of the vibrations. However their results, which focused on the prediction of the characteristic frequencies, were preliminary and inconclusive.

The observations of the phenomenon at both Salime and Gordon plants suggest that the vibrations take place when the tightening force is not high enough and the resulting sealing is not perfect due to manufacturing or mounting defects, i.e., when there is some leakage between the ball and casing of the valve. Nonetheless, the mechanism that excites the vibrations is unclear, as well as what conditions in the system can lead to the development of the vibrations or preclude them.

1.3 Objectives of this research

The general purpose of this doctoral thesis has been the elaboration of a simplified theoretical model for the hydraulic-mechanical system of interest, i.e., that of conventional hydro power units at shutdown state that include spherical valves with sliding seal rings, so that the model can:

- simulate the transient behavior of the system as a function of the relevant physical and geometrical parameters,
- reproduce and explain the mechanism that excites the vibrations observed at the Salime plant and
- advise on the conditions under which the vibrations may develop, and the conditions needed to ensure safe operation without vibrations.

In relation to that general purpose, several specific objectives were considered, some of them methodological and some other focused on the phenomenon under study, as follows:

Methodological objectives:

- determine the hypothesis and the key components of the mechanical-hydraulic system that are necessary for the vibration development,
- propose models for the annular seals as the dynamic structural element of the system,
- propose unsteady formulations for the flow through the system under both incompressible and compressible assumptions,
- explore formulations in the time and frequency domains and
- determine the non-dimensional parameters that are relevant for the phenomenon.

Phenomenological objectives:

- determine the fluid-dynamic forces on the annular seals and the resulting frequency and damping characteristics of the system,
- explain the nature of the mechanism that triggers the vibrations, as well as the observations made at the Salime and Gordon plants,
- establish limit or critical conditions for the development of the vibrations,
- explain the effect of the gross head and other relevant parameters of the system,
- propose correction or design measures that help prevent the vibrations.

1.4 Contents of the thesis book

Following this introduction chapter, Chapter 2 provides a brief overview of the fundamental aspects relative to modeling transient flows in pipes, which need to be considered for the elaboration of the theoretical model of the system of interest, as well as the general types of fluid-dynamic excitation that can take place in hydraulic systems and the corresponding response of the affected structures in the form of vibration. Finally, a literature survey is provided on published studies related to vibrations with valves in hydraulic plants and, since those studies are very few, also with other types of valves that have elastically supported restriction elements.

Chapter three comprises the theoretical models utilized to explain the hydraulic transient behavior occurred at the Salime power plant. To explain this phenomenon two models are presented in chapter three. The first model is the incompressible flow model considering linear and non-linear head losses, while the second model is the compressible flow model, which considers linear friction losses. In each model system governing equations are presented as well as the reasons behind each model development. Moreover, the annular seal characteristics such as annular seal mass, stiffness, and damping coefficients are estimated at the beginning of the chapter.

Chapter four is the results and discussion chapter. In chapter four results developed from the previously mentioned models are presented and discussed.

Chapter five is the conclusion chapter. The conclusion chapter presents the fulfillment of research objectives, the main finding of the research and the different model's ability to explain the phenomenon. Furthermore, future work research possibilities are outlined at the end of the chapter.

Appendixes A and B at the end of the book give an abundant derivation of the governing equations and the dimensionless analysis Π-groups for the two mentioned theoretical models.

2. CHAPTER TWO: FUNDAMENTALS AND LITERATURE SURVEY

2.1 Modeling of unsteady flow in hydraulic systems

Any problem of structural vibration in a hydraulic system for which some type of fluid-dynamic excitation is presumed must consider the associated unsteady flow along the conduits of that system. In general the unsteady flow in pipes can be divided into two categories: slowly varying flows and rapidly varying flows.

In the case of slowly varying flows or slow transients, the local flow acceleration induces pressure variations in the pipes that may be significant but not high enough for the fluid to exhibit compressibility effects. Therefore, in the case of a hydraulic pipeline, the flow can be considered fully incompressible (*Karney 1990*). Slowly varying unsteady flow in a pipe between two positions *1* and *2*, with energy heads H_{e1} and H_{e2}, can be modeled by means of a 1D energy equation that incorporates an inertial head term H_{IN} (*Massey and Ward-Smith 2006*):

$$H_{e1} - H_{e2} = h_p + H_{1N}$$

where h_P represents the viscous head loss and, for a common pipe with constant cross-section A and a distance L_{12} between positions *1* and *2*:

$$H_{1N} = \frac{1}{g}\int_{1}^{2} \frac{\partial v}{\partial t}\, dx = \frac{1}{g}\int_{1}^{2} \frac{\partial Q}{\partial t}\, dx = \frac{L_{12}}{gA}\frac{\partial Q}{\partial t}$$

This means that the flow rate Q depends on time but, at any given time instant, the flow rate along the pipe is constant. In the case of a hydraulic network with several pipes, the application of the energy equation leads to a system of differential equations of first order that are nonlinear depending on the head loss term. That system of differential equations becomes closed when complemented with the continuity equations at the junctions, which are algebraic. Then the flow evolution along time from a given initial state can be calculated numerically by means of a finite difference method, either explicit or implicit (*Wylie and Streeter 1993, Kolkman and Jongeling 2007b*). Alternatively, the system of equations can be linearized about a state of equilibrium in order to analyze the dynamic behavior of the system after a small initial disturbance and estimate the corresponding eigen-frequencies and net damping of the physical system (*Parrondo et al. 2002*).

In the case of rapidly varying flows or fast transients, with high local flow acceleration, the induced pressure variations may be high enough to induce fluid compressibility and pipe elasticity effects. This means that the flow variations do not take place simultaneously along the pipes, but, rather, they propagate at the sound speed of the pipe (*Fox 1977, Wylie and Streeter 1993, Massey and Ward-Smith 2006*):

$$a = \frac{1}{\sqrt{\rho\left(\frac{1}{K} + \frac{d}{t_w\, E}\right)}}$$

A common case of a fast transient is the water hammer induced in pipes after the abrupt closure of a valve. This leads to high amplitude pressure fluctuations at any position in the pipes (*Adamkowski 2001, Karadžić et al. 2010*), which result from the combination of successive transmissions back and forth of perturbations with high and low pressure values after the partial or full reflection at pipe elements (*Massey and Ward-Smith 2006*).

The basic govern equations (continuity and momentum conservation) for 1D unsteady flow with compressibility effects form a system of two differential equations with nonlinear terms and partial derivatives of the pressure head and flow rate with respect to position and time. Considering a horizontal pipe and neglecting the convective variation terms as usually adopted in water hammer studies (*Karney 1990, Wylie and Streeter 1993, Chaudhry 2014*), the govern equations become simplified to:

Continuity equation: $$\frac{g\, A_j}{a_j^2}\frac{\partial H}{\partial t} + \frac{\partial Q}{\partial x} = 0$$

Momentum equation: $$\frac{\partial H}{\partial x} + \frac{1}{g\, A_j}\frac{\partial Q}{\partial t} + \frac{f_j Q^n}{2gd\, A_j^n} = 0$$

The numerical resolution of these equations can be performed in the time domain by means of the method of characteristics (*Wylie and Streeter 1993*), for which the basic equations with partial derivatives are strategically transformed into two other equations (called characteristic equations) that only contain total time derivatives of the pressure head and flow rate. The latter are to be integrated along specific time-space paths so that the values of the velocity and pressure head at a set of nodes along each pipe can be determined for successive time steps. In the case of nodes at the ends of the pipes, specific boundary conditions have to be imposed depending on the type and properties of the next pipe or element connected. Besides, the boundary conditions can vary along time, as happens in cases involving surge tanks, trapped air or pressure relief valves (*Parrondo et al. 2005, Riasi and Tazraei 2017*).

Alternatively, the numerical resolution can be performed in the frequency domain under the assumption of low amplitude perturbations about the equilibrium state of the system so that the govern equations can be linearized. Two techniques are usually considered, often in combined form: the impedance method and the transfer matrix method. The former is based on establishing relationships between the fluctuations in head pressure and mass velocity at specific positions of the domain of interest. The method of transfer matrices, as the name implies, is based in matrices that allow to determine the fluctuations in head pressure and mass velocity at a given node of the hydraulic system if those fluctuations are known at another node (*Wylie-Streeter 1993, Chaudhry 2014*). Each component in the system has its own transfer matrix between the end nodes, with entries that are complex (modulus and argument, or real and imaginary parts) and dependent on the fluctuation frequency. For instance, the transfer matrix corresponding to a pipe of length L between the end positions, denoted as L and R, is given by (*Chaudhry 2014*):

$$\begin{bmatrix} q \\ h \end{bmatrix}^L = \begin{bmatrix} \cosh(\mu L) & -\frac{1}{Z}\sinh(\mu L) \\ -Z\sinh(\mu L) & \cosh(\mu L) \end{bmatrix} \begin{bmatrix} q \\ h \end{bmatrix}^R$$

where μ is the complex wave number of the pipe and Z is the pipe characteristic impedance (see section 3.4.1).

2.2 Types of fluid-dynamic excitation and structure response

Whenever there is a transient flow in a system, or a flow with velocity components fluctuating about local average values, there exists some degree of unsteady stress in the flow field. This unsteady stress, which comprises both shear stress and normal or pressure stress, is usually referred to as fluid-dynamic excitation, because it produces a dynamic load on any given surface that bounds the flow or is immersed in it. In consequence, any structure with elastic properties (as is the case of all real structures) will produce some response in the form of unsteady deformation, i.e, vibration. Different types of flow excitation and structure response may be considered, which require different approaches for their analysis (*Naudascher and Rockwell 1994*).

Fluid-dynamic excitation may be provoked by an external source or may be self-generated in the flow itself (*Naudascher 1991*). The former implies that the flow domain possesses boundaries with properties that change in time. For instance, this would be the case of ducts or pipes with walls vibrating due to being structurally linked to an external motor, engine or any another vibrating structure. It would also be the case of having a partially pulsating flow as typically supplied by reciprocating machinery or even turbomachinery like centrifugal pumps when operating at off-design conditions. Often such fluctuations involve normal stresses that propagate through the fluid medium at the speed of sound. This excitation can be discrete at one or several frequencies, e.g., at the rotation frequency or the blade-passing frequency of a pump (*Parrondo et al. 2002, Hayashi and Kaneko 2014*), or may have a broad-band frequency distribution, e.g., turbulence of the incoming flow or random wall vibration.

On the other hand, even when the boundaries of the flow domain are totally stationary, an initially steady flow may happen to be unstable so that flow fluctuations grow up to a certain level. Frequently the instability processes are associated to shear flow, like in the turbulent boundary layers adjacent to walls, or the shear layers of wakes from immersed bodies (*Naudascher 1991*). These processes are usually dependent on the Reynolds number. They produce fluctuations in the form of eddies that travel downstream convected by the flow, and also produce fluid-dynamic acoustic noise that propagates at the speed of sound. Flow unsteadiness can be also produced by other types of phenomena such as interface instability, swirling-flow instability, bi-stable flow switching, cavitation, chemical processes, etc. (*Naudascher 1991, Blevins 2001*). Again, the associated flow excitation can have a broad-band spectrum, like cavitation or the turbulence itself, or can be discrete, like the periodic vortex shedding from bluff bodies.

According to the relationship between fluid-dynamic excitation and structural response, three categories are usually considered: forced excited vibrations, self-controlled vibrations and self-induced vibrations (*Naudascher and Rockwell 1994*).

2.2.1 Forced excited vibrations

They are also referred to as extraneously induced vibrations (*Naudascher and Rockwell 1994*). This category covers the cases in which the flow excitation is not affected by the response of the neighboring structures. In such cases the frequencies of the induced vibrations are equal to the frequencies of the excitation forces. In general, the amplitude of the vibrations induced in this category is not large, and, from a structural point of view, the possibility of failure is usually related to long-term fatigue. Nonetheless, the vibration response for a given value of excitation magnitude is frequency dependent and the vibration amplitude can increase considerably as the excitation frequency approaches the natural frequencies of the structure, i.e., when there is structural resonance (*Budynas and Nisbett 2017, Rao 2017*). Since the structure response is frequency dependent it can be characterized by means of force-displacement transfer functions. Examples of forced vibrations are the turbulent buffeting on structures subject to wind or cylinder arrays under cross-flow (*Weaver and Fitzpatrick 1988, Païdoussis 2006*).

Therefore, in the case of hydraulic systems subject to forced excitation, the analysis of the system may be conducted in two separate independent stages: one to determine the fluid-dynamic forces applied on the structure without any consideration of the structure response, and the other one to characterize the vibration response of the structure when subject to some given force pattern of interest, without any consideration to the fluid-dynamics processes that produce that force. This is usually referred to as one-way flow-structure interaction.

2.2.2 Self-controlled vibrations

They are also referred to as movement-controlled vibrations (*Naudascher and Rockwell 1994*). If, due to some fluid-dynamic excitation initially present in the flow, a structure vibrates with large amplitude, then the surrounding unsteady flow may be significantly affected by the structure motion, up to the point of becoming modulated or controlled by the vibration itself. A classical example is the lock-in phenomenon of cylinders under cross flow when experiencing vortex shedding with an excitation frequency that approaches the natural frequency of the structure (added mass included): then the expected vortex shedding frequency (as would correspond to a Strouhal number dependent on geometry and Reynolds number) can shift to the natural frequency of the structure where large amplitude vibrations take place due to structural resonance. Similar behavior can occur in case of acoustic resonance, i.e., when the frequency of the fluid-dynamic excitation approaches an acoustic natural frequency of the hydraulic system so that a high amplitude standing wave develops (*Weaver and Fitzpatrick 1988, Blevins 2001*).

From the point of view of excitation removal to prevent vibrations, this category of vibrations still can be treated as pure forced excited vibrations since there would exist flow excitation even if the structure was unable to vibrate (one-way flow-structure interaction). However the prediction of the response of the structure requires the joint consideration of both unsteady flow and structure motion, as corresponds to a two-way flow-structure interaction.

2.2.3 Self-induced vibrations

They are also referred to as self-excited vibrations and movement induced vibrations (*Naudascher and Rockwell 1994*). In this class of vibration phenomena, if the motion of the structures immersed in some flow is totally impeded, then the flow exhibits no fluctuation or excitation on the structures. Only when the motion restriction is removed and a structure departs from equilibrium, for instance due to a streak of turbulence, and starts to oscillate, does the flow show fluctuations, the greater the oscillations the greater the amplitude of flow fluctuations. This is so because the incoming flow around the structure has to evolve in order to adapt to the changing geometric contour; therefore, the associated fluctuating pressure field results in a dynamic force on the structure at the same frequency of the vibration. It is then the motion itself of the structure and the continuous reorganization of the surrounding flow that originates the fluid-dynamic force. Usually, the phase of the force relative to the displacement is such that the force opposes the motion, and the vibration gets damped quickly. Then the system is said to be dynamically stable. On the contrary, if the relative phase is such that the force supports the vibration, then the amplitude, which initially can be very small, can be expected to increase progressively. In consequence the vibrations are denoted as self-induced or self-excited (*Naudascher and Rockwell 1994, Blevins 2001, Kolkman and Jongeling 2007a*).

A system developing self-excited vibrations can be interpreted as a system whose net damping is negative, i.e., the system would be dynamically unstable. In these cases the vibration amplitude usually grows up until stabilizing at a high value, denoted as limit cycle oscillation. At this state of limit cycle oscillations, the influence of non-linear response terms compensates the driving fluid-dynamic forces, resulting in a zero net damping. Besides, there must be a continuous supply of energy from the incoming flow to the structure, where it is finally dissipated to heat due to the internal material deformations that manifest as positive structural damping. (*Naudascher and Rockwell 1994*).

Examples of hydraulic systems with potential to develop self-excited vibrations can be found in hydraulic gates (*Kolkman and Jongeling 2007b*), pumping systems (*Parrondo et al. 2005*), turbine systems (*Zhou et al. 2011, Valentín et al. 2017, Palikhe et al. 2019, Zhao et al. 2021*), hydraulic drives (*Schröders and Fidlin 2021*), cross-flow heat exchangers (*Weaver and Fitzpatrick 1988*), devices with leaking flows (*Inada and Hayama 1990a-b, Païdoussis 2006*), check valves (*Weaver et al. 1978, Wang et al. 2012*), energy harvesting devices (*Abdelkefi 2016, Wang et al. 2020*), etc.

The analysis of systems with self-excited vibrations always requires considering both flow excitation and structure motion jointly, as corresponds to a two-way flow-structure interaction problem. Hence, time-domain methods involving the continuity and momentum conservation flow equations together with the structure motion equation can allow to estimate the instantaneous values of the fluid-dynamic forces and the vibratory response, as well as its growth up to a limit cycle state if proper non-linear force terms and geometric boundary conditions are used (*D'Netto and Weaver 1987, Kolkman and Jongeling 2007b, Schröders and Fidlin 2021*).

A simplified approach is to linearize the governing equations by assuming small fluctuations about equilibrium. In particular, this can be used to estimate the frequency and net damping of the coupled hydro-mechanical system and to determine if it is dynamically stable or unstable. Besides, this may also be done in the frequency-domain by means of the transfer matrix method, which is efficient in characterizing the response of the systems of interest as a function of the frequency and in analyzing resonances (*Chaudhry 2014, Okasha et al. 2016*). However, the analysis of the linearized system, either in the time or the frequency domain, is not adequate to estimate the progression of the system to a limit cycle oscillation state, because that state is the result of non-linearities related to the structural properties (*Amabili 2018*) or boundary restrictions to amplitude growth that would lead to chattering (*Du and Zhang 2019, Gad 2021*).

2.3 Literature survey

2.3.1 Self-excited vibrations in hydraulic systems with leaking valves

According to the observations reported at the Salime Hydro Plant (*Saltos del Navia 2014*) on the vibration phenomena affecting the service seal of the spherical valves in closed state (see Section 1.2), it may be deduced that they correspond to the category of self-excited vibrations. This is in line with the conclusion of the study conducted by *Caney and Zulovic (2004)* for a similar vibration problem at the Gordon Power Station (see Section 1.2). While it is likely that the same sort of vibration phenomena has occurred at other hydro plants or hydraulic systems that use large spherical valves with annular seals, apparently the scientific literature does not contain any recent systematic study on the topic.

Probably the closest case is the vibration problem reported for the Bersimis hydro plant at Niagara Falls (USA) in the 1960s by *Abbott et al. (1963)*. Like in the present case for the Salime plant, large pressure fluctuations were observed in one of the penstocks of the plant, of 3.7 m in diameter, while the spherical valve was closed. In that case however, the seal was not a metallic ring but an inflatable one, as was customary at the time. The origin of the excitation was attributed to a slight leakage due to insufficient pressure on the inflatable seal, as it was found in experimental tests that the developed vibrations could be suppressed by opening a bypass from inlet to outlet of the leaking valve. In particular the bypass should be opened if the seal pressure was lower than the penstock pressure.

Wylie and Streeter (1965) continued the investigation by *Abbott et al. (1963)* on the vibration phenomena at the Bersimis plant, considering experiments with different configurations of seal tightness and state of valves and bypasses of the penstocks in the system. The analysis was accomplished by using the impedance method to detect the resonance conditions and the method of characteristics to model the whole system. The first case study considered that all penstock valves were closed, and all bypass valves were open except for penstock # 2. The second case study considered a leakage flow in penstock # 1 due to service seal pressure dropping to 30 % of the normal pressure. On this occasion, penstock valves # 2, 3 and 4 had no flow, but penstock valve # 5 was open. Finally, the last case considered a drop-down of service seal pressure to zero with operating turbines # 2 and 5 and standing turbines # 1 and 4. Impedance results on the characteristic frequencies of the system showed a significant agreement with both experimental data and the method of characteristics. Also, the predicted pressure and discharge oscillations exhibited good agreement with the experimental data. These results confirmed the key role of the leakage flow in the development of the vibrations.

Based on that study for the Bersimis plant, *Wylie et al. (1993)* and *Chaudry (2014)* compared the conditions of the leaking system leading to instability by means of the diagram of figure (2.1). For a normal stable valve, as in figure (2.1 a), it is noticed that a system disturbance developed by varying the leakage flow velocity from V_o to V_1 will decay over time until returning to steady-state conditions. In contrast, in figure (2.1 b) a system disturbance is amplified overtime for a leaking valve. The occurrence of one or another situation depends on how the pressure drop changes with the leaking flow: if the characteristic curve of the valve has a positive slope (the higher the flow rate the higher the pressure drop) then the system is stable. However if that slope is negative, as may occur if the seal clearance increases for lower pressure drop due a lower tightening force, then the system is unstable.

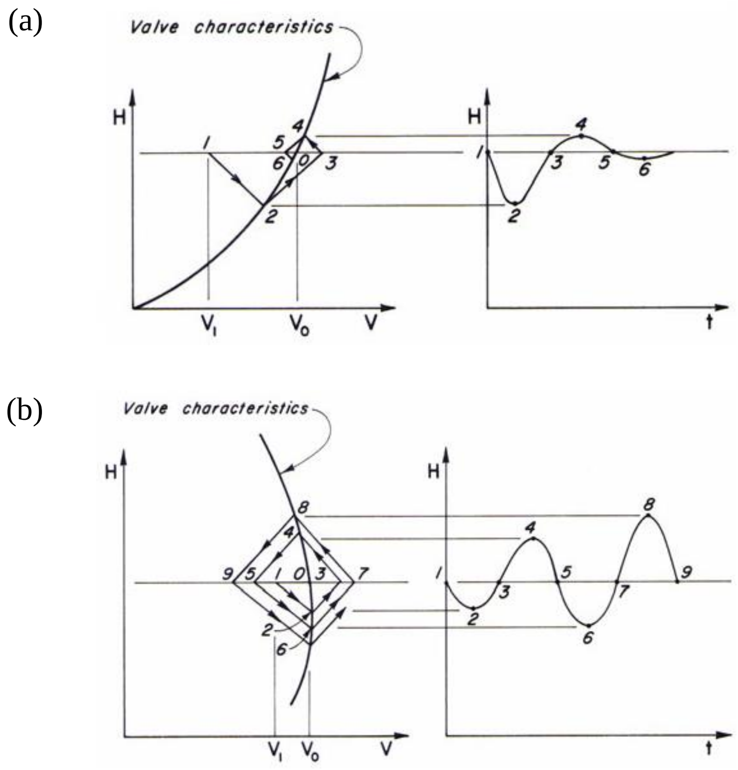

Figure 2.1: Stable (a) and unstable (b) behavior of a leaking valve (*Chaudry 2014*).

Another interesting vibration problem with a closed valve in a hydro plant was reported by *Gummer (1995)*, though in this case the valve was a head gate by the penstock intake. Gummer reported on severe penstock resonances registered at unit G1 of the Maraetai No. 1 hydro station (New Zealand). The penstock resonances were developed at load rejection or during priming. Again, the reason behind the penstock resonance development was found to be a seal malfunction at the head gate, resulting from poor oil pressure application. Experiments and analysis by means of the impedance method showed that resonance was developed at penstock second harmonic.

Mateos et al. (1996) reported another case of self-excited oscillations in a hydraulic pipeline with a gate valve in closed state, but with some leakage due to imperfect sealing. The authors analyzed the dynamic behavior of the system by means of the transfer matrix method, obtaining a good comparison with the experimental data on excited frequencies.

Kube et al. (2010). studied the penstock resonance phenomenon at Gordon hydro-electric power station (Australia) with the aid of commercial software named “Hytran solution”. The commercial software works on the principles of the method of characteristics and impedance model. Penstock resonance was found to be self-excited by seal leakage on the turbine main inlet valve. Results mentioned that the impedance model could locate the natural frequencies of the pipe network. However, a detailed study of the leaking valve seal characteristics and dynamics is still required to evaluate the risk of the self-excited penstock resonance phenomenon.

2.3.2 Self-excited vibrations with other types of valves partially opened

Contrary to the cases of vibrations with large leaking valves, the scientific literature contains many studies related to other types of valves, mainly check valves and, overall, pressure relief valves:

- Check valves are expected to fully open when flow goes in one direction and to close in the other direction. They may have a shifting or swinging plug or plate, or have an elastic component that opens or closes depending on flow drag (like in the duckbill valves).
- Pressure relief valves are very common, for instance, in high pressure hydraulic driving systems. Pressure relief valves are usually closed unless the fluid pressure goes above a certain critical value, which makes an internal plug element shift against a pre-loaded spring, thus opening the valve. The plug is usually a poppet (conical plug) or just a cover plate, though many other shapes are also possible. Besides, they are can be directly operated by the pressure of the incoming flow or pilot operated through certain valve passages.

In the case of check valves, vibration problems may appear if there is a pulsating flow, either externally imposed or self-generated. On the other hand, some pressure-relief valves happen to be prone to develop self-excited vibrations, i.e., they can easily induce fluctuating fluid-dynamic forces on the plug element that have a component in phase with the instantaneous velocity of the plug or closing element while it is oscillating. Indeed these two valve types are very different from the case of the spherical valves typical of hydro plants, both in terms of valve geometry and size and also with regards to the hydraulic system where the valves are installed. Nonetheless, similarities can still be established for the corresponding leak flows and the physical aspects involved in the induction of the destabilizing forces on the vibrating element.

In general, two types of physical phenomena can be considered to determine the phase between force and motion of the vibratory element:

- The inertia of the flow while trying to adapt to the continuous gap change during each oscillation.
- The acoustic impedance of the hydraulic system, including both upstream and downstream regions, which can produce acoustic resonance and amplify the excitation source (fluctuating gap).

The first studies, developed from the 80´s of the last century, focused mostly on the effects of flow inertia and so the formulations usually considered the case of unsteady incompressible flow. Some of the first relevant studies were conducted by Weaver and several co-workers for swinging check valves, duckbill valves and other types (*Weaver et al. 1978, Weaver and Ziada 1980, D'Netto and Weaver 1987, Wang et al. 2012*). Other related studies were conducted by *Hayashi (1995)* and *Hayashi et a. (1997)* on a poppet valve, *Moussou et al. (2010), Ecker and Tondl (2011) Peng et al. (2017) and Jia et al. (2019)* for pressure relief valves.

Soon, it was found that, especially when dealing with high pressure relief valves, in many cases the experimental results on different test devices could be affected by the acoustic response of the hydraulic system, i.e., the effects of fluid compressibility and pipe elasticity were significant if not decisive on the resulting fluid-dynamic forces on the vibratory element. In consequence the assumption of incompressible flow had to be discarded in favor of a formulation analogous to the one of the classical water hammer studies, usually by means of the method of characteristics or, more often, by means of the transfer matrix method. The combination of different plug and seat shapes for the pressure relief valves with the acoustic features of the rest of the system can produce a huge variety of possible configurations to be studied.

In this group of studies combining flow inertia and acoustic transmission, (*El Bouzidi et al. (2018a, 2018b and 2019*) have considered the case of pressure relief valves with a spring loaded cover plate. A similar case has also been investigated by (*Ma et al. 2019*). The case of pressure relief valves with a spring loaded poppet has been considered by *Misra et al. (2002)* and, overall, by Hős and several coworkers (*Bazsó and Hős 2013, Bazsó et al. 2014, Hos et al. 2014, Erdődi and Hős 2016-2017,* *Burhani and Hős 2021*). Two recent works (*Allison et al. 2016, Hao et al. 2019*) have dealt with pressure relief valves with a pilot-operated plug. In this case the system possesses auxiliary branches that make the acoustic effects more complex. This configuration of a main pipeline with an auxiliary pilot line is coincidental with the lay-out of the hydraulic system of interest for the vibration problem of the Salime plant.

Recently, a number of studies have focused on the details of the unsteady flow through the valve passages during the closing or opening processes, in order to determine the influence of the geometrical details of the clearance on the resulting fluid-dynamic forces. Most of these studies have been based on CFD simulations of the flows of interest, usually incorporating moving boundaries. Some examples are the studies conducted by *Beune et al. (2012), Song et al. (2014)* and *Scuro et al. (2018)* on opening pressure safety valves, *Sun et al (2015)* on a high pressure regulating valve and *Liu et al. (2017)* on a large flow regulating valve.

With a similar objective but intended on large spherical valves of hydro power plants, a recent experimental study by *Zhang et al. (2019)* explored the dynamic response of the valves during closure, in order to assess on possible stability issues. Nonetheless, it is worth no notice as that state of the spherical valves during closure operation is very different from the final closed state, at which the annular seal must have been tightened.

3. CHAPTER THREE: THEORETICAL MODEL

As mentioned in chapter 1, one of the main aims of the presented work is to develop a simplified theoretical model that can estimate the transient behavior in Salime power plant due to turbine inlet valve seal leakage. Therefore, two models are developed in the presented study. The first model considers seal dynamics and an unsteady, unidirectional, incompressible, and viscous flow. In contrast, the second model utilizes water hammer equations and transfer matrix method to study fluid compressibility and pipeline wall elasticity effects on the same phenomenon. In the first model, linear and nonlinear friction losses will be considered to exhibit the influence of nonlinear losses on the phenomenon. While in the second model, the friction losses are linearized, and steady-state friction losses are considered.

3.1 Seal specifications

As mentioned in chapter 1, section 1.2, the periodic seal vibrations are related to a gap that exists between the ball surface and the seal. Accordingly, it is expected that one portion of the seal will stick to the ball surface, while the defected part will develop periodic vibrations, such as in figure (3.1 c).

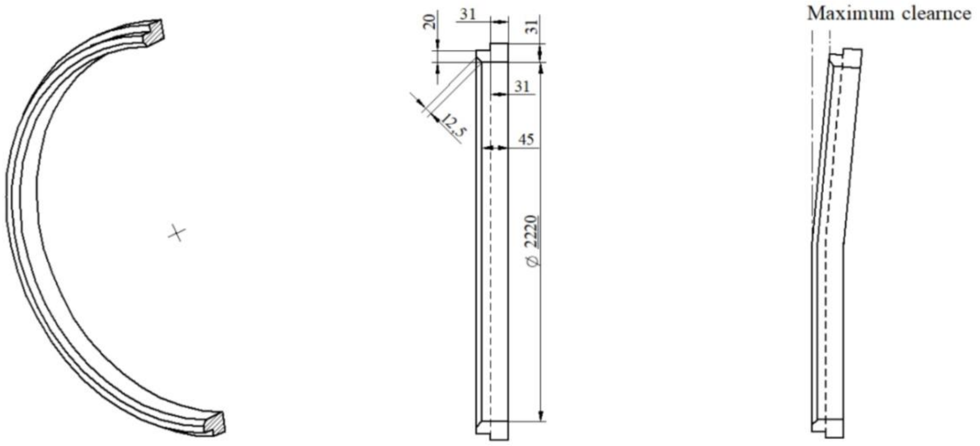

a) Annular seal section view

b) Un-deformed annular seal side view (dimensions in mm)

c) Deformed annular seal side view

Figure 3.1: Sliding annular seal specifications.

The developed periodic seal vibrations can vary along the defected part of the seal due to seal clearance variation. Although, since the aim of the study is to develop a simplified theoretical model that can explain the phenomenon, then it is adequate to work on considering mean clearance thickness y_{av} and mean seal vibration displacement y.

3.1.1 Annular seal characteristics

In order to compute the equation of motion for the vibrating seal, the equivalent structural characteristics corresponding to the gap circumferential length, namely the stiffness, mass and damping, must be computed first as follows.

Annular seal stiffness coefficient

To compute the annular seal stiffness, the annular seal deflection due to the applied load is required. This can be done by means of Castigliano's theorem.

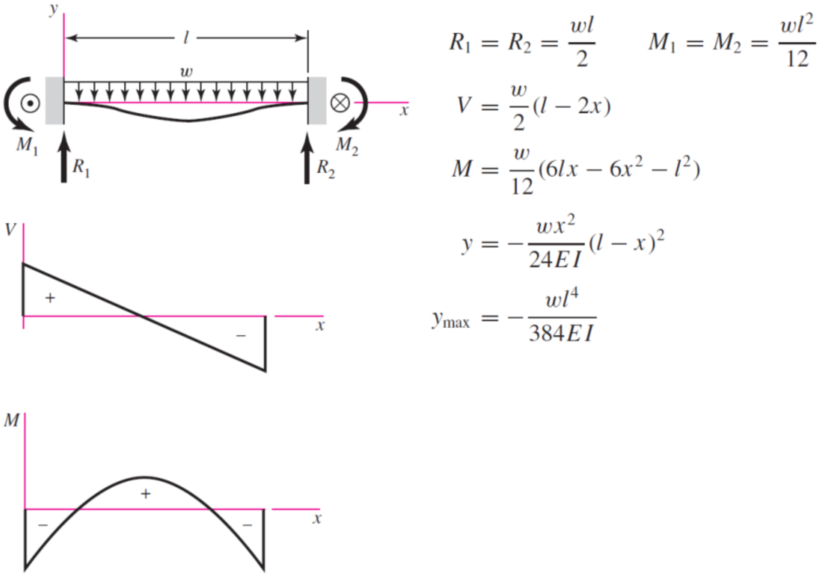

Figure 3.2: Fixed support- uniform load analysis, (*Budynas and Nisbett 2017*).

Castigilano's theorem states that the deflection of a curved beam in the direction of the applied force can be computed by differentiating the total strain energy with respect to the applied force. For the case under consideration, since the ratio between the seal radius and thickness is very large (>>10) and the difference between the radius of curvature and the radius of the centroid axis is very small, the deflection of the annular seal can be computed as in the case of a straight beam with clamped-clamped supports and a uniform load as in figure (3.2) (*Budynas and Nisbett 2017*).

By integrating the deflection equation in figure (3.2) from *x=0* to *x=L*, to estimate the area of deflection, the average deflection y_{av} can be determined as:

.

$$y_{av} = \frac{F\,L^4}{720\,E\,I} \qquad \text{Eq.(1)}$$

The annular seal stiffness k_s can be calculated as the ratio between the applied load and the average deflection y_{av}.

$$k_s = \frac{F\,L}{y_{av}} = \frac{720\,E\,I}{L^3} \qquad \text{Eq.(2)}$$

To calculate the annular seal stiffness k_{sg} corresponding to a certain gap circumferential length, L in Eq.(2) is to be replaced by the gap circumference length L_o as in Eq.(3), in which θ_{gap} is the gap angle of the seal, θ_s is the total angle of the annular seal and ϕ is the seal diameter.

$$k_{sg} = \frac{720\,E\,I}{L_o^3}, L_o = L_s\frac{\theta_{gap}}{\theta_s}, L_s = \pi\phi \qquad \text{Eq.(3)}$$

Annular seal mass coefficient

The equivalent seal mass corresponding to the gap circumference length can be computed as a fraction of the total seal mass as follows:

$$m_{sg} = m_s\frac{\theta_{gap}}{\theta_s} = m_s\frac{L_o}{L_s} \qquad \text{Eq.(4)}$$

Annular seal damping coefficient

Once the values of the annular seal mass m_{sg} and stiffness k_{sg} corresponding to the seal gap circumferential length are determined, the seal damping coefficient c_{sg} can be estimated from the damping factor equation (*Raw 2017*) as follows:

$$c_{sg} = 2\zeta\sqrt{k_{sg}\,m_{sg}} \qquad \text{Eq.(5)}$$

3.2 Incompressible flow linear model (1st Model):

In order to make the theoretical model as simple as possible while containing all the real plant relevant data, it was decided to consider the spherical valve scheme of figure (3.3) as well as the mechanical-hydraulic system representing each group of the Salime power plant as in figure (3.4).

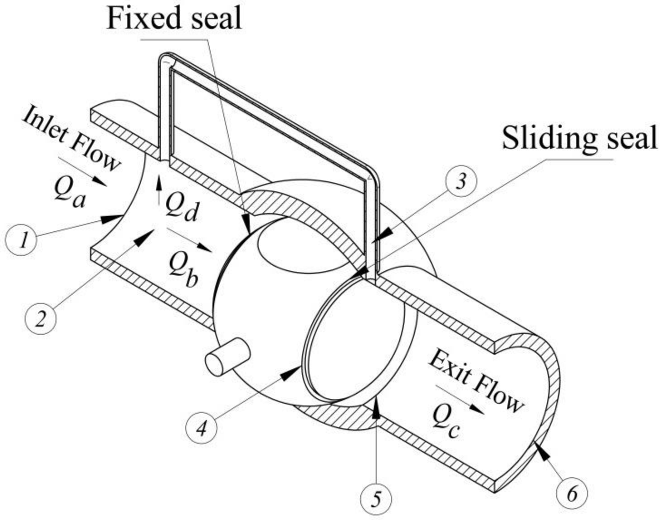

Figure 3.3: Simplified diagram of the closed valve with relevant positions.

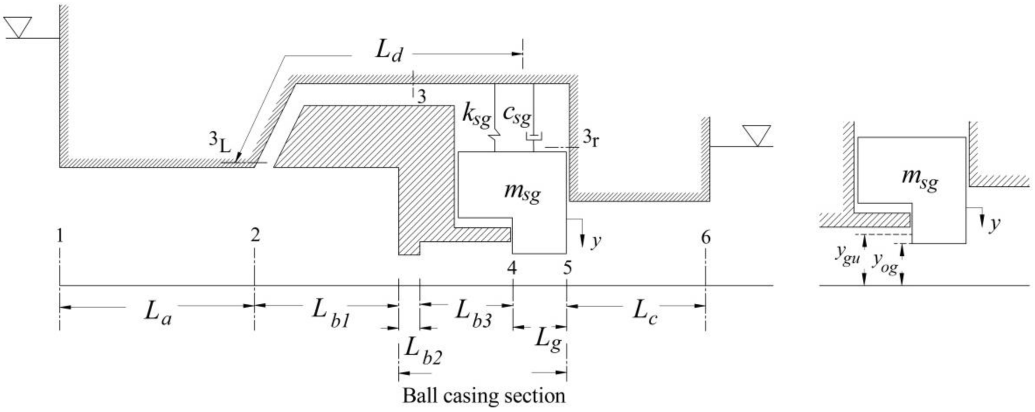

Figure 3.4: Simplified mechanical-hydraulic system for each group of the hydroelectric power station with seal clearance geometrical.

The relevant positions in this system are:

Point 1: Penstock entrance.
Point 2: Pilot pressure take off point.
Point 3: External face of the annular seal on which the pilot pressure is applied.

Point 4: Inlet to seal gap.

Point 5: Exit from seal gap.

Point 6: Discharge chamber.

The relevant dimensions of the system are:

L_a is the penstock length up to valve inlet.

L_{b1} is the duct length through the spherical valve to the ball surface.

L_{b2} is the fixed seal length in the flow direction.

L_{b3} is the Length between the fixed seal and the sliding seal.

L_g is the gap length in flow direction.

L_c is the pipeline length from the ball exit to the discharge chamber.

L_d is the pilot pipeline length.

y_{gu} is the unloaded clearance thickness, as the seal is unstrained neither statically nor dynamically.

y_{og} refers to the average gap thickness after being stressed statically.

y is the vibration displacement of the sliding seal from the static equilibrium position (i.e. y_{og}).

3.2.1 Salime Power plant specifications

Power plant specifications such as number of generating units, nominal head, rated output power, pipelines dimensions, and seal specifications are mentioned in the following table:

Table 3.1: Salime power plant specifications.

Power plant number of generating units:	**4**	
Francis turbine rated power output:	40	MW
Power plant nominal head:	105	m
L_a	80	m
d_a	2.5	m
L_{b1}	6	m
d_{b1}	2	m
A_{b2}	0.0697	m^2
A_{b3}	1.69	m^2

L_d	15	m
d_d	0.03	m
L_c	15	m
d_c	2	m
L_g	12.5	mm
Fluid (water) density:	1000	kg m^{-3}
Fluid Kinematic viscosity:	10^{-6}	m^2 s^{-1}
Fluid dynamic viscosity:	$1.002\text{x}10^{-3}$	N s m^{-2}
Seal damping factor (assumed) ζ **:**	0.1	
Seal circumference length L_s**:**	6.97	m
Seal diameter ϕ **:**	2.22	m
Seal modulus of elasticity (steel) :	200	GPa
Seal density(steel):	7850	kg m^{-3}

3.2.2 1st Model system governing equations

According to figures (3.3 & 3.4), to obtain the pressure and flow rate at the relevant sections, the unsteady Bernouli energy equation for an unsteady, unidirectional, incompressible, and viscous flow (*Massey and Ward-Smith 2006*) will be utilized with the continuity equation at the relevant junctions (*Cimbala and Cengel 2009*) and seal equation of motion. The system governing equations for every section are presented as follows:

Section 1-2:
$$H_{e1} - H_{e2} = \frac{L_a}{g\,A_a}\frac{dQ_a}{d\,t} + Q_a^2\,K_a \qquad \text{Eq.(6)}$$

Section 2-3:
$$H_{e2} - H_{e3} = \frac{L_d}{g\,A_d}\frac{dQ_d}{d\,t} + Q_d\,K_d \qquad \text{Eq.(7)}$$

Section 2-4: $$H_{e2} - H_{e4} = \frac{L_{b1}}{g\,A_{b1}}\frac{dQ_b}{d\,t} + Q_b^2\,K_b \qquad \text{Eq.(8)}$$

Section 2 continuity equation: $$Q_a = Q_b + Q_d \qquad \text{Eq.(9)}$$

Where:

$$K_a = \frac{\mathrm{f}_a L_a}{2\,g\,d_a A_a^2} + \frac{K_{La}}{2\,g\,A_a^2}\ ,\ K_b = \frac{\mathrm{f}_{b1} L_{b1}}{2\,g\,d_{b1} A_{b1}^2} + \frac{K_{Lb}}{2\,g\,A_{b1}^2} + \frac{\left(\frac{1}{A_{b2}} - \frac{1}{A_{b3}}\right)^2}{2\,g}\ ,$$

Since the flow velocity in the pilot pipeline (i.e., from section 2 to section 3) is expected to be small, hence the head losses through the pilot pipeline are computed for laminar flow and proportional to the flow rate (*Cimbala and Cengel 2009*) as follows:

$$K_d = \frac{32\nu\,L_d}{g\,A_d d_d^2} + K_{Ld}$$

K_{Ld} is the minor loss coefficient of the pilot pipeline d. K_{Ld} is utilized only to evaluate the influence of changing the pilot pipeline head losses on system stability. Other than that $K_{Ld} = 0$. K_{Ld} can represent the resistance developed by closing a valve in the pilot pipeline or any other mechanism that can augment the head losses in the pilot pipeline.

The flow rate through the gap cross section can be calculated as follows:

$$Q_g = Q_b + A_{ss}\frac{dy}{dt} = Q_c \qquad \text{Eq.(10)}$$

Equation of motion of the annular seal vibration:

$$m_{sg}\ddot{y} + c_{sg}\dot{y} + k_{sg}\,y = F(\,t\,) \qquad \text{Eq.(11)}$$

where, $F(t) = P_3 A_{os} - P_4 A_{ss}$

Section 4-5: $$H_{e4} - H_{e5} = \frac{Q_c^2 \left(\frac{1}{A_g} - \frac{1}{A_c} \right)^2}{2g}$$ Eq.(12)

Section 5-6: $$H_{e5} - H_{e6} = \frac{L_c}{g A_c} \frac{dQ_c}{dt} + Q_c^2 K_c$$ Eq.(13)

where, $K_c = \frac{f_c L_c}{2 g d_c A_c^2} + \frac{K_{Lc}}{2 g A_c^2}$

Gap cross-sectional area:

$$A_g = L_o (y_{o_g} - y)$$ Eq.(14)

Input reservoir energy level at section 1:

$$H_{e1} = variable$$ Eq.(15)

Discharge chamber energy level at section 6:

$$H_{e6} = 0$$ Eq.(16)

Pressure at sections 3 and 4:

$$P_3 = \rho g \left(H_{e3} - \frac{Q_d^2}{2 g A_d^2} \right)$$ Eq.(17)

$$P_4 = \rho g \left(H_{e4} - \frac{Q_g^2}{2 g A_g^2} \right) = \rho g H_{e5}$$ Eq.(18)

The flow rate through section 2-3:

$$Q_d = A_{os} \frac{dy}{dt} \qquad \text{Eq.(19)}$$

3.2.3 Dynamic system modeling using the perturbation technique

The energy head and flow rate at the relevant sections of figure (3.4) are solved using the perturbation technique. By using the perturbation technique, system variables are divided into steady-state components and time-dependent components superimposed over them ($H_{ej} = H_{eoj} + h_{ej}$ and $Q_j = Q_{oj} + q_j$), where subscribe j resembles the relevant section number. To use the perturbation technique, the nonlinear equations must be linearized. Therefore, the Taylor series function is utilized to linearize the nonlinear equations.

After adopting the perturbation technique, the governing equations are divided into steady-state and time-dependent equations. First, steady-state equations are solved to obtain steady-state variables. Afterward, time-dependent equations are solved using the steady-state variables to compute the time-dependent variables. Steady-state equations and time-dependent equations after being linearized are mentioned in appendix A. 1 and A.2.

3.2.4 1st Model dimensionless analysis

In order to gain a deep understanding of the parameters affecting the phenomenon, a dimensionless analysis is carried out with some simplifications. Firstly, the mainline hydraulic losses at sections 1-2, 2-4, and 5-6 are neglected because of their negligible value compared to the input reservoir energy level and the gap leakage kinetic energy. Secondly, the gap pressure head is assumed to be H_{e5} (i.e., see Eq.(18)), as the gap kinetic energy is lost by Borda's loss in section 4-5 (i.e., see Eq.(12)). By applying the mentioned simplifications, the dimensionless added water mass, damping and stiffness coefficients $\left(c_W^*, k_W^*, m_W^*\right)$ (mentioned briefly in appendix A.3) are function of the following Π-groups:

$$\left(m_w^*, c_w^*, k_w^*\right) = f\left(\Pi_1, \Pi_2, \Pi_3, \Pi_4, \Pi_a, \Pi_b, \Pi_c, \Pi_d\right) \qquad \text{Eq.(20)}$$

$$\Pi_1 = \frac{\text{Main line Inertia}}{\text{Input reservoir energy level}} = \frac{I_m \omega_{ref} Q_{og}}{H_{e1}},$$

$$\Pi_2 = \text{Gap reduced velocity} = \frac{v_{og}}{L_g \omega_{ref}}, \Pi_3 = \frac{\text{Main line inertia}}{\text{Pilot line head loss}} = \frac{I_m \omega_{ref} Q_{og}}{K_d Q_{og}},$$

$$\Pi_4 = \frac{A_{ss}}{A_{os}}, \ \Pi_a = \frac{I_a}{I_m}, \ \Pi_b = \frac{I_b}{I_m}, \ \Pi_c = \frac{I_c}{I_m} \text{ and } \Pi_d = \frac{I_d}{I_m}$$

where, $I_j = \dfrac{L_j}{g A_j}$, $I_m = I_a + I_b + I_c$, $\omega_{ref} = \sqrt{\dfrac{k_s}{m_s}}$

3.2.5 1st Model condition of stability

Since the vibrated seal oscillatory motion supports the fluid dynamic force, thus the case of interest is related to movement-induced excitation flow-induced vibrations (*Naudascher and Rockwell 1994*). In this type of vibrations, the hydrodynamic force acting on the seal (i.e., presented in Eq.(11)) can be presented as terms proportional to the seal's vibration motion y, $\dot{y}$ and $\ddot{y}$ (*Naudascher and Rockwell 1994*). Therefore, after applying the dimensionless analysis mentioned in section 3.2.4, the seal equation of motion can be computed as in Eq.(21). In which, m_w^*, c_w^* and k_w^* resemble the dimensionless hydrodynamic force acting on the seal, as terms proportional to the dimensionless seal's vibration components $\ddot{y}^*$, $\dot{y}^*$, and y^*.

$$\ddot{y}^* \underbrace{\left(\frac{m_{sg}}{\rho g I_m A_{os}^2} + m_w^*\right)}_{m_{eq}^*} + \dot{y}^* \underbrace{\left(\frac{c_{sg}}{\rho g I_m A_{os}^2 \omega_{ref}} + c_w^*\right)}_{c_{eq}^*} + y^* \underbrace{\left(\frac{k_{sg}}{\rho g I_m A_{os}^2 \omega_{ref}^2} + k_w^*\right)}_{k_{eq}^*} = 0 \qquad \text{Eq.(21)}$$

where:

$$m_{eq}^{*} = \left(\frac{m_{sg}}{\rho g \, I_m \, A_{os}^2} + m_w^{*} \right)$$

$$c_{eq}^{*} = \left(\frac{c_{sg}}{\rho g \, I_m \, A_{os}^2 \, \omega_{ref}} + c_w^{*} \right)$$

$$k_{eq}^{*} = \left(\frac{k_{sg}}{\rho g \, I_m \, A_{os}^2 \, \omega_{ref}^2} + k_w^{*} \right)$$

Eq. (21) presents the dimensionless equation of motion for a free vibration damped system of a single degree of freedom. For such a system, the damped frequency is the inherent oscillation frequency ω, where ω can be estimated through Eq.(22) (*Raw 2017*).

$$\omega = \omega_{ref} \sqrt{\frac{k_{eq}^{*}}{m_{eq}^{*}}} \sqrt{1-\zeta^2}\,, \qquad \text{Eq.(22)}$$

where: $\zeta = \dfrac{c_{eq}^{*}}{2\sqrt{k_{eq}^{*} \, m_{eq}^{*}}}$

For the movement-induced excitation flow-induced vibration systems (i.e., such as the case under consideration), the equivalent damping coefficient c_{eq} is the term that indicates system stability (*Naudascher and Rockwell 1994*). If the value of the added water damping c_w is positive, thus the flow force damps system oscillations. In this situation, the equivalent damping coefficient is positive, and the system is dynamically stable since system disturbance will decay over time, reaching steady-state condition. On the other hand, if the added water damping c_w is negative, thus the fluid force excites system oscillations rather than damping it. In this situation, two dynamic behaviors may be developed. If the equivalent damping coefficient is zero, the system disturbance will keep on oscillating with constant amplitude. In this case, the seal behavior represents the behavior of a free vibration undamped system, and the system is said to be critically stable. In contrast, if the value of the equivalent damping coefficient c_{eq} is negative. In this case, the system is said to be dynamically unstable. In this situation, a slight system disturbance leads to oscillations of incrementing amplitude over time, leading to a dynamically unstable system.

In addition to the dynamic stability limit ($c_{eq} \geq 0$), there is also a static stability limit because the thickness of the seal clearance depends on the seal's hydro-pressure force. So, if the average seal clearance under static load is equal to zero, hence no leakage flow is developed, and the seal could not undertake vibrations.

3.2.6 1st Model computation procedures

Evaluation of system stability conditions is one of the main objectives of the study to provide recommendations for system stability enhancement. The dimensionless force coefficients m_W^* , c_W^* and k_W^* identify the system's dynamic stability. These coefficients are a function of the seal oscillation frequency ω and the Π-groups presented in section 3.2.4. During the evaluation of system stability, a particularly Π-group varies through a specific range, while the other Π-groups are constant. The aim of varying this specified Π-group is to show its influence on the dynamic system stability. The problem in computing the dimensionless force coefficients is that they are a function of the seal oscillation frequency ω which is unknown. Therefore, an iteration loop is constructed to calculate the correct values of the dimensionless force coefficients and the seal oscillation frequency.

The iteration loop starts by inserting an initial guess for the frequency $\omega = \omega_{int}$, in addition to the Π-groups values. Afterward, Eqs (21 and 22) calculates the force coefficients (m_W^*, c_W^* and k_W^*) and the damped frequency $\omega = \omega_{cal}$. If the relative error between the calculated frequency ω_{cal} and the initial guess ω_{int} is smaller than 10^{-3}, the solution convergence is achieved. In contrast, If the relative error between the frequency values (ω_{cal} and ω_{int}) is > 10^{-3}, the calculated frequency is inserted as the guessed value $\omega_{int} = \omega_{cal}$, and the iteration loop operates for one more iteration until solution convergence is achie

3.3 Incompressible flow non-linear model (1st Model)

The shortage of the 1st Model linear analysis is the inability to estimate the limit cycle oscillations. If the seal is subjected to a disturbance and the seal is dynamically unstable, thus the seal oscillates with increasing amplitude since the modeling of the system considers linear friction losses. On the other hand, if the nonlinear head losses are considered in the modeling of the system and the seal is dynamically unstable then the amplitude of the seal oscillation increases and the head losses increase nonlinearly. In this case, the head losses keep on increasing till reaching a point where the energy supplied by the fluid to the system is the same as the energy dissipated by the system. At this point the system oscillations continue but with a constant amplitude which is known by the limit cycle oscillations.

According to what mentioned above, the aim of the nonlinear model is to show the influence of the nonlinear head losses on reaching the limit cycle oscillations. The model works on the same governing equations (6-19) as in the previous model but with considering the nonlinear friction terms. The governing equations are solved using the MATLAB toolbox Simulink as in figure (3.5), where the Simulink solver is ODE 45 and the value of the variables at time $t=0$ will be as their steady-state values (i.e., $Q_j(t=0)=Q_{oj}, H_{ej}(t=0)=H_{oej}$). Each subsystem in figure (3.5) represents a governing equation of the system that comprises its inputs and outputs. The mentioned subsystems are presented through figures (3.6-3.17).

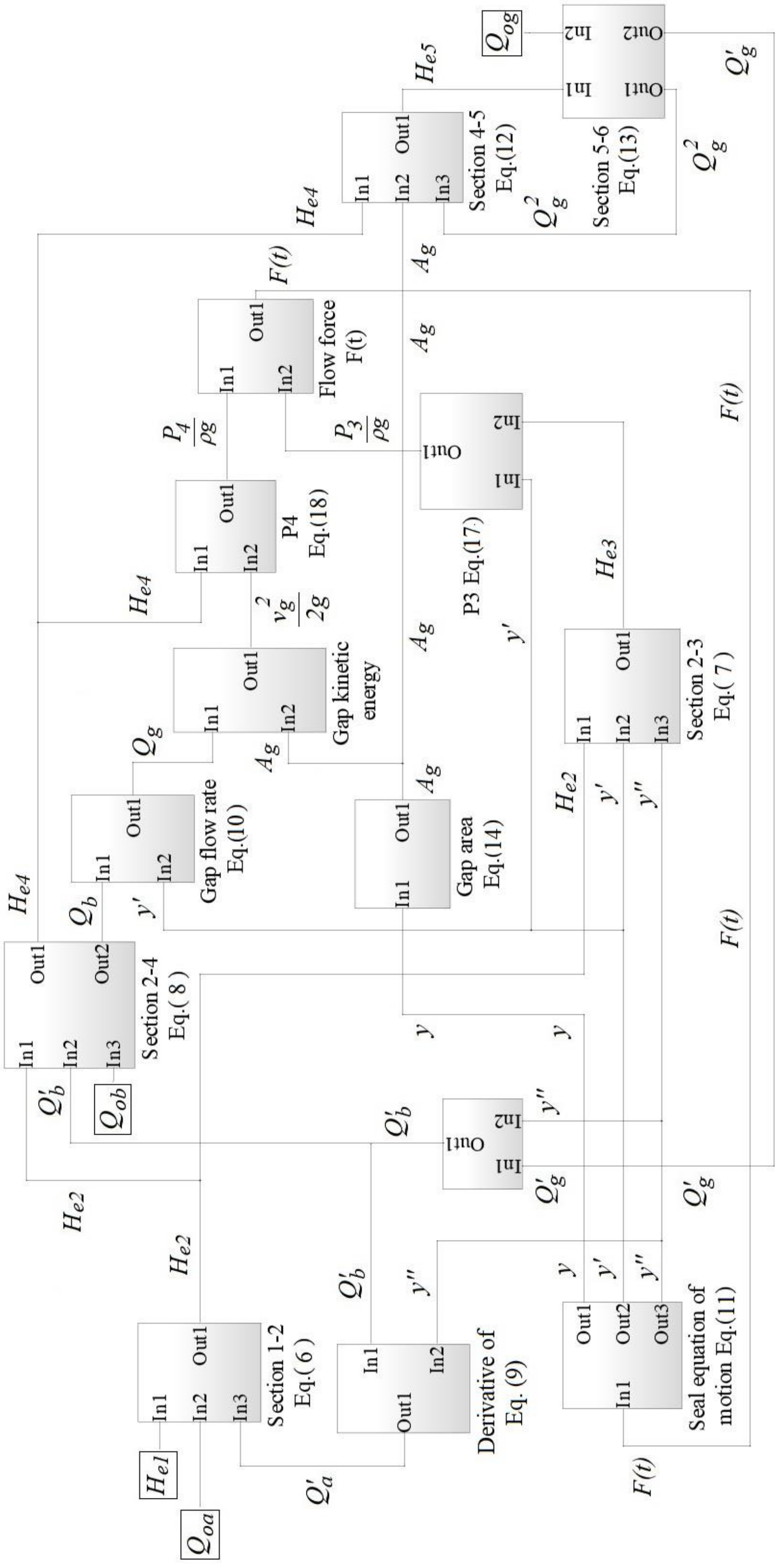

Figure 3.5: MATLAB Simulink diagram of the non-linear model simulation.

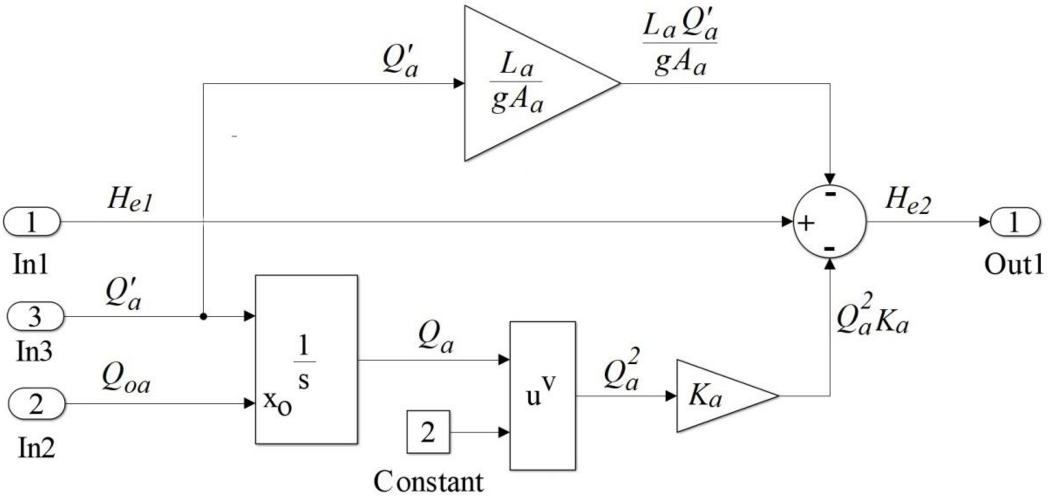

Figure 3.6: Section 1-2 Eq.(6) subsystem configuration.

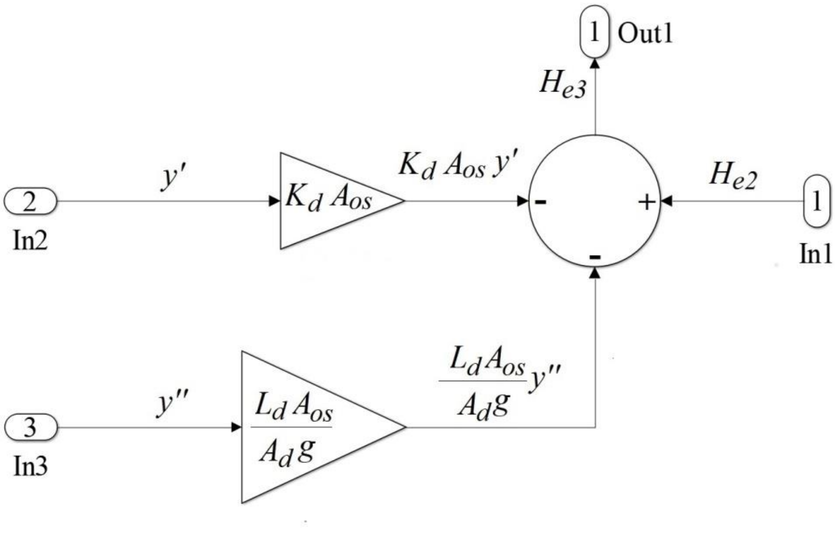

Figure 3.7: Section 2-3 Eq.(7) subsystem configuration.

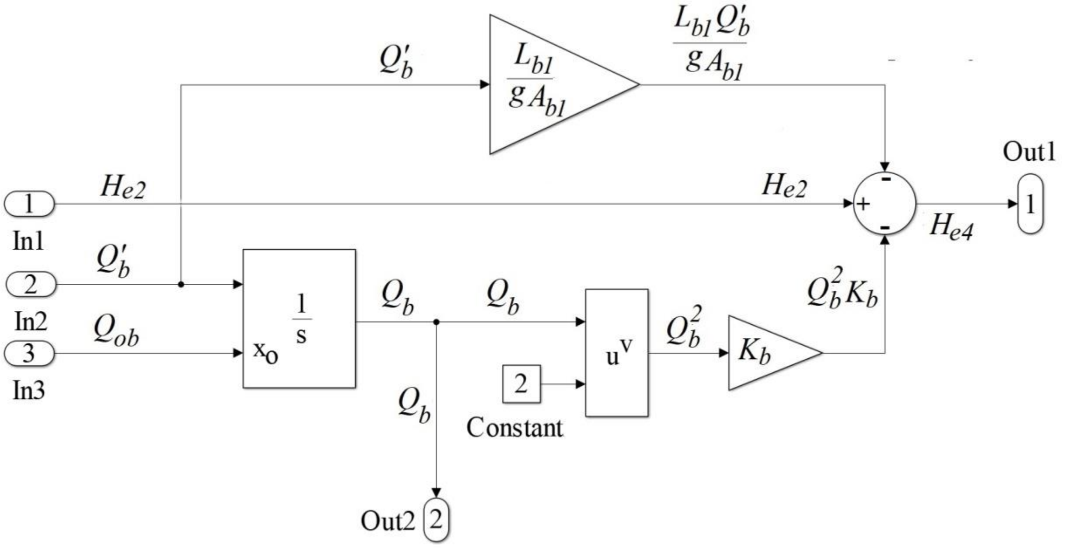

Figure 3.8: Section 2-4 Eq.(8) subsystem configuration.

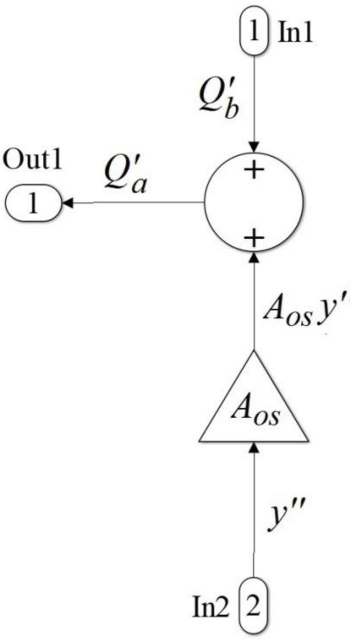

Figure 3.9: Derivative of penstock flow rate Eq.(9)

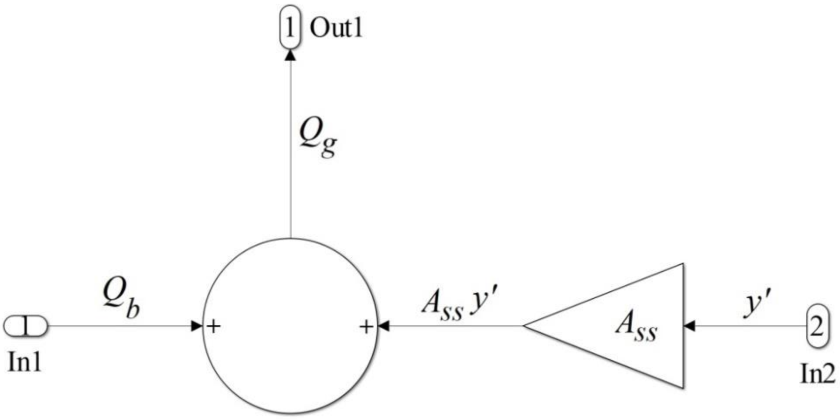

Figure 3.10: Gap flow rate Eq.(10) subsystem configuration.

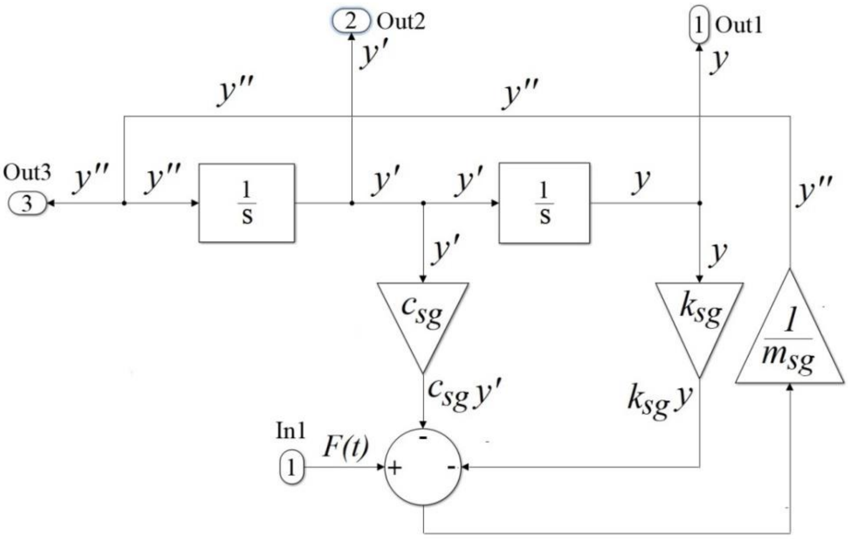

Figure 3.11: Seal equation of motion Eq.(11) subsystem configuration.

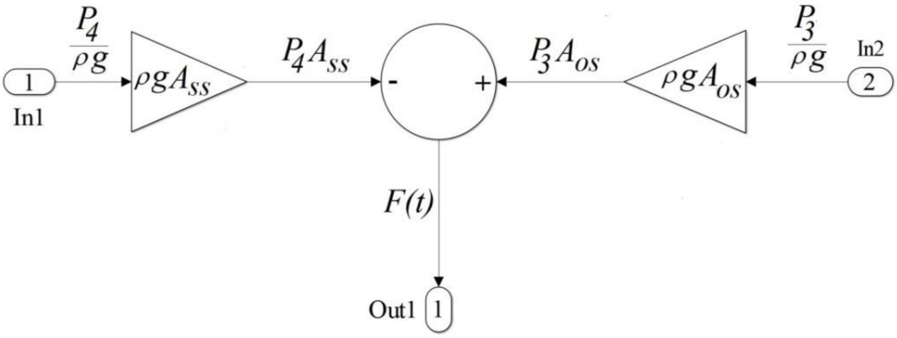

Figure 3.12: Flow force F(t) subsystem configuration.

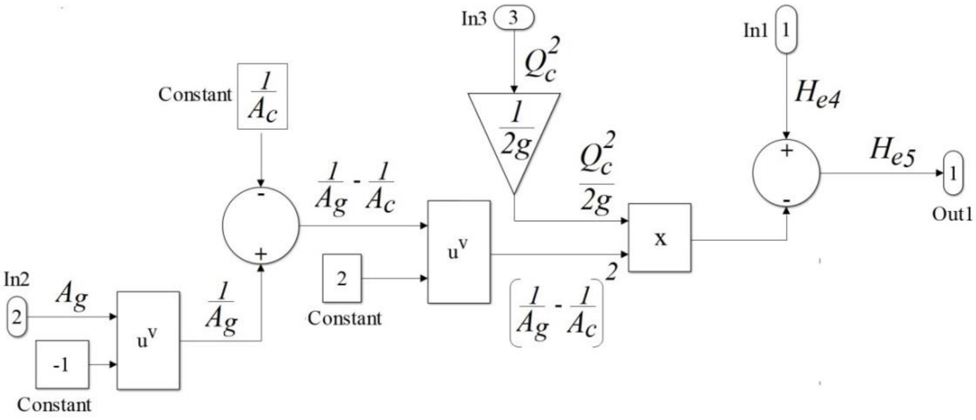

Figure 3.13: Section 4-5 Eq.(12) subsystem configuration.

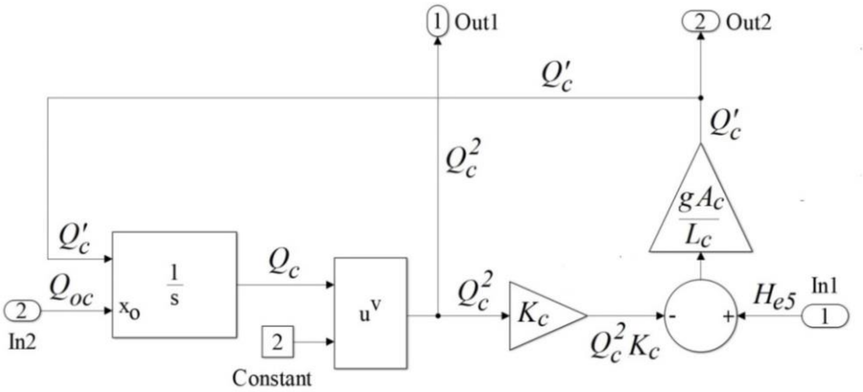

Figure 3.14: Section 5-6 Eq.(13) subsystem configuration.

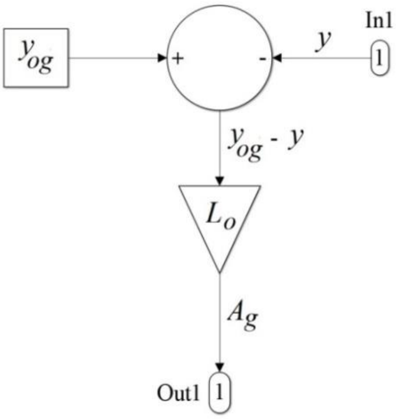

Figure 3.15: Gap cross-section area Eq.(14) subsystem configuration.

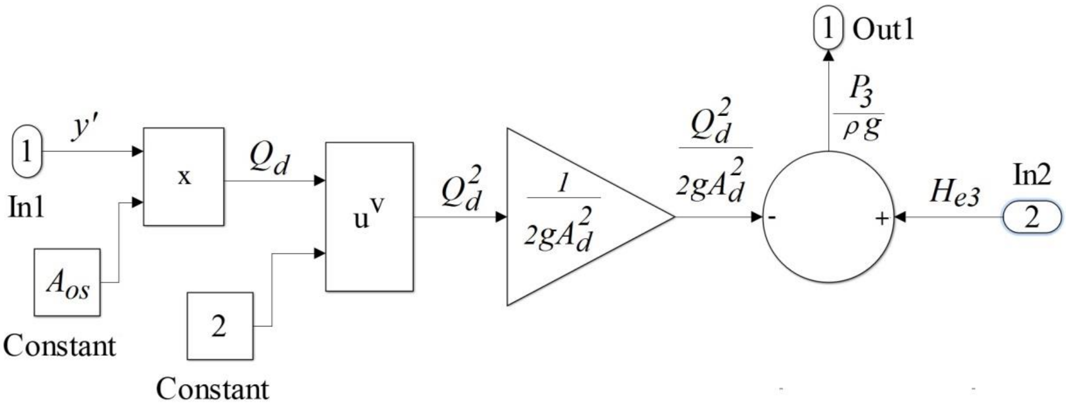

Figure 3.16: Pressure at section 3 Eq.(17) subsystem configuration.

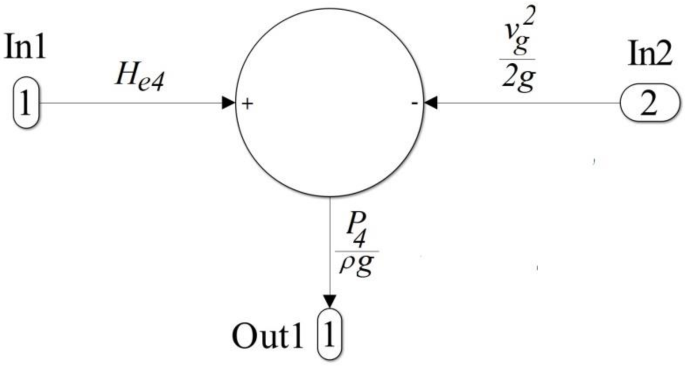

Figure 3.17: Pressure at section 4 Eq.(18) subsystem configuration.

3.4 Compressible flow linear model (2^{nd} Model)

A disturbance in the steady-state fluid condition of a pipeline may induce significant pressure variations, particularly for compressible fluids such as water. Therefore, transient analysis is significant to ascertain pipeline safe operation and integrity.

Karney 1990 interprets that the internal energy stored in a pipeline flow assesses the significance of the fluid compressibility effect on system transient behavior. For cases where the flow conditions vary rapidly, such as valve sudden closure due to instantaneous load rejection, the compressibility effect should be considered due to high energy conversion rates. Also, for applications that comprise long pipelines, after a system disturbance a pressure wave is developed traveling upstream and downstream from the source of excitation. During the pressure wave travel fluid keeps on entering the pipeline at the initial rate. This additional volume of fluid to the pipeline augments the internal energy of the flow and flow pressure fluctuations.

The shortage of the 1st Model analysis is that it neglects the fluid compressibility and pipeline wall elasticity effects, which is not proper in hydropower plants since the penstocks are usually of a significant length. Therefore, the second model objective is to exhibit the influence of fluid compressibility and pipeline wall elasticity on the dynamic stability of the system.

Water hammer theory is usually adopted for transient analysis considering pipeline wall elasticity and fluid compressibility effects (*Chaudhry 2014*). Therefore, to solve the system’s pressure and flow rate oscillations, the water hammer equations are utilized in cooperation with the vibrating seal equation of motion and system boundary conditions. Besides, since the developed study considers sinusoidal flow rate and pressure oscillations, linear boundary conditions, and linear friction losses, thus the transfer matrix method is adopted to compute the transient behavior of the system by solving the system governing equations in the frequency domain.

3.4.1 Transfer matrix method

By considering a general system as in figure (3.18) with input variables of $x_1, x_2, \ldots, x_n$ and output variables of $y_1, y_2, \ldots, y_n$. By relating the input and output variables, we will have n simultaneous equations, which can be represented as follows:

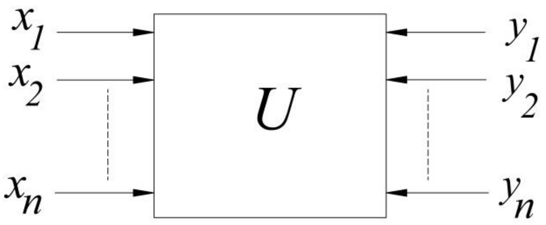

Figure 3.18: Single component block diagram.

$$\begin{aligned}
y_1 &= u_{11}x_1 + u_{12}x_2 + \ldots\ldots\ldots\ldots + u_{1n}x_n \\
y_2 &= u_{21}x_1 + u_{22}x_2 + \ldots\ldots\ldots\ldots + u_{2n}x_n \\
&\vdots \\
y_n &= u_{n1}x_1 + u_{n2}x_2 + \ldots\ldots\ldots\ldots + u_{nn}x_n
\end{aligned}$$

A matrix form can represent the n simultaneous equations such as:

$$\begin{bmatrix} y_1 \\ y_2 \\ \vdots \\ y_n \end{bmatrix} = \begin{bmatrix} u_{11} & u_{12} & \cdots & u_{1n} \\ u_{21} & u_{22} & \cdots & u_{2n} \\ & & \vdots & \\ u_{n1} & u_{n2} & \cdots & u_{nn} \end{bmatrix} \begin{bmatrix} x_1 \\ x_2 \\ \vdots \\ x_n \end{bmatrix} \quad or\ \boldsymbol{Y} = \boldsymbol{U}\,\boldsymbol{X}$$

where $\boldsymbol{Y}$ is the output column vector, $\boldsymbol{U}$ is the transfer matrix, and $\boldsymbol{X}$ is the input column vector. The given system in figure (3.18) comprises one component. In actual engineering applications, usually, several components make up the system. In these systems, a transfer matrix represents each component. Afterward, the overall transfer matrix is estimated by multiplying these components transfer matrices in a specific sequence.

For transient analysis, three types of transfer matrices are estimated:

1. Field transfer matrix **“F_j”**, relating state variables (i.e. pressure and flow rate oscillations) at the upstream and downstream end of a pipeline j.

2. Point transfer matrix ***"P_j"***, relating state variables at both sides of a *j* boundary condition.
3. Overall transfer matrix ***"U"***, relating the upstream and downstream state variables of a system.

Field transfer matrix F_j

As mentioned before, the field transfer matrix relates the state variables (i.e., pressure and flow rate oscillations) at the upstream and downstream ends of a pipeline *j*. So, to calculate pressure and flow rate oscillations at these pipeline sections, the continuity and momentum equations representing the water hammer equations are utilized as follows:

Continuity equation: $$\frac{g A_j}{a_j^2}\frac{\partial H}{\partial t}+\frac{\partial Q}{\partial x}=0 \qquad \text{Eq.(23)}$$

Momentum equation: $$\frac{\partial H}{\partial x}+\frac{1}{g A_j}\frac{\partial Q}{\partial t}+\frac{\mathrm{f}_j Q^n}{2gd\, A_j^n}=0 \qquad \text{Eq.(24)}$$

a_j is pipeline *j* wave speed, n is the exponent of velocity in friction loss term, and *x* is the distance along the pipeline *j*. By utilizing the transfer matrix method, the instantaneous pressure head *H* and discharge *Q* are split into mean components and time-dependent components superimposed over them (i.e., $Q=Q_o+q$ and $H=H_o+h$). The oscillated pressure head *h* and discharge *q* are complex variables function of time *t* and distance *x* as follows:

$$h=\mathrm{Re}\,(h(x)\,e^{i\omega t}) \qquad \text{Eq.(25)}$$

$$q=\mathrm{Re}(\,q(x)\,e^{i\omega t}) \qquad \text{Eq.(26)}$$

h(x) and *q(x)* are complex variables function of *x* only, *ω* is the oscillation frequency, and Re stands for the real part of the complex variable. Since the mean flow rate and pressure head are time-invariant, then the partial differential terms of Eqs (23 and 24) can be presented as follows:

$$\frac{\partial Q}{\partial x}=\frac{\partial Q_o}{\partial x}+\frac{\partial q}{\partial x}=\frac{\partial q}{\partial x}$$ Eq.(27)

$$\frac{\partial Q}{\partial t}=\frac{\partial Q_o}{\partial t}+\frac{\partial q}{\partial t}=\frac{\partial q}{\partial t}$$ Eq.(28)

$$\frac{\partial H}{\partial x}=\frac{\partial H_o}{\partial x}+\frac{\partial h}{\partial x},$$ Eq.(29)

Since friction losses are considered, then $\frac{\partial H_o}{\partial x}$ may vary according to the flow state as:

for turbulent flow: $\frac{\partial H_o}{\partial x}=-\frac{\mathrm{f}_j Q_o^n}{2g\, d_j A_j^n},$

for laminar flow: $\frac{\partial H_o}{\partial x}=-\frac{32\nu Q_o}{g\, A_j d_j^2}$

$$\frac{\partial H}{\partial t}=\frac{\partial H_o}{\partial t}+\frac{\partial h}{\partial t}=\frac{\partial h}{\partial t}$$ Eq.(30)

Since $q \langle\langle Q_o$, then $Q^n=\left(Q_o+q\right)^n=Q_o^n+n\,Q_o^{n-1}q$ where higher-order terms are neglected. Therefore, by neglecting higher-order terms and applying Eqs. (27-30) into Eqs. (23 and 24), the time-dependent continuity and momentum equations are as follows:

Time-dependent continuity equation: $$\frac{\partial q}{\partial x}+\frac{g\, A_j}{a_j^2}\frac{\partial h}{\partial t}=0$$ Eq.(31)

Time-dependent momentum equation: $$\frac{\partial h}{\partial x}+\frac{1}{g\, A_j}\frac{\partial q}{\partial t}+Rq=0$$ Eq.(32)

where:

For turbulent flow: $R = \dfrac{n\,\mathrm{f}_j\,Q_o^{n-1}}{2g\,d_j\,A_j^n}$

For laminar flow: $R = \dfrac{32\nu}{g\,A_j\,d_j^2}$

By multiplying Eq.(31) by $\dfrac{\partial}{\partial x}$ and multiplying Eq.(39) by $\dfrac{\partial}{\partial t}$; *h* can be eliminated as follows:

Continuity equation will be: $\dfrac{\partial^2 q}{\partial x^2} + \dfrac{g\,A_j}{a_j^2}\dfrac{\partial^2 h}{\partial t\,\partial x} = 0$ Eq.(33)

Momentum equation will be: $\dfrac{\partial^2 h}{\partial x\partial t} + \dfrac{1}{g\,A_j}\dfrac{\partial^2 q}{\partial t^2} + R\dfrac{\partial q}{\partial t} = 0$ Eq.(34)

Elimination of *h* from equations Eq.(33) and Eq.(34) yields to:

$$\frac{\partial^2 q}{\partial x^2} = \frac{1}{a_j^2}\frac{\partial^2 q}{\partial t^2} + \frac{g\,A_j\,R}{a_j^2}\frac{\partial q}{\partial t} \qquad \text{Eq.(35)}$$

Also, by substituting Eq.(26) into Eq.(35), $q(x)$ can be computed as:

$$\frac{\partial^2 q(x)}{\partial x^2} = \left(-\frac{\omega^2}{a_j^2} + i\,\frac{g\,A_j\,\omega R}{a_j^2}\right)q(x), \qquad \text{Eq.(36)}$$

where:

$$\mu^2 = -\frac{\omega^2}{a_j^2} + i\,\frac{g\,A_j\,\omega R}{a_j^2}$$

The solution of Eq.(36) is as follows (*Chaudhry 2014*):

$$q(x) = C_1 \sinh(\mu x) + C_2 \cosh(\mu x) \qquad \text{Eq.(37)}$$

C₁ and *C₂* are arbitrary constants, and by utilizing equations Eq. (25) and Eq. (37) in solving equation Eq.(31), *h(x)* can be computed as follows:

$$(C_1 \cosh(\mu x) + C_2 \sinh(\mu x))\ \mu e^{i\omega t} = -i \frac{g A_j \omega}{a_j^2} h(x) e^{i\omega t} \ ,$$

$$h(x) = -\frac{\mu a_j^2}{i g A_j \omega}(C_1 \cosh(\mu x) + C_2 \sinh(\mu x)) \qquad \text{Eq.(38)}$$

In order to relate the flow rate and pressure oscillations at both ends of the pipeline, Eq.(37) and Eq.(38) are solved at both boundaries, as seen in figure (3.19).

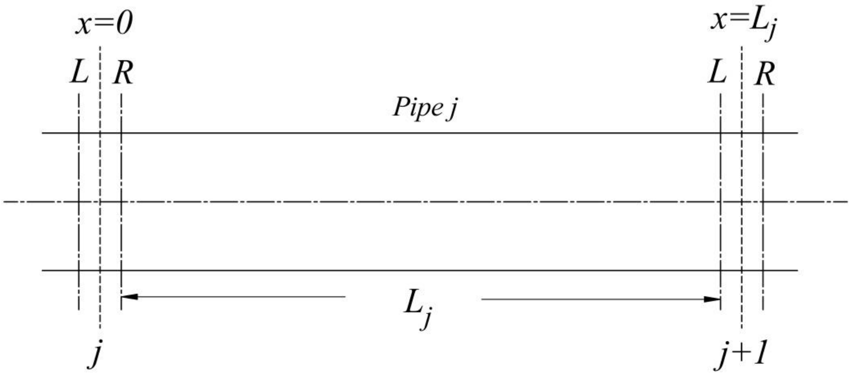

Figure 3.19: Pipeline j boundaries.

By solving Eq.(37) and Eq.(38) at section j where $x = 0, h(x) = h_j^R$ and $q(x) = q_j^R$, then *C₁* and *C₂* can be computed as:

$$C_1 = -i \frac{g A_j \omega}{a_j^2 \mu_j} h_j^R , \qquad \text{Eq.(39)}$$

$$C_2 = q_j^R \qquad \text{Eq.(40)}$$

By substituting Eqs.(39) and Eq.(40) into Eq.(37) and Eq.(38), and solving the developed equations at section *j+1* where $x = Lj, h(x) = h_{j+1}^R$, and $q(x) = q_{j+1}^R$ then:

$$q_{j+1}^L = q_j^R \cosh(\mu_j L_j) - h_j^R \sinh(\mu_j L_j) \frac{1}{Z_c} \qquad \text{Eq.(41)}$$

$$h_{j+1}^{L} = -q_j^R \sinh(\mu_j L_j) Z_c + h_j^R \cosh(\mu_j L_j) \qquad \text{Eq.(42)}$$

where Z_c is the characteristic impedance and can be estimated as :

$$Z_c = \frac{\mu_j a_j^2}{i \omega g A_j}$$

A matrix form can represent Eqs.(41 and 42) as:

$$\boldsymbol{Z_{j+1}^{L}} = \boldsymbol{F_j} \, \boldsymbol{Z_j^{R}}$$

$$\begin{bmatrix} q \\ h \end{bmatrix}_{j+1}^{L} = \underbrace{\begin{bmatrix} \cosh(\mu_j L_j) & -\sinh(\mu_j L_j)\dfrac{1}{Z_c} \\ -\sinh(\mu_j L_j) Z_c & \cosh(\mu_j L_j) \end{bmatrix}}_{\boldsymbol{F\,j}} \begin{bmatrix} q \\ h \end{bmatrix}_{j}^{R} , \qquad \text{Eq.(43a)}$$

In which, $\boldsymbol{Z_{j+1}^{L}}$ and $\boldsymbol{Z_j^{R}}$ represent the state vectors (which comprises the state vectors) at both ends of a pipeline *j*, as in figure (3.19), while $\boldsymbol{F_j}$ resembles the pipeline *j* field transfer matrix.

If the pipeline flow oscillation speed $L_j \, \omega$ is very small compared to the pipeline wave speed a_j, thus the system can be modeled as a lumped system (*Chaudhry 2014*). In this situation, the pipeline disturbance is sensed through the whole system instantaneously, and the field transfer matrix for a lumped frictionless system can be estimated as:

$$\begin{bmatrix} q \\ h \end{bmatrix}_{j+1}^{L} = \underbrace{\begin{bmatrix} 1 & -i\dfrac{g A_j L_j \omega}{a_j^2} \\ -i\dfrac{\omega L_j}{A_j g} & 1 \end{bmatrix}}_{\boldsymbol{F\,j}} \begin{bmatrix} q \\ h \end{bmatrix}_{j}^{R} \qquad \text{Eq.(43b)}$$

Point transfer matrix $\boldsymbol{P_j}$

As mentioned before, the point transfer matrix relates the state vectors at both sides of a boundary such as valves, branch junction with a dead-end or with an oscillating dead-end, series junction, and many other boundaries. Therefore, in this section, the boundaries related to the case under consideration, which are series junction, branch junction with an oscillating dead end, and a valve are explained as follows.

Series junction point transfer matrix

A junction between two pipes with different characteristics such as pipe diameter, wall thickness, wall materials, or any combination of these parameters is called series junction, such as in figure (3.20).

The point transfer matrix of the series junction at section j can be computed by applying the continuity equation and neglecting the junction losses as follows:

Continuity equation at section j: $q_j^R = q_j^L$ Eq.(44)

Neglecting junction losses: $h_j^R = h_j^L$ Eq.(45)

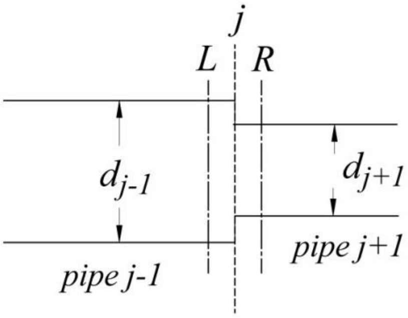

Figure 3.20: Series junction diagram.

By using Eq. (25) and Eq.(26) to convert Eq. (44) and Eq.(45) into the frequency domain, in addition to representing the developed equations in a matrix form, the series-junction point transfer matrix can be computed as follows:

$$\boldsymbol{Z_j^R} = \boldsymbol{P_j}\ \boldsymbol{Z_j^L}$$

$$\begin{bmatrix} q \\ h \end{bmatrix}_j^R = \underbrace{\begin{bmatrix} 1 & 0 \\ 0 & 1 \end{bmatrix}}_{\boldsymbol{Pj}} \begin{bmatrix} q \\ h \end{bmatrix}_j^L \qquad \text{Eq.(46)}$$

where $\boldsymbol{P_j}$ is the point transfer matrix of the series junction, while $\boldsymbol{Z_j^R}$ and $\boldsymbol{Z_j^L}$ are the state vectors at the right side and the left side of the series junction boundary.

Branching junction point transfer matrix

In the branching system shown in figure (3.21), pipeline "*a b c*" is the main line, and "*d N*" is the side branch. The transfer matrix for the pipeline "*a b*" can be computed by using the field matrix derived previously. To calculate the overall transfer matrix for the mainline "*a b c*", the point matrix at junction *b*, relating the state vector on the left side and to that on the right side of the junction is needed. This matrix may be derived if the boundary conditions at point *N* are specified.

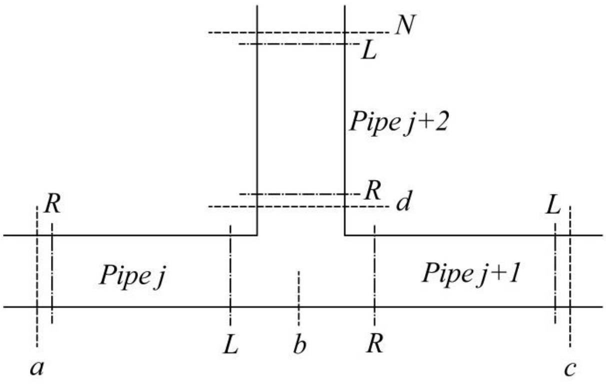

(a) Piping system with notation.

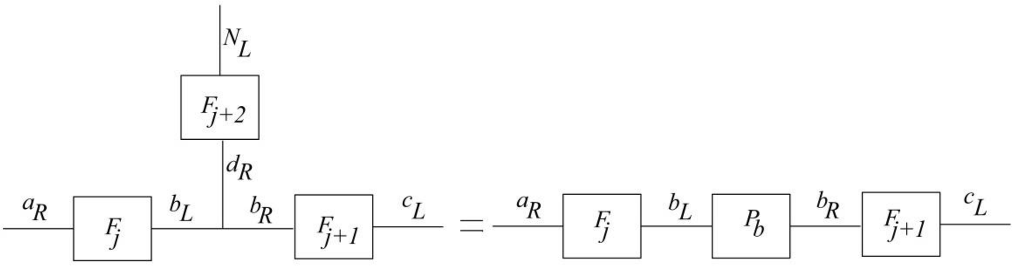

(b) Block diagram

Figure 3.21: Branch junction.

The field transfer matrix of pipeline *j+2* can be expressed by using Eq.(43a) as follows:

$$\begin{bmatrix} q \\ h \end{bmatrix}_N^L = \underbrace{\begin{bmatrix} \cosh(\mu_{j+2} L_{j+2}) & -\sinh(\mu_{j+2} L_{j+2}) \dfrac{1}{Z_c} \\ -\sinh(\mu_{j+2} L_{j+2}) Z_c & \cosh(\mu_{j+2} L_{j+2}) \end{bmatrix}}_{\boldsymbol{F\ j+2}} \begin{bmatrix} q \\ h \end{bmatrix}_d^R \qquad \text{Eq.(47)}$$

Eq.(47) can also be written as:

$$q_N^L = q_d^R F\ j+2_{11} + h_d^R F\ j+2_{12} \qquad \text{Eq.(47a)}$$

$$h_N^L = q_d^R F\ j+2_{21} + h_d^R F\ j+2_{22} \qquad \text{Eq.(47b)}$$

The 1st and 2nd subscripts of the field transfer matrix $\boldsymbol{F_{j+2}}$ represent the number of row and column. As an example, $F_{j+2_{11}}$ is the term at the first row and first column of the field transfer matrix $\boldsymbol{F_{j+2}}$, which is $\cosh(\mu_{j+2} L_{j+2})$

By neglecting the losses at junction *b* and applying the continuity equation, the following equations may be written:

$$q_b^L = q_b^R + q_d^R \qquad \text{Eq.(48)}$$

$$h_b^L = h_b^R = h_d^R \qquad \text{Eq.(49)}$$

By substituting Eq.(49) into Eq.(47a), and considering the boundary condition at section *N* as $q_N^L = q_{os}$ (where q_{os} is the oscillating dead-end flow rate), thus the flow rate q_d^R can be expressed by Eq.(47a) as:

$$q_d^R = \frac{q_{os}}{F_{j+2_{11}}} - h_b^L \frac{F_{j+2_{12}}}{F_{j+2_{11}}} \qquad \text{Eq.(50)}$$

Also, by substituting Eq.(50) into Eq.(48), and utilizing Eq.(49), hence q_b^R and h_b^R can be expressed as follows:

$$q_b^R = q_b^L + h_b^L \frac{F_{j+2_{12}}}{F_{j+2_{11}}} - \frac{q_{os}}{F_{j+2_{11}}}$$ Eq.(51)

$$h_b^R = 0\,q_b^L + h_b^L + 0\,q_{os}$$ Eq.(52)

So, by using Eq.(25) and Eq.(26) to convert Eq.(51) and Eq.(52) into the frequency domain, and representing the developed equations in a matrix form, thus the point transfer matrix of the branch junction with an oscillating dead-end can be estimated as follows:

$$\begin{bmatrix} q \\ h \\ 1 \end{bmatrix}_b^R = \underbrace{\begin{bmatrix} 1 & \frac{F_{j+2_{12}}}{F_{j+2_{11}}} & -\frac{q_{os}}{F_{j+2_{11}}} \\ 0 & 1 & 0 \\ 0 & 0 & 1 \end{bmatrix}}_{\boldsymbol{Pb}} \begin{bmatrix} q \\ h \\ 1 \end{bmatrix}_b^L$$ Eq.(53)

where $\boldsymbol{P_b}$ represents the extended point transfer matrix for a branch with an oscillating dead-end.

Valve point transfer matrix $\boldsymbol{P_V}$

In the presented study, three-point transfer matrices are utilized to resemble the valve point transfer matrix $\boldsymbol{P_v}$, as in figure (3.22 b). The first point $\boldsymbol{P_j}$ represents the point transfer matrix at the inlet section of the valve sliding seal. The second point $\boldsymbol{P_{j+1}}$ presents the point transfer matrix between the inlet and exit sections of the oscillating sliding seal at section $j+1$. This point $\boldsymbol{P_{j+1}}$ is named by valve oscillating sliding seal point transfer matrix. Finally, the last point $\boldsymbol{P_{j+2}}$ resemble the point transfer matrix of the valve exit at section $j+2$.

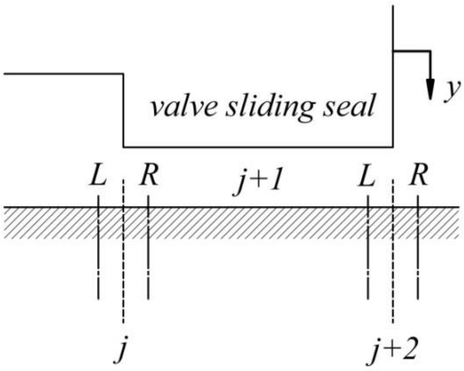

(a) Valve sliding seal notation.

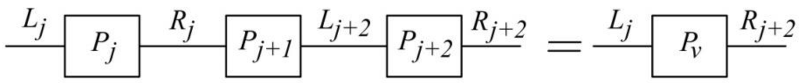

(b) Valve block diagram.

Figure 3.22: Valve point transfer matrix diagram.

Valve sliding seal inlet point transfer matrix $\boldsymbol{P_j}$

The point transfer matrix P_j at the inlet section of the valve sliding seal can be computed by relating the energy head and the flow rate at both sides of section j as in figure (3.22) as follows:

$$H_j^R - H_j^L = \frac{{Q_j^L}^2}{2g\,{A_j^L}^2} - \frac{{Q_j^R}^2}{2g\,{A_j^R}^2} = f\left(Q_j^L, Q_j^R, A_j^R\right) \qquad \text{Eq.(54)}$$

$$Q_j^R = Q_j^L \qquad \text{Eq.(55)}$$

By substituting equation Eq.(55) into Eq.(54), then equation Eq.(54) may be written as:

$$H_j^R - H_j^L = \frac{{Q_j^L}^2}{2g}\left(\frac{1}{{A_j^L}^2} - \frac{1}{{A_j^R}^2}\right) = f\left(Q_j^L,\ A_j^R\right) \qquad \text{Eq.(56)}$$

As mentioned previously, to use the transfer matrix method, non-linear equations such as Eq.(56) must be linearized. Therefore, Eq. (57) represents the time-dependent form of Eq.(56) after being linearized using the Taylor series function, as follows:

$$h_j^R - h_j^L = \frac{\partial f}{\partial Q_j^L}(Q_{oj}^L,\, A_{oj}^R)\, q_j^L + \frac{\partial f}{\partial A_j^R}(Q_{oj}^L, A_{oj}^R)\, A^{*R}_{\ j}$$

$$h_j^R = h_j^L + \frac{Q_{oj}^L}{g}\left(\frac{1}{A_j^{L^2}} - \frac{1}{A_{oj}^{R^2}}\right) q_j^L + \frac{Q_{oj}^{L^2}}{g}\left(\frac{1}{A_{oj}^{R^3}}\right) A^{*R}_{\ j}$$

Since $A_j^R = L_o(y_{o_g} - y)$, then $A^{*R}_{\ j} = -L_o y$ and,

$$h_j^R = \frac{Q_{oj}^L}{g}\left(\frac{1}{A_j^{L^2}} - \frac{1}{A_{oj}^{R^2}}\right) q_j^L + h_j^L - \frac{Q_{oj}^{L^2}}{g}\left(\frac{1}{A_{oj}^{R^3}}\right) L_o y \qquad \text{Eq.(57)}$$

The time dependent equation of Eq.(55) can be presented as follows:

$$q_j^R = q_j^L + 0\, h_j^L + 0\, y \qquad \text{Eq.(58)}$$

By converting Eq.(57) and Eq.(58) into the frequency domain using Eq.(25) and Eq.(26), the extended point transfer matrix of the valve sliding seal inlet $\boldsymbol{P_j}$ can be computed as follows:

$$\begin{bmatrix} q \\ h \\ Y \end{bmatrix}_j^R = \underbrace{\begin{bmatrix} 1 & 0 & 0 \\ \frac{Q_{oj}^L}{g}\left(\frac{1}{A_j^{L^2}} - \frac{1}{A_{oj}^{R^2}}\right) & 1 & -\frac{Q_{oj}^{L^2}}{g}\left(\frac{1}{A_{oj}^{R^3}}\right) L_o \\ 0 & 0 & 1 \end{bmatrix}}_{\boldsymbol{Pj}} \begin{bmatrix} q \\ h \\ Y \end{bmatrix}_j^L \qquad \text{Eq.(59)}$$

where Y is the seal vibration displacement amplitude (i.e., $y = Ye^{(i\omega+\sigma)t}$), and $\boldsymbol{P_j}$ is the extended point transfer matrix of the valve sliding seal inlet.

Oscillating sliding seal point transfer matrix $\boldsymbol{P_{j+1}}$

The point transfer matrix of the oscillating sliding seal $\boldsymbol{P_{j+1}}$ can be computed, by relating the energy head and flow rate at the right side of section *j* and the left side of section *j+2* as in figure (3.22), as follows:

$$H^{L}_{j+2} - H^{r}_{j} = \frac{Q^{R^2}_{j}}{2g\, A^{R^2}_{j}} - \frac{Q^{L^2}_{j+2}}{2g\, A^{L^2}_{j+2}} = f\left(Q^{L}_{j+2}, Q^{R}_{j}, A^{R}_{j}, A^{L}_{j+2}\right)$$

$$\because\ A^{R}_{j} = A^{L}_{j+2}$$

$$\therefore H^{L}_{j+2} - H^{r}_{j} = \frac{1}{A^{R^2}_{j}}\left(\frac{Q^{R^2}_{j}}{2g} - \frac{Q^{L^2}_{j+2}}{2g}\right) = f\left(Q^{L}_{j+2}, Q^{R}_{j}, A^{R}_{j}\right) \qquad \text{Eq.(60)}$$

$$Q^{L}_{j+2} = Q^{R}_{j} + i\omega\, A_{ss}\, y \qquad \text{Eq.(61)}$$

By linearized Eq.(60) using the Taylor series function, the time-dependent equation of Eq.(60) can be computed as follows:

$$h^{L}_{j+2} - h^{R}_{j} = \frac{\partial f}{\partial Q^{L}_{j+2}}(Q^{L}_{o\,j+2},\, Q^{R}_{o\,j}\ ,\ A^{R}_{o\,j})\, q^{L}_{j+2} + \frac{\partial f}{\partial Q^{R}_{j}}(Q^{L}_{o\,j+2},\, Q^{R}_{o\,j}\ ,\ A^{R}_{o\,j})\, q^{R}_{j}$$
$$+ \frac{\partial f}{\partial A^{R}_{j}}(Q^{L}_{o\,j+2},\, Q^{R}_{o\,j}\ ,\ A^{R}_{o\,j})\, A^{*R}_{j}$$

$$h^{L}_{j+2} = h^{R}_{j} - \frac{1}{A^{R^2}_{o\,j}}\left(\frac{Q^{L}_{o\,j+2}}{g}\right) q^{L}_{j+2} + \frac{1}{A^{R^2}_{o\,j}}\left(\frac{Q^{R}_{o\,j}}{g}\right) q^{R}_{j} - \frac{1}{A^{R^3}_{o\,j}}\left(\frac{Q^{R^2}_{o\,j}}{g} - \frac{Q^{L^2}_{o\,j+2}}{g}\right) A^{*R}_{j}$$

Since $Q^{L}_{o\,j+2} = Q^{R}_{o\,j}$

$$h^{L}_{j+2} = h^{R}_{j} + \frac{Q^{L}_{o\,j+2}}{g\, A^{R^2}_{o\,j}}(q^{R}_{j} - q^{L}_{j+2}) \qquad \text{Eq.(62)}$$

The time dependent equation of Eq.(61) can be presented also as:

$$q_{j+2}^{L} = q_j^R + 0\,h_j^R + i\omega\, A_{ss}\, y \qquad \text{Eq.(63)}$$

By substituting Eq.(63) into Eq.(62), then Eq.(62) will be function of h_{j+2}^{R}, h_j^R and y :

$$h_{j+2}^{L} = 0\,q_j^R + h_j^R - \frac{Q_{o\,j+2}^{L}}{g\,A_{o\,j}^{R^2}}(i\omega\, A_{ss}\, y) \qquad \text{Eq.(64)}$$

By converting Eq.(63) and Eq.(64) into the frequency domain and representing the developed equations in a matrix form, the point transfer matrix for an oscillation seal ***P***$\boldsymbol{P_{j+1}}$ can be calculated as follows:

$$\begin{bmatrix} q \\ h \\ Y \end{bmatrix}_{j+2}^{L} = \underbrace{\begin{bmatrix} 1 & 0 & i\,\omega\, A_{ss} \\ 0 & 1 & -i\dfrac{\omega\, A_{ss}\, Q_{o\,j+2}^{L}}{g\,A_{o\,j}^{R^2}} \\ 0 & 0 & 1 \end{bmatrix}}_{\boldsymbol{P\,j+1}} \begin{bmatrix} q \\ h \\ Y \end{bmatrix}_{j}^{R} \qquad \text{Eq.(65)}$$

Valve sliding seal exit point transfer matrix $\boldsymbol{P_{j+2}}$

In section *j+2*, we cannot neglect the head losses as in the previous sections *j* and *j+1* since the head losses are significant due to the difference in the cross-section area between the left and right sides of section *j+2*. So, to relate the pressure head at both sides of section *j+2*, the energy head at both sides are related as follows:

$$(H_{j+2}^{L} + \frac{Q_{j+2}^{L^2}}{2g\,A_{j+2}^{L^2}}) - (H_{j+2}^{R} + \frac{Q_{j+2}^{R^2}}{2g\,A_{j+2}^{R^2}}) = \frac{Q_{j+2}^{L^2}}{2g}\left(\frac{1}{A_{j+2}^{L}} - \frac{1}{A_{j+2}^{R}}\right)^2 \qquad \text{Eq.(66)}$$

Since : $Q_{j+2}^{L} = Q_{j+2}^{R}$ Eq.(67)

and $A_{j+2}^{L} = A_j^R$

Then Eq.(66) can be expressed as:

$$H^{R}_{j+2} - H^{L}_{j+2} = \frac{Q^{L^2}_{j+2}}{g\,A^{R^2}_{j+2}}\left(\frac{A^{R}_{j+2}}{A^{R}_{j}} - 1\right) = f\,(Q^{L}_{j+2}, A^{R}_{j}) \qquad \text{Eq.(68)}$$

By linearizing the nonlinear Eq.(68) using Taylor series function, the time dependent equation can be represented as follows:

$$h^{R}_{j+2} - h^{L}_{j+2} = \frac{\partial f}{\partial Q^{L}_{j+2}}(Q^{L}_{o\,j+2},\, A^{R}_{o\,j})\, q^{L}_{j+2} + \frac{\partial f}{\partial A^{R}_{j}}(Q^{L}_{o\,j+2}, A^{R}_{o\,j})\, A^{*R}_{j}$$

$$h^{R}_{j+2} = h^{L}_{j+2} + \frac{2Q^{L}_{o\,j+2}}{g\,A^{R^2}_{j+2}}\left(\frac{A^{R}_{j+2}}{A^{R}_{o\,j}} - 1\right) q^{L}_{j+2} + \frac{Q^{L^2}_{o\,j+2}}{g\,A^{R^2}_{j+2}}\left(-\frac{A^{R}_{j+2}}{A^{R^2}_{o\,j}}\right) A^{*R}_{j}$$

Since: $A^{R}_{j} = L_o(y_{o_g} - y)$, $A^{*R}_{j} = -L_o\,y$

$$h^{R}_{j+2} = \frac{2Q^{L}_{o\,j+2}}{g\,A^{R^2}_{j+2}}\left(\frac{A^{R}_{j+2}}{A^{R}_{o\,j}} - 1\right) q^{L}_{j+2} + h^{L}_{j+2} + \frac{Q^{L^2}_{o\,j+2}}{g\,A^{R^2}_{j+2}}\left(\frac{A^{R}_{j+2}}{A^{R^2}_{o\,j}}\right) L_o\,y \qquad \text{Eq.(69)}$$

By converting the time-dependent Eq.(67) (i.e. $q^{L}_{j+2} = q^{R}_{j+2}$) and Eq.(69) into the frequency domain, and representing the developed equations into matrix form, the point transfer matrix of the valve sliding seal exit $\boldsymbol{P_{j+2}}$ can be presented, as follows:

$$\begin{bmatrix} q \\ h \\ Y \end{bmatrix}^{R}_{j+2} = \underbrace{\begin{bmatrix} 1 & 0 & 0 \\ \frac{2Q^{L}_{o\,j+2}}{g\,A^{R^2}_{j+2}}\left(\frac{A^{R}_{j+2}}{A^{R}_{o\,j}} - 1\right) & 1 & \frac{Q^{L^2}_{o\,j+2}}{g\,A^{R^2}_{j+2}}\left(\frac{A^{R}_{j+2}}{A^{R^2}_{o\,j}}\right) L_o \\ 0 & 0 & 1 \end{bmatrix}}_{\boldsymbol{P}\,\boldsymbol{j+2}} \begin{bmatrix} q \\ h \\ Y \end{bmatrix}^{L}_{j+2} \qquad \text{Eq.(70)}$$

Overall transfer matrix *U*

For a piping system, the overall transfer matrix ***U*** is utilized to relate the state vectors at one end of a system to the other end. For example, let us consider a well-known problem that comprises a dead-end at the right side, a standing pressure wave at the surface of the input reservoir at the left side, and a series of connected pipelines such as in figure (3.23 a).

To compute the overall transfer matrix ***U*,** which relates the downstream state vector at section $i+3$ to the upstream state vector at section i, a block diagram is drawn as in figure (3.24 b). The blocks in the block diagram represent the transfer matrices of each component in the hydraulic system. The block diagram is very helpful in computing the overall transfer matrix ***U***. The overall transfer matrix is computed by an ordered multiplication of the point and field matrices, from the downstream end $i+3$ to the upstream end i, as in figure (3.24 b).

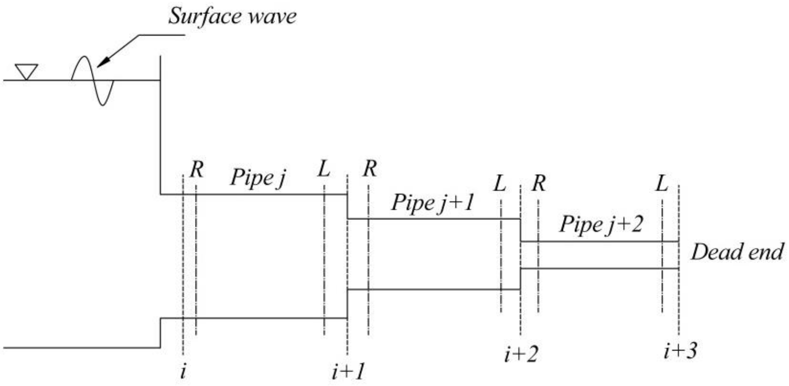

(a) Series piping system with dead end

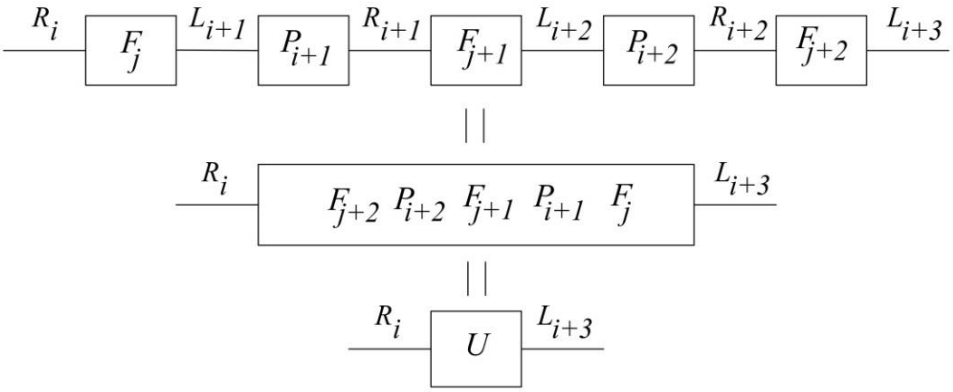

(b) Series piping system with dead end block diagram

Figure 3.23: Series piping with dead end overall transfer matrix.

Frequency response

The transfer matrix method can compute the frequency response for systems comprising more than one periodic forcing function boundaries, devices, or components. Systems containing more than one forcing function are classified into three categories:

1. The first category comprises forcing functions that have the same frequency ω_1. In this category, the transfer matrix method analyzes the system considering all forcing functions simultaneously where extended transfer matrices are utilized with the same frequency ω_1.
2. The second category deals with groups of exciters. A group of exciters operates at a frequency ω_1 while the other exciters operate at a frequency ω_2. In this case, the transfer matrix method obtains the frequency response for each group separately. Afterward, the frequency responses are superimposed to compute the total response of the system, as the transfer matrix method utilizes linear equations.
3. The last category considers a group of exciters where each exciter has its own frequency. In this situation, the transfer matrix method computes the frequency response for each exciter separately, and subsequently, all the frequency responses are superimposed to determine the system's total frequency response.

3.4.2 2nd Model system governing equations

For the case of interest, as the seal vibration is self-excited hence the seal oscillations are of decaying or diverging amplitude depending on system stability. Therefore, the system components transfer matrices (i.e., field and point transfer matrices) are written for the free damped oscillation since decayed or diverged pressure and flow rate oscillations are expected. Accordingly, to represent the free damped oscillations, the estimated transfer matrices are written by replacing $i\omega$ with the complex frequency $i\omega+\sigma$ (*Chaudhry 2014*).

The following sections will present the system governing equations for each section as in figure (3.24), after being computed for free damped oscillations.

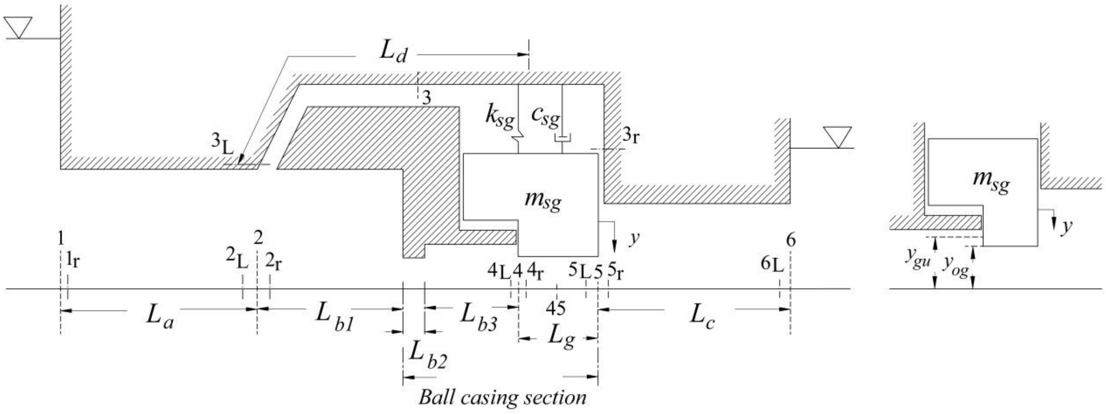

Figure 3.24: Simplified hydro-mechanical diagram for each group of Salime hydro-electric power plant with seal geometrical features, notations and vibration coordinate.

Pipeline a section 1_r-2_L

By applying Eq.(43a) and replacing *iω* by the complex frequency *iω+σ*, the field transfer matrix "$\boldsymbol{F_a}$" of pipeline a for free damped oscillations is calculated as follows:

$$\boldsymbol{Z_2^L} = \boldsymbol{F_a Z_1^r}$$

$$\begin{bmatrix} q \\ h \\ Y \end{bmatrix}_2^L = \underbrace{\begin{bmatrix} \cosh(\mu_a L_a) & -\sinh(\mu_a L_a)\dfrac{1}{Z_a} & 0 \\ -\sinh(\mu_a L_a) Z_a & \cosh(\mu_a L_a) & 0 \\ 0 & 0 & 1 \end{bmatrix}}_{\boldsymbol{Fa}} \begin{bmatrix} q \\ h \\ Y \end{bmatrix}_1^r \qquad \text{Eq.(71)}$$

$$where: \mu_a = \sqrt{\left(\frac{i\omega+\sigma}{a_a}\right)^2 + \frac{g(i\omega+\sigma) R_a A_a}{a_a^2}}\ , Z_a = \frac{\mu_a a_a^2}{g(i\omega+\sigma) A_a}\ , R_a = \frac{\mathrm{f}_a Q_{oa}}{g\, d_a A_a^2}$$

, and Y represents the seal vibration displacement amplitude.

Branch junction 2 section 2_L-2_r

The branch junction at point 2 has an oscillating dead end due to the oscillation of the sliding seal at section 3_r as in figure (3.25). So, by applying Eq.(53), and replacing *iω* with the complex frequency $i\omega+\sigma$, the branch junction with an oscillating dead-end point transfer matrix for point 2 can be written as follows:

$$\boldsymbol{Z_2^r} = \boldsymbol{P_2 Z_2^L}$$

$$\begin{bmatrix} q \\ h \\ Y \end{bmatrix}_2^r = \underbrace{\begin{bmatrix} 1 & \dfrac{F_{c12}}{F_{c11}} & -\dfrac{(i\omega+\sigma)A_{os}}{F_{c11}} \\ 0 & 1 & 0 \\ 0 & 0 & 1 \end{bmatrix}}_{\boldsymbol{P2}} \begin{bmatrix} q \\ h \\ Y \end{bmatrix}_2^L \qquad \text{Eq.(72)}$$

Pipeline d section 3_L-3_r

The field transfer matrix $\boldsymbol{F_d}$ of pipeline d for free damped oscillations is estimated in the same manner as in pipeline a. However, the losses in pipeline d are considered for laminar flow as it is expected to have a small flow rate in pipeline d.

$$\boldsymbol{Z_3^r} = \boldsymbol{F_d Z_3^L}$$

$$\begin{bmatrix} q \\ h \\ Y \end{bmatrix}_3^r = \underbrace{\begin{bmatrix} \cosh(\mu_d L_d) & -\sinh(\mu_d L_d)\dfrac{1}{Z_d} & 0 \\ -\sinh(\mu_d L_d) Z_d & \cosh(\mu_d L_d) & 0 \\ 0 & 0 & 1 \end{bmatrix}}_{\boldsymbol{F_d}} \begin{bmatrix} q \\ h \\ Y \end{bmatrix}_3^L \qquad \text{Eq.(73)}$$

$$\text{where}: \mu_d = \sqrt{\left(\frac{i\omega+\sigma}{a_d}\right)^2 + \frac{g(i\omega+\sigma)R_d A_d}{a_d^2}}\ , Z_d = \frac{\mu_d a_d^2}{g(i\omega+\sigma)A_d}\ , R_c = \frac{32\nu}{g d_d A_d^2}$$

Pipeline b1 section 2_r-4_L

The field transfer matrix $\boldsymbol{F_{b1}}$ of pipeline *b1* is estimated as in the same manner of pipeline *a* and *d*. However the loss coefficient R_{b1} differs a little as it considers the Borda's losses due to the cross-section enlargement between A_{b2} and A_{b3}, as in figure (3.24).

$$\boldsymbol{Z_4^L = F_{b1} Z_2^r},$$

$$\begin{bmatrix} q \\ h \\ Y \end{bmatrix}_4^L = \underbrace{\begin{bmatrix} \cosh(\mu_{b1} L_{b1}) & -\sinh(\mu_{b1} L_{b1}) \dfrac{1}{Z_{b1}} & 0 \\ -\sinh(\mu_{b1} L_{b1}) Z_{b1} & \cosh(\mu_{b1} L_{b1}) & 0 \\ 0 & 0 & 1 \end{bmatrix}}_{\boldsymbol{F b1}} \begin{bmatrix} q \\ h \\ Y \end{bmatrix}_2^r \qquad \text{Eq.(74)}$$

$$where: \mu_{b1} = \sqrt{\left(\frac{i\omega+\sigma}{a_{b1}}\right)^2 + \frac{g(i\omega+\sigma) R_{b1} A_{b1}}{a_{b1}^2}} \; , Z_{b1} = \frac{\mu_{b1} a_{b1}^2}{g(i\omega+\sigma) A_{b1}} \; ,$$

$$R_{b1} = \frac{\mathrm{f}_{b1} Q_{ob}}{g\, d_{b1} A_{b1}^2} + \frac{Q_{ob}\left(\frac{1}{A_{b2}} - \frac{1}{A_{b3}}\right)^2}{2g\, L_{b1}}$$

Valve sliding seal inlet point 4 section 4_L-4_r

Point 4 resembles the valve sliding seal inlet boundary. In order to compute the valve sliding seal inlet point transfer matrix Eq.(59) is going to be adopted as follows:

$$\boldsymbol{Z_4^r = P_4 Z_4^L}$$

$$\begin{bmatrix} q \\ h \\ Y \end{bmatrix}_4^r = \underbrace{\begin{bmatrix} 1 & 0 & 0 \\ \dfrac{Q_{ob}}{g}\left(\dfrac{1}{A_{b3}^2} - \dfrac{1}{A_{og}^2}\right) & 1 & -\dfrac{Q_{ob}^2}{g}\left(\dfrac{1}{A_{og}^3}\right) L_o \\ 0 & 0 & 1 \end{bmatrix}}_{\boldsymbol{P4}} \begin{bmatrix} q \\ h \\ Y \end{bmatrix}_4^L \qquad \text{Eq.(75)}$$

Oscillating sliding seal point 4-5 section 4_r-5_L

The oscillating sliding seal point transfer matrix for free damped oscillations can be computed by replacing $i\omega$ in Eq.(65) with the complex frequency $i\omega+\sigma$ as follows:

$$\boldsymbol{Z_5^L = P_{45}\, Z_4^r}$$

$$\begin{bmatrix} q \\ h \\ Y \end{bmatrix}_5^L = \underbrace{\begin{bmatrix} 1 & 0 & (i\omega+\sigma) A_{ss} \\ 0 & 1 & -\dfrac{(i\omega+\sigma)\; A_{ss}\, Q_{og}}{g\, A_{og}^2} \\ 0 & 0 & 1 \end{bmatrix}}_{\boldsymbol{P45}} \begin{bmatrix} q \\ h \\ Y \end{bmatrix}_4^r \qquad \text{Eq.(76)}$$

Valve sliding seal exit point 5 section 5_L-5_r

The valve sliding seal exit point transfer matrix for free damped oscillations can be computed by utilizing Eq.(70) as follows:

$$\boldsymbol{Z_5^r} = \boldsymbol{P_5}\ \boldsymbol{Z_5^L}$$

$$\begin{bmatrix} q \\ h \\ Y \end{bmatrix}_5^R = \underbrace{\begin{bmatrix} 1 & 0 & 0 \\ \frac{2Q_{og}}{g\,A_c^2}\left(\frac{A_c}{A_{og}}-1\right) & 1 & \frac{Q_{og}^2}{g\,A_c^2}\left(\frac{A_c}{A_{og}^2}\right)L_o \\ 0 & 0 & 1 \end{bmatrix}}_{\boldsymbol{P5}} \begin{bmatrix} q \\ h \\ Y \end{bmatrix}_5^L \qquad \text{Eq.(77)}$$

Pipeline *c* section 5_r-6_L

By using Eq.(43a), the discharge pipeline *c* field transfer matrix $\boldsymbol{F_c}$ is computed for free damped oscillations as following :

$$\boldsymbol{Z_6^L} = \boldsymbol{F_c}\,\boldsymbol{Z_5^r}$$

$$\begin{bmatrix} q \\ h \\ Y \end{bmatrix}_6^L = \underbrace{\begin{bmatrix} \cosh(\mu_c L_c) & -\sinh(\mu_c L_c)\frac{1}{Z_c} & 0 \\ -\sinh(\mu_c L_c)Z_c & \cosh(\mu_c L_c) & 0 \\ 0 & 0 & 1 \end{bmatrix}}_{\boldsymbol{F_c}} \begin{bmatrix} q \\ h \\ Y \end{bmatrix}_5^r \qquad \text{Eq.(78)}$$

$$where:\ \mu_c = \sqrt{\left(\frac{i\omega+\sigma}{a_c}\right)^2 + \frac{g\,(i\omega+\sigma)\,R_c\,A_c}{a_c^2}}\ ,\ Z_d = \frac{\mu_c\,a_c^2}{g\,(i\omega+\sigma)\,A_c}\ , R_a = \frac{f_c\,Q_{oc}}{g\,d_c\,A_c^2}$$

Seal equation of motion

Eq.(79) represents the vibrating seal equation of motion as follows:

$$m_{sg}\,\ddot{y} + c_{sg}\,\dot{y} + k_{sg}\,y = F(t) \qquad \text{Eq.(79)}$$

$$where: F(t) = \rho g\,A_{os}\,h_3^r(t) - \rho g\,A_{ss}\left(\frac{h_4^r(t)+h_5^L(t)}{2}\right) = |F|\,e^{i\psi}\,e^{(i\omega+\sigma)t}$$

F(t) represents the fluid forces acting on the seal for free damped oscillations in the time domain. In which |*F*| represents the complex force amplitude, and ψ represents the complex force phase angle.

3.4.3 2nd Model system stability conditions

As the phenomenon under consideration belongs to self-excited vibrations where the fluid force is supported by the seal oscillatory motion, hence the fluid force can be represented as a function of the seal vibration components y , $\dot{y}$ and $\ddot{y}$. Consequently, the vibrating seal equation of motion Eq. (79) can be presented as follows:

$$\underbrace{(m_{sg}+m_{w})}_{m_{eq}}\ddot{y}+\underbrace{(c_{sg}+c_{w})}_{c_{eq}}\dot{y}+\underbrace{(k_{sg}+k_{w})}_{k_{eq}}y=0 \qquad \text{Eq.(80)}$$

m_w, c_w, and k_w represent the added water mass, damping, and stiffness coefficients of the hydrodynamic force acting on the seal.

Since the 2nd Model considers free damped oscillations and the flow forces are in couple and depends on the seal motion, hence the seal equation of motion characteristic root is considered to be the same as the time-dependent pressure and flow rate complex frequency $i\omega+\sigma 0\backslash$. In which, the seal's vibration response and characteristic root can be computed as follows (*Raw 2017*),

$$y=Y\,e^{(i\omega+\sigma)t} \qquad \text{Eq.(81)}$$

$$\omega=\omega_n\sqrt{1-\zeta^2}=\sqrt{\frac{k_{eq}}{m_{eq}}}\sqrt{1-\left(\frac{c_{eq}}{2\sqrt{m_{eq}k_{eq}}}\right)^2} \qquad \text{Eq.(82)}$$

$$\sigma=-\omega_n\zeta=-\sqrt{\frac{k_{eq}}{m_{eq}}}\,\frac{c_{eq}}{2\sqrt{m_{eq}k_{eq}}} \qquad \text{Eq.(83)}$$

With the aid of the seal equation of motion Eq. (79), the seal response Eq. (81), and as concluded in section 4.2.1 (i.e., 1st Model dimensionless results) that the added water mass depends only on m_d ($m_w=m_d=\rho\,L_d\,A_d\left(\frac{A_{os}}{A_d}\right)^2$), hence the added water mass, damping and stiffness coefficients (m_w, c_w, and k_w) can be computed as follows:

By adding $m_w \ddot{y}$ to both sides of the vibrating seal equation of motion Eq. (79) and multiplying both sides by $\frac{Y}{Y}$, thus Eq.(79) can be written as:

$$\left(m_{sg} + m_w\right)\ddot{y} + c_{sg}\,\dot{y} + k_{sg}\,y = F(t) = \frac{F_R}{Y}\,y + i\,\frac{F_I}{Y}\,y + m_w\,\ddot{y} \qquad \text{Eq.(79a)}$$

By using the first and second derivative of the seal's equation of motion response Eq.(81), hence *iy* can be computed as:

$$\dot{y} = (i\omega + \sigma)Y\,e^{(i\omega+\sigma)t} = i\,\omega y + \sigma y$$

$$iy = \frac{\dot{y}}{\omega} - \frac{\sigma}{\omega}\,y \qquad \text{Eq.(81a)}$$

$$\ddot{y} = (i\omega+\sigma)^2\,Y\,e^{(i\omega+\sigma)t} = \left(\sigma^2 - \omega^2\right)y + 2\sigma\,\dot{y} - 2\,\sigma^2\,y$$

$$\ddot{y} = 2\sigma\,\dot{y} - y\left(\sigma^2 + \omega^2\right) \qquad \text{Eq.(81b)}$$

By substituting Eqs.(81a and 81b) into Eq.(79a), the vibrating seal equation of motion can be calculated as follows:

$$m_{sg}\,\ddot{y} + c_{sg}\,\dot{y} + k_{sg}\,y = \underbrace{-\,\ddot{y}\,m_w + \dot{y}\left(\frac{F_I}{Y\omega} + 2\,m_w\sigma\right) + y\left(\frac{F_R}{Y} - \frac{F_I\,\sigma}{Y\omega} - m_w(\sigma^2+\omega^2)^2\right)}_{F(t)} \qquad \text{Eq.(79b)}$$

By comparing the seal equation of motion Eq.(80) with Eq.(79b), the added water mass, damping and stiffness coefficients can be computed as follows:

$$m_w = m_d = \rho\,L_d\,A_d\left(\frac{A_{os}}{A_d}\right)^2 \qquad \text{Eq.(84)}$$

$$c_w = -\frac{F_I}{Y\omega} - 2\,m_w\,\sigma \qquad \text{Eq.(85)}$$

$$k_w = -\left(\frac{F_R}{Y} - \frac{F_I\,\sigma}{Y\omega} - m_w(\sigma^2+\omega^2)^2\right) \qquad \text{Eq.(86)}$$

The vibrating seal equation of motion Eq.(79b) consists of the seal structure's inertia, damping, and stiffness forces and the hydrodynamic force acting on the seal represented by the added water mass, damping and stiffness forces. The complex vector diagram of the seal equation of motion Eq.(79b) can be drawn as in Figure

(3.25), where the vibrating seal equation of motion forces are presented in an equivalent way to the ordinary forced vibration system (*Raw 2017*). The phase angles presented in figure (3.25) are identified in table 3.2.

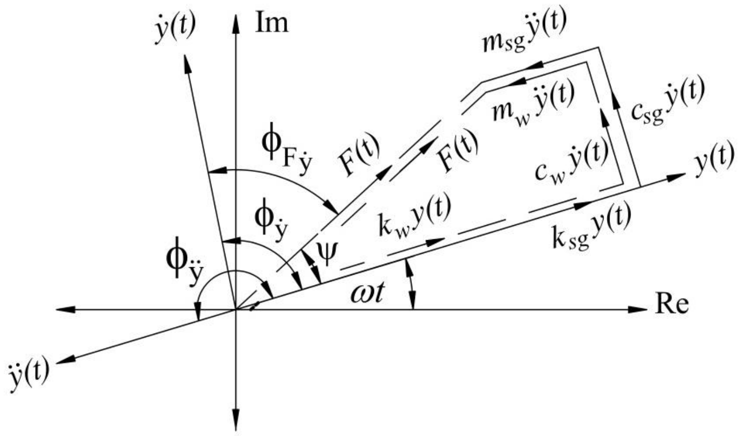

Figure 3.25: Seal equation of motion complex vector diagram.

Table 3.2: Seal equation of motion complex vector diagrams phase angles

ψ	$\psi=\tan^{-1}\left(\frac{I_m(F)}{Re(F)}\right)$	Phase angle between the real and imaginary components of the hydrodynamic force acting on the seal *F(t)*. Also it is the phase angle between the seal's hydrodynamic force *F(t)* and the seal's vibration displacement *y*.
$\phi_{\dot{y}}$	$\phi_{\dot{y}}=\tan^{-1}\left(\frac{\omega}{\sigma}\right)$	Phase angle between the seal's vibration displacement and velocity
$\phi_{\ddot{y}}$	$\phi_{\ddot{y}}=\tan^{-1}\left(\frac{2\sigma\omega}{\sigma^2-\omega^2}\right)$	Phase angle between the seal's vibration displacement and acceleration
$\phi_{F\dot{y}}$		Phase angle between the seal's hydrodynamic force *F(t)* and seal vibration velocity.

The phase angle ψ is the phase angle between the fluid dynamic force acting on the seal and the seal vibration displacement. This phase angle identifies the sign of the added water mass, damping and stiffness coefficients. For example, if the phase angle ψ is in the range of $90^0>\psi>0^0$, thus the fluid dynamic force is in phase with the seal's vibration displacement and velocity and out of phase of the seal vibration acceleration. In this situation, the fluid dynamic force develops a negative added water damping, a negative added water stiffness and a positive added water mass. For this case, the fluid dynamic force tends to excite the seal oscillation since the fluid dynamic force is in the same direction of the seal vibration velocity.

For such a system, the system's dynamic stability is recognized by the seal equivalent damping coefficient c_{eq} and σ values. If c_{eq} <0, thus σ >0 and the system is dynamically unstable. In this situation, the fluid dynamic force tends to excite system oscillations rather than damping it and the seal response will grow exponentially as in Eq. (81).

Since the hydrodynamic force acting on the seal and the seal response are a sinusoidal function of decaying or diverging amplitude according to system stability. Hence the seal's vibration velocity and acceleration are complex numbers, such as in Eq.(87) and Eq.(88).

$$\dot{y} = (i\omega + \sigma)Y\, e^{(i\omega+\sigma)t} \qquad \text{Eq.(87)}$$

$$\ddot{y} = (\sigma^2 - \omega^2 + 2i\sigma\omega)Y\, e^{(i\omega+\sigma)t} \qquad \text{Eq.(88)}$$

By drawing the complex vector diagrams of the seal vibration components $(y, \dot{y}, \text{and } \ddot{y})$ according to the system dynamic stability as in figure (3.26), the following phase angles $\left(\phi_{\dot{y}} \text{ and } \phi_{\ddot{y}}\right)$ can describe the seal behavior in addition to the c_{eq} and σ as in table 3.3.

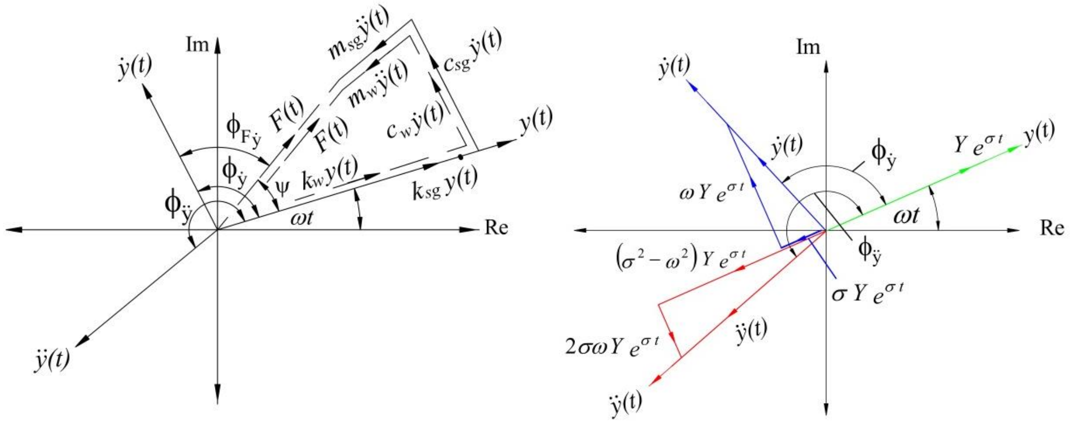

(a) Seal's equation of motion complex vector diagram for a stable system

(b) Seal's vibration components for a stable system

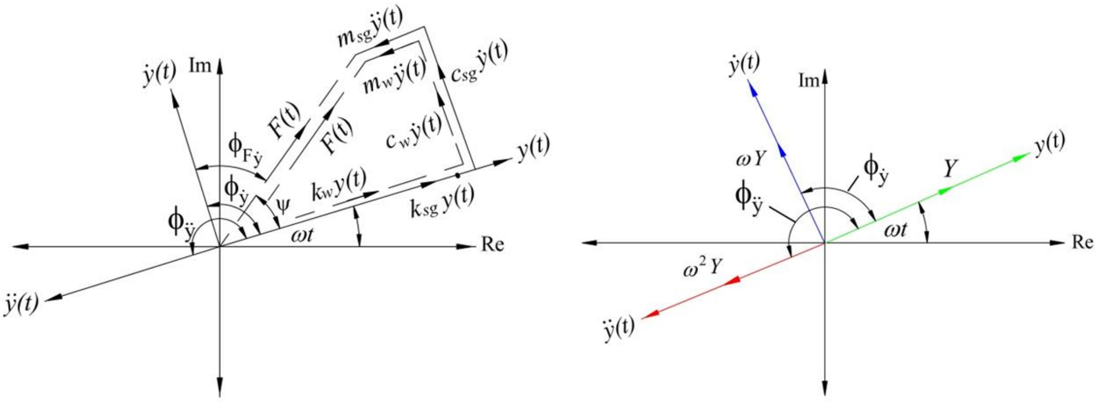

(c) Seal's equation of motion complex vector diagram for a critically stable system

(d) Seal's vibration components for a critically stable system

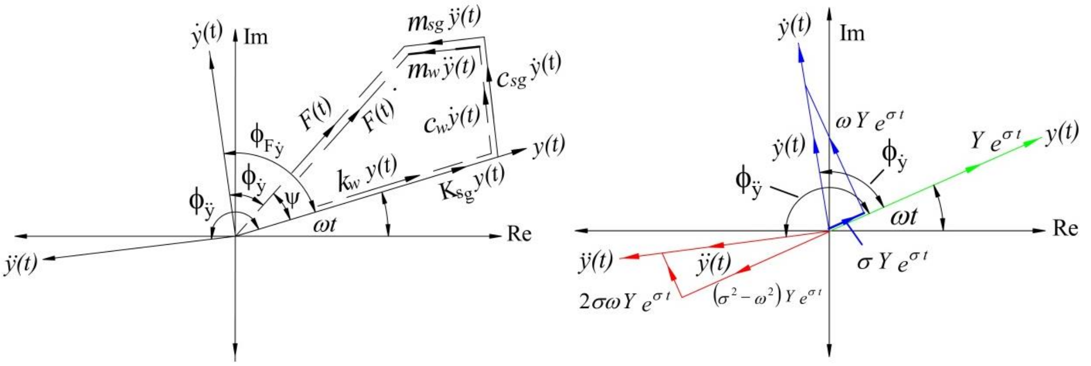

(e) Seal's equation of motion complex vector diagram for an un-stable system

(f) Seal's vibration components for an un-stable system

Figure 3.26: Seal's vibration components y, $\dot{y}$, and $\ddot{y}$ according to system stability

Table 3.3: Phase angles $\left(\phi_{\dot{y}} \text{ and } \phi_{\ddot{y}}\right)$ variation according to system stability

Dynamically stable system	$180^0>\phi_{\dot{y}}>90^0$	$270^0>\phi_{\ddot{y}}>180^0$
Critically stable system	$\phi_{\dot{y}}=90^0$	$\phi_{\ddot{y}}=180^0$
Dynamically unstable system	$0^0<\phi_{\dot{y}}<90^0$	$90^0<\phi_{\ddot{y}}<180^0$

3.4.4 2nd Model dimensionless analysis

Dimensionless analysis is developed as in the 1st model (section 3.2.4.) to know the main parameters affecting the phenomenon but while considering fluid compressibility and pipeline wall elasticity effects. Some assumptions are imposed in the second model analysis. Firstly, the wave speed is assumed to be the same for all pipelines. Secondly, the gap flow kinetic energy is assumed to be the same as the intake reservoir energy level as pipeline losses are negligible compared to the intake reservoir energy level. After applying all mentioned assumptions, the dimensionless analysis (i.e., interpreted in appendix B.1) exhibits that the dimensionless added water mass, damping and stiffness coefficients are functions of four Π-groups as follows:

$$(m_W^*, c_W^*, k_W^*) = f\left(\Pi_1, \Pi_2, \Pi_3, \Pi_4\right) \qquad \text{Eq.(89)}$$

$$\Pi_1 = \frac{Main\ line\ inertia}{Gap\ kinetic\ energy\ head} = \frac{I_m\ \omega_{ref}\ Q_{og}}{H_1}$$

$$\Pi_2 = \frac{Main\ line\ flow\ oscillation\ speed}{Pipeline\ wave\ speed} = \frac{(L_a + L_{b1} + L_g + L_c)\,\omega_{ref}}{a_j}$$

$$\Pi_3 = \frac{Pilot\ pipeline\ flow\ inertia}{Pilot\ Pipeline\ head\ losses} = \frac{I_d\,\omega_{ref}\ Q_{og}}{R_d\,L_d\,Q_{og}}$$

$$\Pi_4 = \frac{A_{ss}}{A_{os}}$$

where: $I_j = \dfrac{L_j}{g\,A_j}$, $I_m = I_a + I_b + I_c$, $\omega_{ref} = \sqrt{\dfrac{k_s}{m_s}}$

3.4.5 2nd Model computational procedure

The frequency response computation is established through several steps as follows:

1. Firstly, each component transfer matrix is estimated such as mentioned in the previous sections
2. Following, system general block diagram is drawn with its simplified version as in figure (3.27).
3. In order to relate the downstream state vector to the upstream state vector, steady-state variables such as steady-state flow rate, pressure head, and seal gap cross-section area must be estimated firstly. Afterward, an expression for the overall transfer matrix ***U*** function of ω and σ can be estimated by adopting the estimated steady-state variables and multiplying the field and point transfer

matrices in order from the downstream end (i.e., the right side starting from ***F***$\boldsymbol{F_c}$) to the upstream end (i.e., the left side ending at $\boldsymbol{F_a}$) such as in figure (3.27).

4.

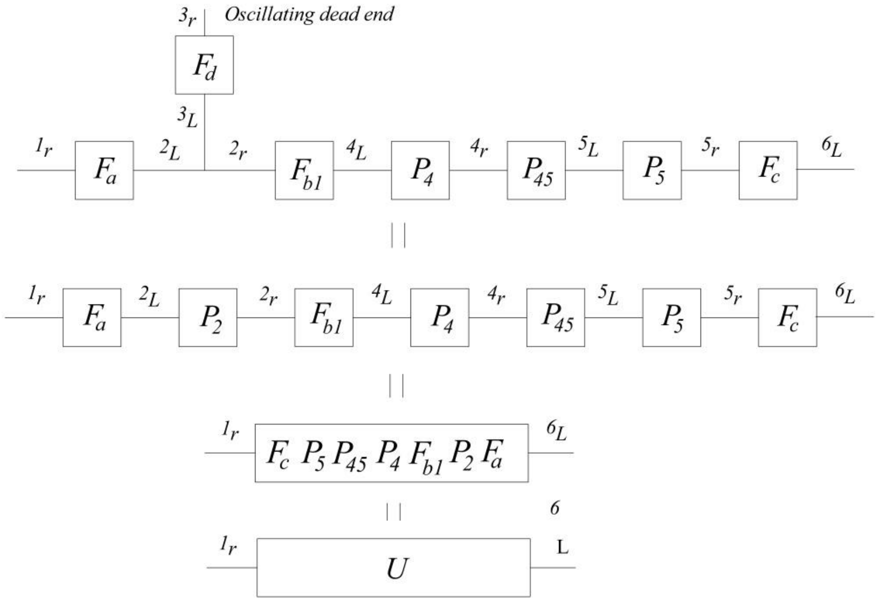

Figure 3.27: 2nd Model block diagram.

5. By applying the free end conditions (i.e $h_1^r = 0$ and $h_6^L = 0$) to the overall transfer matrix ***U***, the fluctuated flow rate at the intake reservoir q_1^r and at the discharge chamber q_6^L can be computed as a function of *ω* and *σ*. Also, the equivalent hydrodynamic force acting on the seal can be computed in the frequency domain as a function of *ω* and *σ* by utilizing the other transfer matrices Eqs.(71-78), q_1^r, and q_6^L.
6. By converting the equivalent hydrodynamic force acting on the seal into added water mass, damping, and stiffness coefficients such as in Eqs.(84, 85, and 86), and by substituting the seal response Eq.(81) into the seal equation of motion Eq.(80), then the complex seal equation of motion Eq.(80) could be adopted to solve *ω* and *σ*.

4. CHAPTER FOUR: RESULTS AND DISCUSSION

4.1 Introduction:

For the case under consideration, the unsteady leaking flow through a fluctuating gap is the main reason for the seal periodic vibrations. The fluid dynamic force created by the unsteady leaking flow identifies the seal behavior. If the fluid dynamic force excites the seal oscillation, thus a negative added water damping is developed. In this case, if the magnitude of the developed added water damping c_w is higher than the seal structure damping c_{sg} then the fluid dynamic force causes the seal to oscillate with increasing amplitude. In this situation, the amplitudes of pressure and flow rate oscillations increase as well, showing a dynamically unstable system. Also, the hydrodynamic force acting on the seal can alter the seal's dynamic response through the added water mass m_w and the added water stiffness k_w coefficients. If the fluid force is in phase with the seal vibration displacement, thus negative added water stiffness k_w and positive added water mass m_w develop. In this situation, the fluid dynamic force increases the seal's equivalent mass coefficient m_{eq} and decreases the seal's equivalent stiffness coefficient k_{eq}. As a result, the seal oscillations are of lower frequency as well as the pressure and the flow rate oscillations. Hence according to what mentioned above, the dynamic characteristics of the seal can describe the hydro-mechanical system dynamic behavior. Therefore, Π_m, Π_c, and Π_k representing the added water mass m_w, damping c_w, and stiffness k_w coefficients ratio to the seal structure mass m_{sg}, damping c_{sg}, and stiffness k_{sg} coefficients are utilized to interpret the system dynamic behavior.

Engineers in hydropower plants are always asked to provide solutions to the encountered problems and maintain system reliability on all occasions. Therefore, system conditions of stable and unstable operation are established and evaluated in order to provide recommendations for system stability enhancement. For this aim, stability charts function of the developed Π-groups is constructed in following results, to evaluate the influence of the Π-groups on the system dynamic behavior.

The dimensionless results presented at the beginning are more related to the scientific point of view and somehow far from the practical point of view. In practice usually, engineers and power plants managers require to be well informed about the reasons behind a phenomenon. However, they want to understand the phenomenon using more familiar parameters utilized at the power plants. That is why following the dimensionless analysis a parametric study based on the Salime power plant configuration is presented to explain the system's dynamic behavior using more familiar parameters in the power plant field.

4.2 1st Model results and discussion:

The first section presents the first model results considering *seal dynamic characteristics* and *an unsteady*, *unidirectional*, *incompressible and viscous flow* (i.e., considering linear head losses).

In the first section of the 1st Model results, the dimensionless analysis evaluates the influence of the developed Π-groups on Π_m, Π_c, and Π_k. Afterward, stability charts function of the developed Π-groups is constructed to evaluate Π-groups influence on system dynamic stability and to provide recommendations for system stability enhancement. Following, a parametric study is developed for the case of the Salime power plant that aims to assess the influence of the input reservoir energy level, gap angle, pilot pipeline geometry and seal unstrained clearance on the seal's dynamic behavior.

4.2.1 1st Model dimensionless analysis:

Figure (4.1) shows the influence of Π_1 (mainline inertia head ratio to H_1) on the dimensionless added water mass Π_m , damping Π_c and stiffness Π_k, as well as on the dimensionless seal oscillation frequency f^*, while keeping the other Π-groups constant *(i.e.,* f^* is the ratio between seal's oscillation frequency f and the seal's structural natural frequency corresponding to the gap angle as follows: $f_{sg} = \sqrt{k_{sg}/m_{sg}} \big/ 2\pi$).

Figure (4.1 b) shows that at low values of Π_1, the dynamic fluid force acting on the seal excites more the seal oscillation as the added water damping has higher negative values. Also, figure (4.1 c) shows that the seal's oscillation frequency is hardly influenced by Π_1 since Π_1 has a small influence on the added water stiffness as in figure (4.1 b) and a negligible influence on the added water mass as in figure (4.1 a).

The dynamic stability of the vibrating seal is identified by the seal equivalent damping coefficient which is function of the seal's structure damping and the added water damping that is created by the action of the fluid dynamic force on the vibrating seal. The seal structure damping is usually of a small value which is nearly negligible compared to the seal structure stiffness. Therefore, any small variation of the added water damping created by the fluid dynamic force should be taken into consideration since the seal structure damping is of a small value. The added water damping created by the fluid dynamic force may enhance or reduce the seal dynamic stability depending on the phase angle ψ. The phase angle ψ is the phase angle between the fluid dynamic force acting on the seal and the seal vibration displacement. If the phase angle ψ as in figure (4.1 c) is in the range of $0^0<\psi<90^0$, the fluid dynamic force is in phase with the seal vibration displacement and velocity. In this case, the fluid dynamic force develops negative added water damping and negative added water stiffness as in figure (4.1 b). Although Π_1 has a negligible influence on the magnitude of the fluid dynamic force $|F^*|$ ($|F^*| = |F| / \rho g H_1 A_{os}$), the phase angle ψ increases by increasing Π_1 as in figure (4.1 c). In this situation, the fluid dynamic force becomes more in phase with the seal vibration velocity, developing a higher negative added water damping as in figure (4.1 b), leading to system dynamic instability as $\Pi_c<-1$.

As mentioned above the phase angle ψ influences both the added water damping and the added water stiffness. The added water stiffness increases by increasing Π_1 as in figure (4.1 b) since the phase angle ψ increases by increasing Π_1 as in figure (4.1 c). However, this added water stiffness has a minimal effect on the seal's oscillation frequency as in figure (4.1 c) since the added water stiffness is of minimal value compared to the seal structure stiffness (i.e., $\Pi_k <<1$) as in figure (4.1 b).

Figure (4.1 a) shows that Π_1 which comprises the input reservoir energy level and the mainline inertia has a negligible effect on the added water mass m_w since the added water mass is nearly constant for all values of Π_1 ($\Pi_m \approx 2188.9$). However, the added water mass m_w depends on the pilot pipeline water mass and the external surface area of the seal A_{os}, as the ratio between m_w and m_d is ≈1 for all values of Π_1 (i.e., $m_d = \rho L_d A_d \left(\frac{A_{os}}{A_d} \right)^2$).

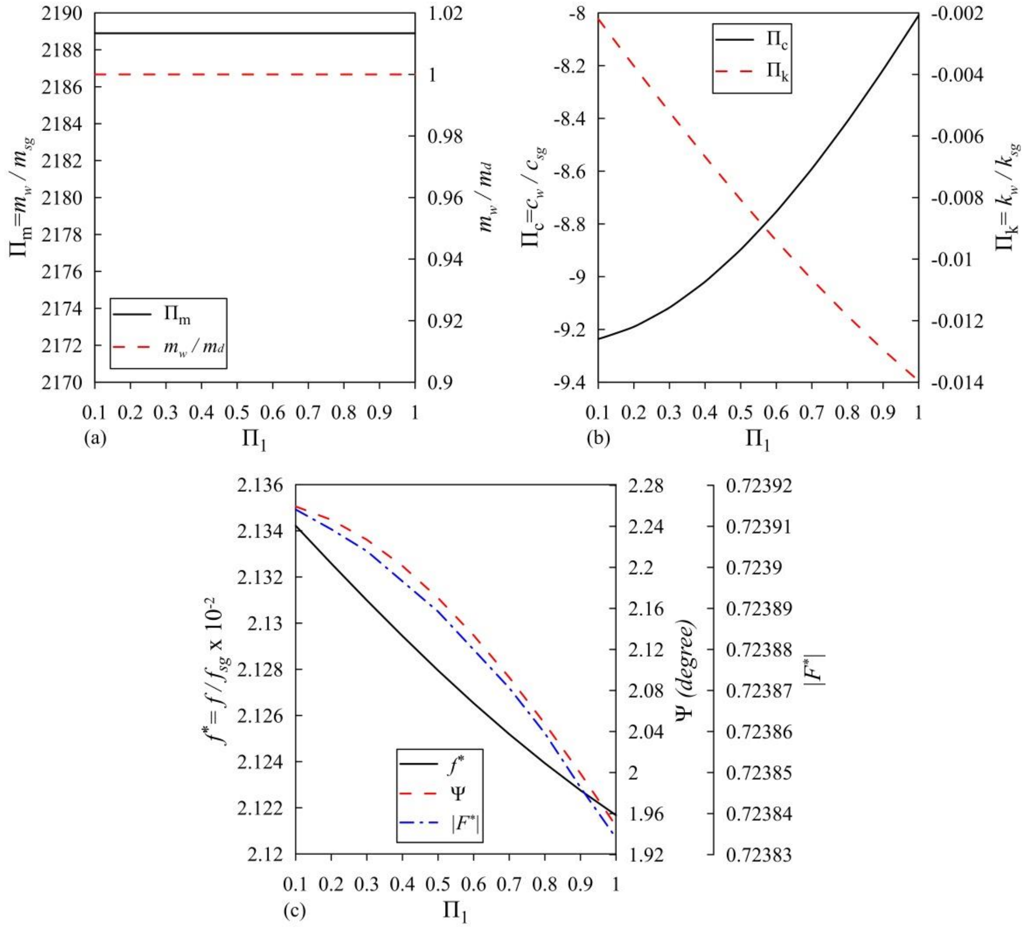

Figure 4.1: (a) Influence of Π_1 on Π_m, and m_w / m_d. (b) Influence of Π_1 on Πc and Π_k. (c) Influence of Π_1 on f^*, ψ, and $|F^*|$. Π_2=90, Π_3=1.5, Π_4=0.4, Π_a=0.7, Π_{b1}=0.08, Π_c=0.2 and Π_d=923.36.

Finally, the dimensionless seal oscillation f^* can describe the significance of the fluid dynamic force influence on the seal behavior. The seal oscillation frequency can be assumed to be the same as the seal oscillation natural frequency since the seal equivalent damping coefficient is very small compared to both the seal's equivalent stiffness and mass coefficients. Accordingly, the seal oscillation frequency can be computed through the flowing relation: $f^* = \frac{f}{f_{sg}} \approx \frac{\sqrt{\frac{k_{sg}+k_w}{m_{sg}+m_w}}}{\sqrt{\frac{k_{sg}}{m_{sg}}}}$. This relation shows that if f^* is in the range of 1, then the added water mass, and stiffness coefficients representing the fluid dynamic force have a negligible influence on the seal behavior. However, if $f^{*} >> 1$ *or* $f^{*} << 1$, as in figure (4.1 c), thus the dynamic fluid force dominates the seal behavior, as the difference between f and f_{sg} is significant.

Figure (4.2) exhibits the influence of Π_2 (ratio between the gap flow velocity and the speed of flow oscillation through the gap) on the same parameters as in the previous figure (4.1)**,** while keeping Π_1=0.1. Figure (4.2 a) demonstrates that the added water mass m_w is independent of Π_2 since the ratio between the added water mass m_w and m_d is $\approx$ 1 for all values of Π_2. On the other hand, figure (4.2 b) shows that by increasing Π_2, the fluid dynamic force excites more the seal oscillations as the added water damping c_w and Π_c have higher negative values. Also, the analysis shows that increasing Π_2 has a minimal effect on the seal's oscillation frequency as in figure (4.2 c) since the added water mass is independent of Π_2 and the added water stiffness influence on the seal structure stiffness is negligible (i.e., Π_k<<1) as in figure (4.2 b).

According to the seal equation of motion Eq.(11) and the gap flow pressure Eq.(18), by increasing the velocity of the gap flow (increasing Π_2), the pressure underneath the seal decreases and the fluid dynamic force acting on the seal increases as in figure (4.2 c). This increment in the fluid dynamic force is combined with an increment in the phase angle between the seal vibration displacement and the fluid dynamic force acting on the seal. As a result, the fluid dynamic force excites more the seal oscillation as the fluid dynamic force is more in phase with the seal vibration velocity. In this situation, an increment in the negative added water damping is established by increasing Π_2 as in figure (4.2 b), due to the increment in the phase angle ψ and the magnitude of the fluid dynamic force $|F^{*}|$ as in figure (4.2 c). In fact, this result matches with the results computed for the vertical vibration of the Hagestein weir gate, where the added water damping magnitude is roughly proportional to the gate flow (*Kolkman, 1964*).

The unusual result here is that by increasing Π_2, the negative added water stiffness increases as in figure (4.2 b), although the fact that the phase angle ψ increases as in figure (4.2 c). By increasing the seal's gap flow velocity, the hydrodynamic force $|F^{*}|$ acting on the seal increases, as in figure (4.2 c). So even if the phase angle ψ increases, it is combined with an increment in the fluid dynamic force, which leads to higher negative added water stiffness as in figure (4.2 b).

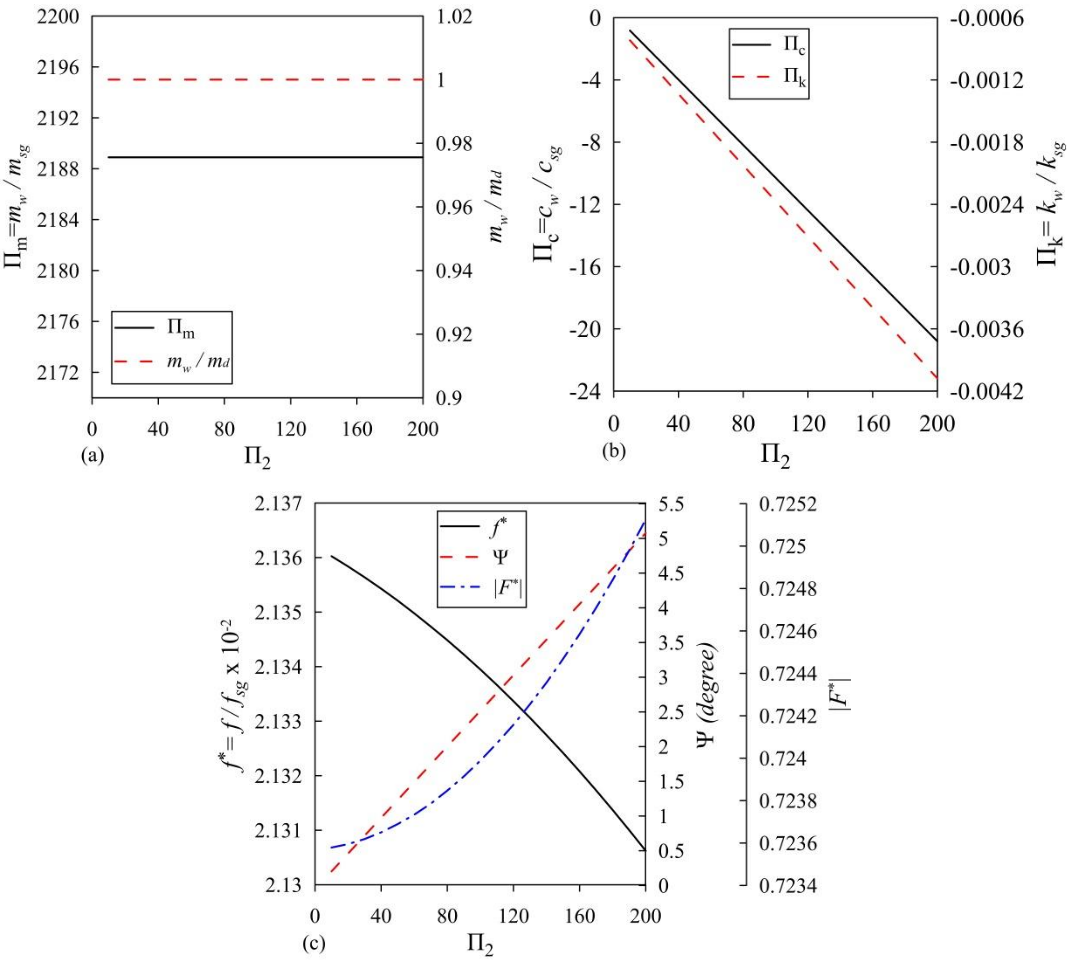

Figure 4.2: (a) Influence of Π_2 on Π_m, and m_w / m_d. (b) Influence of Π_2 on Πc and Π_k. (c) Influence of Π_2 on f^*, ψ, and $|F^*|$. Π_1=0.1, Π_3=1.5, Π_4=0.4, Π_a=0.7, Π_{b1}=0.08, Π_c=0.2 and Π_d=923.36.

Figure (4.3) shows the influence of the pilot pipeline head loss (i.e., as a function of Π_3, Π_3= Mainline inertia / pilot pipeline head losses) on the same parameters while keeping Π_1=0.1, Π_2=90, and Π_4=0.4. Figure (4.3 b) shows that incrementing the pilot pipeline head losses can stabilize the seal behavior since Π_c values are > -1.

Although, the pilot pipeline head losses have a negligible effect on the magnitude of the fluid dynamic force acting on the seal as in figure (4.3 c), increasing the pilot pipeline head losses decreases the phase angle ψ. As a result, the fluid dynamic force is more out of phase of the seal vibration velocity, decreasing the negative added water damping and reducing the fluid dynamic force excitation to the seal oscillation as in figure (4.3 b)

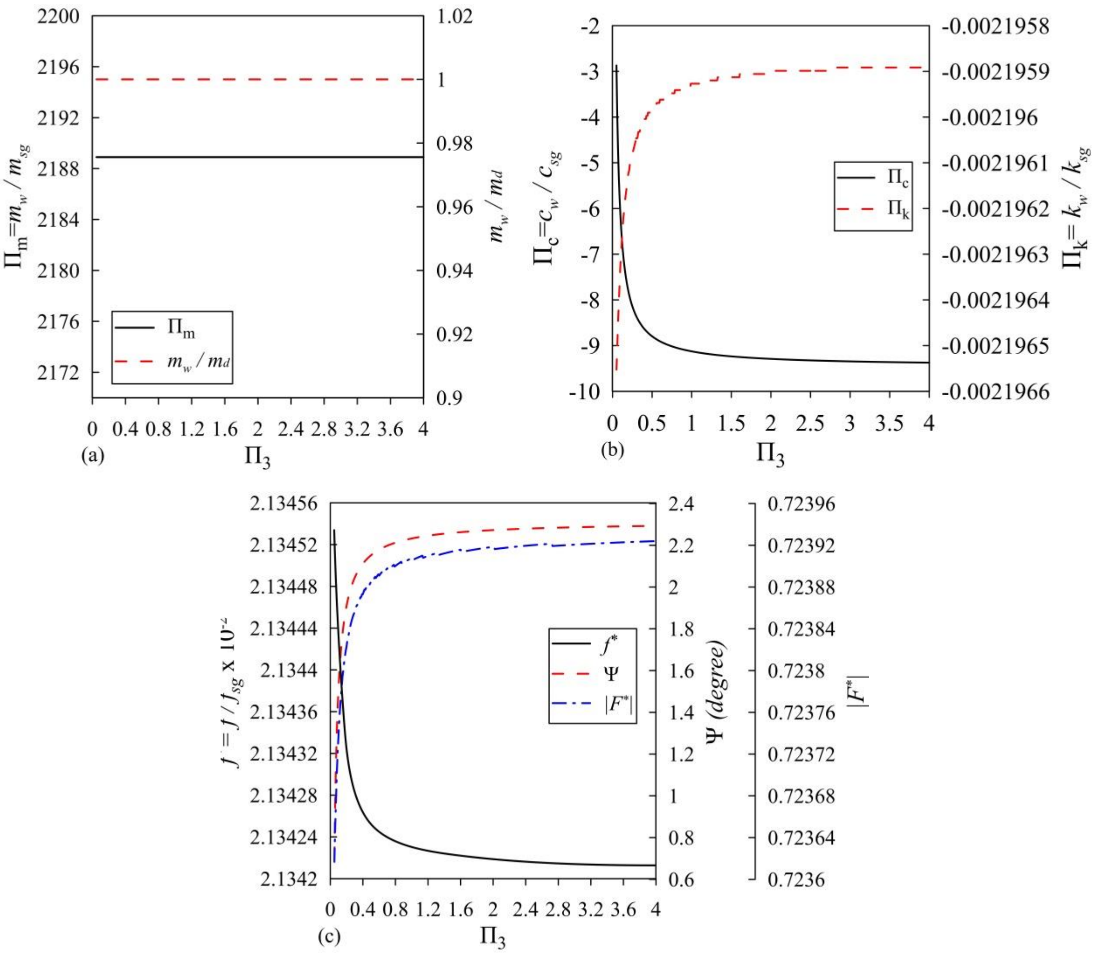

Figure 4.3: (a) Influence of Π_3 on Π_m, and m_w / m_d. (b) Influence of Π_3 on Πc and Π_k. (c) Influence of Π_3 on f^*, ψ, and $|F^*|$. Π_1=0.1, Π_2=90, Π_4=0.4, Π_a=0.7, Π_{b1}=0.08, Π_c=0.2 and Π_d=923.36.

On the other side, Π_3 has a negligible effect on Π_k because the variation of the added water stiffness k_w due to the phase angle ψ and the fluid force $|F^*|$ is very small compared to the seal structure stiffness k_{sg}, as in figure (4.3 b). As a result, the seal's oscillation frequency is nearly unaffected by the pilot pipeline head losses (Π_3), as in figure (4.3 c), particularly since Π_3 has also no effect on the added water mass as in figure (4.3 a).

Figure (4.4) shows the annular seal geometry influence (i.e., as a function of $\Pi_4 = \frac{A_{ss}}{A_{os}}$) on the seal dynamic behavior at the same pilot pipeline flow characteristics Π_3 and at the same Π_1=0.1 and Π_2=90. According to Eqs.(9, 10, and 19), increasing Π_4 decreases the pilot pipeline flow rate and increases the gap flow rate. As the gap flow rate increases, the magnitude of the fluid dynamic force acting on the seal increases with an increment in the phase angle ψ as in figure (4.4 c). This increment in the phase angle ψ and the magnitude of the fluid dynamic force lead to higher negative added water damping as in figure (4.4 b). The same applies to the added water stiffness even if the phase angle ψ increases as in figure (4.4 c). By increasing Π_4, the fluid dynamic force increases, which increases the negative added water stiffness as in figure (4.4 b). However, this change in added water stiffness has a small influence on the seal structure stiffness as Π_k<<1, as in figure (4.4 b). Therefore, the seal oscillation frequency decreases slightly as in figure (4.4 c).

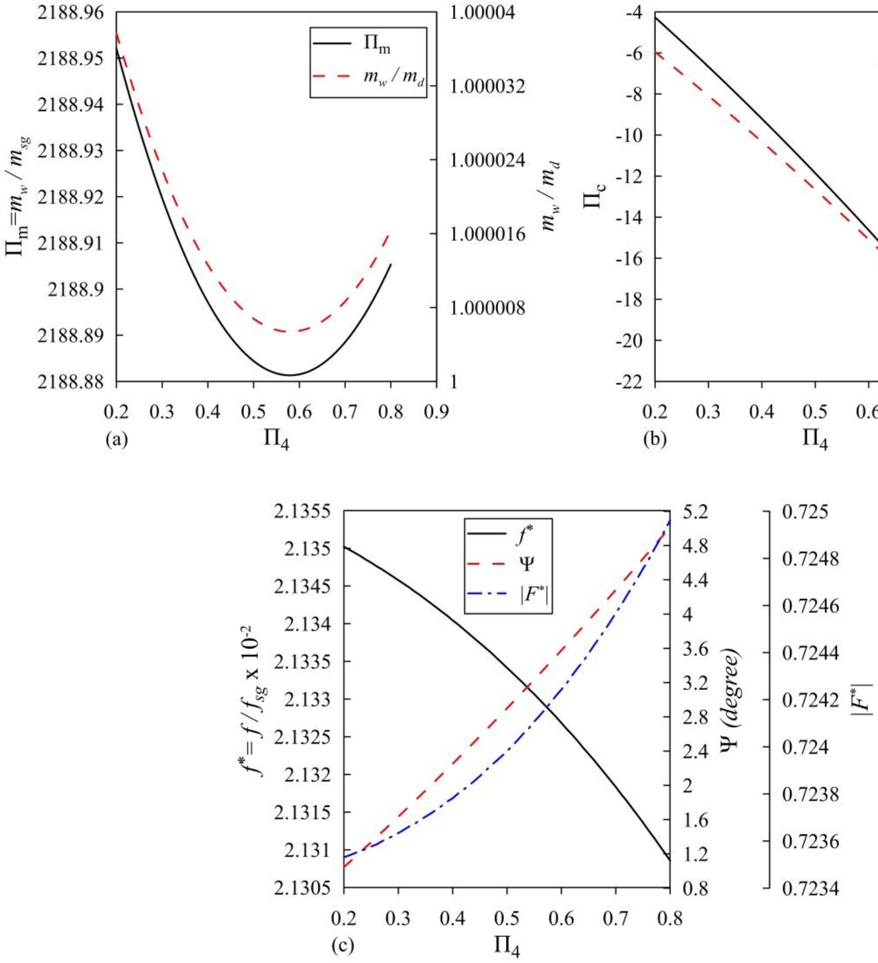

Figure 4.4: (a) Influence of Π_4 on Π_m, and m_w / m_d. (b) Influence of Π_4 on Π_c and Π_k. (c) Influence of Π_4 on f^*, ψ, and $|F^*|$. Π_1=0.1, Π_2=90, Π_a=0.7, Π_{b1}=0.08, Π_c=0.2 and Π_d=923.36.

Figure (4.5) presents the influence of the pilot pipeline geometrical characteristics (i.e., as a function of $\Pi_d = \frac{I_d}{I_m}$, $I_d = \frac{L_d}{g\,A_d}$) on the seal dynamic behavior, while keeping Π_1=0.1, Π_2=90, Π_3=1.5, and Π_4=0.4. According to figure (4.5 c), decreasing

Π_d leads to a significant increment in the phase angle ψ between the fluid dynamic force and the seal vibration displacement. As a result, the fluid dynamic force is more in phase with the seal vibration velocity leading to higher negative added water damping c_w as in figure (4.5 b).

On the other side, since increasing Π_d increases the ratio between the pilot pipeline length and cross-section area L_d / A_d, and the added water mass m_w is a function of m_d, which is directly proportional to the ratio L_d / A_d (i.e., $m_d = \rho L_d A_d \left(\frac{A_{os}}{A_d} \right)^2$). Therefore, incrementing Π_d increases the added water mass m_w and decreases the seal oscillation frequency f^*, as in figures (4.5 a and c).

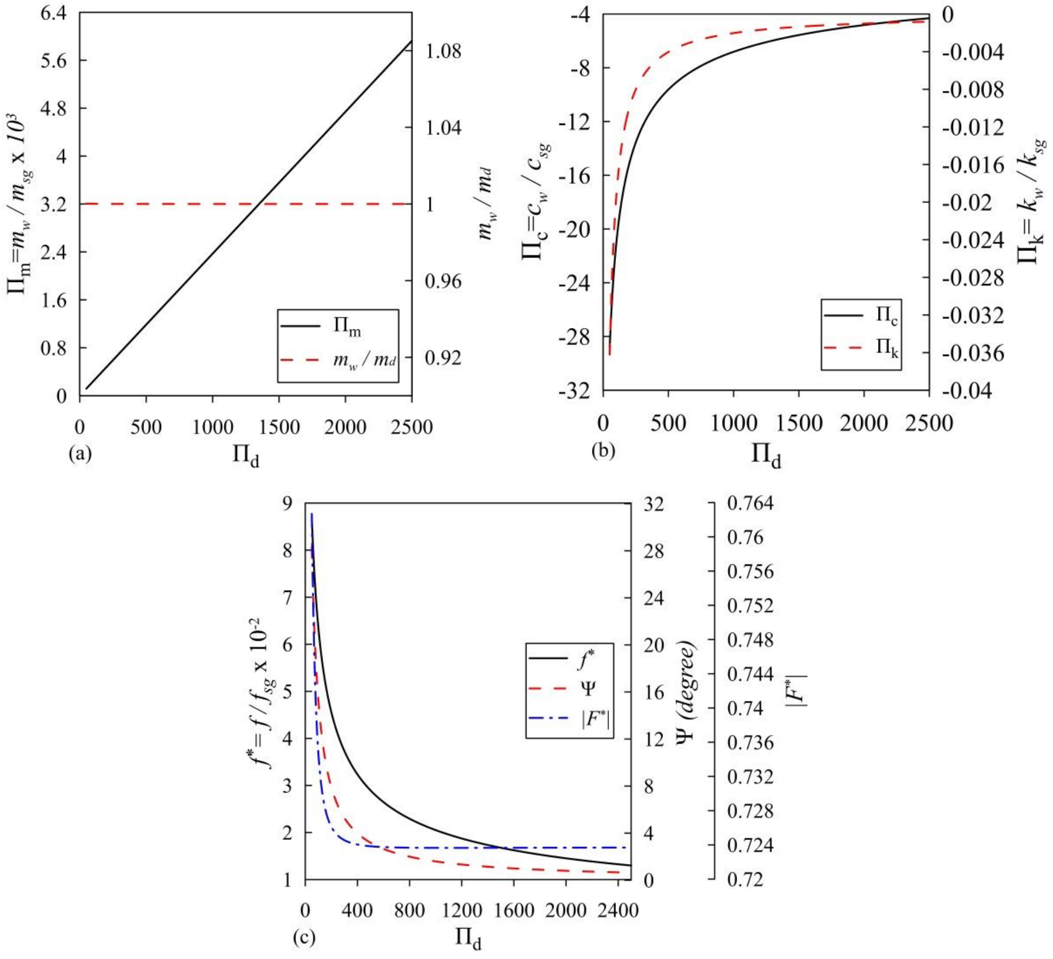

Figure 4.5: (a) Influence of Π_d on Π_m, and m_w / m_d. (b) Influence of Π_d on Πc and Π_k. (c) Influence of Π_d on f^*, ψ, and $|F^*|$. Π_1=0.1, Π_2=90, Π_4=0.4, Π_a=0.7, Π_{b1}=0.08, Π_c=0.2.

4.2.2 1^{st} Model stability charts:

As mentioned at the beginning of the discussion, one of the main aims of the study is to establish and evaluate system stability conditions. Therefore stability charts are drawn function of the developed Π-groups, as in figures (4.6 a, b, and c), to assess Π-groups influence on the system dynamic stability. The lines presented in the stability charts represent the critically damped condition where the equivalent damping coefficient c_{eq} is zero. In addition, the area underneath the curves represents the stable region where $c_{eq}>0$, while the area above the curves represents the unstable region where $c_{eq}<0$ as in figures (4.6 a, b, and c).

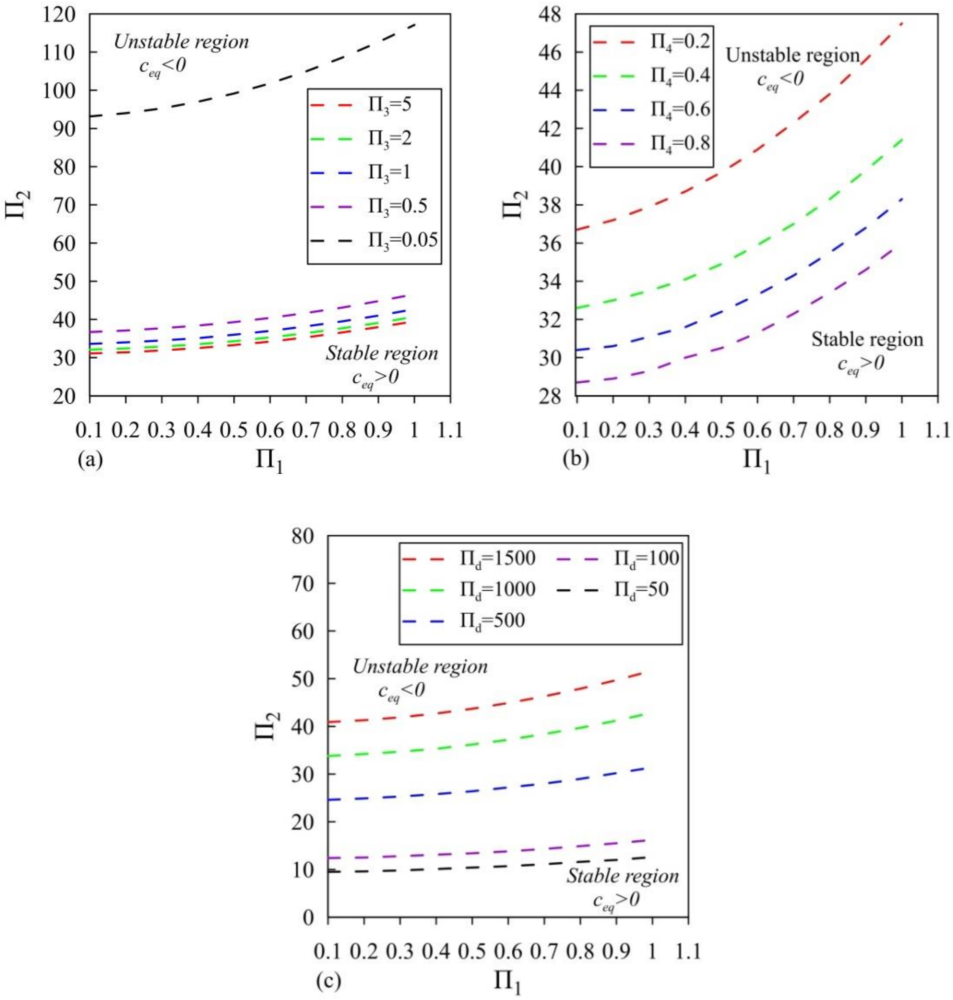

Figure 4.6: (a) System stability chart function of Π_1, Π_2 and Π_3. Π_4=0.4 and Π_d=923.36. (b) System stability chart function of Π_1, Π_2 and Π_4. Π_3=1.5 and Π_d=923.36. (c) System stability chart function of Π_1, Π_2 and Π_d. Π_3=1.5 and Π_4=0.4.

Firstly, all stability charts as in figures (4.6 a, b, and c) show that system stability is proportional to Π_1 and inversely proportional to Π_2. At a constant value of Π_1

increasing Π_2 leads to system instability, while at a constant value of Π_2 increasing Π_1 leads to system stability.

At a constant value of Π_1, increasing Π_2 increases the gap flow rate and the fluid dynamic force excitation to the seal oscillation, as in figure (4.2 c). As a result, a higher negative added water damping c_w is developed as in figure (4.2 b), which leads to system instability, as in figure (4.6 b). On the other hand, at the same value of Π_2, increasing Π_1 decreases the phase angle between the fluid dynamic force and the seal vibration displacement, as in figure (4.1 c). As a result, a lower negative added water damping c_w is developed as in figure (4.1 b), which enhances system stability, as in figure (4.6 b).

Figure (4.6 a) shows the effect of Π_3 on the system dynamic stability as a function of Π_1, Π_2, and Π_3. Figure (4.6 a) demonstrates that increasing the pilot pipeline head losses to a significant value increases the region of system stability along Π_2. At the same pilot pipe line geometry Π_d= 923.36, increasing the pilot pipeline head losses decreases the phase angle ψ, as in figure (4.3 c). Therefore, lower negative added water damping develops as in figure (4.3 b), leading to system stability improvement, as in figure (4.6 a).

Figure (4.6 b) shows that the seal geometry can enhance the system dynamic stability as reducing Π_4 increases the stable region along Π_2, as in figure (4.6 b). Reducing Π_4 decreases the magnitude of the fluid dynamic force acting on the seal and decreases the phase angle ψ, as figure (4.4 c). As a result, lower negative added water damping c_w is developed as in figure (4.4 b), which augments system stability along Π_2, as in figure (4.6 b).

Figure (4.6 c) shows that at the same seal geometry Π_4=0.4, augmenting the pilot pipeline inertia head coefficient I_d $(i..e, \Pi_d = \frac{I_d}{I_m})$, increases the system stability since the area of the sable region increases along Π_2, as in figure (4.6 c). At the same seal geometry Π_4 incrementing the pilot pipeline inertia head I_d (increasing Π_d) decreases significantly the phase angle ψ, as in figure (4.5 c). As a result, lower negative added water damping is developed, as in figure (4.5 b), increasing system stability along Π_2, as in figure (4.6 c).

1st Model dimensionless analysis main findings:

The main findings of the 1st Model dimensionless analysis can be summarized as following:

- Increasing the gap flow velocity (increasing Π_2) and the reducing the external surface area of the seal (increasing Π_4) causes the fluid dynamic force to be more in phase with the seal vibration velocity. In this situation, the fluid dynamic force excites more the seal oscillations, leading to a dynamically unstable system risking the safe power plant operation.
- On the other hand decreasing the input reservoir energy level (increasing Π_1), increasing the pilot pipeline head losses (decreasing Π_3), and increasing the pilot pipeline length (increasing Π_d) decreases the fluid dynamic force excitation to the seal oscillation. In these cases, the fluid dynamic force is more in phase with the seal vibration displacement, establishing lower negative added water damping and enhancing the system dynamic stability.
- The seal oscillation frequency is influenced significantly by the geometry of the pilot pipeline. The added water mass is directly proportional to the pilot pipeline length and inversely proportional to the pipeline cross-section area. Accordingly, incrementing the pilot pipeline inertia head coefficient $I_d=L_d/gA_d$ (increasing Π_d), increases the added water mass, which decreases the seal's oscillation frequency.
- The added water mass is independent of Π_1, Π_2 and Π_3. However it depends on the pilot pipeline geometry and the external surface area of the seal since the ratio of $m_w/m_d \approx 1$ in all cases.
- System dynamic stability is directly proportional to the increase of Π_1, Π_3 and Π_d as the phase angle between the fluid dynamic force and the seal vibration displacement decreases significantly. In contrast, system instability is directly proportional to the increment of Π_2 and Π_4, since higher negative added water damping is developed, decreasing the seal's equivalent damping coefficient.

4.2.3 Parametric study based on the Salime power plant configuration:

This section aims to evaluate the seal behavior using parameters, which are more familiar within the power plant field. Therefore, the following sections present the influence of the input reservoir energy level, gap angle of the seal, the unstrained seal clearance, and pilot pipeline geometry on the seal dynamic behavior.

Figure (4.7) shows the influence of the input reservoir energy level H_1 on the seal behavior at constant values of the seal's gap angle $\theta_{gap}=60^0$, pilot pipeline geometry, and the unstrained seal clearance $y_{gu}=5\ mm$.

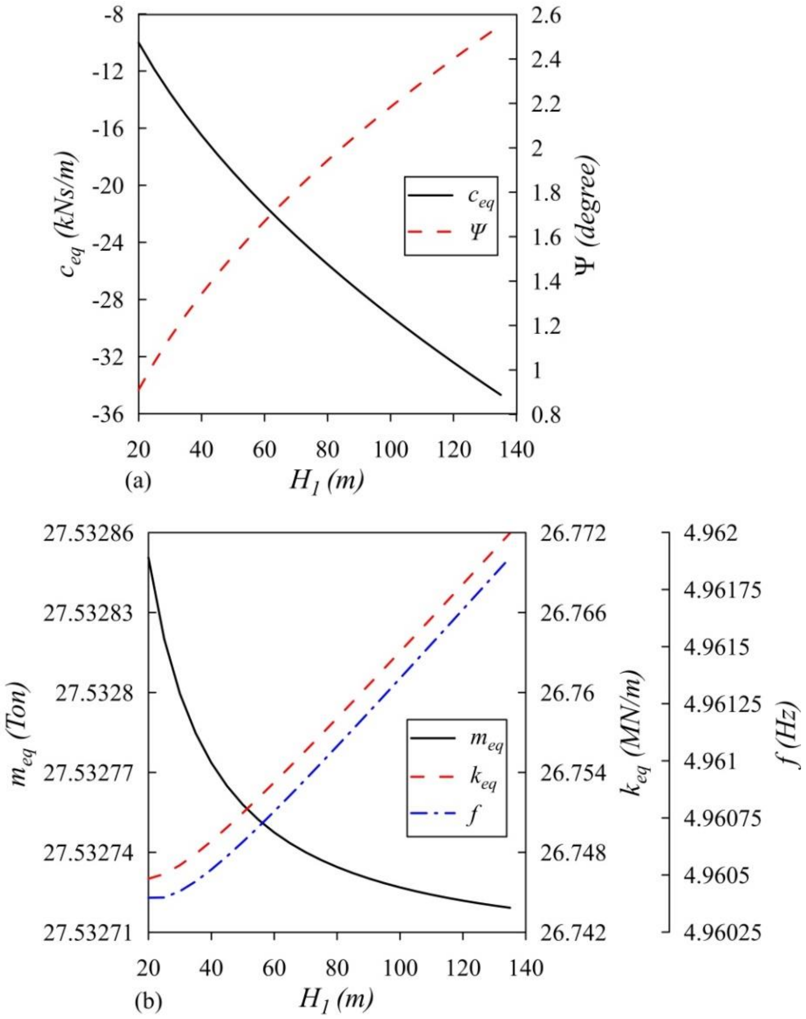

Figure 4.7: Input reservoir H_1 influence on m_{eq}, k_{eq}, f, c_{eq}, ψ and |F|, at $\theta gap=60^0$, $L_d=15m$, $d_d=30\ mm$, and $y_{gu}=5\ mm$.

By increasing the input reservoir energy level, the fluid dynamic force excites more the seal oscillation, as the phase angle ψ increases as in figure (4.7 a). As a result, higher negative added water damping is developed, decreasing the seal's equivalent damping coefficient c_{eq} as in figure (4.7 a). Therefore, for this phenomenon, increasing the input reservoir energy level risks the safe operation of the power plant as the seal's equivalent damping coefficient decreases with increasing H_1.

On the other hand, increasing the phase angle ψ decreases the negative added water stiffness k_w and increases the seal's equivalent stiffness coefficient slightly as in figure (4.7 b). As a result, the seal's oscillation frequency increases slightly, as in figure (4.7 b), particularly since H_1 has a negligible effect on the equivalent mass coefficient; i.e., because the added water mass m_w is mainly influenced by m_d, which is independent of H_1.

Figure (4.8) shows the influence of the gap angle θ_{gap} on the seal behavior at the power plant nominal head $H_1=105\ m$ and at the same pilot pipeline geometry and unstrained seal clearance y_{gu}.

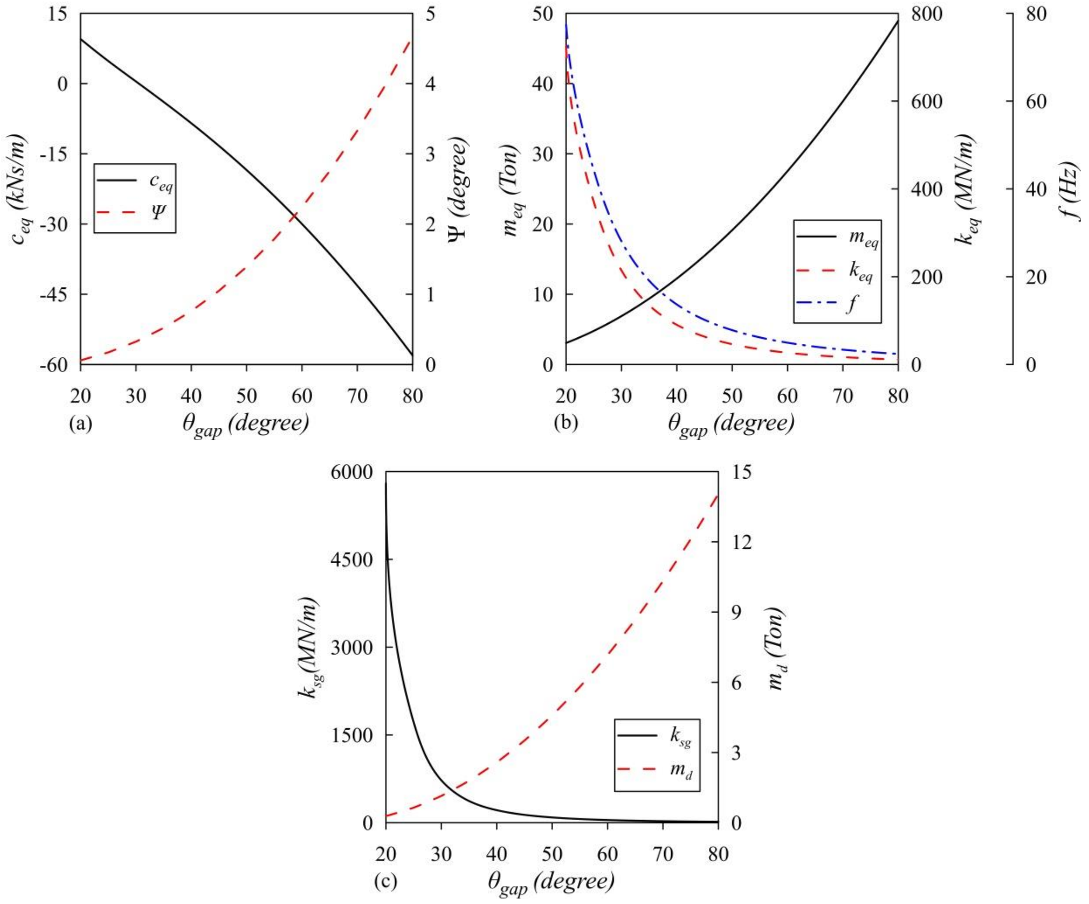

Figure 4.8: Seal gap θ_{gap} influence on m_{eq}, k_{eq}, f, c_{eq}, ψ and $|F|$, at H_1=105 m, L_d=15m, d_d=30 mm, and y_{gu}=5 mm.

Figure (4.8 a) shows that for gap angles lower than $\theta_{gap} < 30^0$ the seal is dynamically stable since the seal's equivalent damping coefficient is positive. However, by increasing the gap angle, the phase angle ψ increases as in figure (4.8 a). As a result, higher negative added water damping is developed, decreasing the seal's equivalent damping coefficient and leading to a dynamically unstable system ($c_{eq} < 0$) as in figure (4.8 a).

On the other hand, by increasing the gap angle of the seal θ_{gap}, the seal oscillation frequency reduces significantly as in figure (4.8 b) for two reasons. Firstly, by increasing the gap angle, the seal structure stiffness k_{sg} is reduced significantly as in figure (4.8 c), since the seal structure stiffness k_{sg} is inversely proportional to the third power of the seal's gap angle θ_{gap} as in Eq.(3). As a result, the seal's equivalent stiffness coefficient decreases as in figure (4.8 b), decreasing the seal oscillation frequency. Also, by increasing the gap angle of the seal, the external surface area of the seal increases. Therefore, the added water mass and the seal's equivalent mass coefficient increase as in figures (4.8 b and c) (i.e., $m_w = m_d = \rho\, L_d\, A_d \left(\frac{A_{os}}{A_d} \right)^2$), which reduces the seal's oscillation frequency as in figure (4.8 b).

Figure (4.9) shows the effect of enlarging pilot pipeline length L_d on the seal behavior while keeping the other parameters the same. Figures (4.9 a and b) shows that varying the pilot pipeline length has a significant influence on the frequency of the seal oscillation combined by a small effect on the seal' equivalent damping coefficient and system stability. Since the added water mass is directly proportional to the pilot pipeline length L_d. Hence, increasing the pilot pipeline length L_d increases the added water mass m_w, and the seal's equivalent mass coefficient m_{eq}. As a result, the seal's oscillation frequency decreases as in figure (4.9 b).

On the other hand, enlarging the pilot pipeline length L_d decreases the phase angle ψ slightly as in figure (4.9 a). As a result, the fluid dynamic force excitation to the seal oscillation decreases, which is represented by lower negative added water damping increasing the seal's equivalent damping coefficient as in figure (4.9a).

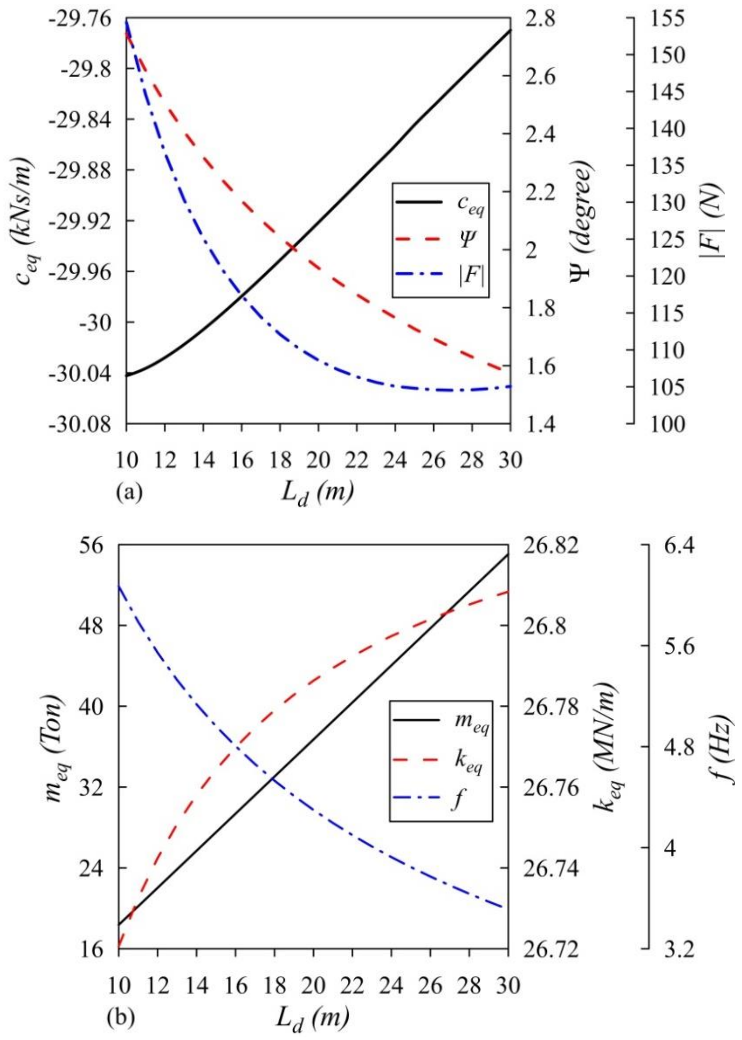

Figure 4.9: Pilot pipeline length L_d influence on m_{eq}, k_{eq}, f, c_{eq}, ψ and $|F|$, at H_1=105 m, θ_{gap}=60^0, d_d=40 mm, and y_{gu}=5 mm

Figure (4.10) shows the influence of the pilot pipeline diameter d_d on the seal behavior. Figure (4.10 a) shows that increasing the pilot pipeline diameter has a varying influence on the added water damping and the seal equivalent damping coefficient due to the significant change in the seal's oscillation frequency as in figure (4.10 b).

According to the seal equation of motion Eq.(11), the added water damping can be written in this form $c_W=-\frac{F_I}{\omega Y}$ as the hydro dynamic force is a complex number. As seen in the mentioned form, the added water damping depends on the ratio between the component of the fluid dynamic force acting along the seal vibration velocity (F_I) and the frequency of the seal oscillation ω. The seal oscillation frequency increases significantly as in figure (4.10 b) due to the seal equivalent mass reduction, since the added water mass decreases significantly by increasing the pilot pipeline diameter ($m_w=m_d=\rho L_d A_d\ (A_{os}/A_d)^2$, $m_{eq}=m_w+m_{sg}$). As a result, the seal oscillation frequency decreases the negative values of the parameter $F_I\,/\,\omega$ at high diameters of the pilot pipeline, which increases the added water damping c_w and the seal's equivalent damping coefficient c_{eq}, as in figure (4.10 a).

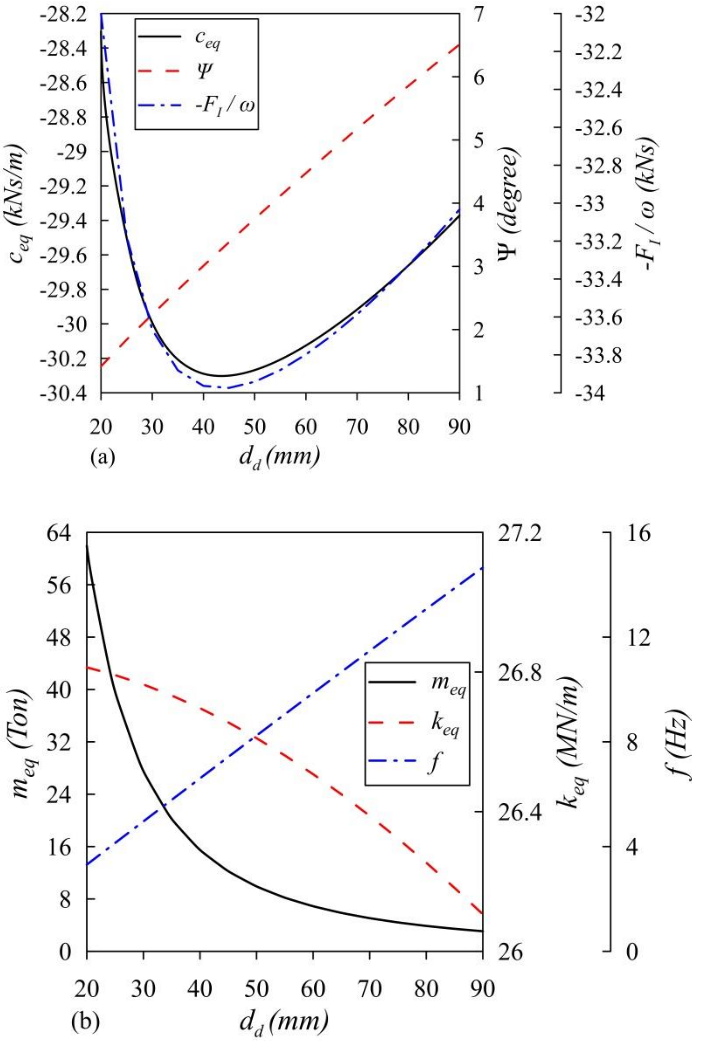

Figure 4.10: Pilot pipeline diameter d_d influence on m_{eq}, k_{eq}, f, c_{eq}, ψ and $-F_I/\omega$, at H_1=105 m, θ_{gap}=60^0, L_d=15 m, and y_{gu}=5 mm

Figure (4.11) shows the influence of the unstrained seal clearance on the seal behavior. Figure (4.11 a) shows that by increasing the unstrained seal clearance, the magnitude of the fluid dynamic force $|F|$ acting on the seal increases with a reduction in the phase angle ψ. As a result, the fluid dynamic force is more in phase with the seal vibration displacement, decreasing the added water stiffness and increasing the added water damping. Accordingly, the seal oscillation frequency decreases due to the seal’s equivalent stiffness coefficient reduction as in figure (4.11b), particularly since the unstrained seal clearance has a negligible effect on the added water mass and the seal’s equivalent mass coefficient as in figure(4.11 b).

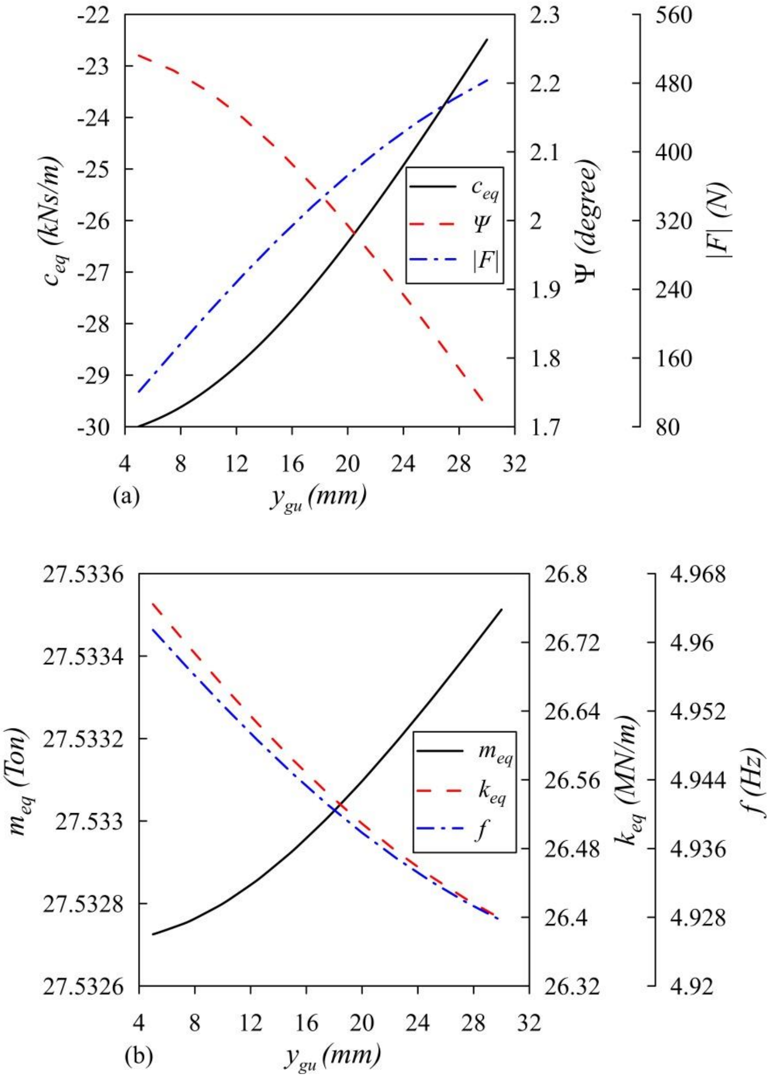

Figure 4.11: Unstrained seal clearance y_{gu} influence on m_{eq}, k_{eq}, f, c_{eq}, ψ and |F|, at H_1=105 m, θ_{gap}=60^0, L_d=15 m, and d_d=30 mm

4.2.4 Steady-state stability analysis:

In addition to the dynamic stability limit ($c_{eq} \geq 0$), there is also a static stability limit (y_{og}=0) because the thickness of the seal clearance depends on the seal's hydro-pressure force. Therefore figure (4.12) shows the influence of the input reservoir energy level H_1 and the seal’s external surface area A_{os} on the seal steady-state seal clearance y_{og}.

Figure (4.12 a) shows that for the same seal geometrical, by increasing the input reservoir energy level, the steady-state hydro pressure force F_o acting on the seal increases. As a result, the steady-state seal clearance y_{og} reduces, establishing static stability condition when $y_{og}=0$. In this situation, no leakage flow develops and the seal could not undertake vibrations. Also, figure (4.12) shows that by increasing the seal external surface area A_{os} facing the pilot pipeline, the static stability condition is achieved at lower input reservoir energy level H_1 as in figure (4.12 b). By increasing A_{os}, the augmentation of the steady-state flow force acting on the seal increases at a higher rate than the seal structure stiffness. As a result, closure of the seal clearance y_{og} is established at lower input reservoir energy level H_1, as in figure (4.12 b).

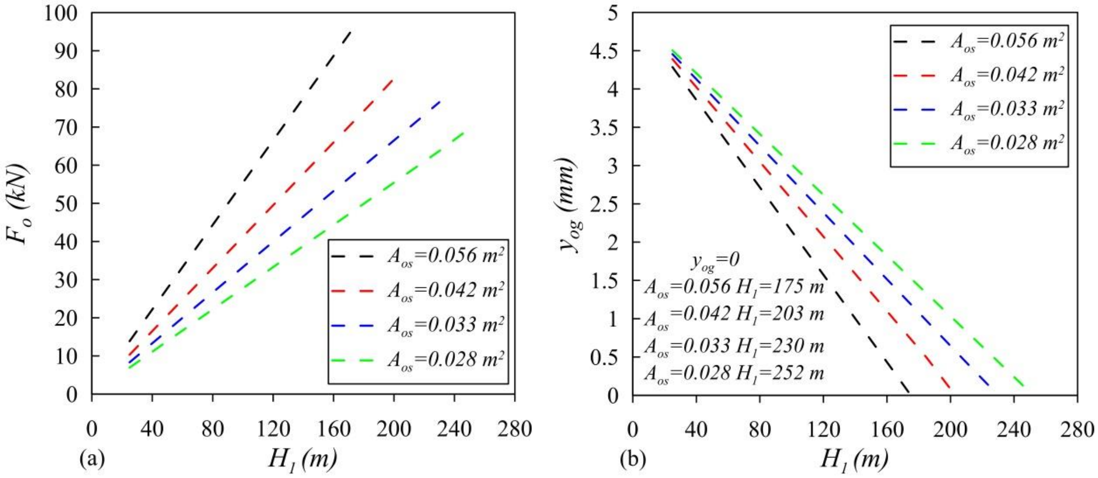

Figure 4.12: F_o and y_{og} relation with H_1 and A_{os}, keeping y_{gu}=5 mm, θ_{gap}=60^0, L_d=15 m, A_{ss}=0.0169 m^2 and d_d=30 mm.

1^{st} Model parametric study main findings:

According to the parametric study developed for the case of Salime power plant, the following point's summaries the main findings:

- The hydro-mechanical system stable behavior depends greatly on the seal's gap angle. At low gap angles such as $\theta_{gap} < 30^0$, the system is dynamically stable for all input reservoir energy levels (i.e., $0 < H_1 < 135$ m). However, by increasing the input reservoir energy level, the system is more prone to be dynamically unstable since the equivalent damping coefficient of the seal decreases.

- Incrementing the pilot pipeline length and diameter lowers the fluid dynamic force excitation to the seal oscillations as lower negative added water damping is developed.
- The oscillation frequency of the hydro-mechanical system is significantly influenced by the seal’s gap angle and pilot pipeline geometry. By increasing the seal’s gap angle and the pilot pipeline length, the seal’s oscillation frequency decreases, while by increasing the pilot pipeline diameter, the seal’s oscillation frequency increases due to the added water mass decrement.
- The oscillation frequency of the hydro-mechanical system is hardly affected by the input reservoir energy level and the unstrained seal clearance thickness.
- Increasing the seal external surface area increases the possibility of establishing the static-stability condition. As by increasing the seal external surface area the steady-state fluid pressure force acting on the seal increases, closing the seal clearance at lower input reservoir energy levels.

4.3 Effects of nonlinear friction terms on seal oscillations

This section aims to present the effect of including the neglected nonlinear hydraulic losses in the first model to observe its effect on reaching the limit cycle oscillation and to compare the seal behavior with the linear model results. Therefore, the results are presented as a function of the dimensionless Π-groups developed in the first model.

Figure (4.13) exhibits the effect of varying Π_1 and Π_2 on the limit cycle oscillation for both linear and nonlinear models at the same seal geometry and pipelines configurations.

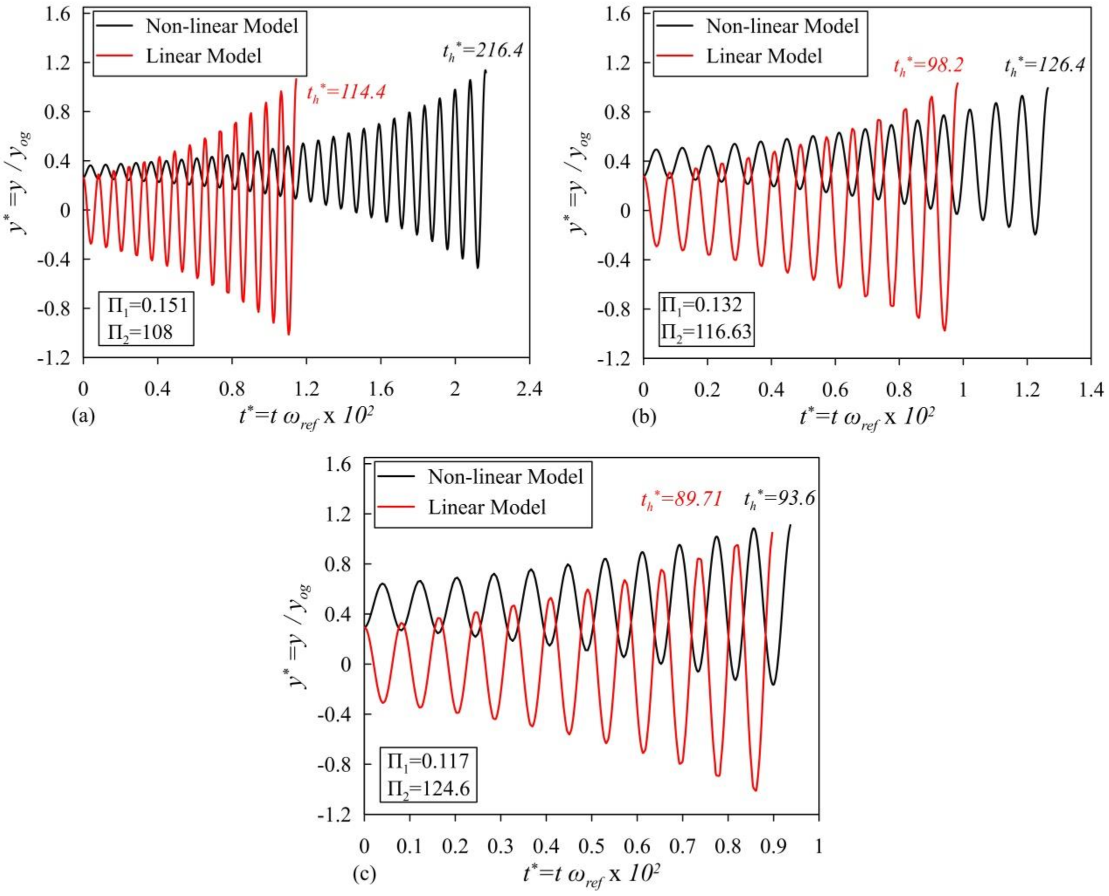

Figure 4.13: Relation between seal vibration displacement y^* and time t^* for the incompressible linear and non-linear models at Π_4=0.4, Π_d=923.36, Π_a=0.7, Π_{b1}=0.08 and Π_c=0.2.

Firstly for all values of Π_1 and Π_2, by including the nonlinear losses, the seal tends to vibrate at lower amplitude compared to the linear model. As a result, the seal needs more time t_h^* to hit the ball surface where the fluctuated seal clearance area A_g reaches *zero* at $y^*=1$. Moreover, as Π_1 decreases and Π_2 increases, the seal tends to hit the ball surface at a lower time t_h^*. As by decreasing Π_1 and increasing Π_2, the negative added water damping increases exciting more the seal oscillation as in figures (4.1 b and 4.2 b).

Figure (4.14) shows the effect of the seal geometry (Π_4) on the seal vibration at different values of Π_1, and Π_2. For all values of Π_1, by decreasing Π_4, the seal hits the ball surface at higher values of t_h^* as in figure (4.14). By increasing the seal external surface area A_{os} and reducing Π_4, the added water damping tends to have lower negative values as in figure (4.4 b). As a result, the fluid dynamic force excitation to the seal oscillation decreases, which also increases the time needed by the vibrating seal to hit the ball surface. Moreover, the seal rigidity increases with reducing Π_4 as in figure (4.4 b), which leads to lower oscillation amplitude and higher t_h^*.

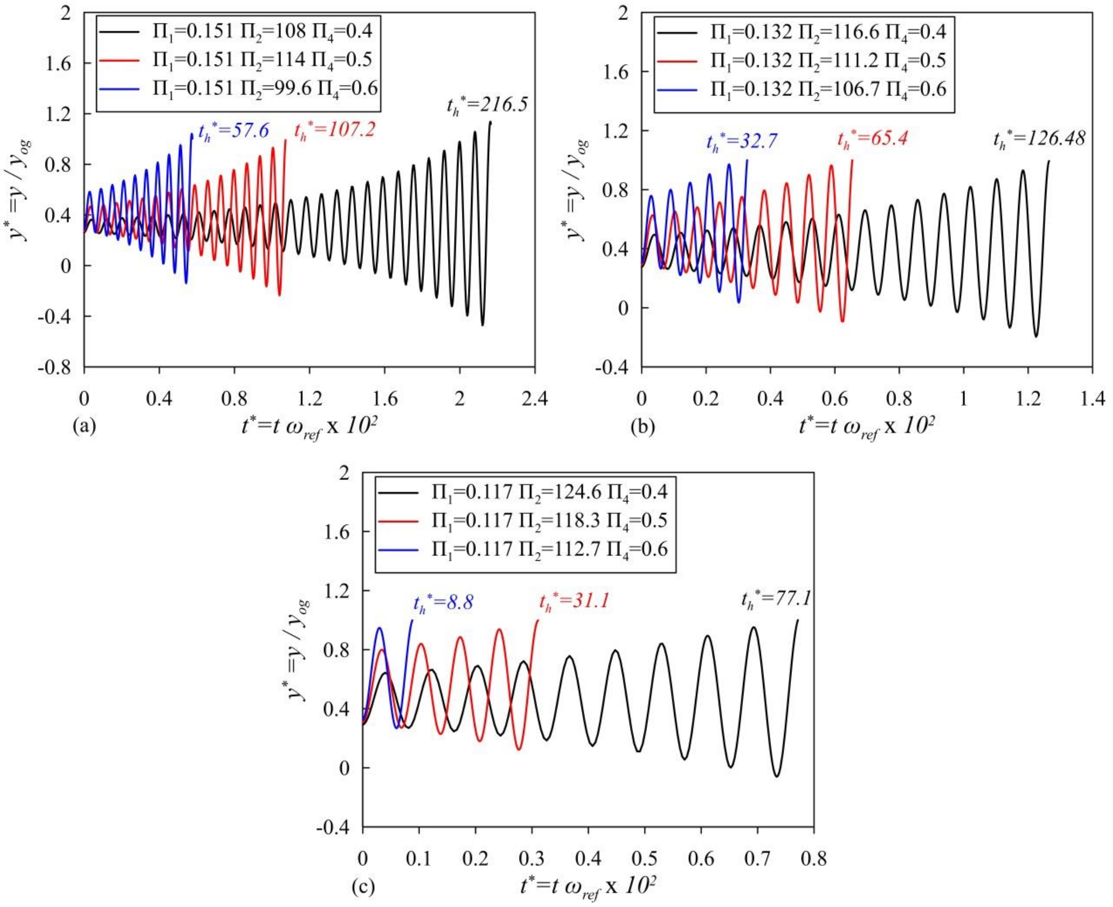

Figure 4.14: Relation between seal vibration displacement y^* and time t^* at a varying Π_1, Π_2 and Π_4. Π_d=923.36, Π_a=0.7, Π_{b1}=0.08 and Π_c=0.2.

Figure (4.15) shows the effect of Π_d (pilot pipeline geometry) variation on the seal vibration displacement. Results exhibit that augmenting the pilot pipeline inertia head coefficient I_d (i.e., increasing $\Pi_d = \frac{I_d}{I_m}$) increases the time needed by the seal to hit the ball surface as in figure (4.15). By increasing Π_d, the added water damping and the added water stiffness tend to have lower negative values as in figure (4.5 b). As a result, the seal equivalent damping coefficient increases, which represents a reduction in the fluid dynamic force excitation to the seal oscillation. In addition, the seal equivalent stiffness coefficient increases by increasing Π_d. Therefore, the seal rigidity increases, which decreases the seal oscillation amplitude, and increases the time needed by the seal to hit the ball surface.

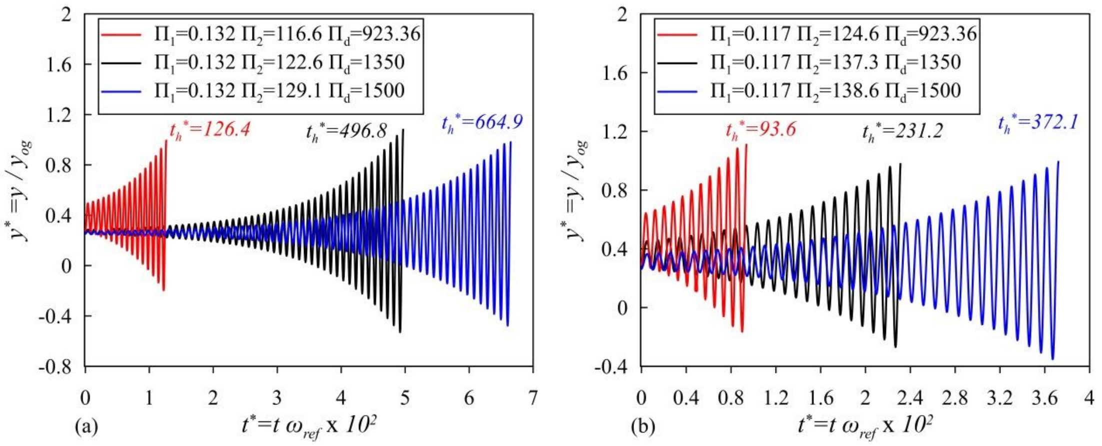

Figure 4.15: Relation between seal vibration displacement y^* and time t^* at a varying Π_1, Π_2 and Π_d. Π_4=0.4, Π_a=0.7, Π_{b1}=0.08 and Π_c=0.2.

Figure (4.16) shows the effect of the pilot pipeline head loss on reaching the limit cycle oscillations and enhancing system stability, keeping Π_d=923.36. The pilot pipeline head loss is varied by changing the pilot pipeline minor loss coefficient K_{Ld} as in figure (4.16). Computed results demonstrated that incrementing pilot pipeline head losses increase the time needed by the seal to hit the ball surface as in figures (14.16 a and b). However, a significant increment in the head loss is required to reach the limit cycle oscillations (i.e., Π_3=0.035) as in figure (4.16 c) since the thickness of the seal gap is very small. Finally, figure (4.16 d) shows that incrementing the pilot pipeline head losses can stabilize the seal dynamic behavior, as increasing the pilot pipeline head losses increase the added water damping as in figure (4.3 b).

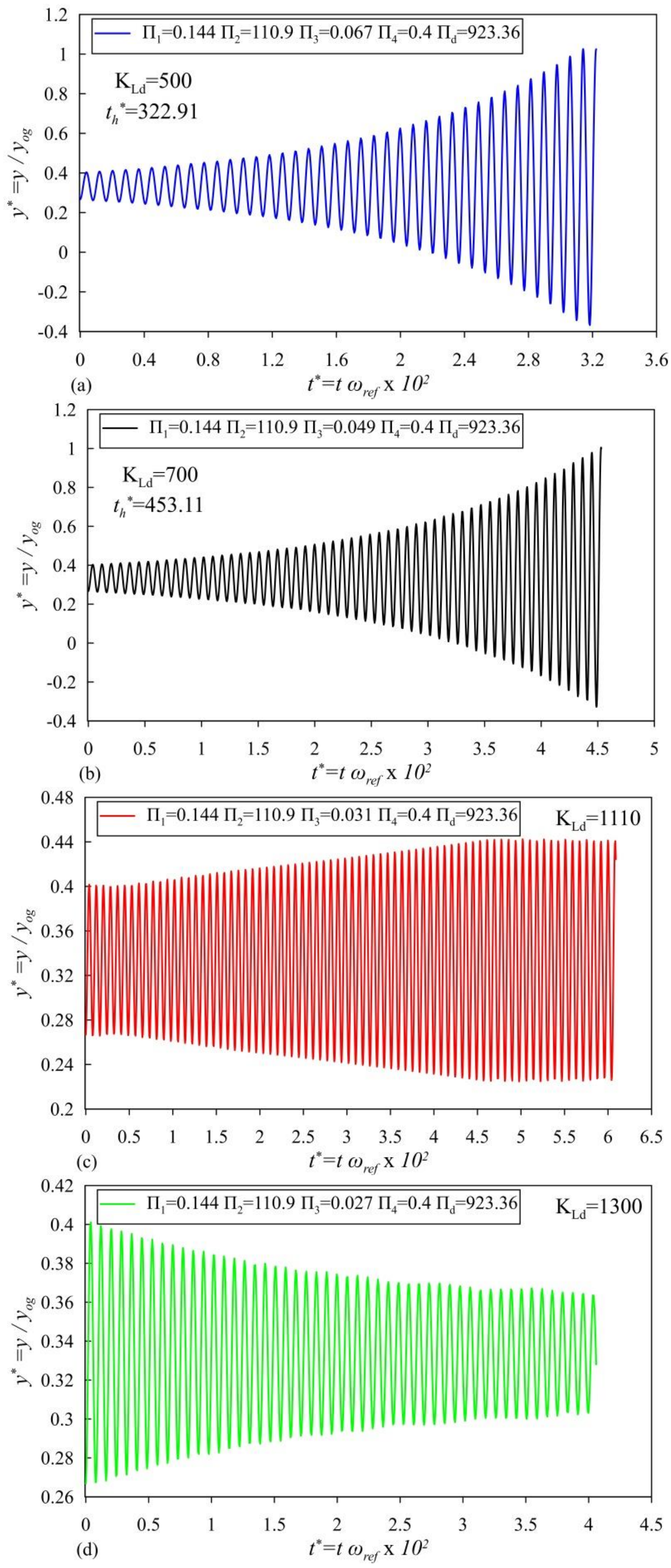

Figure 4.16: Effect of pilot pipe line losses on seal vibration displacement y^* at a varying Π_1 , Π_2 and Π_3.

Main findings of the Incompressible flow non-linear model:

- Nonlinear analysis results showed that the seal behavior matches with the linear model dimensionless analysis.
- Under normal pipeline configuration, the nonlinear hydraulic losses influence cannot establish the seal limit cycle oscillations, as the seal clearance is very small. As a result, if the seal is dynamically unstable, then the seal will hit the ball surface going backward and forward.
- However, if the pipeline resistance is incremented in a away such as installing a valve that can be closed to a certain degree, the limit cycle oscillations can be established and the seal vibrations can also be stabilized by further increment in the pilot pipeline head losses as in figures (4.16 c and d).

4.4 Slightly compressible flow 2nd Model results and discussion:

The second model aims to demonstrate the influence of the developed Π-groups on the hydro-mechanical model dynamic performance while considering *seal dynamics*, *fluid compressibility*, and *pipeline wall elasticity* effects.

The analysis of the 2nd model is constructed in the same manner as in the 1st model analysis. However, after studying Π-groups influence on system stability, a comparison between the incompressible and compressible flow model stability charts is established. This comparison aims to evaluate the influence of fluid compressibility and pipeline wall elasticity on the seal behavior.

4.4.1 2nd MODEL dimensionless analysis

In a hydraulic system that considers fluid compressibility, the liquid may be assumed to be composed of an infinite numbers of masses and springs connected in series, with the springs representing the compressibility of water. Hence, the hydraulic system has infinite modes of oscillations or degrees of freedom, and also has infinite natural periods. The first period is called *fundamental or first harmonic*, and the others are called *higher harmonics (2nd harmonic, 3rd harmonic,…..)*. For the case under consideration, since fluid compressibility is considered in the 2nd model analysis, hence the system is considered a distributed system with infinite number of oscillation frequencies or natural periods. However, the first ten frequencies are of practical importance as mentioned by *(Chaudhry 2014)*.

Figure (4.17) shows the seal behavior and the seal's oscillation frequency at Π_1=0.1, Π_2 ranging from 3 to 6, Π_3=1100, and Π_4=0.4. The values of the Π-groups presented in figure (4.17) are estimated according to the power plant geometrical configuration as in table (3.1), seal geometrical and physical characteristics, input reservoir energy level of *130 m* and pipeline wave speed varying from *800 m/s to 1200 m/s* (*Nourbakhsh et al. 2007*). Figures (4.17 a and b) shows the seal behavior at different values of Π_2 for the 1st ten harmonics where the value of Π_c identify the seal behavior. On the other side, figures (4.17 c and d) show the number of harmonic and the variation of the dimensionless frequency f^* with respect to Π_2 for a specific harmonic. Figure (4.17 a) shows that system dynamic instability is more prone to occur at the lower harmonics since the value of $\Pi_c < -1$, while for higher harmonics the system is dynamically stable since $\Pi_c > -1$.

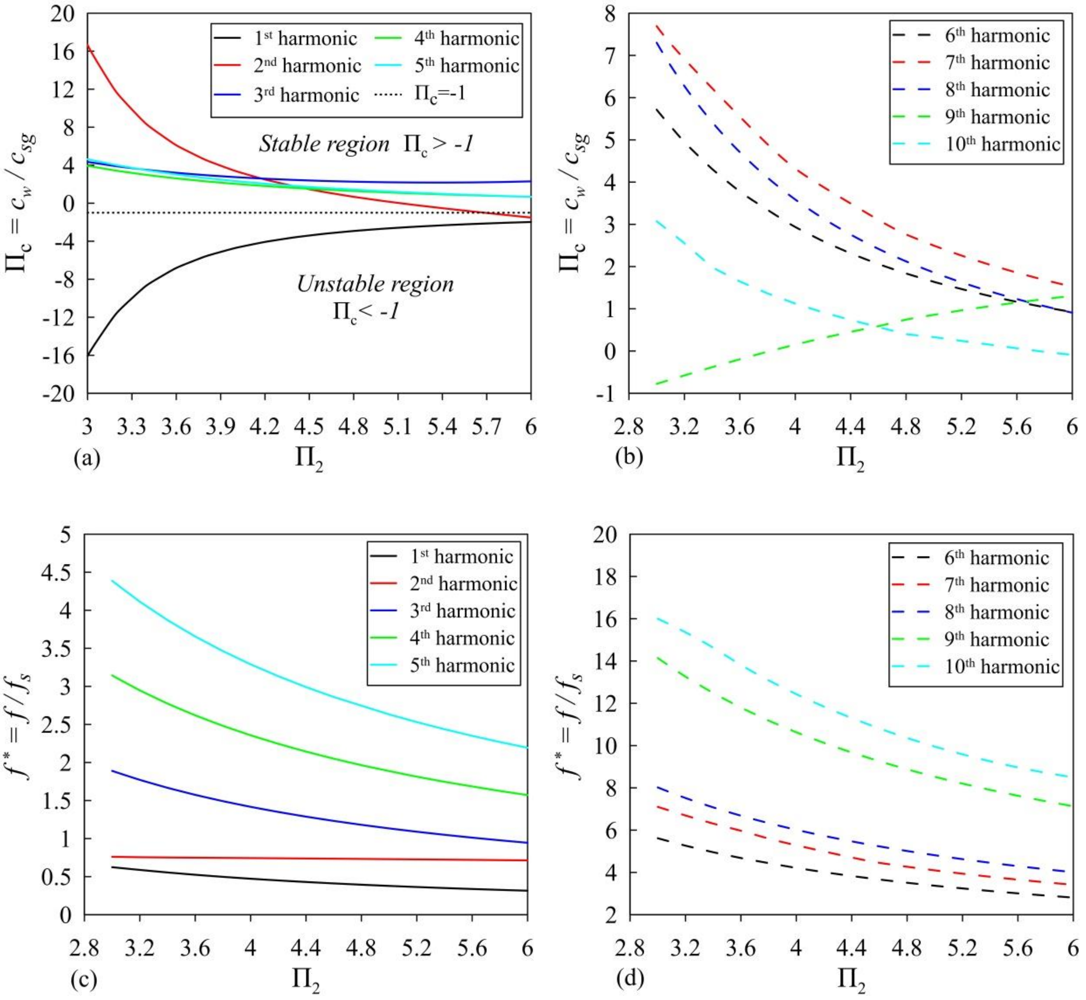

Figure 4.17: Relation between Π_2, Π_c and f * at Π_1=0.1, Π_3=1100 and Π_4=0.4 for the first ten harmonics of the seal oscillation.

At the same value of Π_2, increasing the number of the seal oscillation harmonic increases the magnitude of the fluid dynamic force acting on the seal as in figure (4.18 a), but also decreases the phase angle ψ as in figure (4.18 b). In this situation, the fluid dynamic force acting on the seal is more to be out of phase of the seal vibration velocity (i.e, at $-180 < \psi < 0$). As a result, a positive added water damping is developed leading to system dynamic stability since the fluid force damps the seal oscillation rather than exciting it.

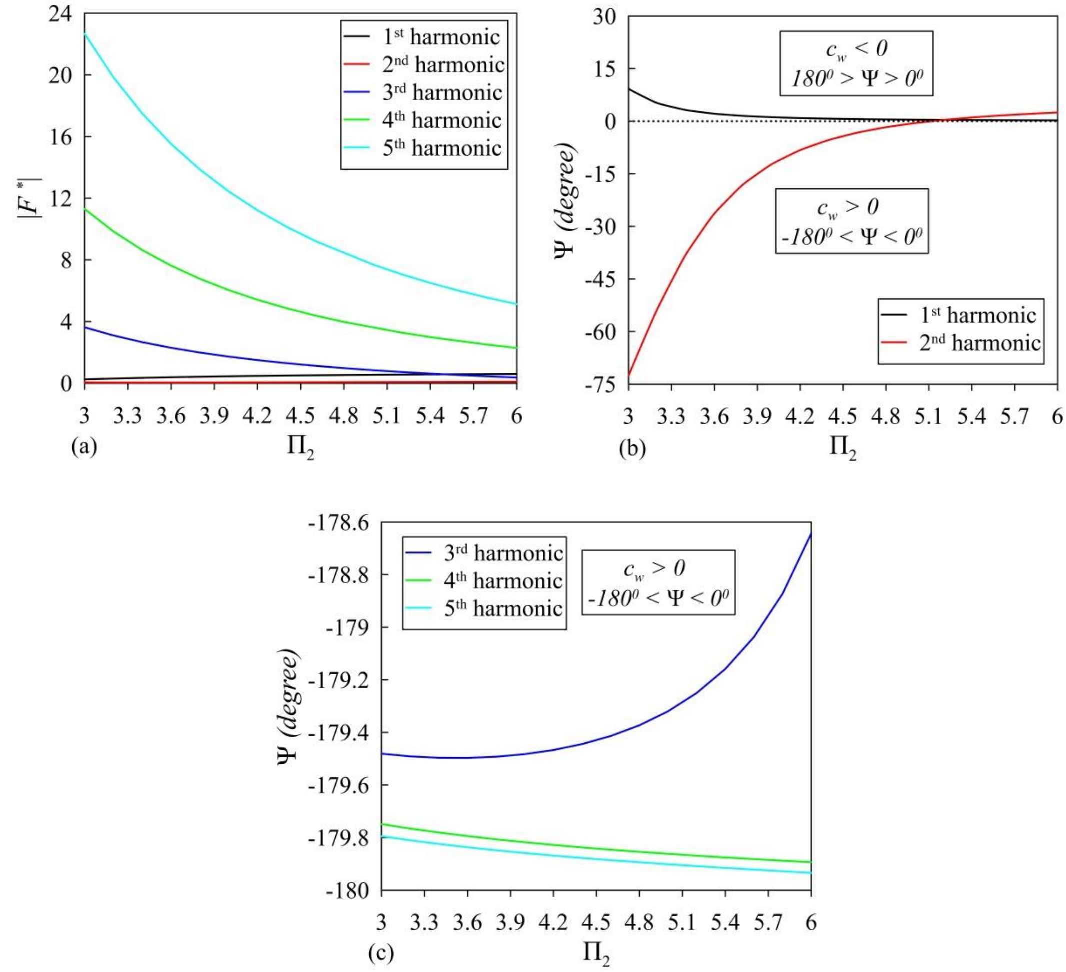

Figure 4.18: Relation between Π_2, $|F^*|$ and ψ, at at Π_1=0.1, Π_3=1100 and Π_4=0.4 for the first five harmonics of the seal oscillation

Since the aim of this study is to evaluate system stability due to the seal vibration, and figure (4.17 a) shows that system instability is only established at the first two harmonics for the lowest value of Π_1 (i.e., which is the worst situation where system instability is more prone to occur), hence the following figures will evaluate the influence of the developed Π-groups on system stability for the first three harmonics.

Figure (4.19) shows the influence of the input reservoir pressure head H_1 (presented by Π_1) on the seal behavior for the same pilot pipeline flow characteristics Π_3=1100 and the same seal geometry Π_4=0.4. Figure (4.19) shows that for the same values of Π_1 and Π_2, the fluid dynamic force tends to excite more the seal oscillation at the lowest harmonic since the added water damping has higher negative values. Also, by increasing Π_1, the fluid dynamic force excitation to the seal oscillation decreases as the added water damping has lower negative or positive values, particularly at the higher harmonics of the seal oscillation as in figure (4.19 c). Finally, system dynamic stability depends on the value of Π_2, since the fluid dynamic force attitude to damp (i.e. positive added water damping $\Pi_c>0$) or excite seal oscillations (i.e. negative added water damping $\Pi c < 0$) depends on the value of Π_2 as in figure (4.19). Such as, at $\Pi_1 = 0.2$ and 0.3, stable system ranges are satisfied for Π_2 ranging from 4.2 to 5.7, and from 3.2 to 5.8, where $\Pi_c>-1$.

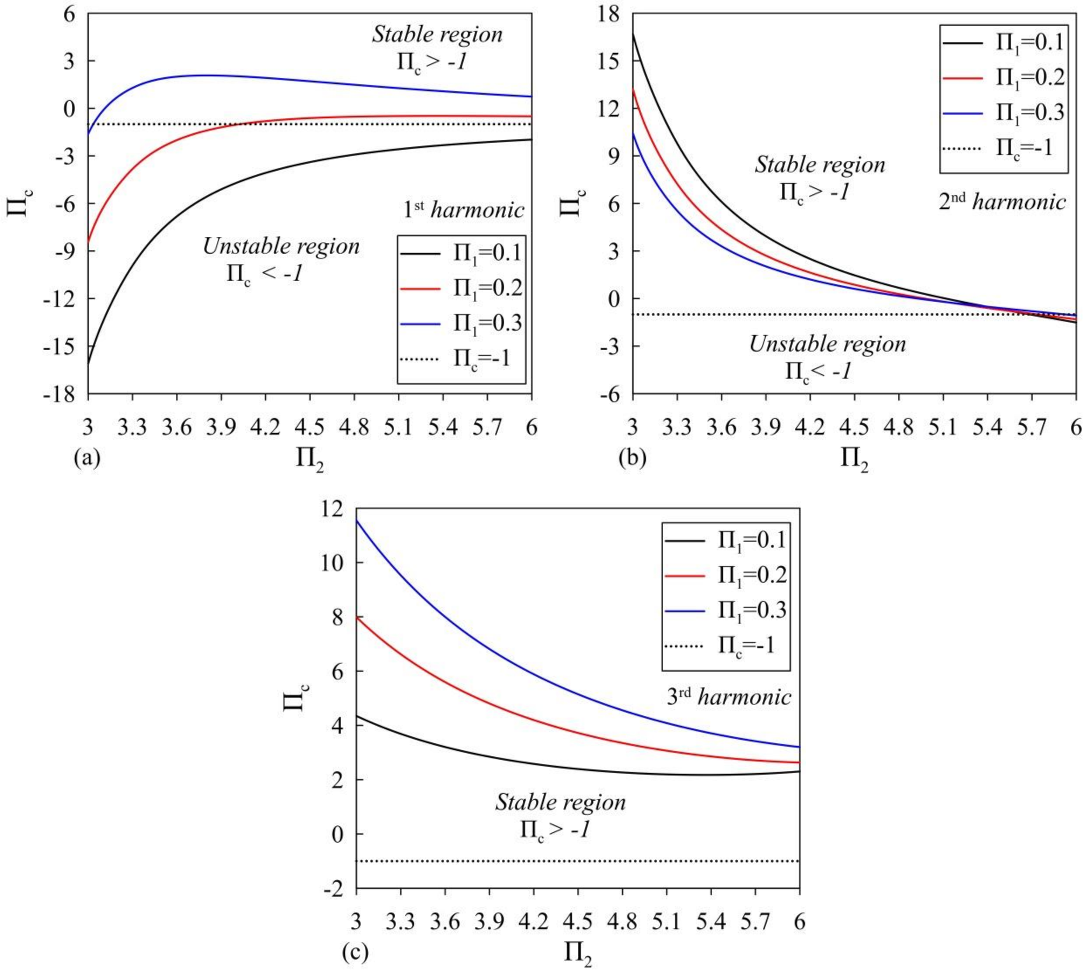

Figure 4.19: Relation between Π_2 and Π_c, at Π_1=0.1, 0.2 and 0.3, Π_3=1100 and Π_4=0.4 for the first three harmonics of the seal oscillations

The fluid dynamic force attitude to excite or damp system oscillations depends on the phase angle ψ between the fluid dynamic force acting on the seal and the seal vibration displacement. If ψ is in the range of $180^0 > \psi > 0^0$ as in figure (4.20 a), then the fluid dynamic force is in phase with the seal vibration velocity, and a negative added water damping is developed as in figure (4.19 a). In this situation, the fluid dynamic force excites the seal oscillation, which may lead to system instability if $\Pi_c < -1$. In contrast, If ψ is in the range of $0^0 > \psi > -180^0$, then the fluid dynamic force is out of phase of the seal vibration velocity, and a positive added water damping is developed. In this situation, the fluid dynamic force damps the seal oscillation, leading to a dynamically stable system (i.e., $\Pi_c > -1$), see figures (4.19 c and 4.20 c). Therefore, the phase angle ψ variation along Π_2 is the reason behind the variation of the added water damping and system stability along Π_2, for all values of Π_1.

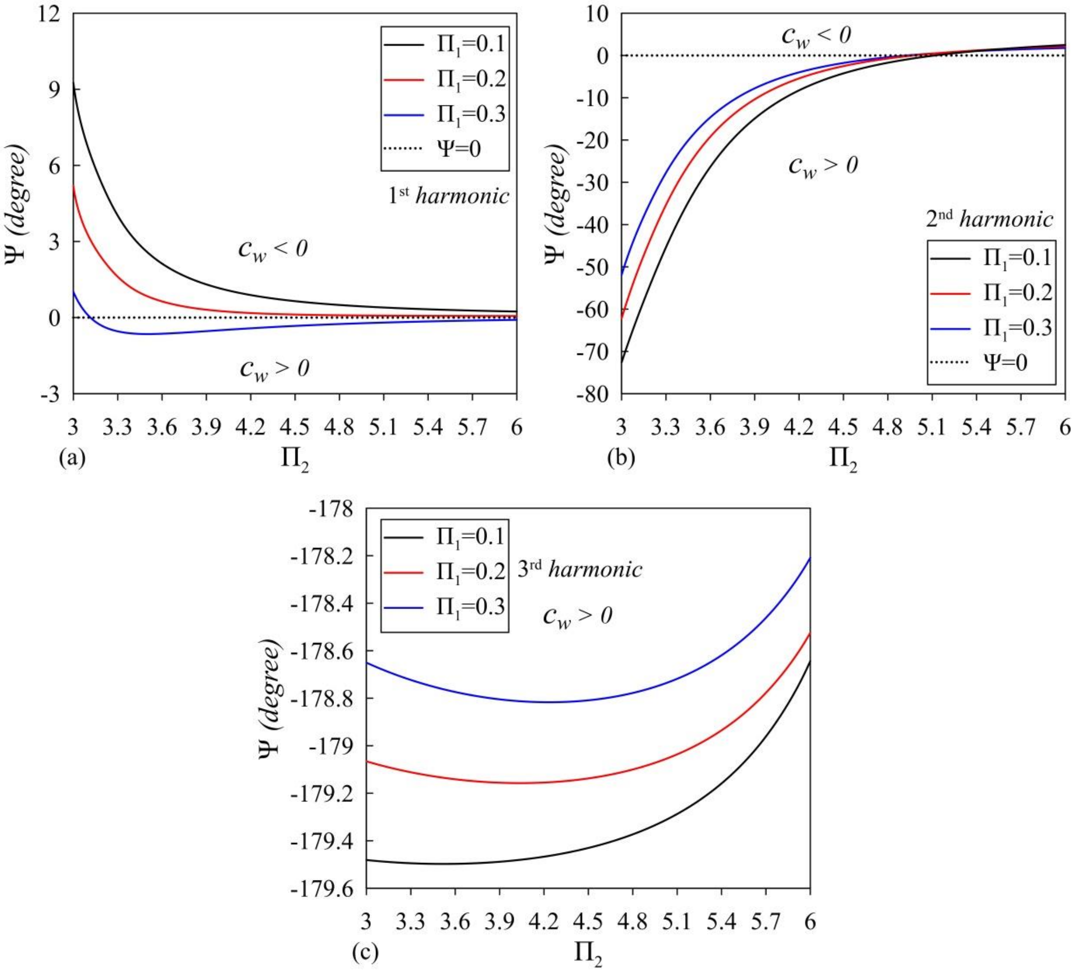

Figure 4.20: Relation between Π_2 and ψ, at Π_1=0.1, 0.2 and 0.3, Π_3=1100 and Π_4=0.4 for the first three harmonics

By increasing the harmonic of the seal oscillation as in figures (4.20 b and c), the phase angle between the fluid dynamic force and the seal vibration displacement has more negative values compared to the seal first harmonic as in figure (4.20 a). As a result, the fluid dynamic force becomes more out of phase of the seal vibration velocity leading to positive added water damping (i.e., $\Pi_c > 0$) as in figures (4.19 b and c).

Figures (4.20 a and b) demonstrates that by increasing Π_1, the magnitude of the positive and the negative values of the phase angle ψ reduces. This reduction in the magnitude of the phase angle ψ develops lower negative added water damping when the fluid dynamic force is in phase with the seal vibration velocity (i.e., $180^0 > \psi > 0^0$). As a result, system stable range along Π_2 increases by increasing Π_1 as lower negative added water damping is developed.

Figure (4.21) shows the influence of Π_1 and Π_2 on the dimensionless seal oscillation frequency f^*, the dimensionless added water stiffness Π_k, and the dimensionless magnitude of the fluid dynamic force acting on the seal $|F^*|$. Figures (4.21 a and b) exhibit that at a specific harmonic, the seal oscillation frequency depends on the added water stiffness coefficient k_w since the added water mass m_w is constant for all values of Π_1 and Π_2 (i.e., $m_w = \rho A_d L_d \ (A_{os}/A_d)^2$). Also, the analysis shows that increasing Π_2 decreases the seal oscillation frequency as higher negative added water stiffness or lower positive added water stiffness is developed as in figure (4.21 b).

The phase angle ψ identifies both the added water stiffness and the added water damping coefficients. If ψ is in the range of $90^0 > \psi > -90^0$, then the fluid dynamic force is in phase with the seal vibration displacement, developing a negative added water stiffness as for the first harmonic in figure (4.21 b). In contrast, If ψ is in the range of $-90^0 > \psi > 90^0$, then the fluid dynamic force is out of phase of the seal vibration displacement as in figure (4.20 c). In this case, positive added water stiffness is developed as for the third harmonic in figure (4.21 b). For the first and second harmonics as in figures (4.20 a and b), the fluid dynamic force becomes more in phase with the seal vibration displacement since the value of ψ reaches zero by increasing Π_2. In this situation, higher negative added water stiffness is developed decreasing the seal oscillation frequency as in figures (4.21 a and b). In contrast, for the third oscillation frequency, the phase angle ψ is in the range of $-90^0 > \psi > 90^0$ where the fluid dynamic force develops positive added water stiffness. However, since increasing Π_2 decreases the magnitude of the fluid dynamic force acting on the seal, as in figure (4.21 c), hence increasing Π_2 decreases the positive added water stiffness and the seal oscillation frequency as in figures (4.21 a and b). Finally varying Π_1 has a negligible effect on the seal oscillation frequency, as in figure (4.21 a), since Π_1 has a negligible effect on the added water stiffness and the fluid dynamic force as in figures (4.21 b and c).

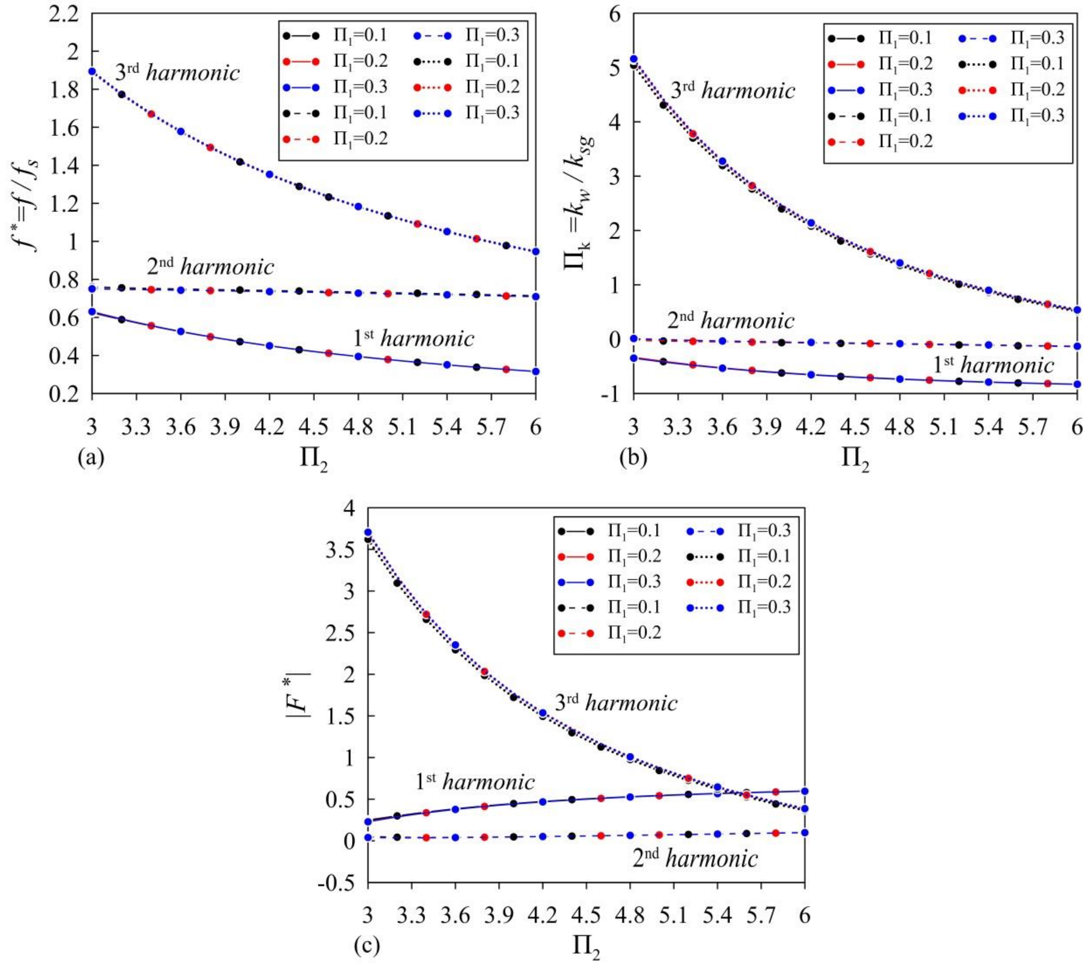

Figure 4.21: Relation between Π_2, f^*, Π_k and $|F^*|$, at Π_1=0.1, 0.2 and 0.3, Π_3=1100 and Π_4=0.4 for the first three harmonics

Figure (4.22) shows the influence of incrementing the pilot pipeline head loss on system stability at the same values of Π_1=0.1 and Π_4=0.4. Figure (4.22) shows that increasing the pilot pipeline head losses enhance system dynamic stability as positive added water damping is established by increasing Π_3 for the first three harmonics.

By incrementing the pilot pipeline head losses, the phase angle ψ decreases as in figure (4.22 d). This reduction in the phase angle ψ causes the dynamic fluid force to be more in phase with the seal vibration displacement and out of phase of the seal vibration velocity. As a result, a lower negative added water damping or a positive added water damping is developed improving system stability, as in figure (4.22).

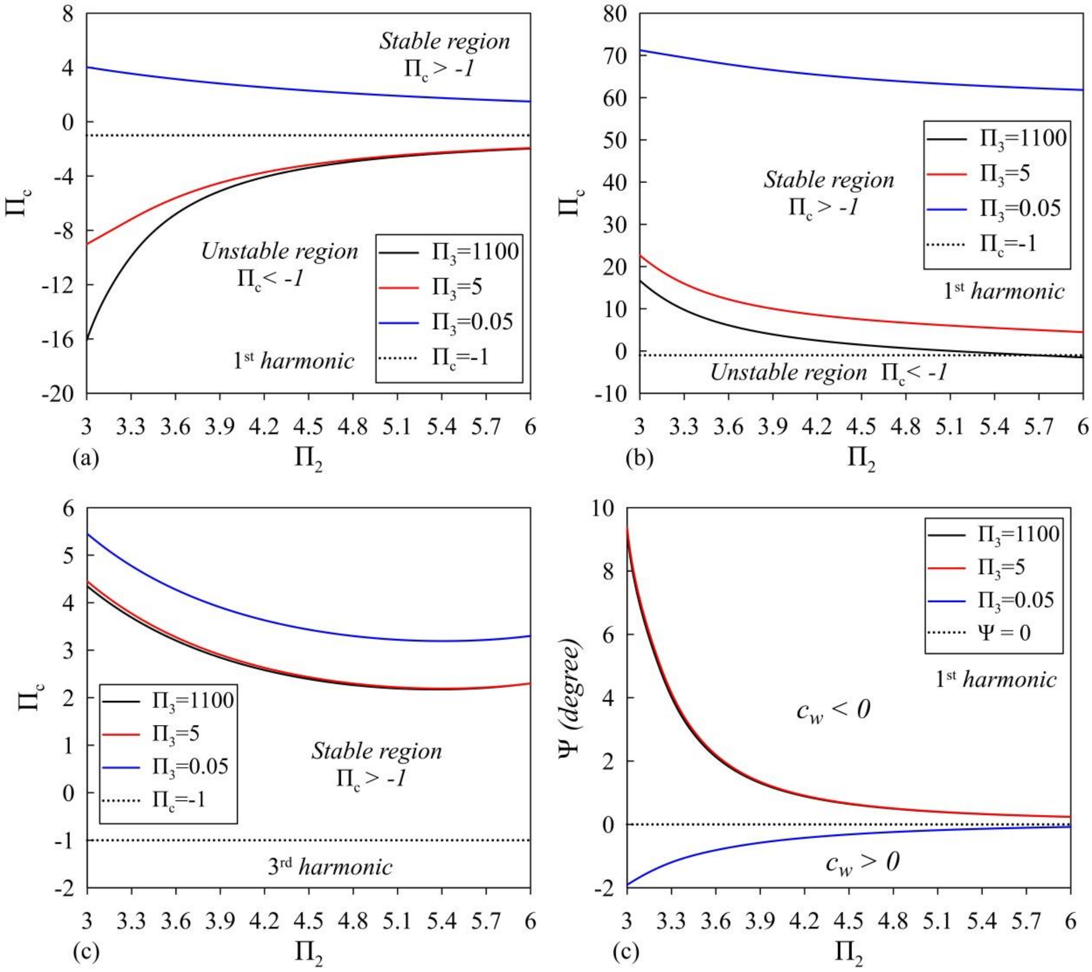

Figure 4.22: Relation between Π_2, Π_c, and Π_3, at Π_1=0.1 and Π_4=0.4 for the first three harmonics

Figure (4.23) shows the influence of incrementing the pilot pipeline head losses (reducing Π_3) on the seal oscillation frequency. Since the added water mass is independent of the pilot pipeline resistance, and Π_3 has a negligible effect on the added water stiffness as in figure (4.23 b), thus varying Π_3 has a negligible effect on the seal oscillation frequency as in figure (4.23 a).

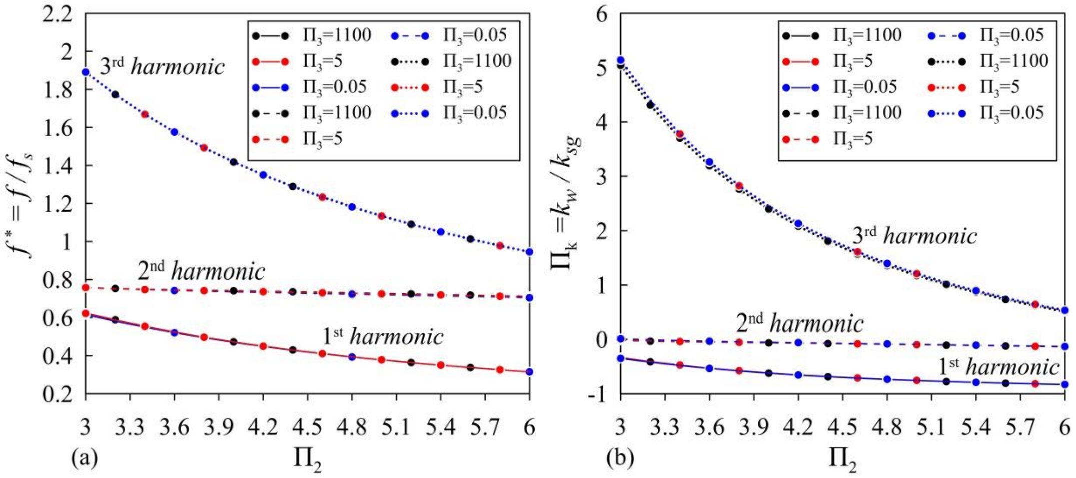

Figure 4.23: Relation between Π_2, Π_3, f^*, and Π_k, for the first three harmonics at Π_1=0.1 and Π_4=0.4

In the previous cases, Π_1 and Π_3 influence on the added water damping and system stability can be explained through the variation of the phase angle ψ as Π_1 and Π_3 have a negligible influence on the added water stiffness, magnitude of the fluid dynamic force and the seal oscillation frequency as in figures (4.20, 4.21, 4.22 and 4.23). However, in this case, by analyzing the seal behavior for different seal geometries (different $\Pi_4=A_{ss}/A_{os}$), it is seen that for the first and third harmonics as in figures (4.24 a and c), the seal oscillates with nearly the same frequency and with the same magnitude of the fluid dynamic force as in figures (4.24 d and f). However, for the second harmonic, the seal oscillation frequency and the fluid dynamic force differ for each value of Π_4 as in figures (4.24 c and e). Since the added water mass is the same for all harmonics of the seal oscillations as in Eq.(84), and as the seal equivalent damping coefficient hardly influence the frequency of the seal oscillation, hence the seal different harmonics are established according to the added water stiffness developed by the fluid dynamic force. So, for the cases of the first and second harmonics, the fluid dynamic force is nearly the same for all values of Π_4 because the frequency of the seal oscillation is nearly the same for all values of Π_4, as in figures (4.24 a, c, d and f). In contrast, for the second harmonic, the frequency of the seal oscillation differs from one case to another, with maximum value for the case of Π_4=0.8, see figure (4.24 b). Therefore, for the case of Π_4=0.8, the fluid dynamic force is maximum, to develop the needed added water stiffness for the seal to oscillate at this specified frequency as in figure (4.24 e).

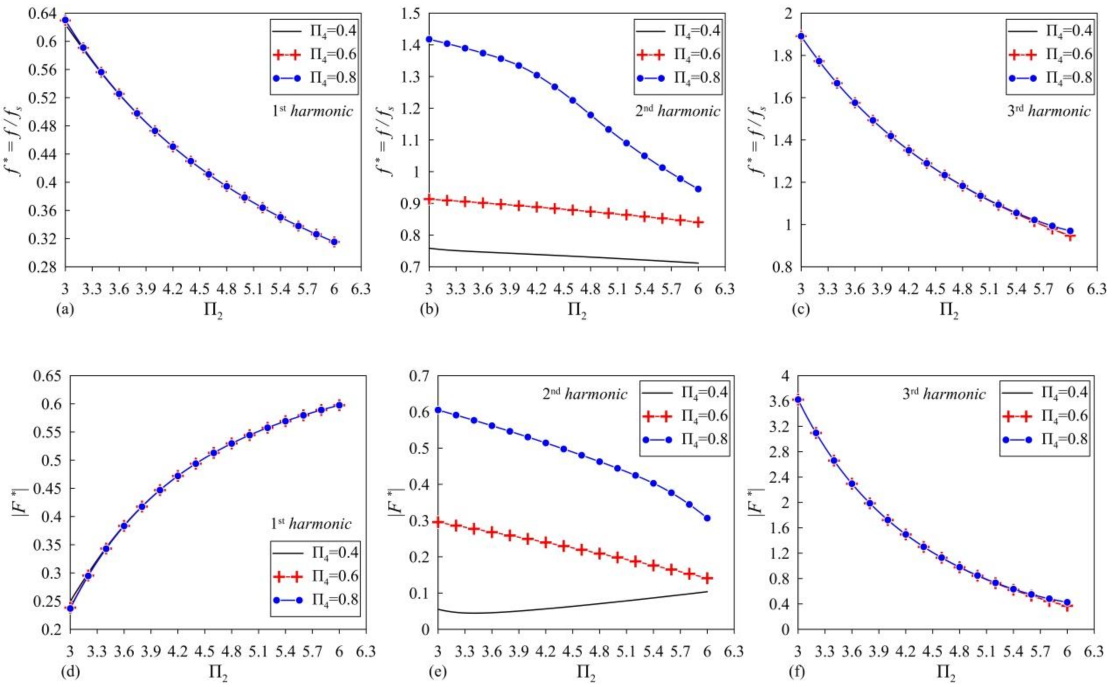

Figure 4.24: (a, b and c) Relation between Π_2 and f^* for the first three harmonics. (c, d, and e) Relation between Π_2 and $|F^*|$ for the first three harmonics. Π_1=0.1, Π_3=1141 and Π_4=0.4, 0.6, and 0.8, for the first three oscillation frequencies of the seal

Another point can be concluded, is that the harmonics of the seal oscillations are responsible for the values of the phase angles in the range of $90^0<\psi<-90^0$. As mentioned before the added water mass is the same for all harmonics, while the added water stiffness is the one responsible to establish a specific oscillation frequency. When the seal oscillations are established at higher harmonics, positive added water stiffness is required to augments the seal oscillation frequency to a specific harmonic (i.e., $\omega \approx \sqrt{\frac{k_w+k_{sg}}{m_w+m_{sg}}}$) For the fluid dynamic force there is only one configuration to create an added water stiffness of positive value, which is to have a phase angle to the seal vibration displacement in the range of $90^0<\psi<-90^0$. In this situation, the fluid dynamic force is out of phase of the seal vibration displacement. As a result, positive added water stiffness is developed, augmenting the seal equivalent stiffness coefficient and the seal's oscillation frequency. That's why for all mentioned results as in figures (4.20 c, 4.21 c and 4.25 f), the phase angle ψ is in the range of $90^0<\psi<-90^0$, particularly after the 2nd harmonic.

Finally, the system dynamic stability is identified by the phase angle ψ as in figures (4.25 a, b and c), where for the first harmonic the seal is dynamically unstable for all values of Π_4 and Π_2, as ψ is in the range of $0^0>\psi<180^0$ and $\Pi_c<-1$. For the third harmonic, the system is dynamically stable for all values of Π_4 since the phase ψ is in the range of $0^0>\psi>-180^0$ and $\Pi_c>-1$. In contrast, system dynamic stability of the second harmonic depends on the values of Π_2 due to the variation of ψ and Π_c along Π_2, as in figures (4.25 b and e).

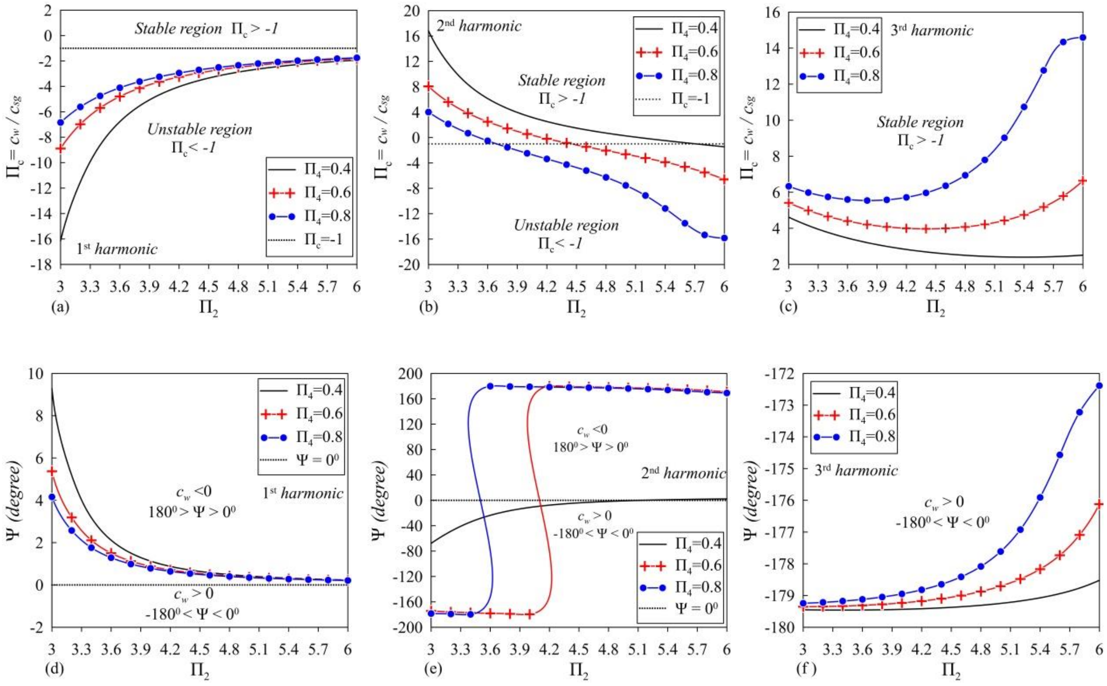

Figure 4.25: (a, b and c) Relation between Π_2 and Π_c. (d, e, and f) Relation between Π_2 and ψ at the first three harmonics. Π_1=0.1, Π_3=1141 and Π_4=0.4, 0.6, and 0.8.

4.4.2 2nd MODEL stability charts:

As mentioned previously one of the main objectives of the study is to develop and evaluate system stability conditions to interpret the influence of the Π-groups on system dynamic stability and to deliver recommendations for improving system dynamic stability. Therefore, three stability charts are drawn function of the developed Π-groups as in figures (4.26 a, b and c). The lines presented in the stability charts present the critically stable condition where c_{eq}=0, while the area enclosed by these lines represents the stable region where $c_{eq} > 0$ and $\Pi_c > -1$. The stable region means that the equivalent damping coefficient is positive for the first ten harmonics, while the unstable region means that one or more than one harmonic is unstable where $c_{eq}<0$. The first stability chart presents the effect of the input reservoir energy head and pipeline characteristics (i.e., pipeline length and wave speed) on system dynamic stability as a function of Π_1 and Π_2. The second chart exhibits the pilot pipeline head loss influence on system stability as a function of Π_3, and finally, the third stability chart presents the seal's geometry influence on system stability as a function of Π_4.

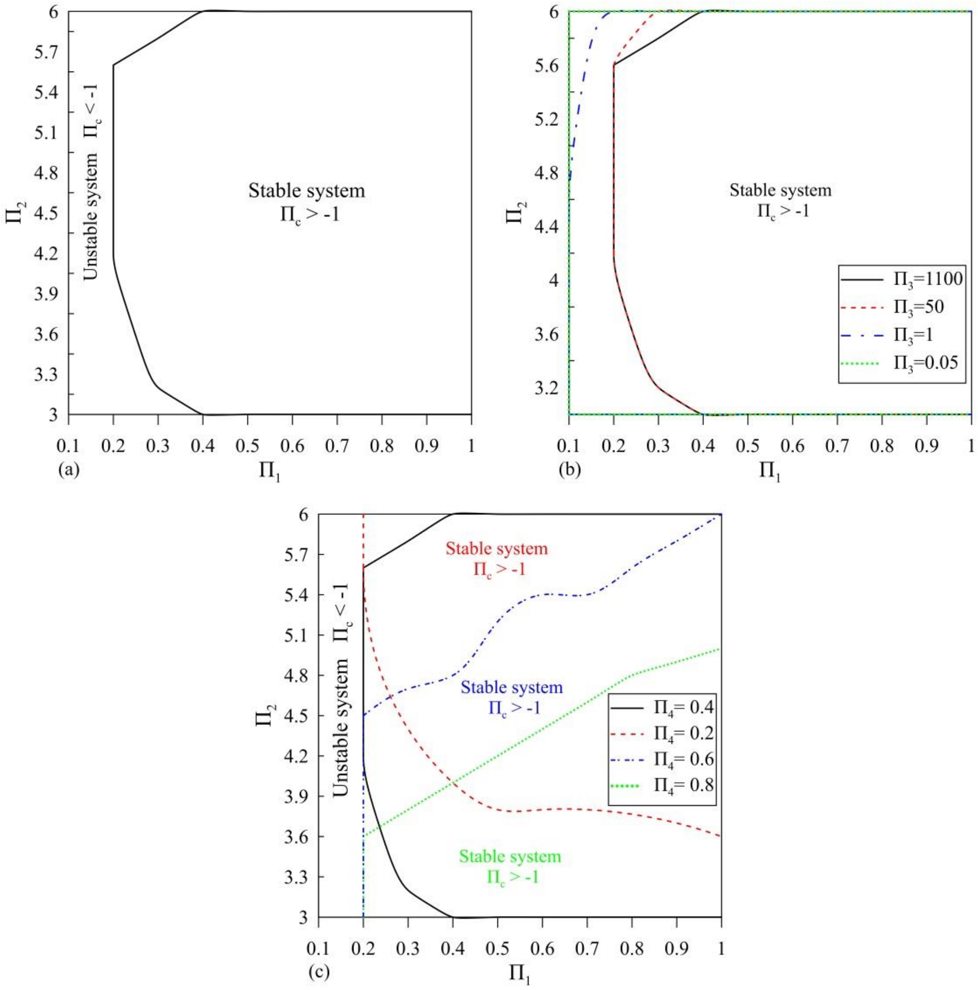

Figure 4.26: (a) System stability chart function of Π_1 and Π_2 at Π_3=1100 and Π_4=0.4 (b) System stability chart function of Π_1, Π_2 and Π_3 at Π_4=0.4. (c) System stability chart function of Π_1, Π_2 and Π_4 at Π_3=1100.

Figure (4.26 a) shows the stable and unstable regions as a function of Π_1 and Π_2, at the same pilot pipeline flow characteristics Π_3=1100 and the same seal geometry Π_4=0.4. Figure (4.26 a) shows that system stability is enhanced by increasing Π_1 for all values of Π_2. By increasing Π_1, the added water damping increases as in figure (4.19 a), leading to a dynamically stable system such as in figure (4.26 a).

Figure (4.26 b) shows the influence of the pilot pipeline flow characteristics on system stability at the same seal geometry Π_4=0.4. Figure (4.26 b) exhibits that by increasing the pilot pipeline resistance (decreasing Π_3) the system stable range along

Π_2 increases. Such as at Π_3=1100 and 1, and Π_2=0.2, the stable system range is satisfied for Π_2 ranging between 4.2 and 5.6 for Π_3=1100, and between 3 and 6 for Π_3=1. Also, the analysis shows that by increasing the pilot pipeline resistance significantly to values such as $\Pi_3 \leq 0.05$, the system will be dynamically stable for all values of Π_2 as in figure (4.26 b). By increasing the pilot pipeline resistance, the phase angle between the fluid dynamic force and the seal vibration displacement decreases as in figure (4.22 c). Therefore, positive added water damping is developed, increasing system stability range along Π_2 as in figure (4.26 b).

Figure (4.26 c) shows the influence of the seal geometry on system stability at the same pilot pipeline flow characteristics Π_3=1100. Figure (4.26 c) demonstrates that enhancement of system dynamic stability can be accomplished by varying the seal geometry but it depends on the values of Π_2. For high values of Π_2 it is preferred to increment the external surface area of the seal since the stability range satisfied along Π_1 increases by reducing Π_4 (i.e., see the stability region of Π_2=0.2). In contrast, for low values of Π_2 it is better to reduce the external surface area of the seal as the stability range satisfied along Π_1 increases by increasing Π_4 (i.e., see the stability region of Π_2=0.8).

By varying the seal geometry, the seal oscillation frequency varies at specific harmonics as seen in figure (2.24 b). This frequency variation causes a variation in the phase angle ψ that may lead to system instability at certain values of Π_2 as in figure (2.25 e). Therefore, the values of Π_2 must be taken into consideration while improving the seal dynamic stability by varying the seal geometry Π_4. Finally, keeping the seal geometry at $\Pi_4=A_{ss}/A_{os}$=0.4 may be considered the best choice, since Π_4=0.4 corresponds to the largest region of system dynamic stability as in figure (4.26 c).

4.4.3 Incompressible flow model and compressible flow model comparison:

The main point distinguishing between the usage of incompressible or compressible flow analysis to predict the system transient behavior is the influence of the pressure wave on the system following a system disturbance. Due to fluid compressibility and pipeline wall elasticity, a positive or negative pressure wave is developed due to the flow disturbance. The pressure wave developed depends on flow velocity variation and pipeline physical and geometrical characteristics, i.e., such as pipeline wave speed, pipeline wall elasticity, and pipeline length and cross-section area. These pressure waves travel forward and backward from the system exciting source (vibrating seal) to the input reservoir at the pipeline wave speed a_j. These waves influence the fluid dynamic force acting on the seal. Therefore, the seal dynamic behavior may change due to these pressure waves, which may risk the safe operation of the plant, if the seal periodic vibration is dynamically unstable.

In order to evaluate fluid compressibility and pipeline wall elasticity influence on the seal dynamic behavior, the seal's behavior will be examined for both models by calculating the complex frequency $i\omega+\sigma$ under different input reservoir energy levels and pipeline wave speeds. The pipeline wave speed a_j will be varied from *1000 m/s* to *6000 m/s*, while the input reservoir energy level H_1 will be varied from 50 m to 130 m. As Π_2 for the 1st model ($\Pi_2= v_{og} / \omega L_g$) and the 2nd model ($\Pi_2= \omega L_m / a_j$) differs, the results are computed dimensionally as mentioned above, but presented with the dimensionless parameters Π_1, Π_2, f^* and σ^*,. Where Π_1, Π_2, f^* and σ^* presented in figures (2.27 and 2.28) are as follows: $\Pi_1=\frac{Q_{og} I_m \omega_{ref}}{H_1}$, $\Pi_2=\frac{L_m \omega_{ref}}{a_j}$, $f^*=\frac{f}{f_s}$, and $\sigma^*=\frac{\sigma}{\omega_{ref}}$, where $\sigma = -\frac{c_{eq}}{2m_{eq}}$.

As seen in figure (2.27 b), the effects of pipeline wall elasticity and fluid compressibility influence the seal dynamic behavior since the seal dynamic stability depends on the value of Π_1, while for the incompressible model the seal is dynamically unstable ($\sigma>0$) for all values of Π_1. Also, the frequency of the seal oscillation differs between both model as in figure (2.27 a).

By considering fluid compressibility effects, the seal is dynamically stable for values of Π_1 greater than 0.206 as in figure (2.27 b), while for values smaller than $\Pi_1=0.206$, the seal is dynamically unstable since $\sigma>0$. Fluid compressibility affects the magnitude of the fluid dynamic force acting on the seal, in addition to the phase angle ψ between the fluid dynamic force and the seal vibration displacement, see figures (2.27 c and d). By considering the fluid compressibility as in figure (2.27 d), for values of $\Pi_1>0.206$, the phase angle ψ is in the range of $-180^0<\psi<0^0$. Therefore, positive added water damping is developed, maintain the system dynamic stability ($\sigma<0$). In contrast, for values of $\Pi_1<0.206$, the phase angle ψ is in the range of

$180^0 > \psi > 0^0$. As a result, fluid dynamic force excites the seal oscillations, leading to a dynamically unstable system since $\sigma > 0$. Therefore, for the case under consideration, fluid compressibility and pipeline wall elasticity effects are of great importance as they affect the seal dynamic behavior as in figure (2.27 b).

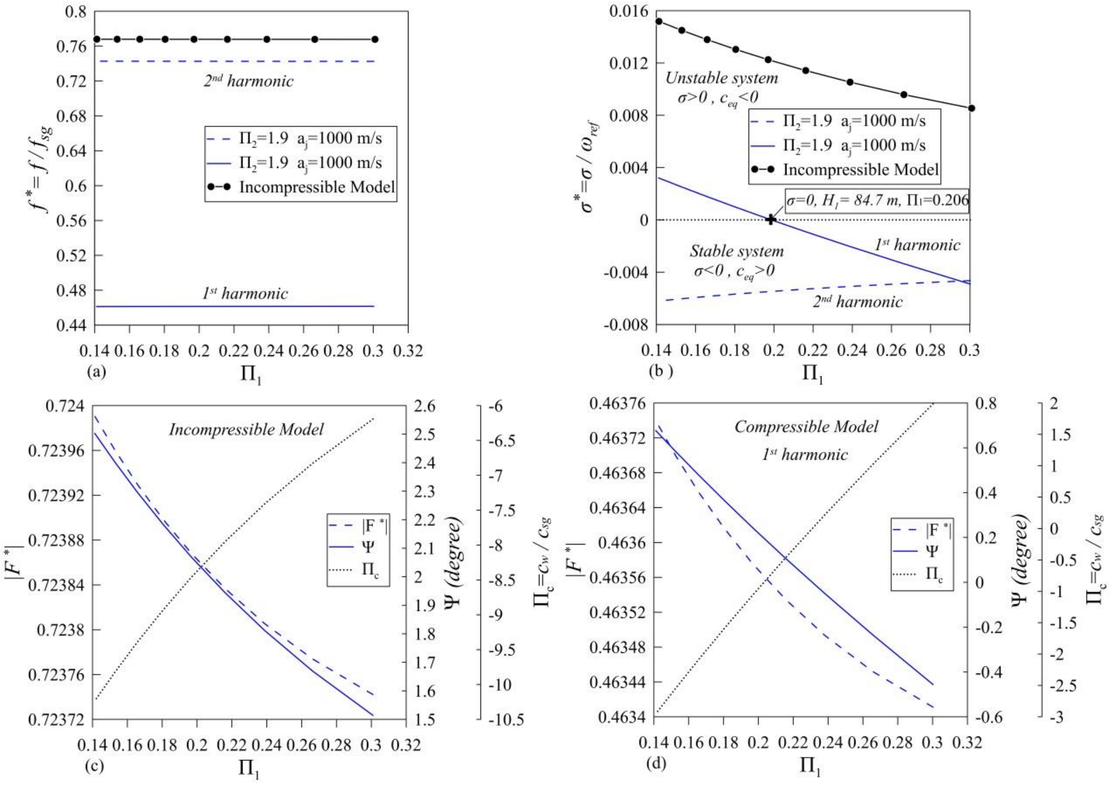

Figure 4.27: Relation between seal complex frequency i*f+σ*, |*F* *|, ψ, and Π_c computed for both Models at a_j=1000 m/s.**

(*Chaudhry 2014*) mentioned that for an oscillating flow in a pipeline, the significance of fluid compressibility and pipeline wall elasticity depends on the ratio between the speed of flow oscillation in a pipeline and pipeline wave speed. If the mentioned ratio is <<1, the fluid system can be considered a lumped system where a system disturbance is sensed through the whole system instantaneously. In this case, the fluid compressibility and pipeline wall elasticity effects are negligible and the fluid flow can be modeled for an incompressible flow. Figure (2.28) shows the effect of the pipeline wave speed and Π_2 on the dimensionless seal complex frequency. The aim of this figure (2.28) is to know the range of Π_2, where fluid compressibility and pipeline wall elasticity effects can be neglected. As seen in figure (2.28), the problem within the incompressible flow model, is that it could not predict the correct seal behavior (identified by the seal's complex frequency) or the different oscillation harmonics at high values of Π_2. However, as Π_2 decreases the seal's different harmonics starts to vanish as in the cases of Π_2= 0.82 and 0.67, see figures (2.28 a and c). Also, the seal behavior starts to coincide between both models as Π_2 values decreases particularly below Π_2=0.67.

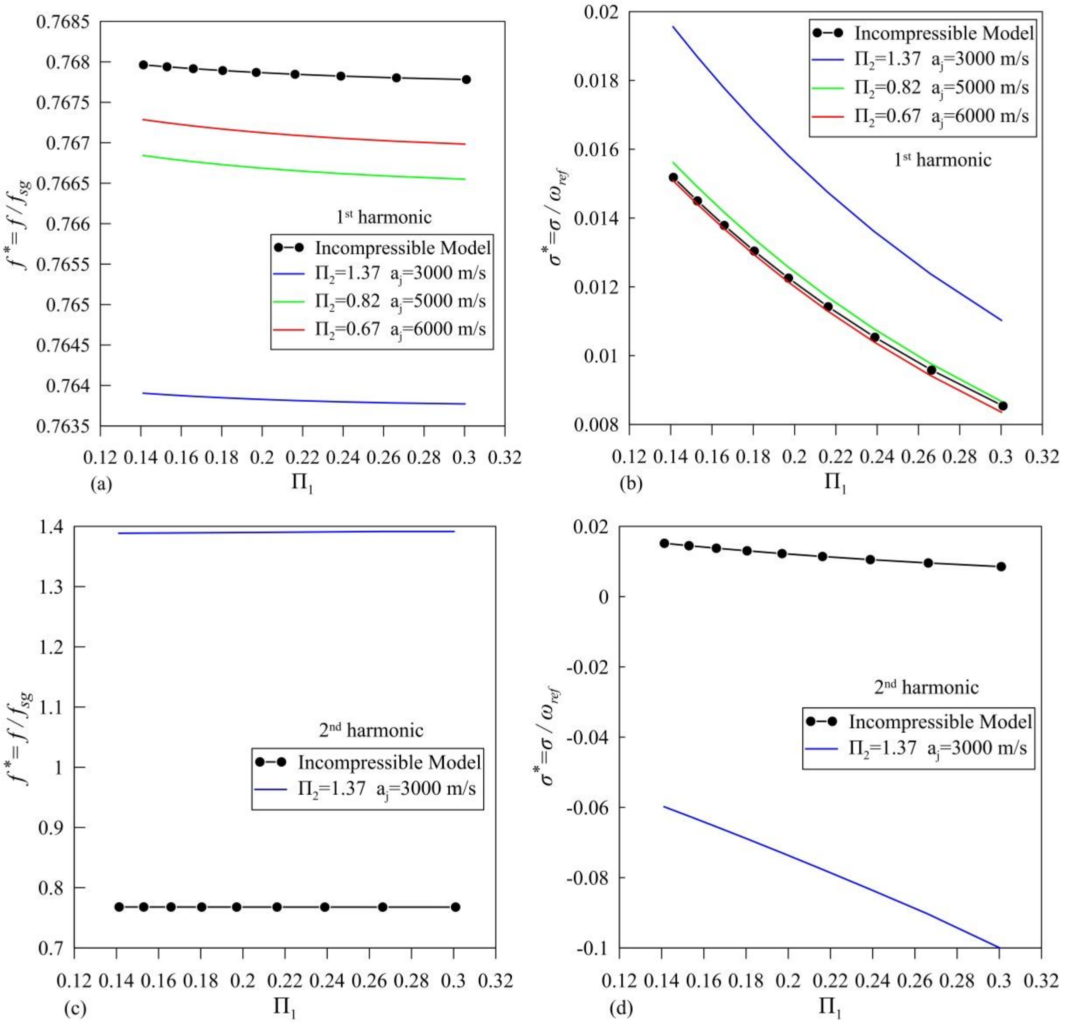

Figure 4.28: seal complex frequency i*f+σ* computed for both Models at a_j=3000, 5000 and 6000 m/s.**

4.4.4 1st MODEL and 2nd MODEL results validation

Table (4.1) shows a comparison between the complex frequencies $i\omega+\sigma$ computed using the compressible flow model in section 3.4 and the incompressible flow model (1st Model) in section 3.2. Both models computations are established at the same power plant physical and geometrical parameters, as in table (4.1). For the compressible model, the system complex frequency is computed at a very high pipeline wave speed of *15000 m/s* to ensure that the flow can be treated as an incompressible flow. In this situation, the complex frequency results should be the same as the one developed from the incompressible flow model (*Chaudhry 2014*). By observing the complex frequency relative error percentages, for the σ values, the maximum relative error percent is *2.2* at $H_1=50$ m, while for the frequency $f=\omega/2\pi$ values, the maximum relative error percent is *0.104* at $H_1=50$ *m*. The relative error is established due to the difference in the function utilized to represent the pressure and flow fluctuations in both models. For the incompressible model, the pressure and flow rate oscillations are assumed to be sinusoidal functions of constant amplitude (i.e, see Appendix A.3, as in Eq.(A.20)), while for the compressible model, the pressure and flow rate oscillations are assumed to be sinusoidal functions but of decaying or diverging amplitude according to system stability, (i.e., $q(t)=Re(q(x))e^{(i\omega+\sigma)t}$ and $h(t)=Re(h(x))e^{(i\omega+\sigma)t}$)

Table 4.1: System complex frequency computation for the compressible flow model and the incompressible flow model (1st model) at H_1=50-130 m and a_j=15000m/s

	Compressible model		**Incompressible model (1st Model)**			
H_1	$f=\dfrac{\omega}{2\pi}$	$\sigma=\zeta\omega_n$	$f=\dfrac{\omega}{2\pi}$	$\sigma=\zeta\omega_n$	*f error %*	*σ error %*
50	4.955487	0.339142	4.960645	0.3466	0.104076	2.198943
60	4.955717	0.382556	4.960779	0.388883	0.102139	1.653726
70	4.955954	0.422244	4.960919	0.427658	0.100182	1.282204
80	4.956197	0.45898	4.961064	0.463675	0.098212	1.022961
90	4.956442	0.493293	4.961212	0.497446	0.09623	0.841919
100	4.95669	0.525561	4.961361	0.529344	0.094238	0.719789
110	4.956939	0.556068	4.961511	0.559648	0.092234	0.643796
120	4.95719	0.585024	4.961663	0.588575	0.090218	0.60713
130	4.957443	0.612596	4.961814	0.616297	0.088188	0.604143

Main findings of the 2^{nd} Model Compressible flow:

The following points summarize the main findings of the compressible flow 2^{nd} Model analysis:

- At all values of Π_1 seal instability depends on the ratio between the mainline flow oscillation speed and pipeline wave speed Π_2.
- By evaluating seal vibration instability at the different harmonics it was found that the instability of seal vibrations mainly occurs at the lower harmonics and particularly at the first two harmonics.
- By increasing Π_1, system stability is enhanced as lower negative added water damping is developed.
- The magnitude of the added water damping is inversely proportional to the seal oscillation frequency as in equation Eq.(85).
- Incrementing pilot pipeline head losses enhance system stability as the seal equivalent damping coefficient increases.
- Compressible flow analysis showed that varying seal surface area doesn’t guarantee an enhancement to system stability as it depends greatly on the values of Π_2. However stability chart concerning seal geometry effect on system dynamic stability demonstrated that keeping the seal geometry the same is the best choice, since the area of the stable system along Π_1 and Π_2 is maximum.
- Finally by comparing the incompressible and compressible flow models stability charts, it’s demonstrated that at Π_2 values > 0.67, pipeline wall elasticity and fluid compressibility has a significant influence on the seal behavior due to the pressure wave effect. However, in situations where $\Pi_2 < 0.67$, the incompressible flow analysis can be adopted as the fluid compressibility and pipeline wall elasticity have a negligible effect.

4.4.5 2^{nd} MODEL parametric study for the Salime power plant

As done in the first model results and discussion, the following sections will present the parametric study for the Salime power plant but while considering pipeline wall elasticity and fluid compressibility effects. Therefore, the following sections exhibit the effect of the input reservoir energy level, gap angle, and pipeline wave speed on the seal behavior.

Figure (4.29) shows the influence of the input reservoir energy level on the seal behavior while considering constant pipeline wave speed a_j=1000 m/s and constant seal gap angle $\theta_{gap}=60^0$. Figures (4.29 a and b) show that the fluid dynamic force tends to excite the seal oscillations at the first harmonic since the seal equivalent damping coefficient has negative values. Also, by increasing the input reservoir energy level, the instability of seal vibration is more often to occur, as increasing H_1 decreases the seal equivalent damping coefficient particularly at the first harmonic, as in figure (4.29 a).

Figures (4.29 c and d) show that the input reservoir energy level has a negligible effect on the seal oscillation frequency. For all values of H_1 the seal vibrates at nearly constant frequency as the input reservoir energy level has a negligible effect on the fluid dynamic force as in figures (4.29 e and f). However, the fluid dynamic force at all values of H_1 are highly influenced by the seal harmonic, as by increasing the seal harmonic the fluid dynamic force increases significantly as in figures (4.29 e and f).

Finally, figure (4.29 a) shows that system instability is established at the first harmonic at 2.98 Hz and 87 m input reservoir energy level. This values match with the information gained from the plant as it was mentioned that the seal develops unstable periodic vibrations noticed as impacts with the rate of 1-3 Hz when the valve is in close position and the input reservoir energy level is below the nominal head of 105 m.

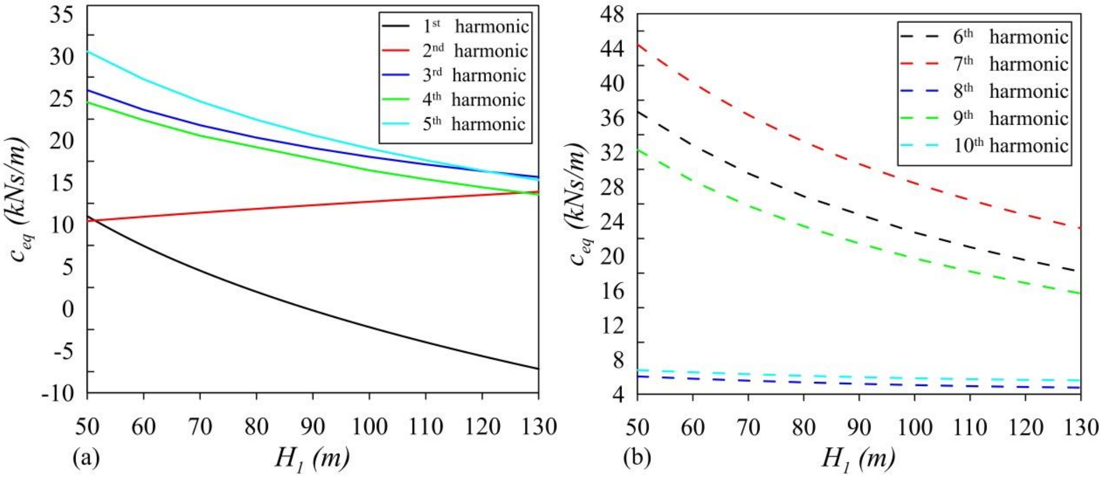

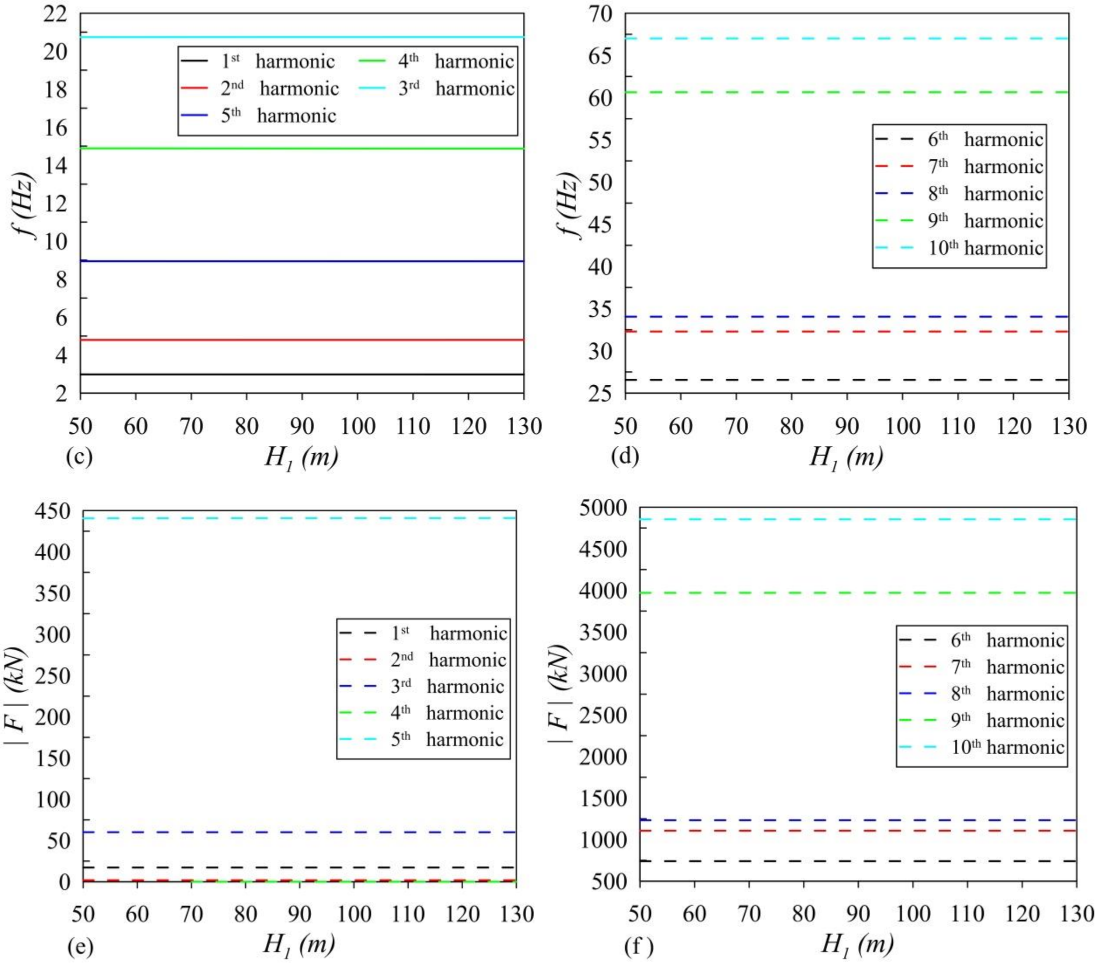

Figure 4.29: relation between H_1, c_{eq}, f and $|F|$ at a_j=1000 m/s and $\theta_{gap}=60^0$ for the first 10 seal harmonics

Figure (4.30) shows the influence of the pipeline wave speed on the seal behavior at H_1=90 m and 100 m, and $\theta_{gap}=60^0$. Figures (4.30 a and b) show that the instability of the seal periodic vibration is established only at the first harmonic of the seal oscillation. Also, by increasing the pipeline wave speed, the instability of the seal periodic vibration are more prone to occur as the seal equivalent damping coefficient has higher negative values. Moreover, by increasing input reservoir energy level the seal can develop unstable periodic vibrations at lower pipeline wave speeds, as higher negative added water damping is developed, decreasing the seal equivalent damping coefficient, such as the case for a_j=900 m/s, see figures (4.30 a and b).

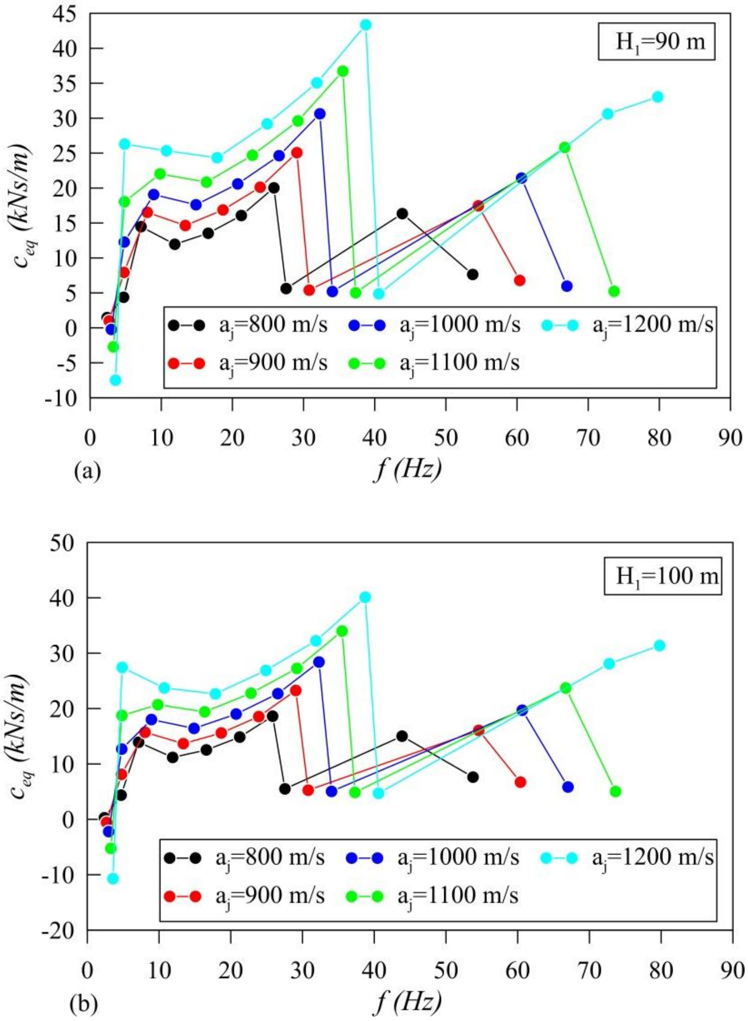

Figure 4.30: Relation between pipeline wave speed a_j and the seal equivalent damping coefficient c_{eq} for the first ten harmonics at H_1= 90 and 100 m, and $\theta_{gap}=60^0$

Finally, figures (4.31 a and b) show that the pipeline wave speed affects the harmonic of the seal oscillation. As by increasing the pipeline wave speed, the seal equivalent stiffness coefficient increases as in figure (4.31 c), increasing the seal oscillation frequency particularly at the higher harmonics.

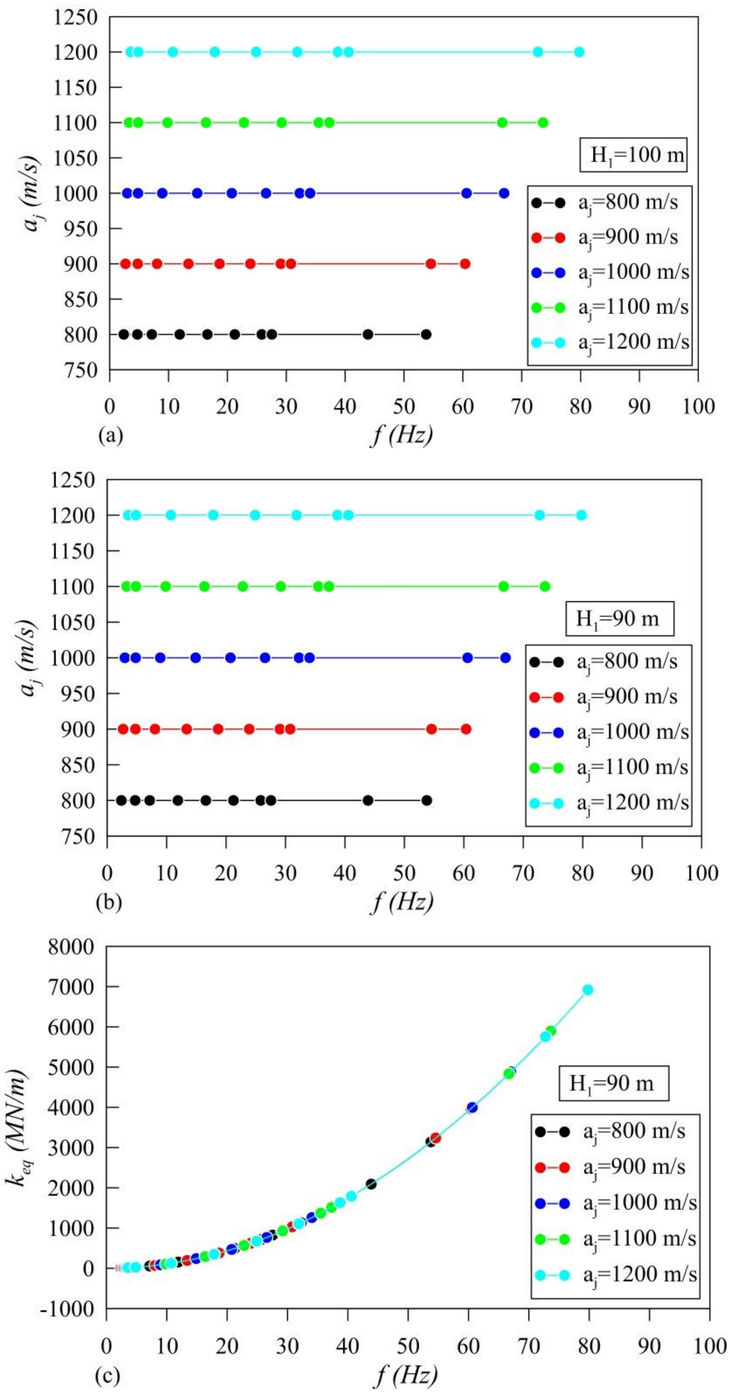

Figure 4.31: Relation between pipeline wave speed a_j, *f* and k_{eq}, for the first ten harmonics at H_1= 90 and 100 m, and $\theta_{gap}=60^0$.

Figure (4.32) shows the influence of the seal gap angle on the seal behavior and the seal oscillation frequency for constant values of pipeline wave speed a_j=1000 m/s and input reservoir energy level H_1=110 m

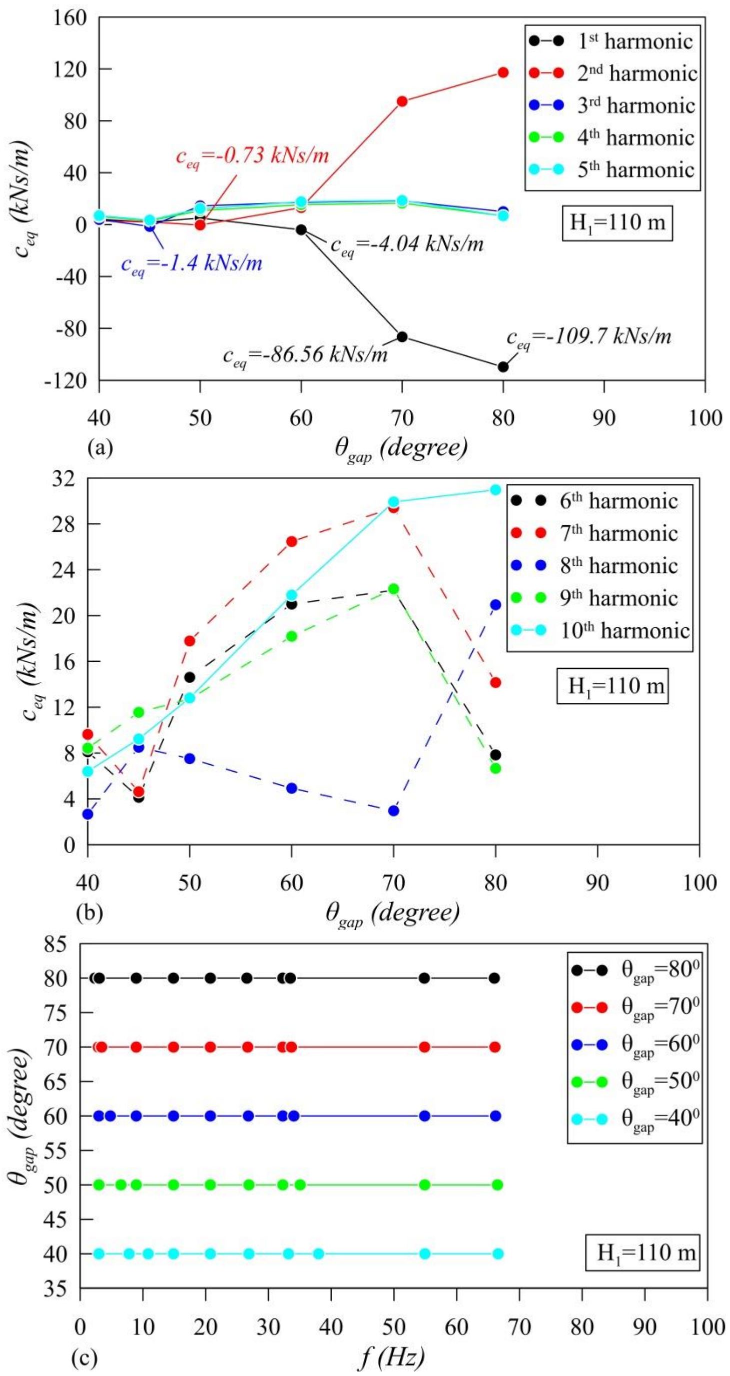

Figure 4.32: Relation between seal gap angle θ_{gap}, c_{eq} and f at a_j=1000 m/s and H_1=110m

. Figures (4.32 a and b) show that at high gap angle from 60^0 to 90^0, the instability of the seal vibration is established at the first harmonic since the seal equivalent damping coefficient has negative values. Also, the analysis demonstrated that the severity of the seal vibration at the first harmonic increases by increasing the gap angle since higher negative added water damping is developed. This negative added water damping decrease the seal equivalent coefficient as in figure (4.32 a), and risks the safe operation of the plant. In contrast, for lower gap angles, the instability of seal vibration is established at higher harmonics. Such as, for the cases of $\theta_{gap}=45^0$ and 50^0, the seal instability occurs at the third and the second harmonics respectively, see figure (4.32 a). Moreover, by increasing the seal closure and reducing the seal's gap angle, such as the case for $\theta_{gap}=40^0$, the seal is dynamically stable for the first ten harmonics since $c_{eq} > 0$.

On the other side, figure (4.32 c) shows that the harmonic of the seal oscillation increases slightly by decreasing the seal's gap angle. By decreasing the gap angle of the seal, the added water mass decreases due to the reduction of the seal external surface area. Also, the seal structure stiffness increases by reducing the gap angle according to Eq.(3). Therefore, reducing the gap angle of the seal increases the seal equivalent stiffness coefficient and the seal oscillation frequency as in figures (4.32 c). However, this frequency result demonstrates that the phenomenon is dominated by the fluid forces since varying the gap angle of the seal changes significantly the seal structure stiffness, see Eq.(3). However, the seal oscillation frequency is still nearly the same for the different harmonics due to the action of the fluid dynamic force on the vibrated seal.

2nd Model parametric study main findings:

At the end of the parametric study for the Salime power plant while considering pipeline wall elasticity and fluid compressibility, the following points can be concluded:

- Increasing input reservoir energy level leads to the instability of the seal periodic vibrations particular at the first harmonic as the negative added water damping increases by increasing the input reservoir energy level.
- For higher seal gap angles vibration instability is more prone to occur at the first harmonic, while at lower seal gap angles, the instability of the seal periodic vibration are established at higher harmonics such as seen in figure (32 a).
- Pipeline wave speed can alter the harmonic of the seal oscillation, as increasing the pipeline wave speed increases the seal equivalent stiffness coefficient increasing the frequency of the seal oscillation.

- Finally, increasing pipeline wave speed can cause instability of the seal periodic vibration, as increasing pipeline wave speed increases the negative added water damping and decreases the seal equivalent damping coefficient, particularly at the first harmonic of the seal oscillation.

5. CHAPTER FIVE: CONCLUSIONS

The main objective of this study has been the development of a simplified theoretical model that can explain and characterize the transient hydraulic behavior observed at the Salime hydro power plant, associated to flow-induced vibrations of the annular seals of the spherical valves in closed state. To achieve this objective, two theoretical models were constructed that assumed incompressible flow one of them, and flow with fluid compressibility and pipe elasticity the other one. Since the seal does not face any external force that may lead to the seal vibration, and the seal problem is solved at the plant by increasing the pressure forces acting on the seal during valve closure, it was thus assumed as a starting hypothesis that the seal periodic vibrations are self-excited due to the presence of a leaking flow between seal and ball seat. The proposed theoretical models are based on this assumption.

The theoretical models developed showed the ability to explain the mechanism behind the periodic seal vibrations. Moreover, they can estimate the transient hydraulic behavior of the plant depending on the relevant physical and geometrical characteristics. The established models include the dynamic seal characteristics, linear and nonlinear friction losses, pipeline wall elasticity and fluid compressibility effects. The developed study using the constructed models has confirmed that the case of interest belongs to the type of flow-induced vibrations denoted as movement-induced excitation, since the periodic seal vibrations result from the unstable coupling between the seal vibration motion and the fluid system. So, even if the seal is initially under equilibrium, a slight disturbance can develop pressure and flow oscillations of decaying (stable system) or incrementing (unstable system) amplitudes depending on the amount of energy supplied by the fluid system to the vibrated seal.

The two developed theoretical models were used to establish conditions for the stable and the unstable seal vibrations, under relevant operating settings. To evaluate the relative influence of the main parameters involved in the phenomenon dimensional analysis was conducted. This analysis showed that the phenomenon under consideration depends on the following main parameters: mainline flow inertia, input reservoir energy level, seal geometry, pilot pipeline flow characteristics and gap flow reduced velocity. Also, pipeline wave speed influences the phenomenon when fluid compressibility and pipeline wall elasticity effects are significant.

Throughout the study steady-state and unsteady-state analysis were conducted to provide recommendations to delimit and extend the operating conditions for safe stable behavior. The steady-state analysis showed that enlarging the seal surface area facing the pilot pipeline can improve the stability of the system. By increasing this area, the hydro pressure force acting on the seal increases. As a result, the total closure of the seal clearance can take place at lower input reservoir energy head, thus preventing seal leakage and eliminating seal vibrations. However, since valve closure has to be established under varying operating conditions, implementing an external auxiliary system that contributes to increase the pressure forces acting on the seal, is a more convenient solution. This explains that installing an auxiliary compressed air system to further tighten the annular seals on the ball of the valves, as done at the Salime power plant, is an effective means to eliminate the seal leakage in practice.

On the other hand, the dynamic stability analysis has yielded the following conclusions:

i) Theoretical model analysis shows that seal instability occurs when the fluid system and the seal motion couple in such a way that the fluid dynamic force is in phase with the seal vibration velocity and the coupled flow-structure system possesses a negative equivalent damping coefficient. In this situation, the seal vibrations are self-excited.

ii) Both models considering incompressible and compressible flow agreed that dynamic seal instability is less prone to occur when operating at low input reservoir energy levels for a given gap size. Also, increasing the gap flow velocity causes the fluid force to be more in phase with the seal vibration velocity. In this case, the fluid force excitation to the seal oscillation increases, leading to seal instability.

iii) Both models agreed that augmenting pilot pipeline friction losses can enhance the dynamic stability of the seal. Therefore, setting up a valve that can be closed to a certain degree at the pilot pipeline can improve system stability.

iv) Both models agreed that decreasing the pilot pipeline inertia head enhances the system stability. Therefore increasing the pilot pipeline diameter or decreasing the pilot pipeline length are advisable measures.

v) Both models showed that the magnitude of the added water damping is inversely proportional to the system oscillation frequency. Also, results showed that fluid forces determine the seal oscillation frequency, as the ratio between the seal oscillation frequency and the seal structural natural frequency is <<1.

vi) The incompressible flow analysis demonstrates that the added water mass is independent of the input reservoir energy level and the mainline flow inertia. However, it depends on the water mass in the pilot pipeline and the seal external surface area.

vii) The non-linear incompressible flow analysis showed that, when the seal is dynamically unstable, the magnitude of the seal vibrations would increase up to a state of limit cycle oscillations whose amplitude would be much larger than the space available for the seal between the seats on the ball and the casing, which is minimal. As a result, during the seal vibration, the seal will hit the ball surface going backward and forward in unstable dynamic situations. In consequence, solving the developed hydro-mechanical models after linearization can be considered adequate and sufficient to characterize the seal behavior.

viii) The slightly compressible flow analysis demonstrated that for any value of energy level in the reservoir, the seal dynamic instability depends on the mainline flow oscillation speed ratio to the pipeline wave speed. Moreover, the seal vibration instability is more often to be established at the 1st harmonic of the seal periodic vibrations where the fluid dynamic force tends to excite more the seal oscillations rather than damping them. .

ix) Comparison of the results from the compressible and incompressible flow models leads to conclude that the incompressible flow analysis may be adopted when the flow oscillation speed to pipeline wave speed ratio, Π_2, is below 0.67. However, if $\Pi_2>0.67$ then the effects of fluid compressibility and pipeline wall elasticity should be considered as they significantly affect the phase and magnitude of the flow disturbances developed in the system as well as the fluid-dynamic forces on the seal.

According to the developed study here are the following topics that can be concerned for future studies.

i) Since fluid-dynamic forces dominate the phenomenon especially when the fluid compressibility and pipeline wall elasticity effects are considered, hence further development of the second model can be conducted so that the analysis includes nonlinear losses, in order to examine its effect on the seal behavior. For that study the water hammer equations can be solved by using the method of characteristics.

ii) In the current research, the flow through the fluctuating gap between seal and ball seat, which is particularly relevant in the flow-structure coupling that can lead to instability, was assumed to be one-dimensional without any consideration of two-dimensional effects. However in reality the gap flow contains two-dimensional features due to boundary layer development and, more important, due to the imposition of a perpendicular component on the local velocity vectors by the instantaneous velocity of the seal. This alternative motion is likely to produce secondary flows in the gap in the form of vortices with alternative rotation direction, and those vortices would travel downstream convected with the main flow. In order to analyze the characteristics of the two-dimensional unsteady flow through the gap between seal and ball seat, it is suggested to conduct a CFD study that includes a wall boundary (the seal surface) with oscillatory motion in perpendicular direction with respect to the main flow, deformable cells and time dependent boundary conditions at inlet and outlet.

iii) Analogously to the previous item, in the current research the local flow at the pilot line, in particular where that line ends at the seal external surface, was also modeled as one-dimensional in a rather simplified way. However in reality the tightening force on the seal is applied from the fluid along an annular duct, located between the external surface of the seal and the valve casing. And that internal duct receives the high pressure water from the external pilot line through several connections in the radial direction around the valve. Therefore it is to be expected that the instantaneous pressure on the seal is not uniform and different from the pressure at the end of the pilot line, both in amplitude and phase. In consequence, in order to pursuit a description of the seal behavior closer to reality, it is suggested to undertake a specific study of the features of the transient flow on the external surface of the annular seal. This can be done by forming a more complex pressure distribution system as a duct network, so that it can be incorporated in the general system of differential equations already formulated to be solved in the time domain, or in the form of additional transfer matrices for the formulation in the frequency domain. Additionally, CFD simulations may be also undertaken to analyze the two-dimensional features in the flow at the external side of the seal.

iv) The results so obtained (previous suggested lines of research) on the two-dimensional details of the unsteady flow at the seal-ball gap and on the external surface of the seal have potential to alter the resulting net fluid-dynamic forces on the seal. Therefore another line of research is suggested in order to incorporate in a simple way the effects of two-dimensional flow in the models developed, and determine its implication on the conditions for system stability.

v) For the developed model considering fluid compressibility, the decaying or diverging rate of the pressure and flow oscillations has been assumed to take place simultaneously at all sections of the plant. However, given the length of the penstock and the size of the whole system, some time delay can be expected between the decays at different positions. In terms of phase delay, the effect can be expected to be more significant for high oscillation frequencies. Such time delay may alter the fluid-dynamic forces on the seal and, consequently, may affect the conditions for the system to be stable or unstable. Therefore it is suggested to explore a modification of the assumptions of the present models in order to include a time delay in the increasing or decreasing progress of flow disturbances in each location of the domain.

CONCLUSIONES

El objetivo principal de este estudio ha sido el desarrollo de un modelo teórico simplificado que pueda explicar y caracterizar el comportamiento hidráulico transitorio observado en la Central Hidroeléctrica de Salime, asociado a las vibraciones inducidas por el flujo en los sellos anulares de las válvulas esféricas cuando están en estado de cierre. Para lograr este objetivo, se construyeron dos modelos teóricos que asumían flujo incompresible uno de ellos y flujo con efectos de compresibilidad del fluido y elasticidad de tubería el otro. Dado que sobre el sello no actúa ninguna fuerza externa que pueda conducir a la excitación de vibraciones, y que en la planta se ha podido resolver el problema del sello aumentando las fuerzas de presión que actúan sobre él durante el cierre de la válvula, se asumió como hipótesis de partida que las vibraciones periódicas del sello se autoexcitan debido a la existencia de un cierto caudal de fuga por un hueco entre el sello y el asiento sobre la bola de la válvula. Los modelos teóricos propuestos se basan pues en esta suposición.

Los modelos teóricos desarrollados han mostrado la capacidad de explicar el mecanismo subyacente a la excitación de las vibraciones del sello. Además, pueden estimar el comportamiento hidráulico transitorio de la planta en función de las características físicas y geométricas relevantes. Los modelos establecidos incluyen las características dinámicas del sello, las pérdidas por fricción lineales y no lineales, la elasticidad de la pared de la tubería y los efectos de la compresibilidad del fluido. El estudio desarrollado basado en los modelos construidos ha confirmado que el caso de interés pertenece al tipo de vibraciones inducidas por flujo conocidas como excitación inducida por movimiento, ya que la vibración del sello se produce por acoplamiento inestable entre el movimiento de vibración del sello y el sistema hidráulico. Por ello, incluso si el sello está en equilibrio inicial, una pequeña perturbación puede desarrollar oscilaciones de presión y flujo de amplitudes decrecientes (sistema estable) o crecientes (sistema inestable), dependiendo de la cantidad de energía suministrada por el sistema de fluido al sello vibrado.

Los dos modelos teóricos desarrollados se emplearon para establecer las condiciones estables e inestables de vibraciones del sello, bajo configuraciones de parámetros correspondientes a entornos operativos relevantes. Para evaluar la influencia relativa de los principales parámetros involucrados en el fenómeno se realizó un análisis dimensional. Este análisis mostró que el fenómeno bajo consideración depende de los siguientes parámetros principales: inercia del flujo de la línea principal, nivel del embalse de la central, geometría del sello, características de flujo de la tubería piloto y velocidad reducida del flujo por el intersticio. Además, para el modelo que contempla la compresibilidad del fluido y la elasticidad de la pared de la tubería, es parámetro de relevancia la velocidad del sonido en cada tramo del sistema.

A lo largo del estudio se realizaron análisis de estado estacionario e no estacionario dirigidas a ofrecer recomendaciones sobre los límites de las condiciones de operación estable segura y sobre cómo poder extender esos límites. El análisis de estado estacionario muestra que el aumento del área de la superficie del sello frente a la tubería piloto puede mejorar la estabilidad del sistema. Al aumentar esta área, aumenta la fuerza de presión hidráulica que actúa sobre el sello. Como resultado, el cierre total de la holgura del sello puede tener lugar para un nivel de embalse más bajo, evitando así la fuga de caudal del sello y eliminando las vibraciones. Sin embargo, dado que el cierre de la válvula debe establecerse bajo diferentes condiciones de operación, resulta más conveniente implementar un sistema auxiliar externo que contribuya a aumentar las fuerzas de presión que actúan sobre el sello. En consecuencia, un sistema auxiliar de aire comprimido para apretar aún más los sellos anulares sobre la bola de las válvulas, como se ha hecho en la central eléctrica de Salime, es un medio eficaz para eliminar la fuga del sello en la práctica.

Por otro lado, el análisis de estabilidad dinámica ha arrojado las siguientes conclusiones:

i) El análisis del modelo teórico muestra que la inestabilidad del sello ocurre cuando el sistema hidráulico y el movimiento del sello se acoplan de tal manera que la fuerza dinámica del fluido está en fase con la velocidad de vibración del sello y al sistema acoplado flujo-estructura le corresponde un coeficiente de amortiguamiento equivalente negativo. En esta situación, las vibraciones del sello son autoexcitadas.

ii) Ambos modelos, que consideran flujo incompresible o compresible, coinciden en que la inestabilidad dinámica del sello es menos propensa a ocurrir cuando se opera con bajo nivel de embalse para un tamaño dado de intersticio de fuga. Además, el aumento de la velocidad de flujo en el intersticio hace aproximar la fase de la fuerza del fluido a la de la velocidad de vibración del sello. En tal caso, la excitación de la fuerza fluido-dinámica sobre el sello aumenta, lo que lleva a inestabilidad.

iii) Ambos modelos coinciden en que el aumento de las pérdidas por fricción de la tubería piloto puede mejorar la estabilidad dinámica del sello. Por lo tanto, la instalación de una válvula que se pueda cerrar hasta cierto punto en la tubería piloto se considera una medida favorecedora para la estabilidad del sistema.

iv) Ambos modelos coinciden en que la disminución de la altura de inercia de la tubería piloto contribuye a mejorar la estabilidad del sistema. Por lo tanto, aumentar el diámetro de la tubería piloto o disminuir la longitud de la tubería piloto son medidas recomendables.

v) Ambos modelos muestran que la magnitud del amortiguamiento añadido por el agua es inversamente proporcional a la frecuencia de oscilación del sistema. Además, los resultados muestran que las fuerzas fluido-dinámicas determinan la frecuencia de oscilación del sello, ya que la relación entre la frecuencia de oscilación del sello y la frecuencia natural estructural del sello es $<< 1$.

vi) El análisis de flujo incompresible demuestra que la masa añadida es independiente del nivel de energía del depósito de entrada y de la inercia del flujo de la línea principal. Sin embargo, sí que depende de la longitud de agua en la tubería piloto y del área de la superficie externa del sello.

vii) El análisis de flujo incompresible con términos no lineales ha mostrado que, cuando el sello es dinámicamente inestable, la magnitud de las vibraciones del sello aumentaría hasta un estado de oscilaciones de ciclo límite cuya amplitud sería mucho mayor que el espacio disponible para el sello entre los asientos de bola y de carcasa, que es mínimo. Por ello, durante la vibración del sello, éste golpeará repetidamente la superficie de la bola con movimientos hacia atrás y hacia adelante en situaciones dinámicas inestables. En consecuencia, la resolución de los modelos hidromecánicos basados en la linealización de las ecuaciones puede considerarse adecuada y suficiente para caracterizar el comportamiento del sello.

viii) El análisis para flujo ligeramente compresible ha mostrado que, para cualquier valor de nivel de embalse, la inestabilidad dinámica del sello depende de la relación de velocidad de oscilación del flujo en la línea principal frente a la velocidad de propagación acústica en esa tubería. Además, la inestabilidad de vibración del sello ocurre más fácilmente a la primera frecuencia fundamental del sistema acoplado resultante, pues a esa frecuencia las fuerzas fluidodinámicas tienden a excitar las vibraciones del sello más que a atenuarlas.

ix) La comparación de los resultados de los modelos de flujo compresible e incompresible lleva a concluir que el análisis de flujo incompresible puede adoptarse cuando la velocidad de oscilación del flujo respecto a la velocidad de onda de la tubería, Π_2, es inferior a 0.67. Sin embargo, si $\Pi_2 > 0.67$, entonces sí se deben considerar los efectos de compresibilidad del fluido y elasticidad de la pared de la tubería, ya que afectan significativamente a la fase y magnitud de las perturbaciones del flujo en el sistema, así como a las fuerzas fluido-dinámicas sobre el sello.

Según el estudio desarrollado se sugieren a continuación varios aspectos que se consideran de interés para estudios futuros.

i) Para una mejor caracterización de las fuerzas fluido-dinámicas que determinan el fenómeno de vibraciones, especialmente cuando se consideran los efectos de la compresibilidad del fluido y la elasticidad de la pared de la tubería, se puede realizar un desarrollo más avanzado del segundo modelo si se incluyen sin linealizar términos tales como las pérdidas de carga, a fin de examinar su efecto sobre el comportamiento del sello. Para ese tipo de estudio, se pueden resolver las ecuaciones del golpe de ariete utilizando el método de características.

ii) En la investigación actual, se asumió que el flujo a través del intersticio fluctuante entre el sello y el asiento sobre la bola, que es particularmente relevante en el acoplamiento flujo-estructura que conduce a la inestabilidad, es unidimensional sin tener en cuenta los efectos bidimensionales. Sin embargo, en realidad, el flujo del espacio contiene características bidimensionales debido al desarrollo de la capa límite y, lo que es más importante, debido a la imposición de una componente perpendicular a los vectores de velocidad local por la velocidad instantánea del sello. Es de esperar que este movimiento alternativo produzca flujos secundarios en el inersticio en forma de vórtices con dirección de rotación alternativa, con lo que esos vórtices viajarían corriente abajo por convección con el flujo principal. Para analizar las características del flujo inestable bidimensional a través del hueco entre el sello y el asiento de la bola, se sugiere realizar un estudio CFD que incluya una condición de contorno de pared (la superficie del sello) con movimiento oscilatorio en dirección perpendicular respecto al flujo principal, así como celdas deformables y otras condiciones de contorno dependientes del tiempo en la entrada y la salida.

iii) De manera análoga al ítem anterior, en la investigación actual el flujo local en la línea de pilotaje, en particular donde esa línea llega a la superficie externa del sello, también se modeló como unidimensional de una forma bastante simplificada. Sin embargo, en realidad, la fuerza de apriete sobre el sello se aplica desde el agua situada a lo largo de un conducto anular interno, ubicado entre la superficie externa del sello y la carcasa de la válvula. Y ese conducto interno recibe el agua a alta presión de la línea de pilotaje externa a través de varias conexiones dispuestas radialmente alrededor de la válvula. Por tanto, es de esperar que la presión instantánea sobre el sello no sea uniforme y que sea diferente de la presión al final de la línea de pilotaje, tanto en amplitud como en fase. En consecuencia, para buscar una descripción del comportamiento del sello más cercana a la realidad, se sugiere emprender un estudio específico de las características del flujo transitorio en la superficie externa del sello anular. Esto se puede hacer formando un sistema de distribución de presión más complejo similar a una red de conductos con varias interconexiones, de modo que se pueda incorporar en el sistema general de ecuaciones diferenciales ya formulado para ser resuelto en el dominio del tiempo, o bien en forma de matrices de transferencia adicionales para la formulación en el dominio de la frecuencia. Además, también se pueden realizar simulaciones CFD para analizar las características bidimensionales en el flujo en el lado externo del sello.

iv) Los resultados así obtenidos (de las líneas de investigación sugeridas en los dos puntos anteriores) sobre los detalles bidimensionales del flujo no estacionario en el hueco entre sello y bola por un lado, y sobre la superficie externa del sello por otro, tienen el potencial de alterar las fuerzas fluido-dinámicas netas resultantes sobre el sello. Por tanto, se sugiere otra línea de investigación con el propósito de incorporar de forma sencilla los efectos del flujo bidimensional en los modelos desarrollados, y determinar su implicación en las condiciones de estabilidad del sistema.

v) Para el modelo desarrollado que considera la compresibilidad del fluido, se ha asumido que el ritmo de disminución o aumento de las oscilaciones de presión y caudal tiene lugar simultáneamente en todas las secciones del sistema hidráulico. Sin embargo, dada la longitud de la tubería forzado y el tamaño de todo el sistema, es de esperar cierto retraso entre las caídas o crecimientos en diferentes posiciones. En términos de fase de retardo, se puede esperar que el efecto sea más significativo para altas frecuencias de oscilación. Tal tiempo de retraso puede alterar las fuerzas fluidodinámicas sobre el sello y, en consecuencia, puede afectar las condiciones para que el sistema sea estable o inestable. Por lo tanto, se sugiere explorar una modificación de los supuestos de los modelos actuales para incluir un tiempo de retraso en el progreso creciente o decreciente de las perturbaciones del flujo en cada ubicación del dominio.

REFERENCES

1. Abbott, H. F., Gibson, W. L. and McCaig, I. W. (1963). Measurements of auto-oscillation in a hydroelectric supply tunnel and penstock system. Journal of Fluids Engineering, Transactions of the ASME, 85(4). doi.org/10.1115/1.3656933
2. Abdelkefi, A. (2016). Aeroelastic energy harvesting: A review. *International Journal of Engineering Science*, *100*, 112–135. doi.org/10.1016/j.ijengsci.2015.10.006
3. Adamkowski, A. (2001). Case Study: Lapino Powerplant Penstock Failure. *Journal of Hydraulic Engineering*, *127*(7). doi.org/10.1061/(asce)0733-9429(2001)127:7(547).
4. Allison, T. C. and Brun, K. (2016). Testing and Modeling of an Acoustic Instability in Pilot-Operated Pressure Relief Valves. *Journal of Engineering for Gas Turbines and Power*, *138*(5). doi.org/10.1115/1.4031623.
5. Amabili, M. (2018). Nonlinear damping in large-amplitude vibrations: modelling and experiments. *Nonlinear Dynamics*, *93*(1), 5–18. doi.org/10.1007/s11071-017-3889-z.
6. Bazsó, C., Champneys, A. R. and Hős, C. J. (2014). Bifurcation analysis of a simplified model of a pressure relief valve attached to a pipe. *SIAM Journal on Applied Dynamical Systems*, *13*(2). doi.org/10.1137/130922598.
7. Bazsó, C. and Hős, C. J. (2013). An experimental study on the stability of a direct spring loaded poppet relief valve. *Journal of Fluids and Structures*, *42*. doi.org/10.1016/j.jfluidstructs.2013.08.008.
8. Beune, A., Kuerten, J. G. M. and van Heumen, M. P. C. (2012). CFD analysis with fluid-structure interaction of opening high-pressure safety valves. *Computers and Fluids*, 64, 108-116.doi.org/10.1016/j.compfluid.2012.05.010.
9. Blevins, R.D. (2001). *Flow-Induced Vibration (Second Edition)*. Krieger Publishing Co.
10. Budynas, R. G. and Nisbett, J. K. (2017). *Shigley's Mechanical Engineering Design*, *9th Edition*. McGraw-Hill.
11. Burhani, M. G. and Hős, C. (2021). An experimental and numerical analysis on the dynamical behavior of a safety valve in the case of two-phase non-flashing flow. *Periodica Polytechnica Chemical Engineering*, 65(2), 251–260. doi: 10.3311/PPch.16262.
12. Caney, K. and Zulovic, E. (2004). Self-excited penstock pressure oscillations at Gordon Power Station in Tasmania and other similar events. *WaterPower XIV*, 2004. Austin.
13. Chaudhry, M. H. (2014). *Applied Hydraulic Transients* (Third Edition). Springer-Verlag, New York. doi.org/10.1007/978-1-4614-8538-4.

14. D’Netto, W. and Weaver, D. S. (1987). Divergence and limit cycle oscillations in valves operating at small openings. *Journal of Fluids and Structures*, *1*(1). doi.org/10.1016/S0889-9746(87)90146-0.
15. Du, Y. and Zhang, G. (2019). Research on chattering occurrence condition in a vibro-impact system. *Journal of Low Frequency Noise Vibration and Active Control,* 38(3–4), 1202–1213. doi: 10.1177/1461348418813289.
16. Ecker, H.and Tondl, A. (2011). On the suppression of flow-generated self-excited vibrations of a valve. *ICOVP 2011, Springer Proceedings in Physics, 139*, 793-799. https://doi.org/10.1007/978-94-007-2069-5_107.
17. El Bouzidi, S., Hassan, M. and Ziada, S. (2018a). Experimental characterization of the self-excited vibrations of spring-loaded valves. *Journal of Fluids and Structures*, *76*, 558-572. doi.org/10.1016/j.jfluidstructs.2017.11.007.
18. El Bouzidi, S., Hassan, M. and Ziada, S. (2018b). Self-excited vibrations of spring-loaded valves operating at small pressure drops. *Journal of Fluids and Structures*, *83*, 72-90. doi.org/10.1016/j.jfluidstructs.2018.08.018.
19. El Bouzidi, S., Hassan, M. and Ziada, S. (2019). Acoustic methods to suppress self-excited oscillations in spring-loaded valves. *Journal of Fluids and Structures*, *85*, 126-137. doi.org/10.1016/j.jfluidstructs.2018.12.007.
20. Erdődi, I. and Hős, C. (2016). Numerical modelling of a direct spring operated pressure relief valve. *Journal of Computational and Applied Mechanics*, *11*(2). doi.org/10.32973/jcam.2016.009.
21. Erdődi, I. and Hős, C. (2017). Prediction of quarter-wave instability in direct spring operated pressure relief valves with upstream piping by means of CFD and reduced order modelling. *Journal of Fluids and Structures*, *73*, 37-52. doi.org/10.1016/j.jfluidstructs.2017.05.003.
22. Fox, J.A. (1977). *Hydraulic Analysis of Unsteady Flow in Pipe Networks*. McMillan Press.
23. Gad, O. (2021). Modeling of impact of the poppet element on its seat body in pressure relief valves. *Proceedings of the Institution of Mechanical Engineers. Part I: Journal of Systems and Control Engineering*, 235(5), 703–720. doi: 10.1177/0959651820945471.
24. Gummer, J. H. (1995). Penstock resonance at Maraetai 1 hydro station. *International Journal on Hydropower and Dams*, *2*(6).
25. Gummer, J.H. (2016). Hydraulic isolation of hydroelectric units. 6th Int. Conf. and Exhibition on Water Resources and Hydropower Development in Asia. Vientiane.
26. Hao, Q., Wu, W., Liu, Z. and Liang, X. (2019). Abnormal Opening Mechanism of Pilot-Operated Relief Valve under Alternating Pressure. *IEEE Access*, 7, 129709–129718. doi: 10.1109/ACCESS.2019.2939477.
27. Hayashi, S. (1995). Instability of Poppet Valve Circuit. *JSME International Journal, Series C: Dynamics, Control, Robotics, Design and Manufacturing, 38*(3), 357-366. doi.org/10.1299/jsmec1993.38.357.
28. Hayashi, S., Hayase, T. and Kurahashi, T. (1997). Chaos in a hydraulic control valve. *Journal of Fluids and Structures*, *11*(6). doi.org/10.1006/jfls.1997.0096

29. Hayashi, I. and Kaneko, S. (2014). Pressure pulsations in piping system excited by a centrifugal turbomachinery taking the damping characteristics into consideration. *Journal of Fluids and Structures, 45,* 216–234. doi.org/10.1016/j.jfluidstructs.2013.11.012.

30. Hos, C., Bazsó, C. and Champneys, A. (2014). Model reduction of a direct spring-loaded pressure relief valve with upstream pipe. *IMA Journal of Applied Mathematics, 80*(4), 1009–1024. doi.org/10.1093/imamat/hxu034.

31. IEA. (2021). *Global Energy Review 2021*. International Energy Agency.

32. Inada, F. and Hayama, S. (1990a). A study on leakage-flow-induced vibrations. Part 1: Fluid-dynamic forces and moments acting on the walls of a narrow tapered passage. *Journal of Fluids and Structures*, *4*(4), 395-412. doi.org/10.1016/0889-9746(90)90144-T

33. Inada, F. and Hayama, S. (1990b). A study on leakage-flow-induced vibrations. Part 2: Stability analysis and experiments for two-degree-of-freedom systems combining translational and rotational motions. *Journal of Fluids and Structures, 4*(4), 413-428. doi.org/10.1016/0889-9746(90)90151-T.

34. Jia, W., Yin, C., Hao, F., Li, G. and Fan, X. (2019). Dynamic characteristics and stability analysis of conical relief valve. *Mechanika*, 25(1), 25–31. doi: 10.5755/j01.mech.25.1.22881.

35. Karadžić, U., Bergant, A. and Vukoslavčević, P. (2010). Water hammer caused by closure of turbine safety spherical valves. *IOP Conference Series: Earth and Environmental Science*, *12,* 012096. doi.org/10.1088/1755-1315/12/1/012096.

36. Karney, B. W. (1990). Energy Relations in Transient Closed-Conduit Flow. *Journal of Hydraulic Engineering, 116*(10). doi.org/10.1061/(asce)0733-9429(1990)116:10(1180).

37. Kolesnikov, A. and Nikiforov, A. (2014). Influence of the penstock design on the operation of the inlet spherical valves. *IOP Conference Series: Earth and Environmental Science*, *22,* 012034. doi.org/10.1088/1755-1315/22/1/012034.

38. Kolkman, P. A. and Jongeling, T. H. G. (2007a). *Dynamic behaviour of hydraulic structures - Part A Structures in flowing fluid*. Delft Hydraulics.

39. Kolkman, P. A. and Jongeling, T. H. G. (2007b). *Dynamic behaviour of hydraulic structures - Part C Calculation methods and experimental investigations*. Delft Hydraulics.

40. Kube, S. E., Henderson, A. D. and Sargison, J. E. (2010). Modelling penstock pressure pulsations in hydro-electric power stations. *17th Australasian Fluid Mechanics Conference 2010*. Auckland.

41. Liu, J., Xie, H., Hu, L., Yang, H. and Fu, X. (2017). Flow force regulation of the main poppet in a large flow load control valve. *Proceedings of the Institution of Mechanical Engineers, Part A: Journal of Power and Energy,* 231(8). https://doi.org/10.1177/0957650917714370.

42. Ma, W., Ma, F. and Guo, R. (2019). Experimental research on the dynamic instability characteristic of a pressure relief valve. *Advances in Mechanical Engineering*, 11(3), 1-13. doi: 10.1177/1687814019833531.

43. Massey, B. and Ward-Smith, A.J. (2006). *Mechanics of Fluids (Eighth edition)*. Taylor & Francis Group.

44. Mateos, C., Pérez-Andújar, T., Andreu, M. and Cabrera, E. (1996). Self-excited hydraulic oscillations due to unstable valve behaviour. A case study. In *E. Cabrera et al. (eds.), Hydraulic Machinery and Cavitation (Vol II)*, 895-904. Kluwer Academic Publishers. doi.org/10.1007/978-94-010-9385-9_91.

45. Misra, A., Behdinan, K. and Cleghorn, W. L. (2002). Self-excited vibration of a control valve due to fluid-structure interaction. *Journal of Fluids and Structures*, 16(5), 649-665. doi.org/10.1006/jfls.2002.0441.

46. Moussou, P., Gibert, R. J., Brasseur, G., Teygeman, C., Ferrari, J. and Rit, J. F. (2010). Instability of pressure relief valves in water pipes. *Journal of Pressure Vessel Technology, Transactions of the ASME, 132*(4). doi.org/10.1115/1.4002164.

47. Naudascher, E. (1991). *Hydrodynamic Forces*. A.A.Balkema. doi.org/10.1201/9780203751534.

48. Naudascher, E. and Rockwell, D. (1994). *Flow induced vibrations: an engineering guide*. A.A.Balkema. doi.org/10.1201/9780203755747.

49. Nishihara, T., Akimoto, T. and Yamamoto, K. (2003). Self-induced pressure pulsation in penstock caused by movable-seat seal using tapped water from penstock. *Waterpower XIII, 2003*. Buffalo.

50. Okasha, A., Elnady, T. and Åbom, M. (2016). Analysis of pipeline networks using two-ports. *Applied Acoustics, 109*, 44–53. doi.org/10.1016/j.apacoust.2016.02.008.

51. Païdoussis, M. P. (2006). Real-life experiences with flow-induced vibration. *Journal of Fluids and Structures*, 22, 741–755. doi.org/10.1016/j.jfluidstructs.2006.04.002.

52. Palikhe, S., Zhou, J. and Bhattarai, K. P. (2019) Hydraulic oscillation and instability of a hydraulic system with two different pump-turbines in turbine operation, *Water (Switzerland)*, 11(4). doi: 10.3390/w11040692.

53. Parrondo, J., Antuña, J. and Prieto, J. I. (2005). Computation of the unstable behavior of a hydraulic circuit with a centrifugal pump coupled to an air pocket. *Proc. 2005 ASME Fluids Engineering Division Summer Meeting, FEDSM2005-77362*. 1471-1476. doi.org/10.1115/FEDSM2005-77362.

54. Parrondo, J., Antuña, J., González, J. and Fernández, J. (2002a). A study on the unstable coupling between pumps and hydraulic circuits with entrapped gas pockets. *Proc. 2002 ASME Fluids Engineering Division Summer Meeting, FEDSM2002-31317*. 229-234. doi.org/10.1115/FEDSM2002-31317.

55. Parrondo, J., González, J. and Fernández, J. (2002b). The effect of the operating point on the pressure fluctuations at the blade passage frequency in the volute of a centrifugal pump. *Journal of Fluids Engineering, Transactions of the ASME, 124*(3), 784–790. doi.org/10.1115/1.1493814.

56. Peng, J., Youn, C., Takeuchi, T. and Kagawa, T. (2017). Stabilization of pilot valve system using linear flow resistance. *Advances in Mechanical Engineering, 9*(7), 1-9. doi.org/10.1177/1687814017719421.

57. Rao, S.S. (2017). *Mechanical Vibrations, 6th Edition*. Pearson.

58. Riasi, A. and Tazraei, P. (2017). Numerical analysis of the hydraulic transient response in the presence of surge tanks and relief valves. *Renewable Energy, 107*. doi.org/10.1016/j.renene.2017.01.046.

59. Saltos del Navia (2014). *Sobrepresión del grupo nº 3*. Saltos del Navia C.B. Internal report.

60. Saltos del Navia (2021). *Salto de Salime*. Saltos del Navia C.B. Accesed 31 October 2021. https://www.saltosdelnavia.es/salto-de-salime.

61. Schröders, S. and Fidlin, A. (2021) Asymptotic analysis of self-excited and forced vibrations of a self-regulating pressure control valve, *Nonlinear Dynamics*, 103(3), pp. 2315–2327. doi: 10.1007/s11071-021-06241-5.

62. Scuro, N. L., Angelo, E., Angelo, G. and Andrade, D. A. (2018). A CFD analysis of the flow dynamics of a directly-operated safety relief valve. In *Nuclear Engineering and Design* (Vol. 328). doi.org/10.1016/j.nucengdes.2018.01.024.

63. Song, X., Cui, L., Cao, M., Cao, W., Park, Y. and Dempster, W. M. (2014). A CFD analysis of the dynamics of a direct-operated safety relief valve mounted on a pressure vessel. *Energy Conversion and Management, 81*. doi.org/10.1016/j.enconman.2014.02.021.

64. Smith, P. and Zappe, R. W. (2004). *Valve Selection Handbook*. (*Fifth Edition*). Gulf Professional Publishing.

65. Sun, X., Li, X., Zheng, Z. and Huang, D. (2015). Fluid-structure interaction analysis of a high-pressure regulating valve of a 600-MW ultra-supercritical steam turbine. *Proceedings of the Institution of Mechanical Engineers, Part A: Journal of Power and Energy, 229*(3). doi.org/10.1177/0957650914568475.

66. USSD Committee on Hydraulics of Dams (2017). *Improving Reliability of Commonly Used Hydraulic Valves*. United States Society on Dams.

67. Valentín, D., Presas, A., Egusquiza, E., Valero, C., Egusquiza, M. and Bossio, M. (2017). Power swing generated in Francis turbines by part load and overload instabilities. *Energies*, *10*(12). doi.org/10.3390/en10122124

68. Vortex Hydra Dams (2021). *Spherical Valves*. Vortex Hydra Innovation and Engineering. Accessed 29 October 2021. https://www.vortexhydradams.com/hydraulic-works/spherical-valves/.

69. Wang, J., Geng, L., Ding, L., Zhu, H. and Yurchenko, D. (2020). The state-of-the-art review on energy harvesting from flow-induced vibrations. In *Applied Energy*, 267, 114902. doi.org/10.1016/j.apenergy.2020.114902.

70. Wang, J., Weaver, D. S. and Tullis, S. (2012). Simplified fluid-structure model for duckbill valve flow. *Journal of Pressure Vessel Technology, Transactions of the ASME, 134*(4). doi.org/10.1115/1.4005941.

71. Weaver, D. S., Adubi, F. A. and Kouwen, N. (1978). Flow induced vibrations of a hydraulic valve and their elimination. *Journal of Fluids Engineering, Transactions of the ASME, 100*(2). doi.org/10.1115/1.3448639.

72. Weaver, D. S. and Fitzpatrick, J. A. (1988). A review of cross-flow induced vibrations in heat exchanger tube arrays. *Journal of Fluids and Structures*, *2*(1), 73-93. doi.org/10.1016/S0889-9746(88)90137-5.

73. Weaver, D. S. and Ziada, S. (1980). A theoretical model for self-excited vibrations in hydraulic gates, valves and seals. *Journal of Pressure Vessel Technology, Transactions of the ASME, 102*(2), 146-151. doi.org/10.1115/1.3263313

74. Wylie, E. B. and Streeter, V. L. (1965). Resonance in Bersimis no. 2 piping system. *Journal of Fluids Engineering, Transactions of the ASME, 87*(4). doi.org/10.1115/1.3650845.

75. Wylie, E. B., Streeter, V. L. and Suo, L. (1993). *Fluid Transients in Systems.* Prentice Hall.

76. Zhang, F., Fu, J., Liu, D. and Wang, S. (2019). Spherical Valve Stability during Hydrodynamic Closure Process. *IOP Conference Series: Earth and Environmental Science, 304*(2). doi.org/10.1088/1755-1315/304/2/022003.

77. Zhao, W., Presas, A., Egusquiza, M., Valentín, D., Egusquiza, E. and Valero, C. (2021). Increasing the operating range and energy production in Francis turbines by an early detection of the overload instability. *Measurement 181*, 109580. doi.org/10.1016/j.measurement.2021.109580

78. Zhou, J. X., Karney, B. W., Hu, M. and Xu, J. C. (2011). Analytical study on possible self-excited oscillation in S-shaped regions of pump-turbines. *Proc. of the Inst. of Mechanical Eng., Part A: Journal of Power and Energy, 225*(8), 1132-1142. doi.org/10.1177/0957650911419442.

79. Cimbala, J.M. & Cengel, Y.A. (2009). *Fluid Mechanics Fundamentals and Applications*. 2nd edition. McGraw-Hill. New York.

80. Kolkman, P.A. (1964). *Vibrations des vanes en position partiellement montees du barrage de Hagestein*. Soc. Hydrotechnique de France. VIII ieme Journees de l'Hydraulique, Lille.

81. A. Nourbakhsh, A. Jaumotte, C. Hirsch, H. Parizi, (2007), Turbopumps and pumping systems, Springer Berlin Heidelberg, doi.org/10.1007/978-3-540-68214-1

APPENDIX A: 1ST MODEL ANALYSIS:

A.1 Steady state equations

Section 1-2: $H_{eo_1} - H_{eo_2} = Q_{oa}^2 K_a$ Eq.(A6)

Section 2-3: $H_{eo_2} - H_{eo_3} = 0$ Eq.(A7)

Section 2-4: $H_{eo_2} - H_{eo_4} = Q_{ob}^2 K_b$ Eq.(A8)

Section 2 continuity equation: $Q_{oa} = Q_{ob} + Q_{od}$ Eq.(A9)

Seal clearance gap flow rate: $Q_{og} = Q_{ob} = Q_{oc}$ Eq.(A10)

Annular seal equation of motion: $k_{sg} y_{og} = P_{o3} A_{os} - P_{o4} A_{ss}$ Eq.(A11)

Section 4-5: $H_{eo4} - H_{eo5} = \dfrac{Q_{oc}^2 \left(\dfrac{1}{A_{og}} - \dfrac{1}{A_c} \right)^2}{2g}$ Eq.(A12)

Section 5-6: $H_{eo_5} - H_{eo6} = Q_{oc}^2 K_c$ Eq.(A13)

Gap cross-section area: $A_{og} = L_o y_{og}$ Eq.(A14)

Input reservoir energy head: $H_{eo_1} = variable$ Eq.(A15)

Discharge head: $H_{eo6} = 0$ Eq.(A16)

Pressure at section 3: $P_{o3} = \rho g H_{eo3}$ Eq.(A17)

Pressure at section 4: $P_{o4} = \rho g H_{eo5}$ Eq.(A18)

Pilot pipeline flow rate: $Q_{od} = 0$ Eq.(A19)

A.2 Time dependent equations

Section 1-2: $h_{e1} - h_{e2} = \frac{L_a}{g A_a} \frac{d q_a}{d t} + 2 Q_{oa} q_a K_a$ Eq.(A6*)

Section 2-3: $h_{e2} - h_{e3} = \frac{L_d}{g A_d} \frac{d q_d}{d t} + q_d K_d$ Eq.(A7*)

Section 2-4: $h_{e2} - h_{e4} = \frac{L_{b1}}{g A_{b1}} \frac{d q_b}{d t} + 2 Q_{ob} q_b K_b$ Eq.(A8*)

Section 2 continuity equation: $q_a = q_b + A_{os} \frac{d y}{d t}$ Eq.(A9*)

Gap flow rate : $q_g = q_b + A_{ss} \frac{d y}{d t} = q_c$ Eq.(A10*)

Annular seal equation of motion: $m_{sg} \ddot{y} + c_{sg} \dot{y} + k_{sg} y = p_3 A_{os} - p_4 A_{ss}$ Eq.(A11*)

Section 4-5:

$$h_{e4}-h_{e5}=\frac{Q_{oc}\left(\frac{1}{A_{og}}-\frac{1}{A_c}\right)^2}{g}q_c+\frac{Q_{oc}^2\left(\frac{1}{A_c\,A_{og}^2}-\frac{1}{A_{og}^3}\right)}{g}A_g \qquad \text{Eq.(A12*)}$$

Section 5-6:

$$h_{e5}-h_{e6}=\frac{L_c}{g\,A_c}\frac{d\,q_c}{d\,t}+2Q_{oc}q_cK_c \qquad \text{Eq.(A13*)}$$

Gap cross-section area: $A_g=-L_o\,y$ Eq.(A14*)

Input reservoir energy head: $h_{e1}=0$ Eq.(A15*)

Discharge head: $h_{e6}=0$ Eq.(A16*)

Pressure at section 3: $P_3=\rho\,g\;e_3$ Eq.(A17*)

Pressure at section 4: $P_4=\rho\,g\,e_5$ Eq.(A18*)

Pilot pipeline flow rate: $q_d=A_{os}\dfrac{dy}{d\,t}$ Eq.(A19*)

A.3 Dimensionless added water mass, stiffness and damping coefficients

By using Eqs.(A9*, A10*, A13* & A16*) into Eq.(A12*), neglecting discharge line losses, and working on the bases of having a sinusoidal flow and energy head oscillations (i.e. $q_j=\overline{q_j}\,e^{iwt}$ and $h_{e\,j}=\overline{h_{e\,j}}\,e^{iwt}$ where $\overline{q_j}$ and $\overline{h_{e\,j}}$ are oscillation flow rate and energy head amplitudes), then the time dependent head at section 4 as in figures (3.3 and 3.4) can be represented as:

$$h_{e4} = \left(q_a + \dot{y}\left(A_{ss} - A_{os}\right)\right)\left(i\,\omega\, I_c + \frac{2\,H_{eL45}}{Q_{og}}\right) + 2\,KE_g\left(1 - \frac{A_{og}}{A_c}\right)\frac{y}{y_{og}} \qquad \text{Eq.(A20)}$$

where: $H_{eL45} = \dfrac{Q_{og}^2\left(\dfrac{1}{A_{og}} - \dfrac{1}{A_c}\right)^2}{2g}$, $KE_g = \dfrac{Q_{og}^2}{2g\,A_{og}^2}$, $I_c = \dfrac{L_c}{g\,A_c}$

By using Eqs.(A6*, A8* & A9*), neglecting the pipeline friction loss terms, and working on the bases of having a sinusoidal flow and energy head oscillations, the time dependent penstock flow rate can be represented such as:

$$q_a = -\frac{h_{e2}}{i\,\omega\, I_a} = i\,\frac{\left(h_{e4} + i\, I_b\,\omega\, q_b\right)}{I_a\, w} = i\,\frac{h_{e4}}{\omega\, I_a} - \frac{I_b}{I_a}\left(q_a - A_{os}\,\dot{y}\right)$$

$$q_a = \frac{1}{I_a + I_b}\left(i\,\frac{h_{e4}}{\omega} + I_b\, A_{os}\,\dot{y}\right) \qquad \text{Eq.(A21)}$$

By substituting Eq.(A21) into Eq.(A20):

$$h_{e4} = \left(\frac{1}{I_a + I_b}\left(i\,\frac{h_{e4}}{\omega} + I_b\, A_{os}\,\dot{y}\right) + \dot{y}\left(A_{ss} - A_{os}\right)\right)\left(i\,\omega\, I_c + \frac{2\,H_{eL45}}{Q_{og}}\right) + 2\,KE_g\left(1 - \frac{A_{og}}{A_c}\right)\frac{y}{y_{og}}$$

$$h_{e4}\left(\frac{I_a + I_b + I_c - i\,2\,\dfrac{H_{eL45}}{\omega\, Q_{og}}}{I_a + I_b}\right) = \left(\dot{y}\left(\frac{I_b\, A_{os}}{I_a + I_b} + A_{ss} - A_{os}\right)\left(i\,\omega\, I_c + 2\,\frac{H_{eL45}}{Q_{og}}\right) + 2\,KE_g\left(1 - \frac{A_{og}}{A_c}\right)\frac{y}{y_{og}}\right)$$

$$h_{e4}=\frac{1}{I_m-i\dfrac{H_{eL45}}{\omega Q_{og}}}\left(\begin{array}{l}\dot{y}\left(A_{ss}I_b+I_a\left(A_{ss}-A_{os}\right)\right)\left(i\omega I_c+\dfrac{2H_{eL45}}{Q_{og}}\right)\\ +2KE_g\left(1-\dfrac{A_{og}}{A_c}\right)\dfrac{y}{y_{og}}\left(I_a+I_b\right)\end{array}\right) \qquad \text{Eq.(A22)}$$

By substituting Eqs.(A6* & A15*) into Eq.(A8*) the time dependent head at section 2 as in figures (3.3 and 3.4) can be presented as follows:

$$\begin{aligned}h_{e2}&=h_{e4}+i\omega I_b\ \left(q_a-A_{os}\dot{y}\right)\\ &=h_{e4}+i\omega I_b\ \left(-\frac{h_{e2}}{i\omega I_a}-A_{os}\dot{y}\right)\\ &=h_{e4}+I_b\left(-\frac{h_{e2}}{I_a}-i\omega A_{os}\dot{y}\right)\end{aligned}$$

$$h_{e2}=\frac{I_a}{I_a+I_b}h_{e4}-\frac{I_aI_b}{I_a+I_b}A_{os}\ddot{y} \qquad \text{Eq.(A23)}$$

By substituting Eq.(A22) into Eq.(A23):

$$h_{e2}=\frac{I_a}{I_m-i\dfrac{H_{eL45}}{\omega Q_{og}}}\left(\dot{y}\left(\frac{A_{ss}}{\dfrac{I_a}{I_b}+1}+\frac{A_{ss}-A_{os}}{\dfrac{I_b}{I_a}+1}\right)\left(i\omega I_c+\frac{2H_{eL45}}{Q_{og}}\right)+2KE_g\left(1-\frac{A_{og}}{A_c}\right)\frac{y}{y_{og}}\right)-\frac{A_{os}}{\dfrac{1}{I_a}+\dfrac{1}{I_b}}\ddot{y}$$

$$=\frac{I_a}{I_m-i\dfrac{H_{eL45}}{\omega Q_{og}}}\left(\dot{y}\left(\frac{A_{ss}(I_a+I_b)}{I_a+I_b}-\frac{A_{os}}{\dfrac{I_b}{I_a}+1}\right)\left(i\omega I_c+\frac{2H_{eL45}}{Q_{og}}\right)+2KE_g\left(1-\frac{A_{og}}{A_c}\right)\frac{y}{y_{og}}\right)-\frac{A_{os}}{\dfrac{1}{I_a}+\dfrac{1}{I_b}}\ddot{y}$$

$$h_{e2} = \frac{I_a}{I_m - i\dfrac{2H_{eL45}}{\omega Q_{og}}}\left(\begin{gathered} \dot{y}\left(A_{ss} - \frac{A_{os}}{1+\dfrac{I_b}{I_a}}\right)\left(i\omega I_c + \frac{2H_{eL45}}{Q_{og}}\right) \\ + 2KE_g\left(1 - \frac{A_{og}}{A_c}\right)\frac{y}{y_{og}} \end{gathered} \right) - \frac{A_{os}}{\dfrac{1}{I_a}+\dfrac{1}{I_b}}\ddot{y} \qquad \text{Eq.(A24)}$$

By substituting Eqs.(A7*, A17*, A18* & A19*) into Eq.(A11*) and neglecting the higher order nonlinear terms, then the seal equation of motion can be presented as follows:

$$m_{sg}\ddot{y} + c_{sg}\dot{y} + k_{sg}y = \rho g\left(A_{os}\, h_{e2} - I_d\, A_{os}^2\,\ddot{y} - K_d\, A_{os}^2\,\dot{y} - A_{ss}\, h_{e5}\right) \qquad \text{Eq.(A25)}$$

By substituting Eq.(A23) into Eq.(A25):

$$m_{sg}\ddot{y} + c_{sg}\dot{y} + k_{sg}y = \rho g\left(A_{os}\left(\frac{I_a}{I_a+I_b}h_{e4} - \frac{I_a I_b}{I_a+I_b}A_{os}\ddot{y}\right) - I_d\, A_{os}^2\,\ddot{y} - K_d\, A_{os}^2\,\dot{y} - A_{ss}\, h_{e5}\right)$$

$$m_{sg}\ddot{y} + c_{sg}\dot{y} + k_{sg}y = \rho g\left(\frac{A_{os}}{1+\dfrac{I_b}{I_a}}h_{e4} - \left(\frac{1}{\dfrac{1}{I_a}+\dfrac{1}{I_b}} + I_d\right)A_{os}^2\,\ddot{y} - K_d\, A_{os}^2\,\dot{y} - A_{ss}\, h_{e5}\right) \qquad \text{Eq.(A26)}$$

By substituting Eqs.(A9*, A10* & A21) into Eq.(A13*), the time dependent energy head at section 5 as in figures (3.3 and 3.4) can be estimated as:

$$\begin{aligned} h_{e5} &= i\omega I_c\left(q_b + A_{ss}\dot{y}\right) = i\omega I_c\left(q_a + \left(A_{ss} - A_{os}\right)\dot{y}\right) \\ &= i\omega I_c\left(\frac{1}{I_a+I_b}\left(i\frac{h_{e4}}{\omega} + I_b A_{os}\dot{y}\right) + \left(A_{ss} - A_{os}\right)\dot{y}\right) \\ &= i\omega I_c\left(\frac{i\, h_{e4}}{\omega\left(I_a+I_b\right)} + \frac{I_b A_{os}}{I_a+I_b}\dot{y} + \left(A_{ss} - A_{os}\right)\dot{y}\right) \end{aligned}$$

$$h_{e5} = -h_{e4}\frac{I_c}{I_a + I_b} + \ddot{y} I_c \left(\frac{A_{os}}{1 + \frac{I_a}{I_b}} + A_{ss} - A_{os}\right) \qquad \text{Eq.(A27)}$$

By substituting Eq.(A27) into Eq.(A26), the seal equation of motion will be as:

$$m_{sg}\ddot{y} + c_{sg}\dot{y} + k_{sg}y$$

$$= \rho g \left(\frac{A_{os}}{1 + \frac{I_b}{I_a}} h_{e4} - \left(\frac{1}{\frac{1}{I_a} + \frac{1}{I_b}} + I_d \right) A_{os}^2 \ddot{y} - K_d A_{os}^2 \dot{y} + h_{e4}\frac{A_{ss} I_c}{I_a + I_b} - \ddot{y} I_c A_{ss} \left(\frac{A_{os}}{1 + \frac{I_a}{I_b}} + A_{ss} - A_{os}\right) \right)$$

$$= \rho g \left(\frac{A_{os} I_a + A_{ss} I_c}{I_a + I_b} h_{e4} - \left(\left(\frac{1}{\frac{1}{I_a} + \frac{1}{I_b}} + I_d\right) + I_c \frac{A_{ss}}{A_{os}} \left(\frac{1}{1 + \frac{I_a}{I_b}} + \frac{A_{ss}}{A_{os}} - 1\right) \right) A_{os}^2 \ddot{y} - K_d A_{os}^2 \dot{y} \right)$$

$$m_{sg}\ddot{y} + c_{sg}\dot{y} + k_{sg}y =$$

$$\rho g \left(\begin{array}{l} \frac{I_a A_{os} + I_c A_{ss}}{I_a + I_b} h_{e4} - \left(\left(\frac{1}{\frac{1}{I_a} + \frac{1}{I_b}} + I_d \right) + I_c \frac{A_{ss}}{A_{os}} \left(\frac{A_{ss}}{A_{os}} - \frac{1}{1 + \frac{I_b}{I_a}} \right) \right) A_{os}^2 \ddot{y} \\ - K_d A_{os}^2 \dot{y} \end{array} \right) \qquad \text{Eq.(A28)}$$

By substituting Eq.(A22) into Eq.(A28):

$$m_{sg}\ddot{y} + c_{sg}\dot{y} + k_{sg}y = \rho g\, A_{os}^2 \left(\begin{array}{l} \frac{I_a + I_c \frac{A_{ss}}{A_{os}}}{I_m - i2\frac{H_{eL45}}{\omega Q_{og}}} \left(\begin{array}{l} \dot{y} \left(\frac{I_b}{I_a + I_b} \frac{A_{ss}}{A_{os}} + \frac{I_a}{I_a + I_b} \left(\frac{A_{ss}}{A_{os}} - 1 \right) \right) \left(i\omega I_c + 2\frac{H_{eL45}}{Q_{og}} \right) \\ + 2KE_g \left(1 - \frac{A_{og}}{A_c} \right) \frac{y}{y_{og} A_{os}} \end{array} \right) \\ - \left(\left(\frac{1}{\frac{1}{I_a} + \frac{1}{I_b}} + I_d \right) + I_c \frac{A_{ss}}{A_{os}} \left(\frac{A_{ss}}{A_{os}} - \frac{1}{1 + \frac{I_b}{I_a}} \right) \right) \ddot{y} - K_d \dot{y} \end{array} \right)$$

$$= \rho g\, A_{os}^{2} \begin{pmatrix} \dfrac{I_a + I_c \gamma}{I_m - i2\dfrac{H_{eL45}}{\omega Q_{og}}} \left(\dot{y} \left(\gamma - \dfrac{1}{1+\dfrac{I_b}{I_a}} \right) \left(i\,\omega I_c + 2\dfrac{H_{eL45}}{Q_{og}} \right) + 2KE_g \left(1 - \dfrac{A_{og}}{A_c} \right) \dfrac{y}{y_{og} A_{os}} \right) \\ - \left(\left(\dfrac{1}{\dfrac{1}{I_a} + \dfrac{1}{I_b}} + I_d \right) + I_c \gamma \left(\gamma - \dfrac{1}{1+\dfrac{I_b}{I_a}} \right) \right) \ddot{y} - K_d\, \dot{y} \end{pmatrix}$$

$$= \rho g\, A_{os}^{2} I_m \begin{pmatrix} \dfrac{I_a^* + I_c^* \Pi_4}{1 - i2\dfrac{1}{\Pi_1 \omega^*}} \left(\dot{y} \left(\Pi_4 - \dfrac{I_a^*}{I_a^* + I_b^*} \right) \left(i\,\omega I_c^* + 2\omega \dfrac{1}{\Pi_1 \omega^*} \right) + 2\,KE_g \left(1 - \dfrac{A_{og}}{A_c} \right) \dfrac{y}{y_{og} A_{os} I_m} \right) \\ - \left(\left(\dfrac{1}{\dfrac{1}{I_a^*} + \dfrac{1}{I_b^*}} + I_d^* \right) + I_c^* \Pi_4 \left(\Pi_4 - \dfrac{I_a^*}{I_a^* + I_b^*} \right) \right) \ddot{y} - \dfrac{K_d}{I_m} \dot{y} \end{pmatrix}$$

$$= \rho g\, A_{os}^{2} I_m \begin{pmatrix} \dfrac{I_a^* + I_c^* \Pi_4}{1 - i2\dfrac{1}{\Pi_1 \omega^*}} \left(\dot{y} \left(\Pi_4 - \dfrac{I_a^*}{I_a^* + I_b^*} \right) \left(i\,\omega I_c^* + 2\omega \dfrac{1}{\Pi_1 \omega^*} \right) + 2\dfrac{1}{\Pi_1 \omega^*} \left(1 - \dfrac{A_{og}}{A_c} \right) \Pi_4 \dfrac{\Pi_2}{\omega^*} \omega^2 y \right) \\ - \left(\left(\dfrac{1}{\dfrac{1}{I_a^*} + \dfrac{1}{I_b^*}} + I_d^* \right) + I_c^* \Pi_4 \left(\Pi_4 - \dfrac{I_a^*}{I_a^* + I_b^*} \right) \right) \ddot{y} - \dfrac{1}{\Pi_3 \omega^*} \omega \dot{y} \end{pmatrix}$$

$$m_{sg} \ddot{y} + c_{sg} \dot{y} + k_{sg} y =$$

$$\rho g\, A_{os}^{2} I_m \begin{pmatrix} \left(\dfrac{\Pi_d}{1 - i\,2\dfrac{1}{\Pi_1 \omega^*}} \right) \left(\dot{y} \left(-\beta + \dfrac{I_c^*}{1 - I_c^*} \right) \left(i\,\omega I_c^* + 2\,\omega \dfrac{1}{\Pi_1 \omega^*} \right) + \dfrac{2 \Pi_4 \Pi_2 A^* \omega^2}{\Pi_1 \omega^{*2}} y \right) \\ - \left(I_p^* + I_c^* \Pi_4 \left(-\beta + \dfrac{I_c^*}{1 - I_c^*} \right) \right) \ddot{y} - \dfrac{1}{\Pi_3 \omega^*} \omega\, \dot{y} \end{pmatrix} \qquad \text{Eq.(A29)}$$

Where:

$$I_j^* = \frac{I_j}{I_m} \;,\; \Pi_1 = \frac{I_m\,\omega_{ref}\,Q_{og}}{H_{eL45}} = \frac{I_m\,\omega_{ref}\,Q_{og}}{KE_g} = \frac{I_m\,\omega_{ref}\,Q_{og}}{H_{e1}} ,\; \Pi_2 = \frac{V_{og}}{L_g\,\omega_{ref}} \;,\; \Pi_3 = \frac{I_m\,\omega_{ref}\,Q_{og}}{K_c\,Q_{og}} ,$$

$$\Pi_4 = \frac{A_{ss}}{A_{os}}, A^* = \left(1 - \frac{A_{og}}{A_c}\right) \;,\; I_p^* = \frac{1}{\frac{1}{I_a^*} + \frac{1}{I_b^*}} + I_d^* \;,\; \Pi_d = I_a^* + I_c^*\,\Pi_4 = 1 - I_b^* - I_c^*\left(1 - \Pi_4\right),$$

$$\Pi_4 - \frac{I_a^*}{I_b^* - I_a^*} = \Pi_4 - \frac{1 - I_b^* - I_c^*}{I_b^* + 1 - I_b^* - I_c^*} = \Pi_4 - \frac{1 - I_b^*}{1 - I_c^*} + \frac{I_c^*}{1 - I_c^*} = -\beta + \frac{I_c^*}{1 - I_c^*} \;,\; \omega^* = \frac{\omega}{\omega_{ref}}$$

Since I_c^* is very small in comparison to $1 - I_c^*$, the term $\frac{I_c^*}{1 - I_c^*}$ in Eq.(A36) can be neglected. Also, by multiplying the term $1 - i\,2\frac{1}{\Pi_1\,\omega^*}$ by its conjugate, the seal equation of motion can be presented such as:

$$m_{sg}\,\ddot{y} + c_{sg}\,\dot{y} + k_{sg}\,y =$$
$$\rho g\, A_{os}^2\, I_m \left(\begin{array}{l} \left(\dfrac{\Pi_d + i\,2\,\Pi_d \dfrac{1}{\Pi_1}}{1 + 4\left(\dfrac{1}{\Pi_1 \omega^*}\right)^2} \right) \left(\dot{y}(-\beta)\left(i\,\omega\, I_c^* + 2\,\omega \dfrac{1}{\Pi_1\,\omega^*} \right) + \dfrac{2\,\Pi_4\,\Pi_2\,A^*\,\omega^2}{\Pi_1\,\omega^{*2}}\,y \right) \\ -\left(I_p^* + I_c^*\,\Pi_4\left(-\beta\right)\right)\ddot{y} - \dfrac{1}{\Pi_3\,\omega^*}\,\omega\,\dot{y} \end{array} \right) \qquad \text{Eq.(A30)}$$

Working on the hypothesis of having variables of sinusoidal fluctuation and converting the vibration components $\ddot{y}, \dot{y}, y$ into dimensionless form $\ddot{y}^*, \dot{y}^*, y^*$, then the dimensionless seal equation of motion can be presented as follows:

$$
\begin{aligned}
&\frac{m_{sg}\, y_{og}\, \omega_{ref}^{2}}{\rho g\, A_{os}^{2} I_m\, y_{og}\, \omega_{ref}^{2}} \ddot{y}^{*} + \frac{c_{sg}\, y_{og}\, \omega_{ref}}{\rho g\, A_{os}^{2} I_m\, y_{og}\, \omega_{ref}^{2}} \dot{y}^{*} + \frac{k_{sg}\, y_{og}}{\rho g\, A_{os}^{2} I_m\, y_{og}\, \omega_{ref}^{2}} y^{*} \\
&= \ddot{y}^{*}\left(-\frac{\Pi_d}{1+4\left(\frac{1}{\Pi_1 \omega^{*}}\right)^{2}} \beta I_c^{*} - I_p^{*} + I_c^{*} \Pi_4 \beta \right) \\
&+ \dot{y}^{*} \frac{\frac{\Pi_d}{1+4\left(\frac{1}{\Pi_1 \omega^{*}}\right)^{2}} \left(2\frac{1}{\Pi_1 \omega^{*}} \omega \beta \left(I_c^{*} - 1\right) + \frac{4 \Pi_4 \Pi_2 \omega A^{*}}{\Pi_1^{2} \omega^{*3}} \right) - \frac{1}{\Pi_3 \omega^{*}} \omega}{\omega_{ref}} \\
&+ y^{*} \frac{\frac{\Pi_d}{1+4\left(\frac{1}{\Pi_1 \omega^{*}}\right)^{2}} \left(\frac{2 \Pi_4 \Pi_2 \omega^{2} A^{*}}{\Pi_1 \omega^{*2}} + 4 \omega^{2} \beta \left(\frac{1}{\Pi_1 \omega^{*2}}\right)^{2} \right)}{\omega_{ref}^{2}}
\end{aligned}
\tag*{Eq.(A31)}
$$

By rearrangement Eq.(A31):

$$
\begin{aligned}
&\ddot{y}^{*}\left(\frac{m_{sg}}{\rho g\, A_{os}^{2} I_m} + \underbrace{\frac{\Pi_d}{1+4\left(\frac{1}{\Pi_1 \omega^{*}}\right)^{2}} \beta I_c^{*} + I_p^{*} - I_c^{*} \Pi_4 \beta}_{m_w^{*}} \right) \\
&+ \dot{y}^{*}\left(\frac{c_{sg}}{\rho g\, A_{os}^{2} I_m\, \omega_{ref}} + \underbrace{\frac{\Pi_d}{1+4\left(\frac{1}{\Pi_1 \omega^{*}}\right)^{2}} \left(2\frac{1}{\Pi_1} \beta \left(1 - I_c^{*}\right) - \frac{4 \Pi_4 \Pi_2 A^{*}}{\Pi_1^{2} \omega^{*2}} \right) + \frac{1}{\Pi_3}}_{c_w^{*}} \right) \\
&+ y^{*}\left(\frac{k_{sg}}{\rho g\, A_{os}^{2} I_m\, \omega_{ref}^{2}} + \underbrace{\frac{\Pi_d}{1+4\left(\frac{1}{\Pi_1 \omega^{*}}\right)^{2}} \left(-\frac{2 \Pi_4 \Pi_2 A^{*}}{\Pi_1} - 4\beta \left(\frac{1}{\Pi_1}\right)^{2} \right)}_{k_w^{*}} \right) = 0
\end{aligned}
\tag*{Eq.(A32)}
$$

Eq.(A32) represents the equation of motion of a free vibration damped system. In which, m_w^{*}, c_w^{*} and k_w^{*} represent the dimensionless added water mass, damping and stiffness coefficients as well as the dimensionless hydrodynamic force acting on the seal.

$$m_W^* = \frac{\Pi_d}{1+4\left(\frac{1}{\Pi_1 \omega^*}\right)^2} \beta I_c^* + I_p^* - I_c^* \Pi_4 \beta$$

$$c_W^* = \frac{\Pi_d}{1+4\left(\frac{1}{\Pi_1 \omega^*}\right)^2} \left(2\frac{1}{\Pi_1} \beta \left(1 - I_c^*\right) - \frac{4\Pi_4 \Pi_2 A^*}{\Pi_1^2 \omega^{*2}} \right) + \frac{1}{\Pi_3}$$

$$k_W^* = \frac{\Pi_d}{1+4\left(\frac{1}{\Pi_1 \omega^*}\right)^2} \left(-\frac{2\Pi_4 \Pi_2 A^*}{\Pi_1} - 4\beta \left(\frac{1}{\Pi_1}\right)^2 \right)$$

where: $\omega^* = \frac{\omega}{\omega_{ref}}$

APPENDIX B: 2ND MODEL ANALYSIS:

B.1 Dimensionless analysis

The aim of the dimensionless analysis is to gain more knowledge on the main parameters affecting the phenomena. So, the following sections will present the dimensionless analysis carried out on the 2nd model system governing equations of section 3.4.2.

Pipeline field transfer matrix

By converting each variable of the continuity equation Eq.(24) and the momentum equation Eq.(25) into dimensionless form as:

$$h_j^* = \frac{h_j}{H_1},\ q_j^* = \frac{q_j}{Q_{og}},\ x^* = \frac{x}{L_j},\ t^* = t\omega$$

Where h_j^*, q_j^*, x^* and t^* are the dimensionless time dependent head, time dependent flow rate, distance along pipeline and time. Then the dimensionless continuity and momentum equation can be estimated as follows:

Continuity equation:

$$\frac{Q_{og}}{L_j}\frac{\partial q_j^*}{\partial x^*} + \frac{g A_j}{a_j^2} H_1 \omega \frac{\partial h_j^*}{\partial t^*} = 0$$

By multiplying both sides by $\frac{L_j}{Q_{og}}$ and assuming $H_1 = \frac{Q_{og}^2}{2 g A_{og}^2}$

$$\frac{\partial q_j^*}{\partial x^*} + \frac{g A_j Q_{og}^2 \omega L_j}{a_j^2 Q_{og} 2g A_{og}^2}\frac{\partial h_j^*}{\partial t^*} = 0$$

$$\frac{\partial q_j^*}{\partial x^*} + \frac{V_{og}^2}{2a_j^2}\frac{A_j}{A_{og}}\frac{\omega L_j}{V_{og}}\frac{\partial h_j^*}{\partial t^*} = 0$$

$$\frac{\partial q_j^*}{\partial x^*} + \frac{\Pi_5^2}{2\Pi_2}\frac{A_j}{A_{og}}\frac{\partial h_j^*}{\partial t^*} = 0 \qquad \text{Eq.(1.B)}$$

Where Π_5 resembles gap flow Mach number as $\Pi_5 = \frac{V_{og}}{a_j}$, while Π_{2j} represent pipeline j reduced velocity as $\Pi_2 = \frac{V_{og}}{\omega L_j}$.

Momentum equation:

$$\frac{H_1}{L_j}\frac{\partial h_j^*}{\partial x^*} + \frac{Q_{og}\,\omega}{g\,A_j}\frac{\partial q_j^*}{\partial t^*} + R_j Q_{og}\, q_j^* = 0$$

By multiplying both sides by $\frac{L_j}{H_1}$

$$\frac{\partial h_j^*}{\partial x^*} + \frac{Q_{og}\,\omega L_j}{g\,A_j H_1}\frac{\partial q_j^*}{\partial t^*} + R_j Q_{og}\, q_j^* \frac{L_j}{H_1} = 0$$

$$\frac{\partial h_j^*}{\partial x^*} + \frac{L_j\,\omega Q_{og}}{g\,A_j H_1}\frac{\partial q_j^*}{\partial t^*} + \frac{H_{Lj}}{H_1} q_j^* = 0$$

$$\frac{\partial h_j^*}{\partial x^*} + \frac{L_j\,\omega Q_{og}}{g\,A_j H_1}\frac{\partial q_j^*}{\partial t^*} + \frac{H_{Lj}}{H_1} q_j^* = 0$$

$$\frac{\partial h_j^*}{\partial x^*} + \Pi_{1j}\frac{\partial q_j^*}{\partial t^*} + \Pi_{3j}\, q_j^* = 0 \qquad \text{Eq.(2.B)}$$

Π_{1j} represents pipeline j flow inertia ratio to input reservoir energy level as: $\Pi_{1j} = \dfrac{L_j \omega Q_{og}}{g A_j H_1}$, while Π_{3j} represents pipeline j steady state losses H_{Lj} ratio to input reservoir energy level as $\Pi_{3j} = \dfrac{H_{Lj}}{H_1}$.

By replacing iω in equations Eq.(1.B) and Eq.(2.B) by the complex frequency iω+σ, and applying the same steps as applied in the field transfer matrix section 3.4.1; the dimensionless field transfer matrix of a pipeline j for a free damped oscillations can be computed as follows:

$$Z^{*L}_{j+1} = F^*_j \, Z^{*R}_j \qquad \text{Eq.(3.B)}$$

$$\begin{bmatrix} q^* \\ h^* \end{bmatrix}^L_{j+1} = \underbrace{\begin{bmatrix} \cosh(\mu^*_j) & -\sinh(\mu^*_j)\dfrac{1}{Z^*_{cj}} \\ -\sinh(\mu^*_j)\, Z^*_{cj} & \cosh(\mu^*_j) \end{bmatrix}}_{F^*_j} \begin{bmatrix} q^* \\ h^* \end{bmatrix}^R_j$$

Where:

$$\mu^*_j = \sqrt{\frac{\Pi_{1j}\,\Pi^2_{5j}\,(i\omega^* + \sigma^*)^2 A^*_j}{2\,\Pi_{2j}} + \frac{\Pi_{3j}\,\Pi^2_{5j}\,A^*_j\,(i\omega^* + \sigma^*)}{2\,\Pi_{2j}}} \quad , \quad Z^*_j = \frac{2\,\mu^*_j\,\Pi_{2j}}{\Pi^2_{5j}\,(i\omega^* + \sigma^*)\,A^*_j} \quad ,$$

$$\Pi_{1j} = \frac{L_j\,\omega_{ref}\,Q_{og}}{g\,A_j\,H_1},\ \Pi_{2j} = \frac{V_{og}}{\omega_{ref}\,L_j}\ ,\ \Pi_{3j} = \frac{H_{Lj}}{H_1},\ \Pi_{5j} = \frac{V_{og}}{a_j}\ , and\ A^*_j = \frac{A_j}{A_{og}}$$

Branch junction point transfer matrix

By applying Eq.(3.B) to the pilot pipeline, converting equations Eq.(48) and Eq.(49) into dimensionless form, and applying the same steps as in the branch junction point transfer matrix section, then the dimensionless branch junction with an oscillating dead point transfer matrix for a free damped oscillations can be computed as follows:

$$\begin{bmatrix} q^* \\ h^* \\ 1 \end{bmatrix}_b^R = \underbrace{\begin{bmatrix} 1 & \dfrac{F^*{}_{j+2_{12}}}{F^*{}_{j+2_{11}}} & -\dfrac{q^*_{os}}{F^*{}_{j+2_{11}}} \\ 0 & 1 & 0 \\ 0 & 0 & 1 \end{bmatrix}}_{P_b^*} \begin{bmatrix} q^* \\ h^* \\ 1 \end{bmatrix}_b^L \qquad \text{Eq.(4.B)}$$

Where for the case under consideration q^*_{os} represents the dimensionless flow rate developed by the seal external surface oscillation as follows:

$$q^*_{os} = \frac{(i\,\omega^* + \sigma^*)\,\mathrm{A_{os}}\,Y}{\mathrm{Q_{og}}} = \frac{\omega_{ref}\,(i\,\omega^* + \sigma^*)\,\mathrm{A_{os}}\,Y}{\mathrm{V_{og}}\,\mathrm{A_{og}}} = \frac{(i\,\omega^* + \sigma^*)\,\mathrm{A_{os}}\,Y\,\omega\mathrm{A_{ss}}}{\mathrm{V_{og}}\,y_{og}\,L_o\,\mathrm{A_{ss}}}$$

Where, $A_{ss} = L_o L_g$ *and* $A_{og} = L_o y_{og}$

Then,

$$q^*_{os} = (\mathrm{i}\,\omega^* + \sigma^*)\frac{Y}{y_{og}}\frac{\omega_{ref}\,L_o L_g}{\mathrm{V_{og}}\,L_o}\frac{\mathrm{A_{os}}}{\mathrm{A_{ss}}} = (\mathrm{i}\,\omega^* + \sigma^*)\frac{y^*}{\Pi_{2g}\,\Pi_4}$$

Where, $\Pi_{2g} = \dfrac{V_{og}}{\omega_{ref}\,L_g}$, $\Pi_4 = \dfrac{\mathrm{A_{ss}}}{\mathrm{A_{os}}}$,and $y^* = \dfrac{Y}{y_{og}}$

Valve sliding seal inlet point transfer matrix

By converting the linearized seal inlet time dependent energy relation, Eq.(57) into dimensionless form and the seal inlet flow rate Eq.(58) into dimensionless form, then the dimensionless seal inlet point transfer matrix can be estimated by representing the two developed equations in matrix notation as follows:

$$\begin{bmatrix} q^* \\ h^* \\ y^* \end{bmatrix}_j^R = \underbrace{\begin{bmatrix} 1 & 0 & 0 \\ 2(\Pi_6 - \Pi_7) & 1 & -2\Pi_7 \\ 0 & 0 & 1 \end{bmatrix}}_{P_j^*} \begin{bmatrix} q^* \\ h^* \\ y^* \end{bmatrix}_j^L \qquad \text{Eq.(5.B)}$$

Where:

$$\Pi_6 = \frac{Q_{o\,j}^{L^2}}{2g\, A_j^{L^2} H_1} \quad \& \quad \Pi_7 = \frac{Q_{o\,j}^{L^2}}{2g\, A_{o\,j}^{R^2} H_1}$$

Oscillating sliding seal point transfer matrix

By converting Eq.(63) and Eq.(64) of the oscillating sliding seal into a dimensionless form; the dimensionless oscillating sliding seal point transfer matrix for free damped oscillations can be computed as:

Eq.(63) will be:

$$q^{*L}_{\;j+2} = q^{*R}_{\;j} + 0\, h^{*R}_{\;j} + i \frac{\omega A_{ss}}{Q_{og}}\, y$$

As, $Q_{og} = V_{og} A_{og}$, $A_{ss} = L_g L_o$, $A_{og} = L_o y_{og}$ and $i\omega$ is replaced by $i\omega + \sigma$

Then:

$$q^{*L}_{\;j+2} = q^{*R}_{\;j} + 0\, h^{*R}_{\;j} + \frac{(i\omega^* + \sigma^*)\,\omega_{ref}\, L_g L_o}{V_{og} L_o y_{og}}\, y$$

$$q^{*L}_{\;j+2} = q^{*R}_{\;j} + 0\, h^{*R}_{\;j} + \frac{(i\omega^* + \sigma^*)\,\omega_{ref}\, L_g}{V_{og}}\, \frac{y}{y_{og}}$$

$$q^{*L}_{\;j+2} = q^{*R}_{\;j} + 0\, h^{*R}_{\;j} + \frac{(i\omega^* + \sigma^*)}{\Pi_{2g}}\, y^* \qquad \text{Eq.(6.B)}$$

Eq.(64) will be:

$$h^{*L}_{j+2} = h^{*R}_{j} - \frac{Q^{L}_{o_{j+2}}}{H_1 g A^{R^2}_{o_j}} (i\omega A_{ss} y)$$

By multiplying the right side by $\frac{Q^{L}_{o_{j+2}}}{Q^{L}_{o_{j+2}}}$, replacing $i\omega$ by $i\omega+\sigma$, and as

$$Q^{L}_{o_{j+2}} = Q_{o_g} = V_{o_g} A_{o_g} = V_{o_g} L_o y_{o_g}$$

$$h^{*L}_{j+2} = h^{*R}_{j} - 2\frac{Q^{L^2}_{o_{j+2}}}{H_1\, 2\, g A^{R^2}_{o_j}} \frac{(i\omega^* + \sigma^*)\, \omega_{ref} L_o L_g y}{V_{o_g} L_o y_{o_g}}$$

$$h^{*L}_{j+2} = h^{*R}_{j} - 2\frac{Q^{L^2}_{o_{j+2}}}{H_1\, 2\, g A^{R^2}_{o_j}} \frac{(i\omega^* + \sigma^*)\, \omega_{ref} L_g}{V_{o_g}} y^*$$

$$h^{*L}_{j+2} = h^{*R}_{j} - 2\frac{\Pi_7 (i\omega^* + \sigma^*)}{\Pi_{2g}} y^* \qquad \text{Eq.(7.b)}$$

By writing Eq.(6.B) and Eq.(7.B) in a matrix form, the dimensionless oscillating sliding seal point transfer matrix for a free damped oscillations can be represented as follows:

$$\begin{bmatrix} q^* \\ h^* \\ y^* \end{bmatrix}^{L}_{j+2} = \underbrace{\begin{bmatrix} 1 & 0 & \frac{(i\omega^* + \sigma^*)}{\Pi_{2g}} \\ 0 & 1 & -2\frac{\Pi_7}{\Pi_{2g}}(i\omega^* + \sigma^*) \\ 0 & 0 & 1 \end{bmatrix}}_{P^*_{j+1}} \begin{bmatrix} q^* \\ h^* \\ y^* \end{bmatrix}^{R}_{j} , \qquad \text{Eq.(8.B)}$$

$$where: \Pi_{2_g} = \frac{V_{o_g}}{\omega_{ref} L_g} \;, \; \Pi_7 = \frac{Q^{L^2}_{o_{j+2}}}{H_1\, 2\, g A^{R^2}_{o_j}}$$

Valve exit point transfer matrix

By converting the linearized time dependent valve seal exit section energy relation Eq.(69) and the seal exit flow rate Eq.(67) into dimensionless form ; the dimensionless valve exit point transfer matrix can be estimated as follows:

By converting Eq.(69) into dimensionless form, Eq.(69) can be presented as follows:

$$H_1 h^{*R}_{j+2} = \frac{2Q^{L}_{o\,j+2}}{g\,A^{R^2}_{j+2}}\left(\frac{A^{R}_{j+2}}{A^{R}_{o\,j}}-1\right)Q_{og}\,q^{*L}_{j+2} + H_1 h^{*L}_{j+2} + \frac{Q^{L^2}_{o\,j+2}}{g\,A^{R^2}_{j+2}}\left(\frac{A^{R}_{j+2}}{A^{R^2}_{o\,j}}\right)L_o\, y^*\, y_{og}$$

$$h^{*R}_{j+2} = 4\frac{Q^{L^2}_{o\,j+2}}{2g\,A^{R^2}_{j+2}\,H_1}\left(\frac{A^{R}_{j+2}}{A^{R}_{o\,j}}-1\right)q^{*L}_{j+2} + h^{*L}_{j+2} + 2\frac{Q^{L^2}_{o\,j+2}}{2g\,A^{R^2}_{j+2}\,H_1}\left(\frac{A^{R}_{j+2}}{A^{R}_{o\,j}}\right)y^*$$

$$h^{*R}_{j+2} = 4\Pi_8(A^{*R}_{j+2}-1)\;q^{*L}_{j+2} + h^{*L}_{j+2} + 2\Pi_8\;A^{*R}_{j+2}\;y^* \qquad \text{Eq.(9.B)}$$

Where:

$$\Pi_8 = \frac{Q^{L^2}_{o\,j+2}}{2g\,A^{R^2}_{j+2}\,H_1} \qquad \& \qquad A^{*R}_{j+2} = \frac{A^{R}_{j+2}}{A^{R}_{o\,j}}$$

Also by converting Eq.(67) into dimensionless form, Eq.(67) can be expressed as:

$$q^{*R}_{j+2} = q^{*L}_{j+2} + 0\,h^{*L}_{j+2} + 0\;y^* \qquad \text{Eq.(10.B)}$$

By representing Eq.(9.b) and Eq.(10.B) in matrix notation, the dimensionless seal exit point transfer matrix for a free damped oscillations can be computed as:

$$\begin{bmatrix} q^* \\ h^* \\ y^* \end{bmatrix}^{R}_{j+2} = \underbrace{\begin{bmatrix} 1 & 0 & 0 \\ 4\Pi_8(A^{*R}_{j+2}-1) & 1 & 2\Pi_8\;A^{*R}_{j+2} \\ 0 & 0 & 1 \end{bmatrix}}_{P^*_{j+1}} \begin{bmatrix} q^* \\ h^* \\ y^* \end{bmatrix}^{L}_{j+2} \qquad \text{Eq.(11.B)}$$

Where, $\Pi_8 = \dfrac{Q_{o\,j+2}^{L^2}}{2g\, A_{j+2}^{R^2}\, H_1}$ & $A^{*R}_{j+2} = \dfrac{A^R_{j+2}}{A^R_{o\,j}}$

Seal equation of motion

The seal equation of motion, Eq.(79), can be converted into dimensionless form as follows:

Eq.(79):

$$M_{sg}\,\ddot{y} + C_{sg}\,\dot{y} + K_{sg}\,y = \rho g(\,A_{os}\,h_3^r(t) - A_{ss}\,h_4^r(t))$$

By dividing both sides by $\rho g\, H_1 A_{os}$ and converting the vibration components $\ddot{y}, \dot{y}$ and y into dimensionless form; the dimensionless equation of motion will be:

$$\frac{M_{sg}\,y_{og}(\omega - i\sigma)^2}{\rho g\, H_1 A_{os}} \frac{d^2 y^*}{d t^{*2}} + \frac{C_{sg}\,y_{og}(\omega - i\sigma)}{\rho g\, H_1 A_{os}} \frac{d y^*}{d t^*} + \frac{K_{sg}\,y_{og}}{\rho g\, H_1 A_{os}} y^* = (h^{*r}_3(t) - \Pi_4 h^{*r}_4(t))$$

$$M^*_{sg} \frac{d^2 y^*}{d t^{*2}} + C^*_{sg} \frac{d y^*}{d t^*} + K^*_{sg}\, y^* = h^{*r}_3(t) - \Pi_4 h^{*r}_4(t) \qquad \text{Eq.(12.B)}$$

Where: $\Pi_4 = \dfrac{A_{ss}}{A_{os}}$

B.2. 2nd Model dimensionless pi-groups

According to the dimensionless analysis developed in the previous section; the phenomenon under consideration has 9 Π-groups as follows:

$$\Pi_{1j} = \frac{L_j\, \omega_{ref}\, Q_{og}}{g\, A_j\, H_1}, \quad \Pi_{2j} = \frac{V_{og}}{\omega_{ref}\, L_j}, \quad \Pi_{3j} = \frac{H_{Lj}}{H_1}, \quad \Pi_4 = \frac{A_{ss}}{A_{os}}, \quad \Pi_{5j} = \frac{V_{og}}{a_j},$$

$$\Pi_6 = \frac{Q_{ob1}^{L^2}}{2g\, A_{b3}^2 H_1} \quad \Pi_7 = \frac{Q_{og}^2}{2g\, A_{og}^2\, H_1}, \quad \Pi_8 = \frac{Q_{oc}^2}{2g\, A_c^2\, H_1}, \quad \Pi_9 = A_j^* = \frac{A_j}{A_{og}}$$

Although, the aim of this section is to develop the least amount of Π-groups that can explain the phenomenon through the developed 9 Π-groups as following:

1. As Π_{1_j} is the pipeline inertia ratio to input reservoir energy level, then the main line inertia ratio to gap kinetic energy can be estimated by dividing the result of adding pipelines Pi-groups Π_{1_a}, Π_{1_b} and Π_{1_d} by Π_7 (i.e. which is the gap kinetic energy ratio to input reservoir energy level) as follows:

$$\Pi_1 = \frac{\Pi_{1m}}{\Pi_7} = \frac{\Pi_{1_a} + \Pi_{1_b} + \Pi_{1_d}}{\Pi_7} = \frac{I_m \, \omega_{ref} \, Q_{og}}{\dfrac{Q_{og}^2}{2g \, A_{og}^2}} = \frac{I_m \, \omega_{ref} \, Q_{og}}{H_1}$$

Where: $I_j = \dfrac{L_j}{g \, A_j}, I_m = I_a + I_b + I_c$

2. The second Π-group is main line flow oscillation speed ratio to pipeline wave speed. This Π-group can be estimated by the aid of pipelines reduced velocity and gap flow Mach number as follows:

$$\Pi_2 = (\Pi_{2_a}^{-1} + \Pi_{2_{b1}}^{-1} + \Pi_{2_g}^{-1} + \Pi_{2_c}^{-1}) \Pi_{5_j} = \frac{\omega_{ref} \, (L_a + L_{b1} + L_g + L_c)}{a_j}$$

3. According to the case under consideration as the main line losses is negligible in comparison to input reservoir energy level, changing main line geometric characteristics to increment line losses are not of a practical solution, and modifying pilot pipeline flow characteristics (i.e. such as adding a valve to the pilot pipeline to increment pipeline resistance or varying pilot pipeline geometrical characteristics to decrement pilot pipeline flow inertia) is much more easier than modifying mainline flow characteristics, hence the third Π-group concerns pilot line flow inertia ratio to pilot line head losses which is developed by dividing Π_{1_d} (i.e. pilot line inertia ratio to input reservoir energy level) by Π_{3_d} (i.e. which is pilot pipeline loss to input reservoir energy level):

$$\Pi_3 = \frac{\Pi_{1d}}{\Pi_{3d}} = \frac{I_d\,\omega_{ref}\,Q_{og}}{H_{Ld}} = \frac{I_d\,\omega_{ref}\,Q_{og}}{R_d\,L_d\,Q_{og}}$$

4. The forth Π-group concerns seal geometry, where the seal surface area facing leakage flow (i.e. gap flow) is divided by the seal external surface area facing pilot pipeline hydro-pressure forces:

$$\Pi_4 = \frac{A_{ss}}{A_{os}}$$

The rest of the Π-groups are going to be neglected due to the following reasons:

- As $\Pi_6 = \dfrac{Q_{ob}^2}{2g\,A_{b3}^2 H_1}$ appears only in Eq.(5.B) and its value is negligible in comparison to Π_7; hence neglecting the effect of $\Pi_6 = \dfrac{Q_{ob}^2}{2g\,A_{b3}^2 H_1}$ is adequate.

- Π_8 effect is taken into consideration as Π_8 can be computed as a function of Π_7 and Π_9 so there is no need to represent it as a separate Pi-group,

  $$\because Q_{og} = Q_{oc}$$
  $$\therefore \Pi_8 = \frac{\Pi_7}{\Pi_9^2} = \frac{Q_{og}^2}{2g\,A_{og}^2 H_1}\,\frac{A_{og}^2}{A_c^2}$$

- Finally Π_9 influence is already considered since Π_{1j} is function of Π_9 such as follows:

  $$\because Q_{og} = V_{og}\,A_{og}$$
  $$\therefore \Pi_{1j} = \frac{L_j\,\omega_{ref}\,V_{og}}{g\,H_1}\,\frac{A_{og}}{A_j} = \frac{L_j\,\omega_{ref}\,V_{og}}{g\,H_1}\,\frac{1}{\Pi_9}$$